RICE UNIVERSITY

Novel Material Behavior in Carbon Nanotube/Elastomer Composites

by

Brent J. Carey

A THESIS SUBMITTED
IN PARTIAL FULFILLMENT OF THE
REQUIREMENTS FOR THE DEGREE

Doctor of Philosophy

APPROVED, THESIS COMMITTEE

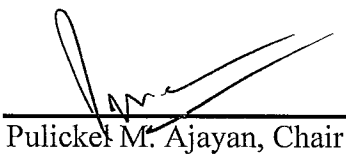

Pulickel M. Ajayan, Chair
Benjamin M. and Mary Greenwood
Anderson Professor of Engineering

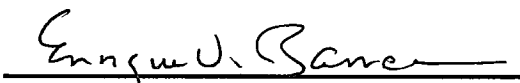

Enrique V. Barrera
Professor of Mechanical Engineering &
Materials Science

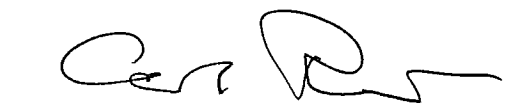

Carl Rau
Professor of Physics & Astronomy

HOUSTON, TEXAS
November 2011

ABSTRACT

Novel Material Behavior in Carbon Nanotube/Elastomer Composites

by

Brent J. Carey

Composites are multiphasic materials with individual constituent parts that work cooperatively to produce some desired result. For the common case of structural composites, the use of nanoscale additives does not always yield a predictable outcome due to the complex interactions that occur in the interfacial region where a reinforcing filler meets the supporting matrix. It stands to reason, however, that the thoughtful and deliberate exploitation of unusual effects in this region could lead to the development of nanocomposite materials with extraordinary properties. In this thesis work, I will introduce two such responses in a compliant nanocomposite consisting of highly-aligned carbon nanotubes (CNTs) encased within a poly(dimethylsiloxane) (PDMS) matrix. It is first demonstrated that the material exhibits extremely anisotropic dynamic mechanical behavior. The composite will behave in a way that is evocative of the neat polymer when deformed orthogonal to the CNT alignment direction, yet will exhibit strain softening when cyclically compressed along their axis due to the collective buckling of the nanotube struts. Next, it is shown that this nanocomposite material has the ability to respond and adapt to applied loads. Independent, yet complimentary tests reveal that the structure of the polymer in the presence of nanoscale interstitials will evolve during

dynamic stressing, an effect that was predicted nearly 50 years ago. With support from both recent and established literature, an updated mechanism is proposed. Collectively, these results provide insight into the complicated mechanics between polymer matrices and embedded nanoparticles, and assist in the design of advanced synthetic materials with unique physical properties

.

Acknowledgments

The path to PhD has been a strenuous, yet enriching experience. I've grown tremendously over the past 5 years, and never would have reached this point without the help of everyone mentioned below.

I'd first like to show gratitude to my advisor, Prof. Pulickel M. Ajayan, for providing the driving force behind my research. In addition to his scientific expertise, he has constantly encouraged me to explore my interests, both academic and extracurricular. He is a patient and approachable mentor, and has treated me with the utmost respect during my time in his group, a reality that not all graduate students share. I'd also like to thank the other members of my committee, Prof. Enrique V. Barrera and Prof. Carl Rau, for their thoughtful feedback on my research.

I am indebted to the numerous researchers with whom I have collaborated along the way, including Dr. Lijie Ci. Dr. Kevin Yager, Prof. Glaura Silva, Dr. Shashi Karna, Dr. Jerome Tzeng, Dr. Myung Gwan Hahm, Prof. Andrew Gouldstone, and Dr. Meng Qu. Appreciation is also shown to Prof. Rafael Verduzco, Dr. Mary Jane O'Rourke, and Prof. Edwin Thomas for meaningful discussions.

I'd like to specifically mention Prof. Prabir Patra, as he had the foresight to procure the DMA for our group, and has gone out of his way over the years to maintain contact with me and encourage my progress. His dedication to my growth as a scientist is deeply appreciated.

Of course, this research would not be possible without the financial support of the NASA Graduate Student Researchers Program (GSRP). I owe many thanks to the nanomaterials group at the Johnson Space Center, including Dr. Brad Files, Dr. Ed Sosa, Dr. Rodrigo Devivar, and Mr. Eric Malroy, for their support and hospitality.

The support staff of both the Applied Physics degree program and the Mechanical Engineering and Materials Science department have played a pivotal role in helping me navigate formalities, and Dr. Bruce Johnson, Ms. Yvonne Kambourelis, Ms. Carolyn Aresu, Ms. Sherry Vanderslice, and Ms. Linda Lerma are thanked for their assistance. Also, gratitude is shown to Dr. Jan Hewitt for her help in scientific writing and presenting, as well as the unsung heroes of the Fondren Library, who hunted down all of the obscure journal articles I requested.

Not to be forgotten is the incredible social structure for graduate students at Rice University. This whole process would have been much more wearisome had there not been a place to hang my hat and commiserate with other burgeoning (read: struggling) researchers. Viva Valhalla.

Finally, I owe the most to my incredible family. My parents have always encouraged me to reach higher, and their support has given me the confidence to achieve this life-long goal. My wife, Sarah, deserves recognition for her unwavering support over the years, and particularly for relocating to Houston so that I could pursue my degree. She has been my rock, and is a saint for tolerating the long (and often miserable) hours that graduate study requires. For these and many other reasons, I wouldn't be where I am today without her.

Contents

List of Figures

List of Tables

List of Equations

Nomenclature

PDMS	Poly(dimethylsiloxane)
CNT	Carbon Nanotube
A-CNT	Aligned Carbon Nanotube
SWNT	Single-Walled Carbon Nanotube
DWNT	Double-Walled Carbon Nanotube
FWNT	Few-Walled Carbon Nanotube
MWNT	Multi-Walled Carbon Nanotube
CVD	Chemical Vapor Deposition
SEM	Scanning Electron Microscopy
TEM	Transmission Electron Microscopy
DMA	Dynamic Mechanical Analysis
DSC	Differential Scanning Calorimetry
TGA	Thermogravimetric Analysis
AFM	Atomic Force Microscopy
CTE	Coefficient of Thermal Expansion
SAXS	Small-Angle X-Ray Scattering
WAXS	Wide-Angle X-Ray Scattering
tan δ	Tangent δ (damping)
T_g	Glass Transition Temperature
T_c	Crystallization Temperature
T_{m1}	First Crystal Melting Temperature
T_{m2}	Second Crystal Melting Temperature

Chapter 1

Introduction

1.1. Introduction to Carbon Nanotubes

Since the highly-cited 1991 paper that first confirmed their existence [1], carbon nanotubes (CNTs) have been the focus of considerable attention due to their extensive array of truly remarkable properties [2]. Over the past two decades, CNTs have seen application in chemical sensing [3], hydrogen storage [4], field emission [5], artificial muscles [6], the filtration of both pathogens [7] and heavy metals [8], thermal management [9], and have served as electrodes for capacitors [10], not to mention the fact that they have even been commissioned as the axles in the first "nano-sized" vehicles [11]. The dizzying array of applications for which CNTs have been envisaged is a testament to the impressive breadth of their fundamental properties.

This wide range of applications can be attributed to the fact that the physical properties of these macromolecules exceed virtually all other materials. Specifically, it has been reported that CNTs are capable of ballistic electrical conduction [12], their axial tensile strength has been shown to be on the order of 1 TPa [13], and their thermal conductivity at room temperature has a theoretical limit of 6,600 $\frac{W}{m-K}$ [14]. Given these complimentary attributes, it is perhaps not surprising that CNTs have been lauded as some of the most perfect molecules that could exist.

Perhaps even more interestingly, the commonly used title "carbon nanotube" encompasses a broad range of tubular carbon allotropes with markedly different properties. As a quasi-one-dimensional molecule, CNTs can range from a few dozen nanometers [15] up to over 18 cm in length [16]; with diameters ranging from the sub-nanometer regime [17] to well over 100 nm, the aspect ratio of these structures can be as low as 45:1 and as staggeringly high as 132,000,000:1. While CNTs are generally envisaged as a single sheet of graphene rolled into a tube, other geometries are common and, in some cases, desired.

CNTs come in "single" (SWNT; Figure 1.1a) and "multi-walled" (MWNT; Figure 1.1b) varieties, with special cases such as those which are "double-walled" (DWNT) or "few-walled" (FWNT). While MWNTs are regarded for their superior stiffness [18] and electrical conductivity [19], SWNTs remain the most desirable due to their high thermal diffusivity [19], well-defined electronic band structure [20], and flexibility at the microscale [21]. Furthermore, DWNTs are of particular interest

due to their SWNT-like mechanical resilience [22] while having an outer wall that can be chemically modified without compromising the pristine structure of the core tube [23].

Adding further depth to the assortment of CNTs described above, the helicity (Figure 1.1c) and handedness (Figure 1.1d) of individual nanotube walls—denoted a CNT's "chirality"—greatly affects its electrical behavior; specific chiralities conduct as metals, while others behave as semiconductors. However, due to the complexity of a MWNT and the lack of control over the chirality of each of its individual walls, this term is almost exclusively used for SWNTs. The desire to utilize specific SWNT chiralities has spawned research efforts to isolate them [24], including separation via ultracentrifugation [25], and the growth of specific chiralities by "cloning" seed nanotubes [26], [27] or exclusively synthesizing metallic/semimetallic CNTs [28]. These distinctions can be further complicated by the introduction of elemental interstitials into the CNT structure [29]. Dopants such a boron [30–32] and nitrogen [33–35] have been credited for abnormalities such as "bamboo-like" tubes and "stacked cone" structures.

1.1.1. A Brief History of Carbon Nanotube Synthesis

CNT synthesis has remained an active area of research since nanotubes were first discovered. While the early techniques are still used today, the process of growing carbon nanotubes has expanded considerably over the past twenty years.

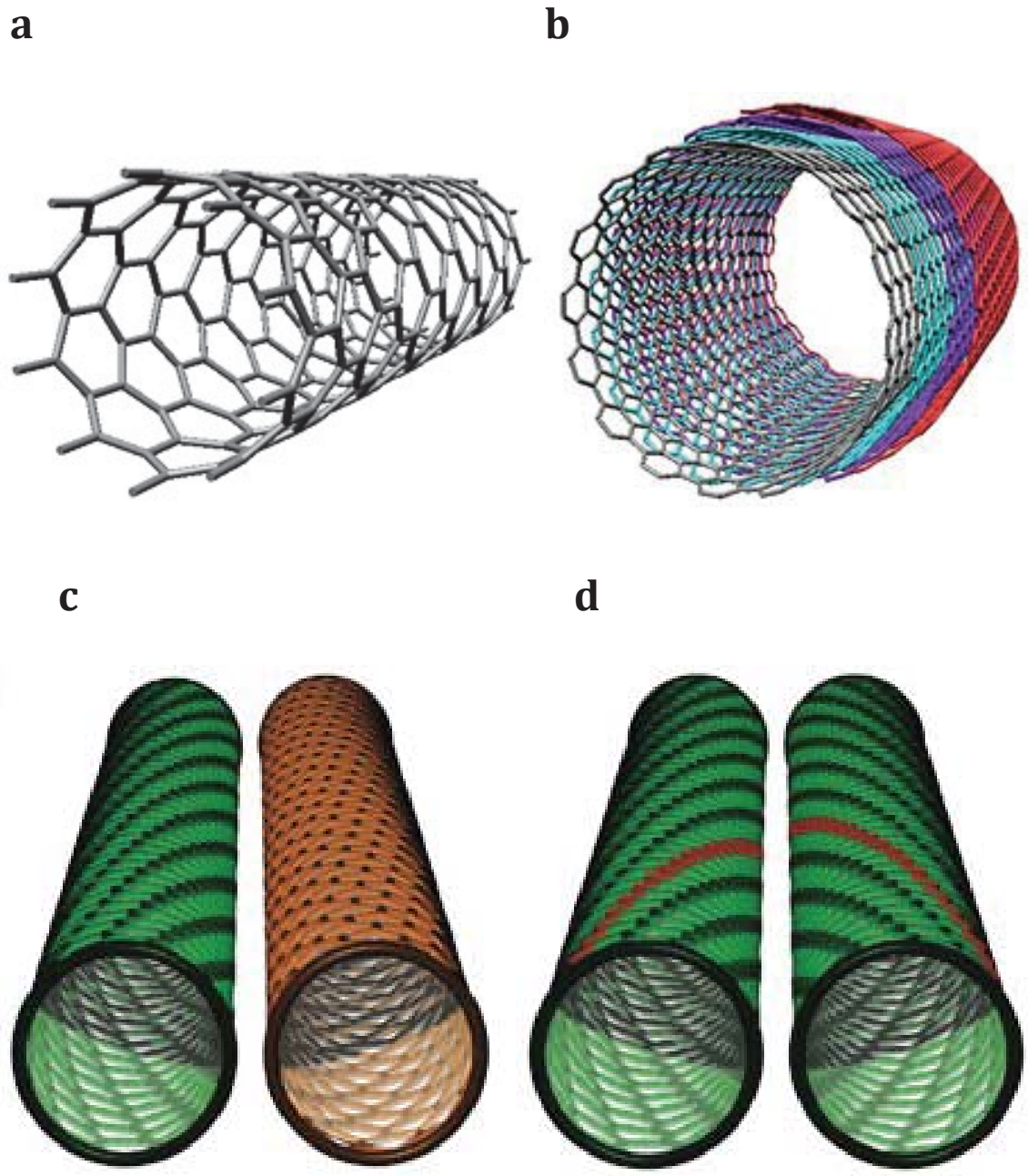

Figure 1.1 – Schematics of (a) single-walled and (b) multi-walled carbon nantotubes (SWNTs and MWNTs, respectively; adapted from [36]), as well as examples of differences in SWNT (c) chirality and (d) handedness (adapted from [24]).

The idealized properties mentioned previously are generally accepted as theoretical limits, though in practice, the synthesis of such high-quality CNTs is prohibitively expensive (if even feasible) for large quantities. Arc discharge was indeed the first method of producing CNTs (first reported by Iijima in 1991 [1] and then expanded a few years later by Ebbeson & Ajayan [37]), and it remains the method of choice for producing the least defective CNTs if there is little concern for their length. In this method, graphitic rods are arced in a sub-atmospheric inert environment (such as helium) to produce a plasma that will provide sufficient energy for synthesis.

Smalley and co-workers then developed the laser ablation technique in 1995 [38], a technique which was heralded for its predominantly SWNT yield. In this procedure, a composite target consisting of graphitic carbon and a high-purity transition metal or metal oxide is vaporized with a laser in the presence of an inert gas. Subsequently, the carbon will condense on cool surfaces in the reaction chamber, where CNTs will form. Despite this process' efficiency in producing moderately large quantities of quality CNTs, the prohibitive cost has hindered its viability as a large-scale production method.

As first reported in 1993 by José-Yacamán *et al.* [39], nanoparticles of certain transition metals in an ~700–900 °C environment will consume the byproducts of decomposed hydrocarbons to catalyze the growth of CNTs. This chemical vapor deposition (CVD) process was expanded upon by Endo *et al.*, who adapted a technique similar to what was used to synthesize vapor-grown carbon nanofibers to

devise a method of growing CNTs off of floating catalyst particles [40]. Despite the fact that CVD generally produces CNTs with a greater degree of defects as compared to arc discharge and other high-energy techniques [41], this method would grow in popularity to become the method of choice for the large-scale, low-cost production of carbon nanotubes.

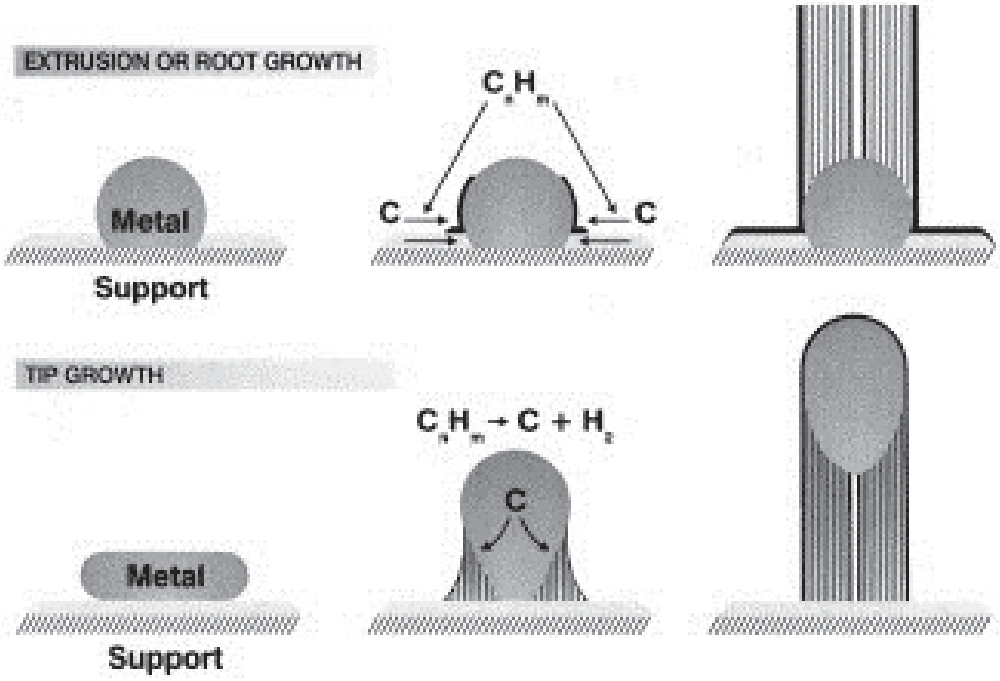

Figure 1.2 – Schematic illustrating proposed root growth and tip growth mechanisms for CNTs synthesized off of a substrate [42].

In particular, the floating catalyst CVD method has seen numerous successful iterations which have grown into viable commercial ventures. The early floating catalyst procedures as reported by Nikolaev *et al.* [43] and Kitiyanan *et al.* [44] served as the basis for the popular HiPCO™ and CoMoCAT™ procedures, respectively. The quality of these and other commercially-produced CNTs has

increased notably in the recent past, while the cost-per-gram has also steadily decreased. Today, commercial providers are a reliable source of CNTs for researchers as well as end users, and further scaling of production will soon bring the cost of CNTs into a regime where they can be adopted for a wide range of commercial applications.

a

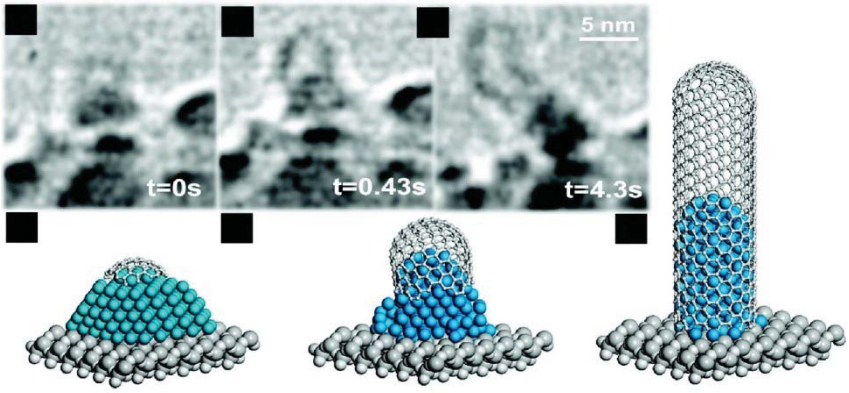

b

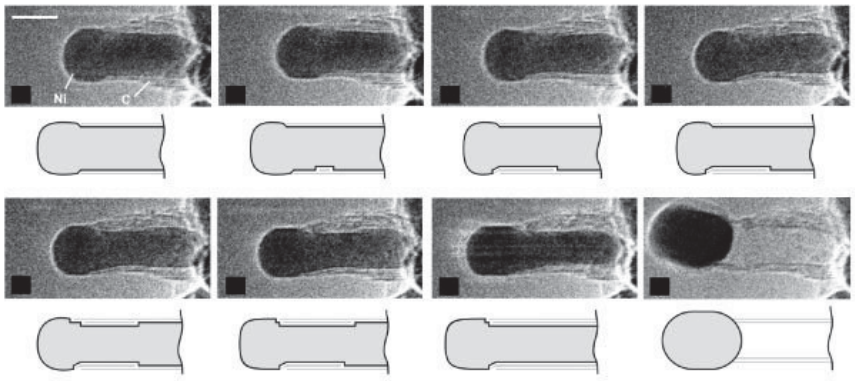

Figure 1.3 – Transmission electron microscopy (TEM) evidence of (a) root and (b) tip growth of carbon nanotubes from a substrate (adapted from [45] and [46], respectively).

Despite these advances, the mechanism(s) of CNT synthesis are still not yet completely understood. CVD growth remains an active area of carbon nanotube research to this day, and many modeling efforts have begun to unravel the complex high-temperature mechanisms responsible for the initiation and termination of CNT synthesis [47], [48].

1.1.2. Growing Vertically-Aligned Arrays of Carbon Nanotubes

CVD has proven to be a remarkably adaptable synthesis technique, and one such variation of the method enables the synthesis of self-assembled architectures. As first reported by Li *et al.* in 1996 [49], nanotubes can be synthesized collectively and simultaneously off of a substrate. A year later, plasma would be introduced to a similar process where "forests" or "carpets" of highly-aligned CNTs (A-CNTs) were grown off of a single-crystal nickel substrate [50]. The output of these early methods was rather limited, and they exclusively produced MWNTs with lengths less than 40 μm.

Sinnot *et al.* would propose two possible mechanisms for the substrate growth of CNTs (Figure 1.2) involving a catalyst that either remains anchored to the substrate (root growth) or one that becomes detached from the substrate and rises normal to the surface while continually building off of the seeded CNT (tip growth) [42]. Evidence of catalyst dynamics matching both of these growth mechanisms would subsequently be validated via the *in situ* transmission electron microscopy (TEM) observations of CNT synthesis by Hofman *et al.* [45] and Helveg *et al.* [46], respectively (Figure 1.3).

Present-day techniques for the CVD synthesis of CNT forests can largely be categorized by two methods of catalyst introduction: (1) the pre-deposition of the catalyst directly on the desired substrate, and (2) the vapor-phase delivery of the catalyst along with the carbon source.

By pre-depositing the catalyst directly on the desired substrate via either sputter coating or electron beam evaporation, it is possible to control the resultant CNTs that will comprise the forest. This method allows for a tight distribution of CNT diameters, and the measure of those diameters has been shown to scale with the thickness of the catalyst layer [51], [52]. This layer, which generally measures between .5 to 5 nm, can be patterned on the substrate, allowing for the surface-mediated growth of 2D structures such as towers or columns [53].

As with all CVD methods though, the success and ultimate height of the forest is largely dependent on the efficiency of the catalyst and, implicitly, how long it remains active during growth. The premature termination of synthesis has been attributed to the formation of an amorphous carbon layer on the surface of the catalyst particles [46]. To address this issue, Hata and Futaba *et al.* introduced water to the reaction chamber during growth to serve as a weak oxidant and prevent such a layer from "poisoning" the catalyst [54]. Their method—termed "supergrowth"—allowed for the growth of truly macroscopic A-SWNT forests that measured up to 2.5 mm tall (Figure 1.4). In contrast, Amama and co-workers suggested that the water's success in supergrowth is due to the attachment of hydroxide species on the inter-catalyst substrate area, thereby retarding the

Ostwald ripening of the catalyst particles and maintaining their efficacy [55]. The further refinement of supergrowth has resulted in the growth of forests up to 5 mm tall [56].

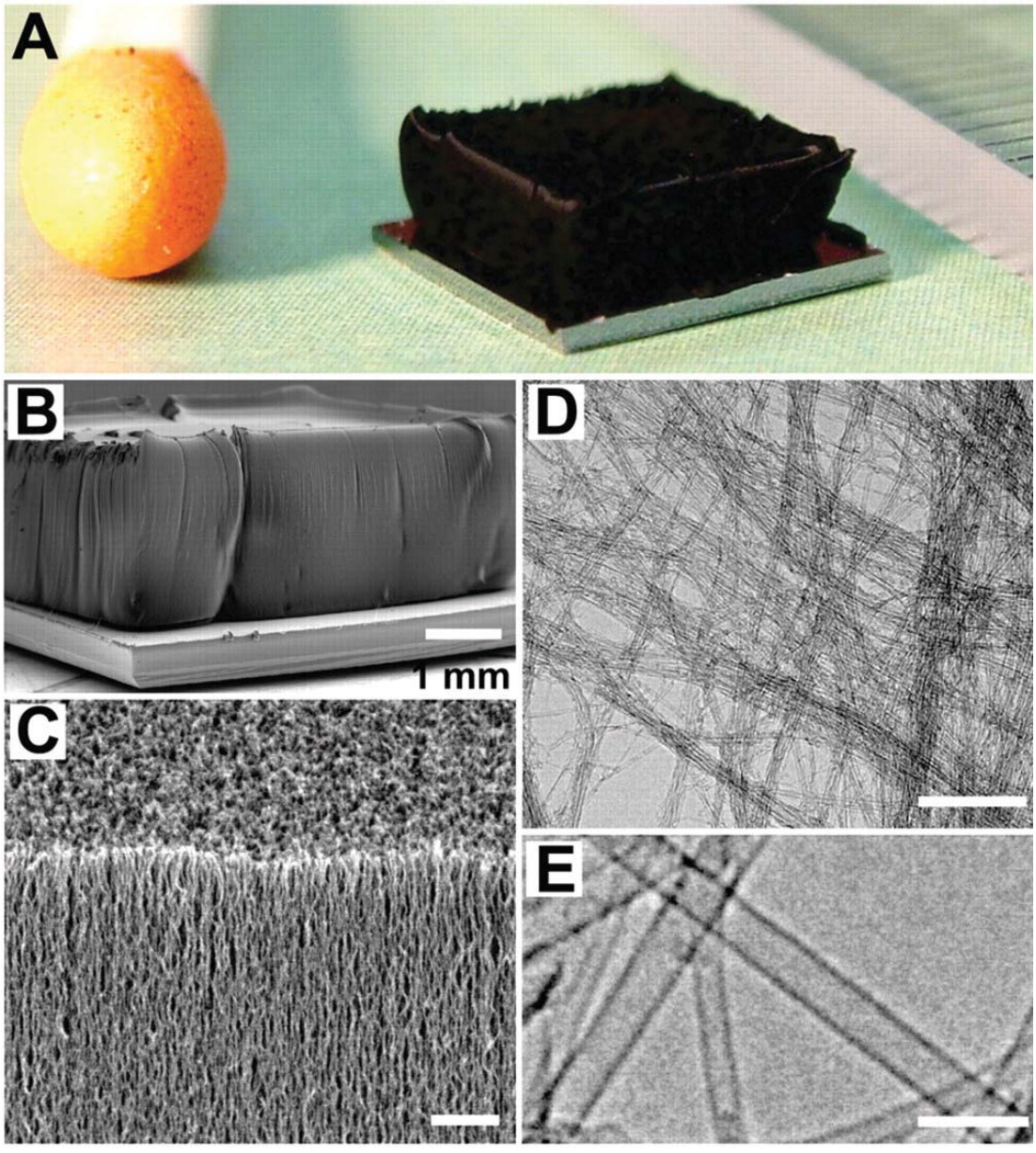

Figure 1.4 – (a) SWNT forest grown via "supergrowth". (b, c) Scanning electron microscopy (SEM) and (d, e) TEM of the same forest indicate the extreme length and quality of the CNTs [54].

The aforementioned relationship between the thickness of the catalyst layer and the resultant CNTs has proven useful in the engineering of substrates capable of producing CNT forests consisting of similar nanotubes [51], and one such example is the synthesis of predominantly double-walled CNT forests [52]. DWNTs had previously been synthesized in gram quantities by a floating catalyst method [57], and their dual-wall structure has been promoted as desirable for the effective mechanical reinforcement of polymers with carbon nanotubes [58].

In contrast to the pre-deposited catalyst method, where the substrate complexity is constrained to patterning on planar surfaces, vapor-phase CVD can be utilized to nucleate CNTs off of complex structures and surfaces. This is generally done by dissolving the catalyst source in an organic solvent and introducing the mixture to the growth environment using injection [59], spray [60], or atomization [61] and using a secondary heater to vaporize the precursors before they enter the growth environment. Under the proper conditions, the liberated catalyst will deposit on compatible surfaces to form the nucleation sites for growth. This technique has been used for synthesis on various substrates, including oxidized silicon, quartz, and even directly on the surface of carbon fibers [62]. Additionally, one can pattern an oxide layer to selectively designate growth regions to enable the creation of 2D and even 3D structures such as pillars and "daisies" [63].

Unfortunately, the CNTs synthesized by vapor-phase CVD are generally of a much lower quality than those grown using a pre-deposited catalyst. This is largely due to the fact that the catalyst is not nearly as well-controlled in this method, which

results in nanotubes that tend to have an inconsistent number of concentric walls and, correspondingly, a much wider distribution of diameters. Furthermore, the CNTs produced by this method are liable to have many more defects and a pyrolized carbon sheath that is graphitic, yet not concentric. Despite these limitations, the vapor-phase method enables otherwise unfeasible growth procedures, such as the recent application of a "conveyor belt" system to enable continuous growth on a long fiber (Figure 1.5) [64].

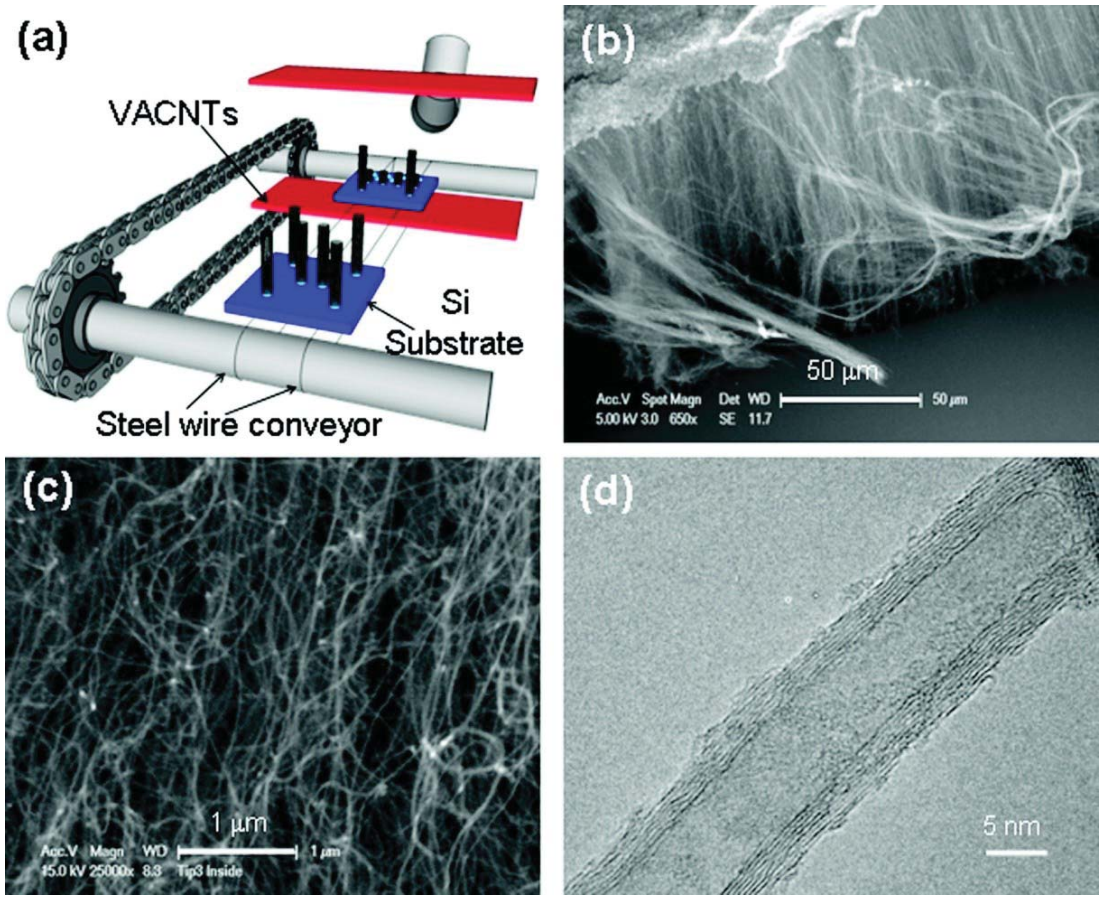

Figure 1.5 – Vapor-phase growth allows for the flexibility of using (a) a "conveyor-belt" growth process. However, (b–d) the quality of the resultant CNTs is lower than those produced via a pre-deposited catalyst [64].

1.2. Introduction to Nanocomposite Materials

By definition, nanocomposites are multi-phasic materials where at least one phase has a physical dimension that measures between 1–100 nm. This is typically achieved by adding a nanoscale filler that is either zero-dimensional (e.g. nanoparticles), one-dimensional (e.g. nanofibers, nanotubes), two-dimensional (e.g. nanoplatelets, nanoribbons, graphene), and even three-dimensional (e.g. a percolated network of nanoscale fillers) [65].

The engineering of such composites poses unique challenges, but the inherent complexity afforded by the surface area of nanostructures provides an opportunity to design materials with remarkable properties and/or functionality. In fact, nature is rife with examples of nanostructured materials such as nacre, the iridescent material in seashells. This assembly of otherwise weak components owes its impressive toughness to their nanoscale hierarchical organization (Figure 1.6a) [66], [67]. Similarly, bones are capable of bearing impressive loads due to their structure, which consists of thin apatite nanocrystals supported by a collagen-rich matrix [68].

Lessons such as these can be learned from nature to inspire the design of synthetic materials that have truly remarkable properties [69]. For example, sea cucumbers have the ability to quickly and reversibly adjust the stiffness of their inner dermis by regulating the interactions in a matrix of collagen fibrils [70]. A composite reinforced with cellulose nanofibers was subsequently developed that

mimics this effect through chemical switching, enabling nearly a three order-of-magnitude change in strength (Figure 1.6b).

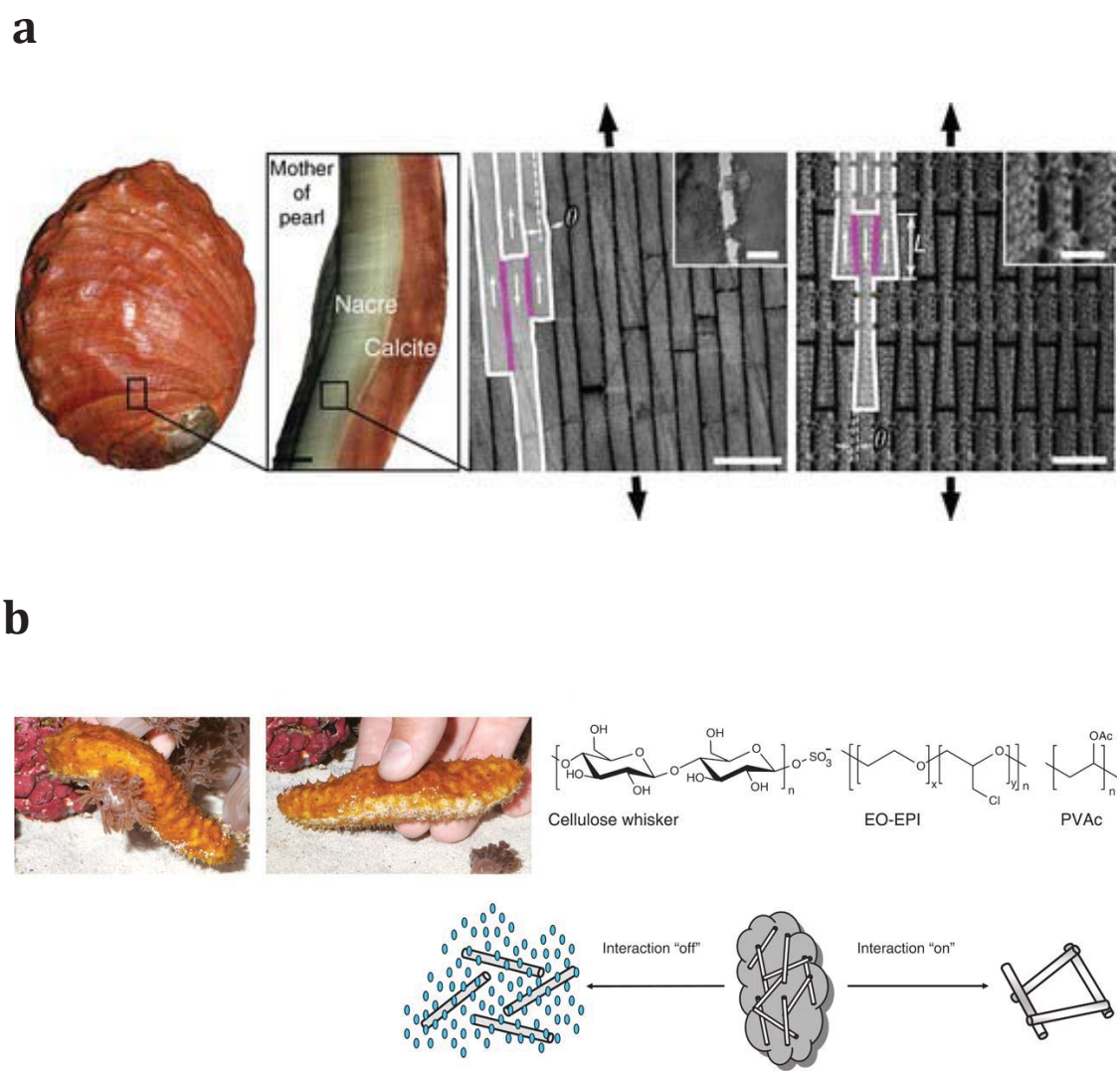

Figure 1.6 – Examples of nanoscale (a) hierarchical organization and (b) structure-property behavior can be found in nature, and have been mimicked in the development of impressive synthetic materials (adapted from [67] and [70], respectively).

1.2.1. Comparing Various Matrices and Fillers

Of course, the effect of additives and the approach in incorporating them depends greatly on the desired matrix. Ceramic matrix nanocomposites have only been modestly explored, though it has been reported that CNT inclusions can contribute to a notable increase in the fracture toughness of alumina [71], [72]. While they would not rigidly be considered a "composite material", ceramics with two distinct nanocrystalline phases have also been shown to have superior mechanical properties as compared to traditional ceramic materials [73].

Metal matrix nanocomposites have been studied more thoroughly, though many processing difficulties still remain. Like their ceramic matrix counterparts, many metals have been modified with nanocrystalline phases [74]. By the way of nanostructured additives, many groups have attempted to incorporate CNTs into surface coatings using techniques such as electroless plating [75], [76], thermal spray [77], as well as cold spray [78], with varying degrees of success. Tribologically (or, pertaining to surface sliding and friction), the use of CNTs in such coatings has been shown to enhance the resistance to wear for aluminum [79] and nickel [76] matrices due to the effect they have on reducing the grain size of the metal and the inherent lubricity that their presence provides.

For the enhancement of bulk properties in metal matrix nanocomposites, nanomaterials have been incorporated using many methods including ball milling [80], cold [81] and hot pressing [82], and even high-pressure torsion [83]. These methods have produced materials that have displayed increased mechanical

properties such as elastic modulus [78], [81], [84], [85], hardness [85], [86], and tensile strength [84], as well as thermal conductance [87], [88], electrical conductance [89], [90], and thermal expansion [91]. Many of these enhancements are governed by unpredictable behavior at the interface between the metal matrix and the additive. This has been reported for copper [92], [93] and aluminum [80], [94], which—in the case of CNT fillers—will form carbides in this region (Figure 1.7). Furthermore, the survivability of nanoparticles during the aggressive metal processing methods (e.g. ball milling and extrusion [80], [95], thermal spray [96]) is still not clear.

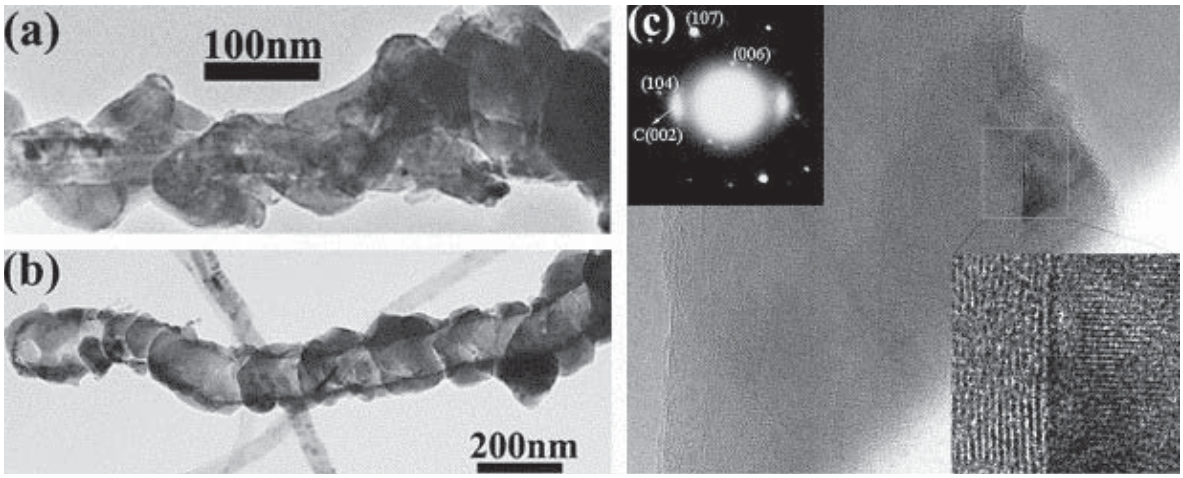

Figure 1.7 – A carbide will form at the interface between aluminum and interstitial carbon nanotubes to facilitate enhanced interaction between the two phases [94].

While there have been advances in both ceramic and metal matrix nanocomposite materials, the term "nanocomposite" is most commonly associated with polymeric nanocomposites. Since the early 1900's, carbon black has been

added to rubber in the production of tires, increasing its tensile strength and wear resistance while also imparting its characteristic black color [97]. The use of nanomaterials for the enhancement of polymers has expanded in recent times to include various inorganic nanoparticles [98], [99], nanoclay platelets [100–102], and, recently, graphene [103], [104] to impart flame retardancy [100], [101], electroluminescence [99], [105], and mechanical improvement [102–104].

For the following sections and the entirety of this thesis, the terms "composite" and "nanocomposite" are used to exclusively refer to polymer matrix composites.

1.2.2. Managing Aggregation and Dispersion

Irrespective of the desired matrix material, the greatest challenge to manufacturing ideal nanocomposite materials is arguably the homogeneous dispersion of the fillers. This is largely due to the fact that the impressive, interesting, or otherwise useful characteristics of nanoscale materials are not effectively imparted upon the matrix if these particles or macromolecules are bound within aggregates.

This is somewhat of an ironic problem, as the diminutive size of these particles also enables the formation of stable aggregates; the small size of the fillers allows for close packing, and this intimate contact results in strong van der Waals attraction. Correspondingly, aggregation poses significant processing difficulties that plague the development of ideal nanocomposites.

Many have attempted to mitigate poor dispersion by intercalating or exfoliating the dense aggregates/bundles [106–108]. Similarly, techniques have also been developed that modify the surface of the fillers to limit interparticle attractions. Such methods include the formation of non-covalent "micellic" structures around the fillers (Figure 1.8) [109], as well as the covalent addition of functional groups [110–112] to buffer against aggregation.

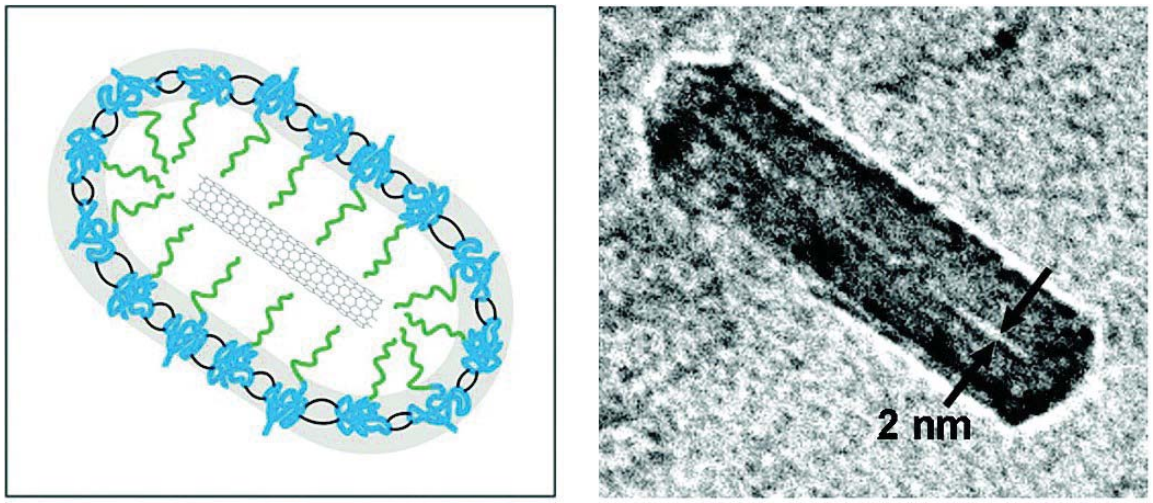

Figure 1.8 – The formation of micellic structures around nanoparticles can help prevent aggregation in nanocomposites [109].

Alternatively, others have attempted to enhance the dispersion of nanofillers in such viscous media through the use of forceful mixing methods. Compounding techniques such as injection molding [113], [114], high-shear mixing [115], [116], and extrusion [117–121] have been used to break up aggregates through strong shearing forces. For example, in the case of nanoplatelet fillers—as illustrated in Figure 1.9—such processing techniques can assist in the shrinking of tactoids,

ultimately leading to their intercalation and exfoliation. However, as with the vigorous processing methods used to disperse nanofillers into metal matrix composites mentioned in Section 1.2.1, it is suspected that these high-energy methods may cleave or otherwise damage high-aspect-ratio nanofillers, potentially compromising percolative networks that can enhance electrical conductivity and reinforcement capacity [122].

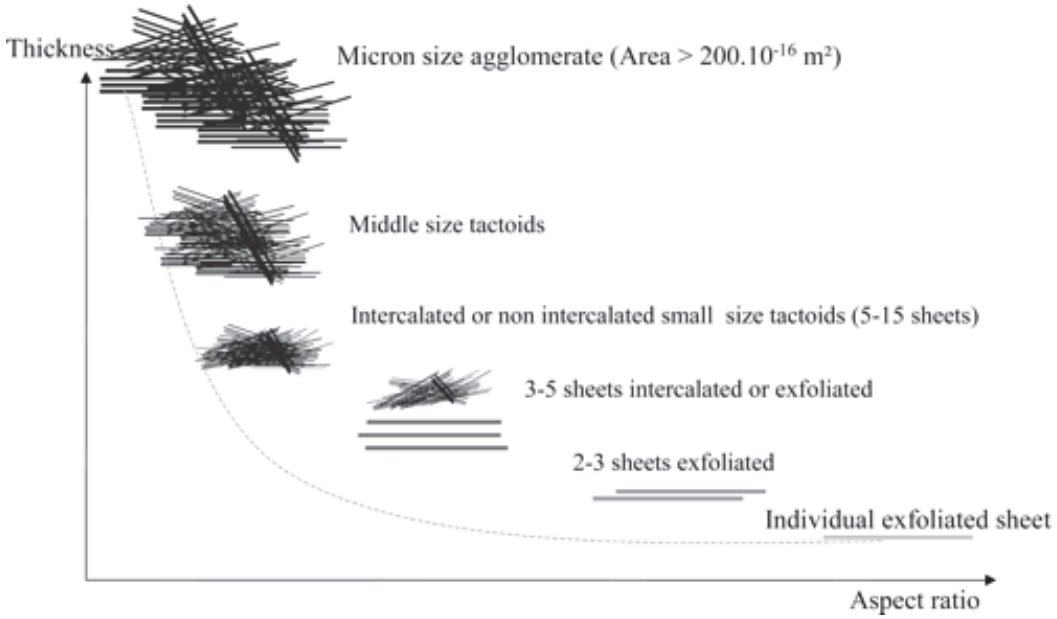

Figure 1.9 – Illustration showing the numerous tactoid classes in the intercalation and exfoliation of nanoplatelets [121].

1.2.3. Understanding the Interface and Interphase

As progress is made in the dispersion of nanomaterials in polymer matrices, a greater degree of the fillers' surface area will be accessible by the surrounding matrix. This region where the two distinct phases meet—commonly known as the

interface—has long been of great interest in polymer composites as it directly governs the effectiveness of load transfer from the matrix to the filler. Due to the immense specific surface area of the nanofillers, the interactions in this region contribute substantively to the bulk properties of the nanocomposite [123].

One method of engineering a strong interaction between these two fillers is by chemically altering the surface of the filler to be more compatible with the matrix. This process, known as either functionalization or grafting, was first explored in the late 1990's [124], [125] and has since been applied to many types of nanofillers [103], [126–128]. Interfacial bonding can facilitate strong interaction between the matrix and the filler [129], [130], yet is not always ideal due to the necessity of bonding sites on the filler's surface. In the case of CNTs, graphene, and other nanomaterials whose properties are sensitive to defects in their bonding structure, the addition of functional groups may compromise that structure and reduce their reinforcement effectiveness.

Alternatively, strong interfacial contact can be enabled through non-covalent interactions such as π-π stacking, van der Waals forces, and charge-transfer interactions (Figure 1.10) [131]. It has even been demonstrated that polymers can be "wrapped" around individual filler particles [132] to enhance interaction without compromising the structure of the filler material.

While the interface has received much attention in the design of polymer nanocomposites, recently there has been strong evidence that the region just beyond the interface (known as the "interphase") also plays a substantial role in the

nanoparticle reinforcement of polymers [133–135]. Polymers are known to behave unusually near surfaces [136–138], and their conformation, morphology, and corresponding dynamics in the interphase can deviate significantly from the bulk [139–141]. Many factors contribute to the presence of the interphase, including intrinsic properties such as the surface chemistry of the fillers [142–144] and the cross-link density of the polymer network [145], [146], as well as ambient characteristics such as temperature [134], [142], [147] and the composite processing method [145].

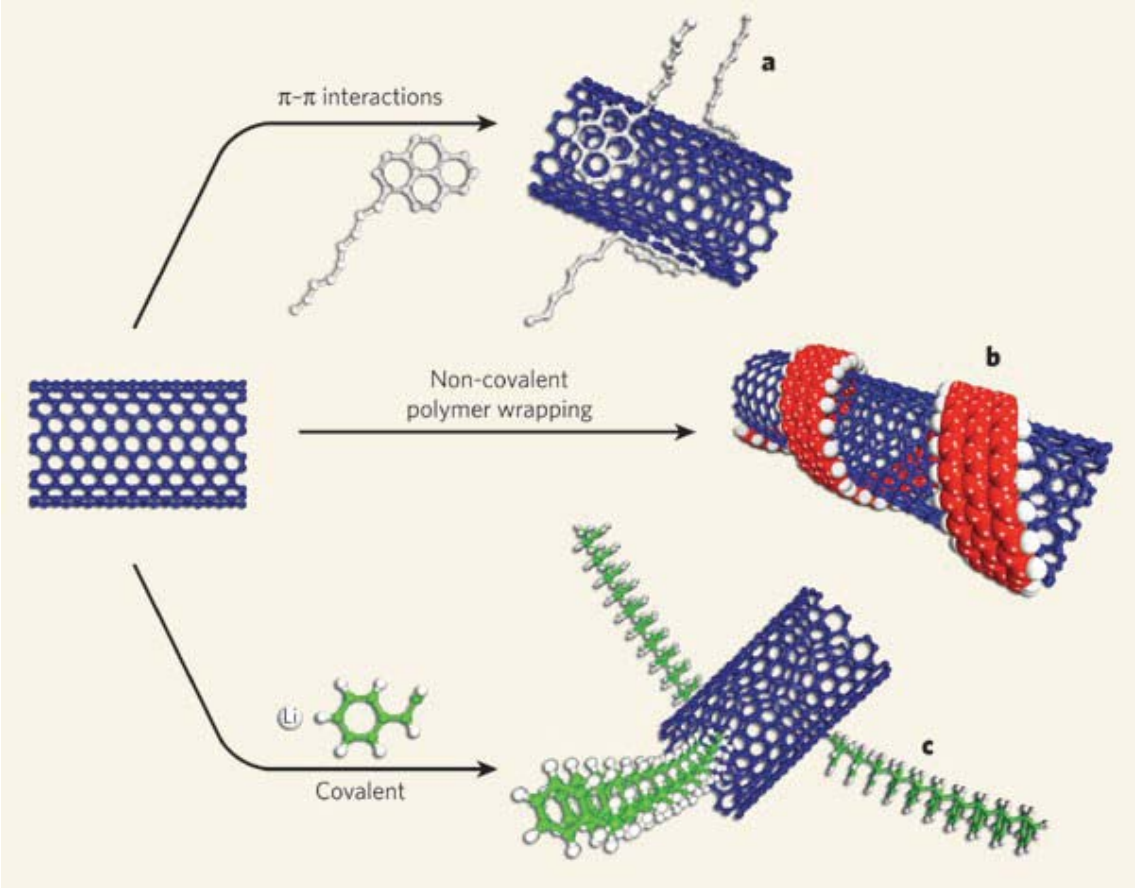

Figure 1.10 – CNTs and other nanomaterials can be compatibilized with a desired matrix through (a, b) non-covalent or (c) covalent means [131].

Collectively, the interface and interphase play a significant role in distribution of applied loads in composite materials. Many independent groups have modeled the contribution of an interfacial/interphasic layer on both particulate and fiber fillers in composites [148–152], and it has been experimentally shown that steric (conformational) limitations and retarded dynamics in these regions can substantially hinder the reinforcement efficacy of nanoscale fillers [146], [153]. Such unpredictability and lack of control in this region is often blamed for the muted success of nanocomposites to date [154].

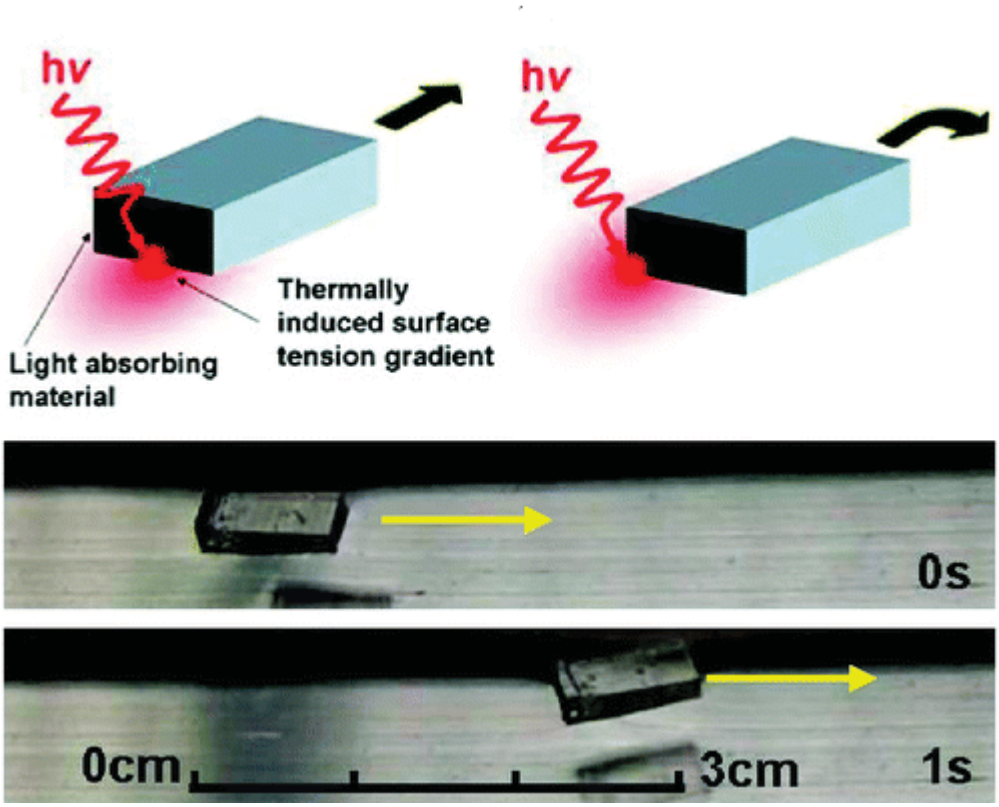

Figure 1.11 – Carbon nanotube composites have been engineered to convert incident electromagnetic radiation to work via the surface tension of a floating composite block [155].

1.3. Carbon Nanotube/Polymer Composites

The act of incorporating carbon nanotubes into polymers was first reported by Ajayan *et al.* in 1994, where it was shown that the cutting of an epoxy/CNT composite could align the CNTs embedded within the matrix [156]. The first report of CNT/polymer composite properties would come four years later, in 1998, with Wagner and co-workers presenting the elastic modulus and interfacial shear strength of a film created by spreading and subsequently curing a urethane/diacrylate oligomer on a dried film of MWNTs [157]. The following year, Jia *et al*. would present the first attempt to develop a bulk CNT nanocomposite by incorporating as-grown CNTs into poly(methyl methacrylate) [158]. It was noted in this early work that the nanotubes were substantially aggregated despite sufficient mixing.

Numerous polymers have served as the matrix material for carbon nanotube composites in the many years since [58], [154], [159], [160]. At the outset, CNTs are an attractive choice for use in nanocomposite materials due to their wide array of attractive properties (as detailed previously in Section 1.1), yet their use for the purposes of mechanical improvement has proven to be the most prolific. Additionally, their distinctly viscoelastic behavior [161] and recent classification as a polymeric material [162] makes them a fundamentally interesting additive. CNTs have been applied in nanocomposite materials that exhibit a range of appealing functionalities, including field emission [163], electrothermal [164], photo [155],

[165], and magnetic actuation [166], electromagnetic shielding [167], and even strain sensing [168], [169] (Figure 1.11).

CNTs have also been used to modify existing composite materials. They have been synthesized directly on the surface of carbon [62] and ceramic fibers [170] to enhance interaction with a polymer matrix, and have also been used as an additive to increase a polymer's toughness [171], [172].

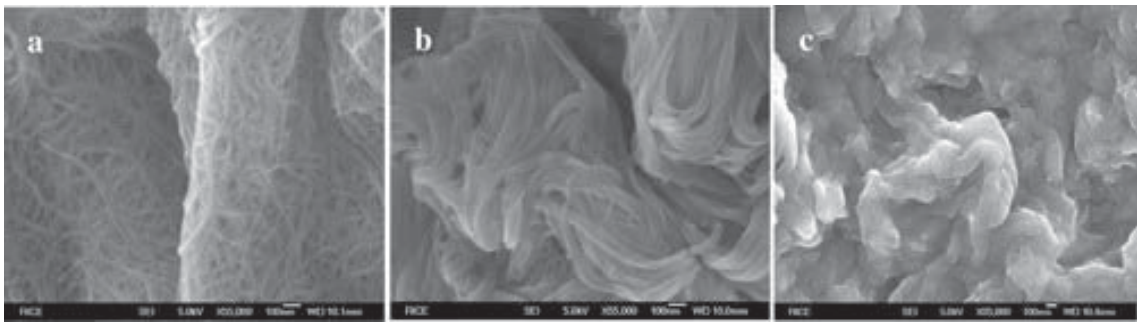

Figure 1.12 – CNTs form (a) highly entangled ropes, and oleum has been shown to be capable of intercalating these bundles so that they can be (b) disentangled and (c) cut to short lengths to improve dispersability [15].

Unfortunately, as with other nanofillers, CNTs do not readily disperse when introduced to a polymer matrix. Due to their high aspect ratio, nanotubes are known for forming dense, stable bundles that can be very difficult to separate. Gong *et al.* were the first to attempt homogenization in CNT/polymer composites with the addition of a solvent, and while they did report nearly a 30% increase in the elastic modulus as compared to the control, it was noted that bundling was still an issue [173].

To aid in dispersion, many have attached functional groups to the surface of CNTs that enhance filler/matrix compatibility [174–176]. While these methods have seen some success, the complete intercalation of these strong bundles is no trivial task, and aggressive solvents such as oleum (fuming sulfuric acid) are necessary to intercalate the tightly-bound SWNT ropes [107]. To further aid in solubility, this oleum dispersion technique was subsequently adapted to include a treatment to cut and functionalize the SWNTs, ultimately trimming them to ~60 nm in length in an effort to decrease the likelihood of further bundling (Figure 1.12) [15].

1.4. Research Motivations

While much progress has been made in the pursuit of functional polymer nanocomposites, many questions still remain with regards to the complex structure-property relationships in these materials [177]. As such, opportunities remain to explore new phenomena, and to further the understanding of how nanomaterials interface with polymers. In this dissertation, I will introduce unusual mechanical behavior that represents new, and unique physical phenomena in polymer nanocomposites while simultaneously providing insight into the subtle interactions that occur between nanostructures and a surrounding polymer matrix.

The composite materials used to examine these properties were prepared through the impregnation of self-assembled forests of vertically-aligned CNTs. In Chapter 2, I will review the methods used to synthesize A-CNT forests consisting of

FWNTs as well as MWNTs, and will outline the methods used to reinforce these structures with a supportive, yet compliant polymer matrix. The subsequent chapters represent the body of this thesis work, which endeavors to address the following specific aims:

I. Provide insight into the mechanics of cyclic deformation for compliant, highly anisotropic, CNT-reinforced polymer composites.

II. Confirm the existence of an observed dynamic-strain-induced self-stiffening response in polymer nanocomposite materials, and determine its experimental limitations.

III. Resolve the structural/morphological changes that take place in this PDMS/CNT material during cyclic stress, and present a viable mechanism for adaptive stiffening in polymeric nanocomposites.

Chapter 2

Manufacturing Nanocomposites with Highly-Aligned Carbon Nanotubes

Due to the high aspect ratio of carbon nanotubes, orienting them inside of a polymer matrix is no trivial task. While it has been demonstrated that interstitial CNTs can be aligned within a polymer through the stretching of thin films [178] or the melt spinning of fibers [179], the deliberate arrangement of these slender fillers has proven difficult for 3D (bulk) nanocomposite materials. Realistically, the only procedure capable of resulting in highly anisotropic bulk CNT nanocomposites is the impregnation of self-assembled architectures.

Furthermore, the diameter and number of walls of a single nanotube play a large role in its mechanical response, and the behavior of a CNT at the nanoscale can range from a filament to a rigid rod. As overviewed in Section 1.1.2, the inter-CNT spacing and individual CNT diameter of nanotube forests can be reasonably controlled through the manner by which the catalyst is applied [19].

In my M.S. thesis dating April of 2010 [180], I outlined the procedure of assembling two individual CVD furnaces to synthesize different types of vertically-aligned CNTs, as well as the considerations that must be made to infiltrate these structures with a curable poly(dimethylsiloxane) (PDMS) matrix. The corresponding composites comprised of FWNTs (1–2 nm in diameter) and MWNTs (up to 100+ nm in diameter) grown via pre-deposited catalyst CVD and vapor-phase CVD, respectively. These nanocomposites have distinct mechanical properties, and each served an explicit role in resolving the phenomena detailed in the specific aims of this thesis.

2.1. Composite Preparation through Forest Impregnation

As mentioned in Section 1.2.2, homogeneously dispersed carbon nanotube composites can be very difficult to prepare through mixing methods. One way of addressing this issue is by organizing the CNTs before introducing them to the polymer. In fact, such a technique was utilized in the earliest CNT composites, where randomly-oriented "buckypapers" were prepared by a filtration technique and then impregnated by the matrix polymer [157]. While such a two-dimensional composite film certainly has potential applications, three-dimensional structures are necessary for many real world applications. Unfortunately, assembling CNTs into 3D architectures is a challenging proposal, and the only practical way of overcoming this difficulty is through self-assembly.

The use of CVD to synthesize aligned arrays carbon nanotubes was discussed previously in Section 1.1.2. These forests can be grown to macroscopic lengths in excess of 1 cm [181], and as shown by Ci, Vajtai, and Ajayan in 2007, can be effortlessly removed from their substrate if a weak oxidant such as water is introduced to the growth environment during cool down [56].

As mentioned previously, these A-CNT structures come in many shapes and sizes. Interestingly, their wettability can be adjusted from superhydrophobic to superhydrophilic through the chemical modification of the individual CNTs and topography of their assembly [182]. In the interest of developing 3D nanocomposites, this adaptability provides an opportunity to tailor a nanostructured framework for infiltration with a desired matrix polymer.

This technique of impregnating 3D CNT assemblages was first reported in 2005 via the infiltration of methyl methacrylate prior to polymerization [183]. Since then, numerous other thermoplastic and thermosetting polymers have been successfully infiltrated into similar nanotube structures, including polystyrene [184], epoxy [185], poly(N-isopropylacrylamide) [186], and PDMS [187].

Moreover, successful impregnation depends greatly on a polymer's degree of interaction with the surface of a CNT. Such compatibility was demonstrated previously by Barber *et al.* for many common matrix polymers [188], and in this report it is shown that PDMS has a particular affinity for carbon nanotubes. This observance of "spontaneous wetting" qualifies PDMS as an attractive candidate for the development of three-dimensional impregnated nanocomposites.

2.1.1. Poly(dimethylsiloxane)

PDMS is a member of the "siloxane" family of polymers that were discovered in the early 20th century. Erroneously termed "silicones" [189], polysiloxanes are ubiquitous in society, spanning a wide range of applications from lubricants, defoaming and mold-release agents, and even cosmetics. These non-toxic polymers are designated by their characteristic $[–Si–O–]_n$ backbone, a structure which is conformationally limber due to its large bond angle (130°) and long bond length (1.63 Å) [190], [191].

The most widely used of the polysiloxanes, PDMS is appealing due to its many complementary properties. Specifically, it is optically clear, chemically stable, biocompatible, and has a Poisson ratio of 0.5 [191], [192]. As illustrated in Figure 2.1, two methyl groups decorate each Si in PDMS; these side groups enable a high degree of molecular lubricity when combined with the flexibility of the siloxane backbone [193]. PDMS is prominently viscoelastic at room temperature and is able to conform to diminutive surface features, making it an attractive candidate for use in microfluidic devices [194].

Despite its ubiquity, PDMS is fundamentally an unusual polymer. It has an extremely low glass transition temperature (T_g) at -129 °C, and will cold crystallize (T_c) in the approximate range of -100 °C to -70 °C. The melting of PDMS crystals is also peculiar, and consists of two distinct melting transitions (T_{m1} and T_{m2}). These transitions have been shown to occur as a function of the cross-link density [195] as well as the rate of cooling [196], and have been explained either by the existence of

two distinct crystal structures [197], [198], or the melting and subsequent coalescing of small and/or less stable crystallites [195], [196].

a

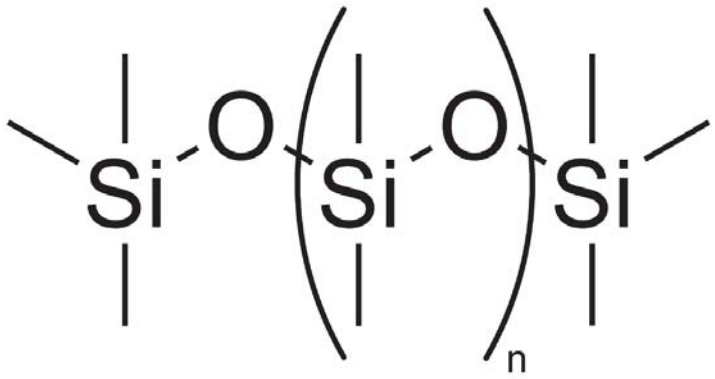

b

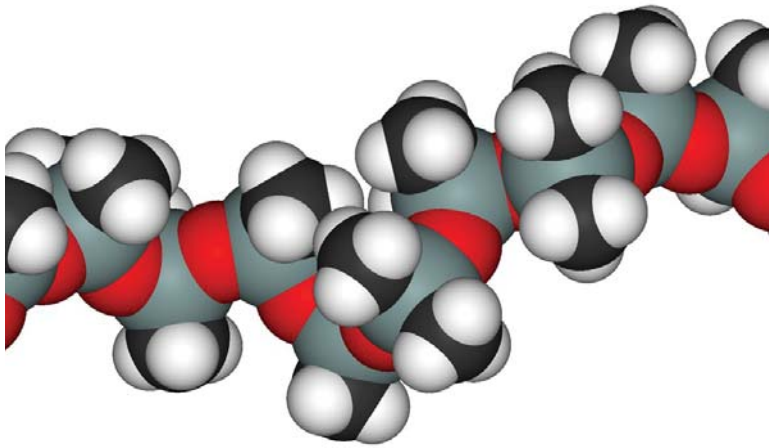

Figure 2.1 – (a) Molecular structure and (b) model of PDMS [199].

The version of PDMS used in the current work is Sylgard 184, a commercially available, room-temperature-vulcanizing (RTV-2) silicone rubber supplied by Dow Corning. This product comes in a two-component kit that contains the "base

elastomer" (a vinyl-terminated oligomer) and a "curing agent" that contains copolymers of methylhydrosiloxane and dimethylsiloxane, along with a platinum complex that initiates the curing (cross-linking) process via free radical polymerization. The post-cured material has a dynamic viscosity of 3900 centipoise, a high dielectric constant (2.65 at 100 Hz), and is thermally stable up to 200 °C. Vulcanized PDMS is also extremely gas permeable [200], [201] and highly sensitive to organic solvents [202]. Sylgard 184 has proven to be an appealing matrix material for carbon nanotube composites, and in fact, many of the actuation and strain sensing applications noted in Section 1.3 utilized it as a matrix material [155], [164], [165], [168].

2.2. Preparing Composites with Vapor-Phase-Grown CNTs

As mentioned in Section 1.1.2, CNTs can be synthesized on a range of substrates via vapor-phase CVD, and even those with a great degree of topographical complexity. For this thesis work, planar silicon substrates were utilized in the interest of growing forests of vertically-aligned CNTs.

2.2.1. Synthesizing Many-Walled CNT Forests via Vapor Phase CVD

For any method of CVD nanotube synthesis, a sufficiently hot reaction zone (generally ~750–800 °C) is necessary [56]. A tube furnace can provide temperatures sufficient for synthesis, while also enabling an even, laminar flow of the reaction gases over the substrate to ensure consistent and repeatable growth. A Lindberg/Blue M M55347 three zone furnace was used to sustain the high

temperature growth environment (Figure 2.2), and by elevating the temperature of the end zones 8 °C higher than the center zone, it is possible to extend the length of the isothermal zone where consistent CNT growth takes place.

Using a vapor-phase CVD method, forests of many-walled CNTs were synthesized off of silicon wafer substrates using ferrocene and xylene as the iron catalyst and carbon precursors, respectively. To simplify the experimental setup and eliminate the need for a secondary heater, an apparatus was designed to utilize waste heat from the furnace to evaporate the growth precursor mixture. To do this, a Masterflex 7523 continuous pump equipped with Viton™ tubing was used to deliver the mixture to a custom fabricated "evaporation cap" positioned at the fringe of the growth zone (Figure 2.2c). The evaporator cap was held consistently at 200 °C, which is sufficiently warm to ensure the full and complete evaporation of the precursor mixture (the boiling point of xylene is 139 °C).

The vaporized precursors are then delivered to the growth zone using two individual buffering gases. The "evaporator gas" ($Q_{\mathbf{e}}$) is used to disperse the growth precursors, while "carrier gas" ($Q_{\mathbf{c}}$) carries the reaction gases through the furnace. These gases consist of 15 vol% hydrogen, balance argon, and are regulated by MKS M100 mass flow controllers and an MKS Type 247 Four-Channel Readout.

Building off of previous work by Li *et al.* [181], the parameters for synthesizing A-CNTs via vapor phase CVD are presented in Table 2.1, and the procedure is as follows:

a

b

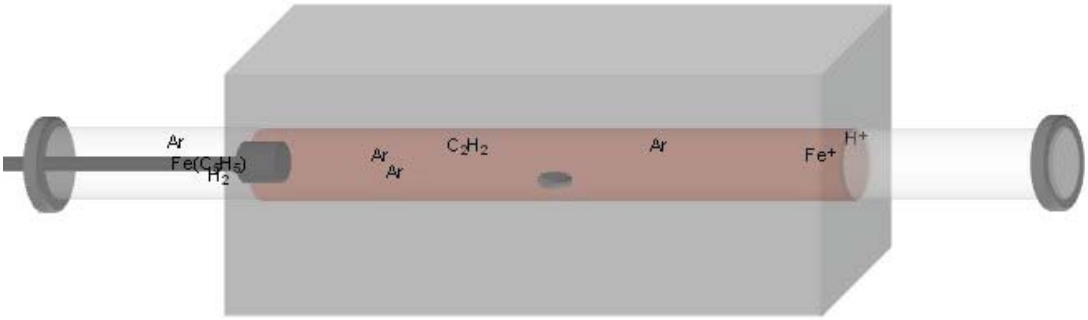

c

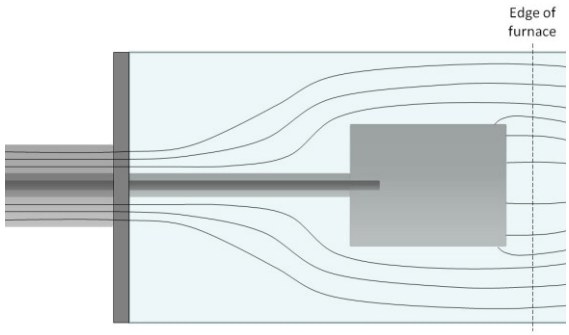

Figure 2.2 – (a) Photograph and (b) schematic of the vapor-phase CVD growth apparatus. (c) Cross-section schematic illustrating the flow of the carrier and evaporator gases as they pass into the reaction zone.

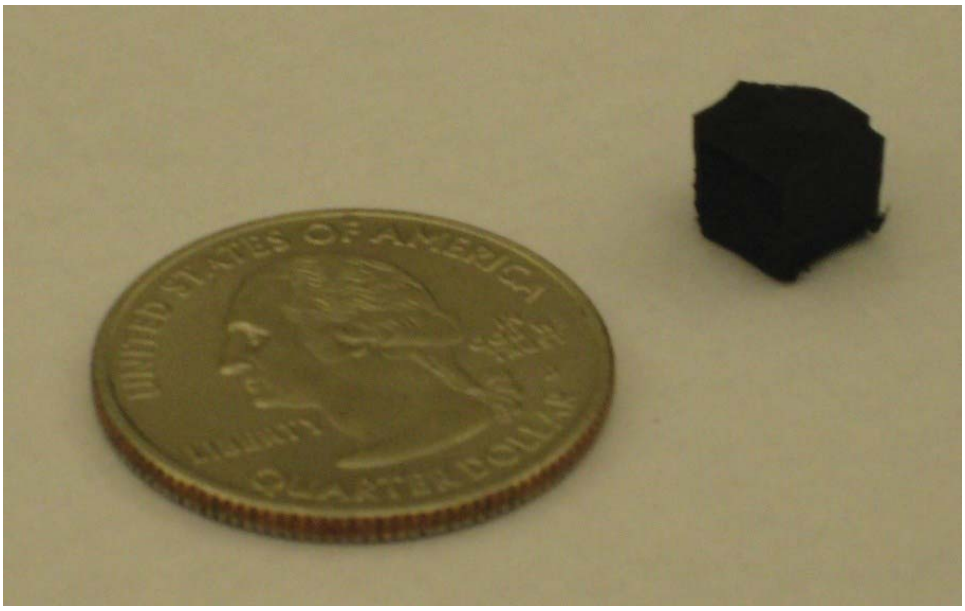

Figure 2.3 – Photograph of an A-CNT forest grown via vapor-phase CVD.

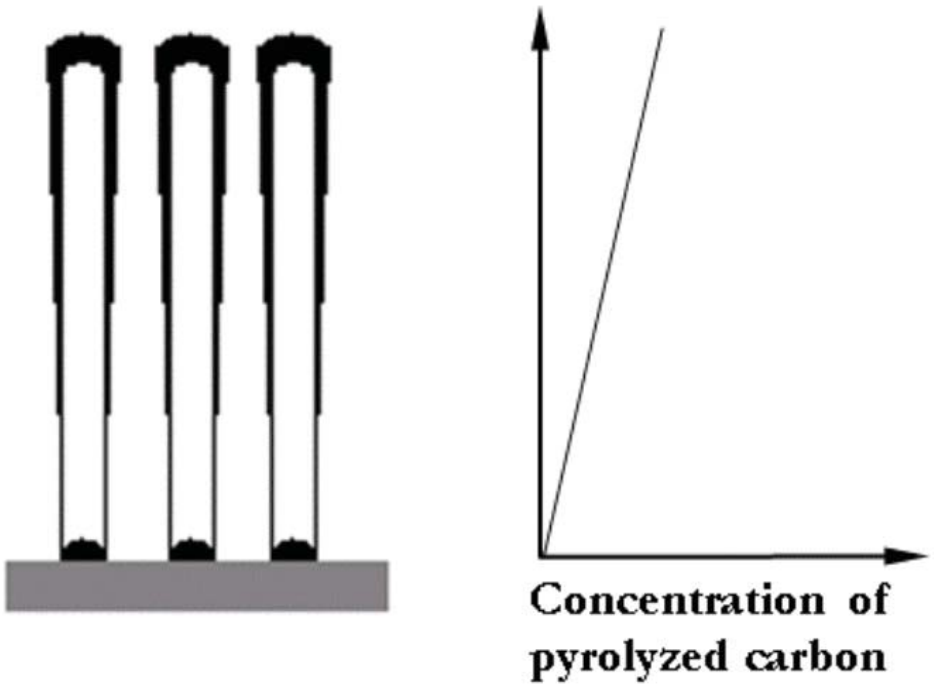

Figure 2.4 – Schematic of vapor-phase CNT thickness as a function of growth height [203].

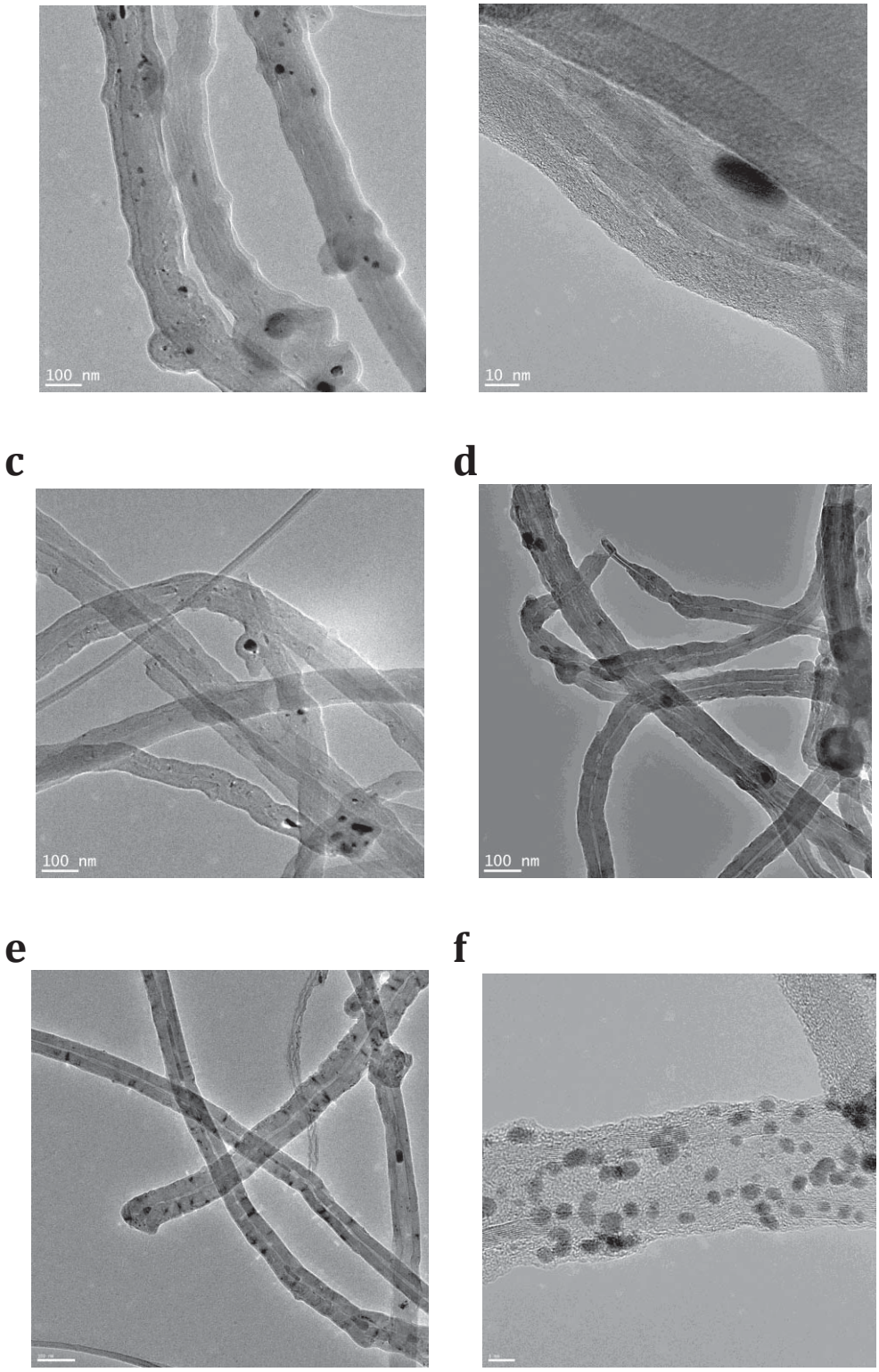

Figure 2.5 – TEM images of the (a, b) "top", (c, d) "middle", and (e, f) "bottom" of xylene/ferrocene A-CNTs.

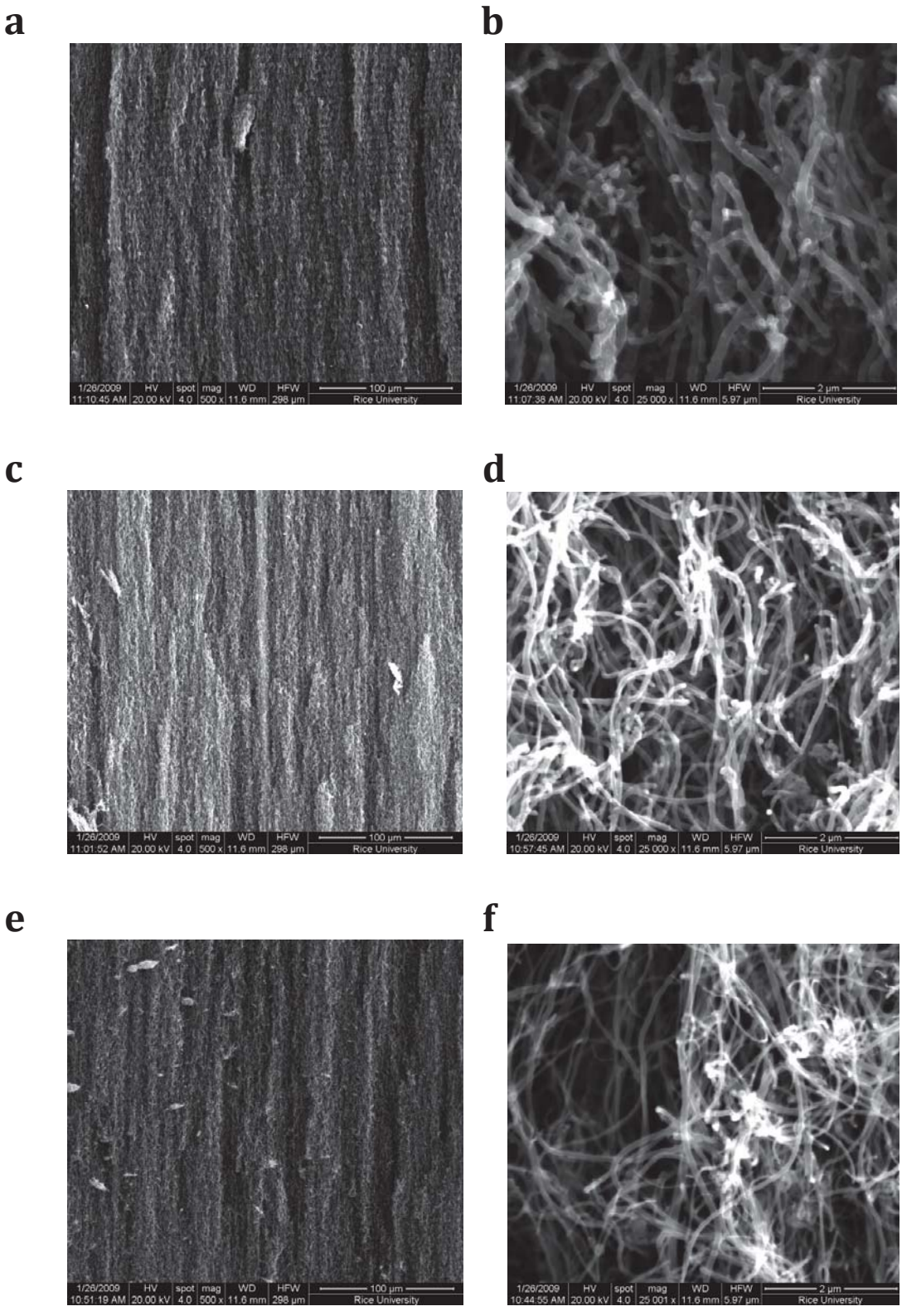

Figure 2.6 – SEM images of the (a, b) "top", (c, d) "middle", and (e, f) "bottom" of xylene/ferrocene A-CNTs.

I. Begin flowing the carrier gas ($Q_{\mathbf{c}}$) and heat furnace up to the introduction temperature (T_{i}).

II. When stable, place substrate into the center of the growth zone and begin heating to the desired set point temperature for the synthesis (T_{s}).

III. At the exact time the set point is reached, begin flow of evaporator gas ($Q_{\mathbf{e}}$) and initiate the flow of the catalyst/carbon source liquid mixture (Q_{ℓ}) which has a specific ratio of catalyst to carbon source (C:CS).

IV. After the desired synthesis time (t_{s}) has elapsed, turn off all flow but the $Q_{\mathbf{e}}$ during cool down.

A representative forest of vapor-phase-grown A-CNTs measuring ~ 4.5 mm tall can be seen in Figure 2.3. Transmission electron microscopy (TEM) in Figure 2.5 reveals that the diameter of these MWNTs typically measure in the ~50 nm to ~100 nm range, and that residual metal catalyst is encapsulated within the concentric walls of the nanotubes, a result of the continuous influx of catalyst during synthesis. It is also seen that the outer layers of the CNTs consist of pyrolized carbon that is graphitic, yet not organized into concentric walls. Scanning electron microscopy (SEM) in Figure 2.6 reveals the structure of the forest, and while it is clear that the CNTs are indeed preferentially aligned, it is noted that there is a level of disorder at the nanoscale. Lastly, as illustrated in Figure 2.4, the diameter of these CNTs is known to taper, with a "top" that has a much larger diameter than the "middle" and "bottom". As explained by Li, this is also due to the constant introduction of catalyst during synthesis [203].

T_i (°C)	T_s (°C)	t_s (min)	$C{:}CS$ ($\frac{mg}{ml}$)	Q_e (sccm)	Q_c (slm)	Q_ℓ ($\frac{ml}{min}$)
300	775	300	.2	500	1	.2

Table 2.1 – Parameters for optimal vapor-phase CVD growth.

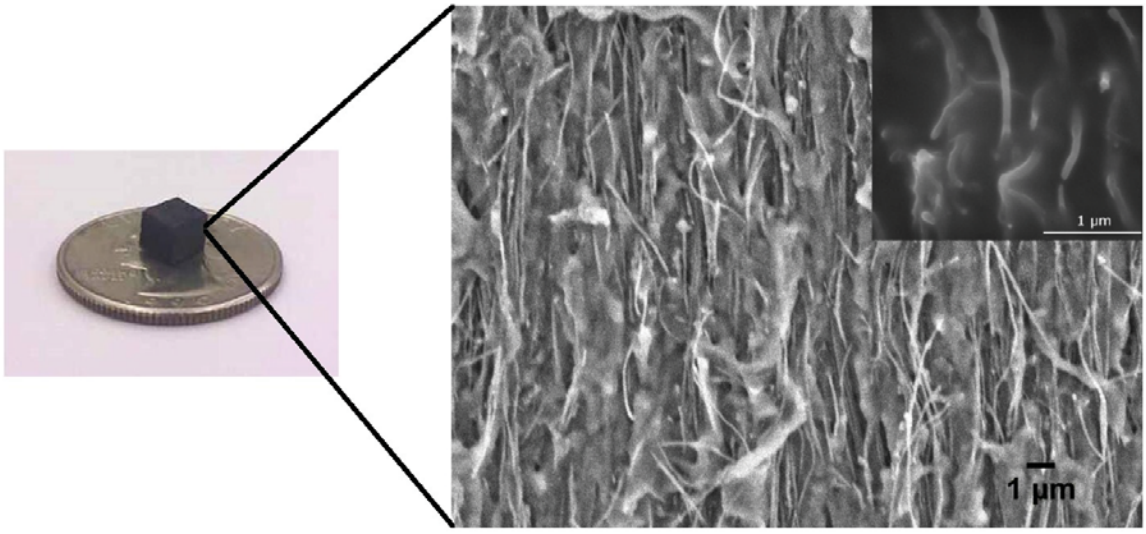

Figure 2.7 – A fully-impregnated composite made using MWNT forests grown via vapor-phase CVD.

2.2.2. Impregnation of Robust MWNT Forests

Due to the large diameter of these CNTs, the forests synthesized by this method are robust and can withstand the force of the infiltrating polymer without the need for external support (Figure 2.7). To impregnate these forests, a technique similar to a previously-reported method was used [187]:

I. Mix the PDMS monomer and the curing agent at a 10:1 ratio and stir for 5 minutes to ensure homogeneity.

II. Place the pre-cured polymer under house vacuum in order to remove any interstitial air. Remove when bubbling has ceased (~10 minutes).

III. Introduce a free-standing mat of A-CNTs by placing it on top of the pre-cure, and "scoop" some of the polymer onto the top of the forest to promote infiltration.

IV. After fully submerged, place the infiltrating composite under a vacuum of 1 Torr for at least 3 hours until bubbling has ceased.

V. When no longer bubbling, subject the sample to 1 hour of 100 °C heat treatment as recommended by the manufacturer to ensure complete curing.

2.3. Preparing Composites with Few-Walled CNTs

The pre-deposited catalyst method requires much greater substrate preparation, but the resultant CNTs display a much narrower distribution of sizes, and are generally of a higher quality.

2.3.1. Synthesizing Few-Walled CNT Forests via Pre-Deposited Catalyst CVD

For this synthesis, a Thermolyne 794000 tube furnace with a 2" quartz reaction tube was used as the growth environment (Figure 2.8). Silicon wafer substrates were pre-deposited via electron beam evaporation with a 1.5 nm catalyst

layer of Fe on top of a 10 nm barrier layer of Al (to prevent catalyst from migrating into the silicon; Figure 2.8c). Such a catalyst layer thickness was previously reported to produce a narrow distribution of FWNTs, consisting predominantly of DWNTs [52].

Three MKS M100 mass flow controllers were again used in tandem with a MKS Type 247 Four-Channel Readout to control the gas flow through the reaction zone. These gases consisted of the ethylene carbon source (Q_h), as well as two 15 vol% hydrogen, balance argon gas flows to pass through a water bubbler (Q_b) and to carry the reaction gases through the growth zone (Q_c).

Based off of the method reported previously [52], the parameters for synthesizing A-CNT forests via pre-deposited catalyst CVD are presented in Table 2.2, and the procedure is as follows:

I. Begin flowing the "carrier gas" (Q_c) and heat furnace up to the "introduction temperature" (T_i).

II. When stable, place substrate into the center of the growth zone and begin heating to the desired set point for the "synthesis temperature" (T_s).

III. At the exact time the set point is reached, begin flow of "bubbler gas" (Q_b) through water bubbler.

IV. After bubbling for the desired "bubbling time" (t_b), initiate the flow of the "hydrocarbon gas" (Q_h).

V. After the desired "synthesis time" (t_s) has elapsed, bypass the bubbler through the three-way valve and turn off all but the Q_b during cool down.

T_i (°C)	T_s (°C)	t_b (min)	t_s (min)	Q_b (sccm)	Q_c (slm)	Q_h (sccm)
300	775	1	30	85	1.3	115

Table 2.2 – Parameters for optimal water-assisted CVD growth.

Using these parameters, regular, even mats of aligned FWNTs were synthesized with high repeatability. As reported elsewhere [52], the growth of CNTs from a catalyst layer measuring 1.5 nm will consist predominantly of DWNTs and other FWNTs measuring ~8 nm in diameter (Figure 2.9). In Figure 2.10, an example forest measuring ~2.5 mm tall can be seen, and SEM images reveal that the CNTs grown through this method exhibit a much higher degree of alignment.

2.3.2. Impregnating Delicate FWNT Forests via "Sandwich" Preparation

Unfortunately, these FWNT forests are not able to withstand the force of the infiltrating pre-cured polymer [180]. It was visibly observed that the forests would consistently "crumple" and buckle as the polymer attempted to displace the interstitial air and impregnate the structure. As observed in the cryofractured sample in Figure 2.11, it is clear that the preferred alignment of the forest is lost after impregnation.

a

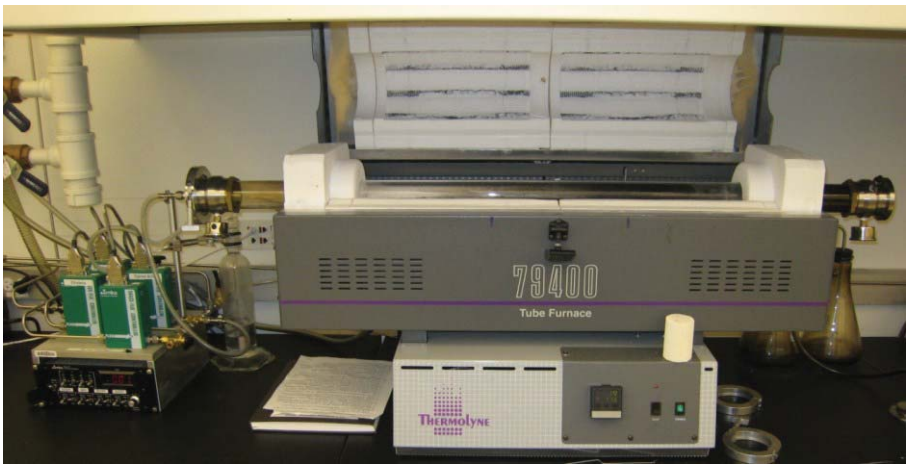

b

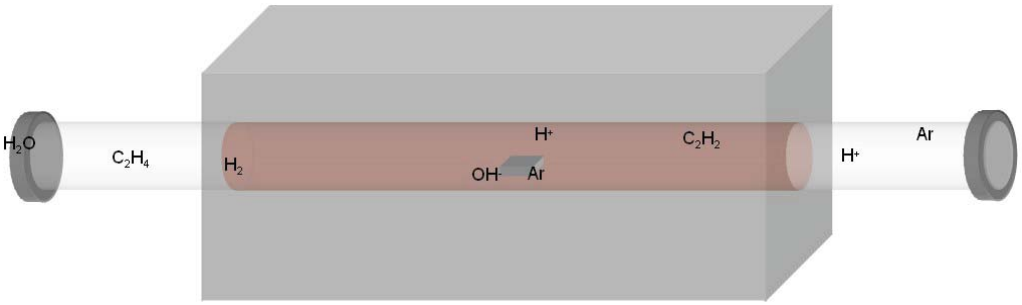

c

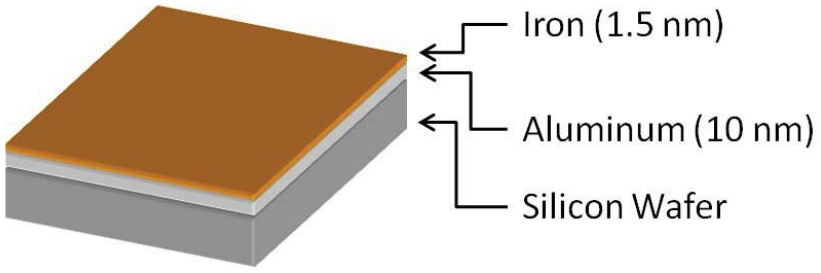

Figure 2.8 – (a) Photograph and (b) schematic of the pre-deposited catalyst CVD apparatus. (c) Schematic of pre-deposited CVD growth substrate (not to scale).

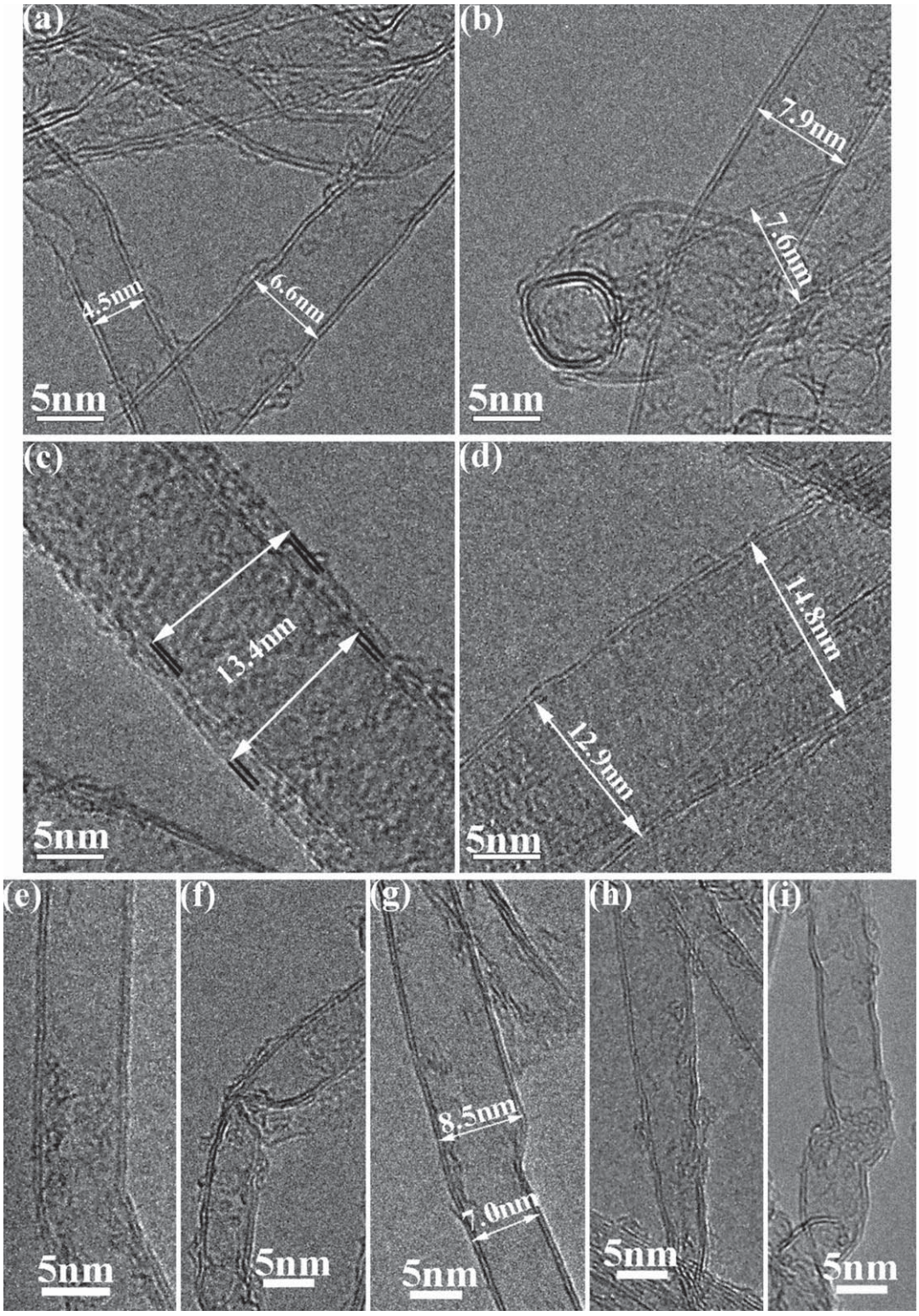

Figure 2.9 – TEM images of FWNTs grown via water-assisted pre-deposited catalyst CVD [52].

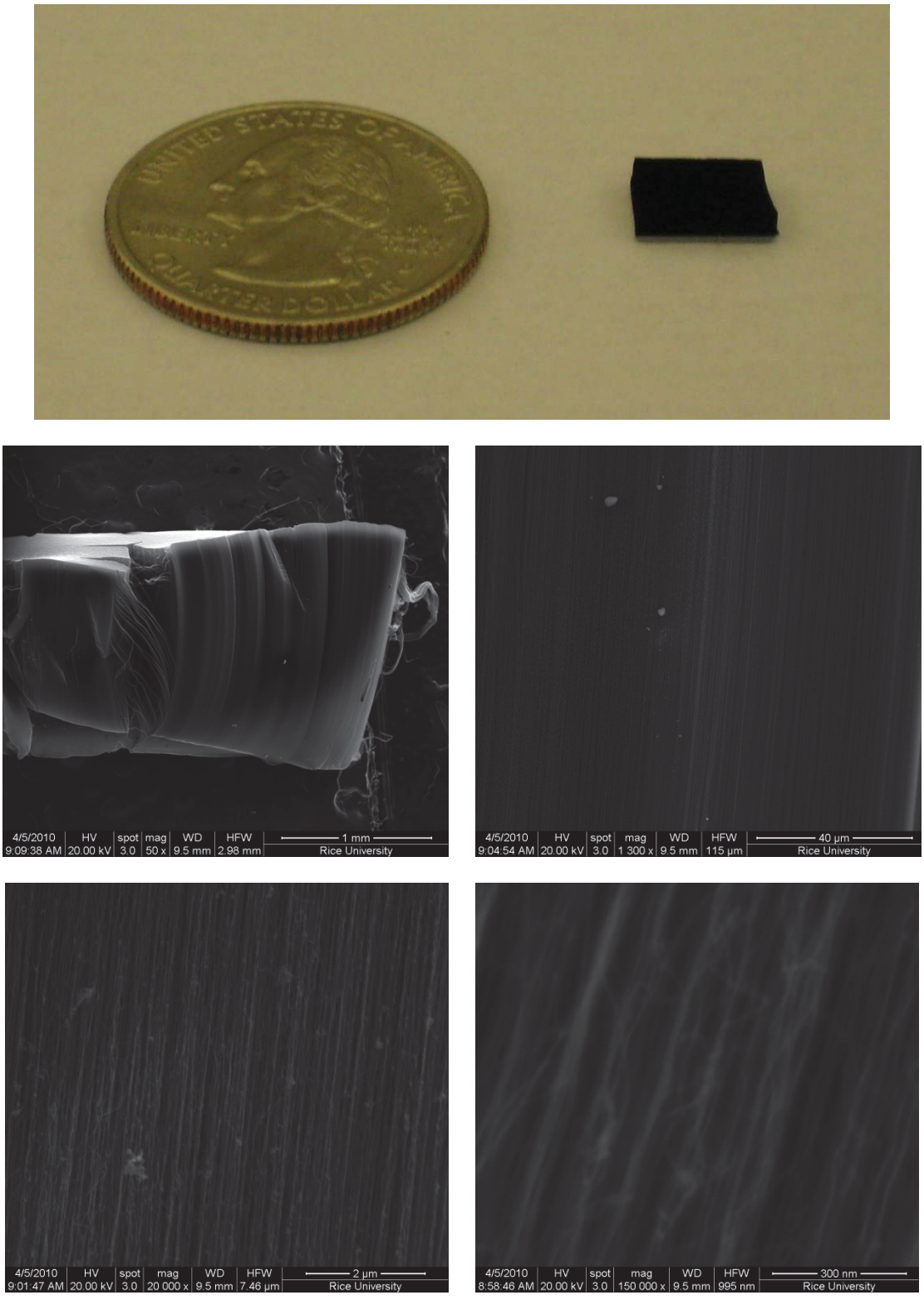

Figure 2.10 – Photographic and SEM images of FWNTs grown via water-assisted pre-deposited catalyst CVD.

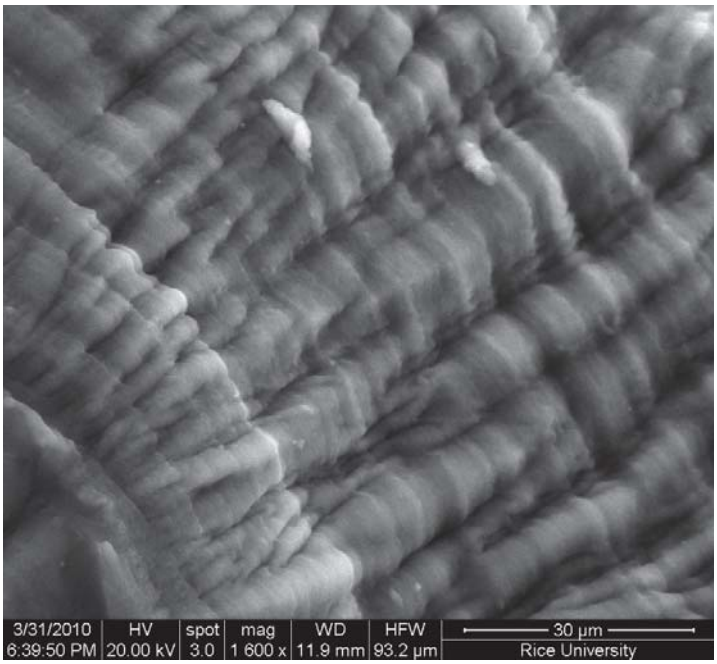

Figure 2.11 – SEM image of a cryofractured FWNT composite. Unsupported FWNT forests are unable to withstand the matrix infiltration.

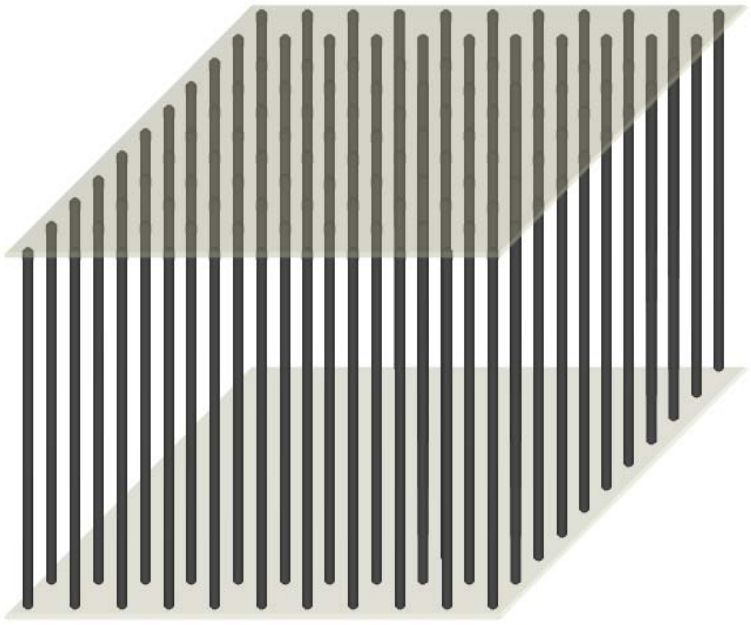

Figure 2.12 – Schematic illustrating how a thin layer of PDMS anchors the tips of a FWNT forest in the preparation of CNT "sandwich structures".

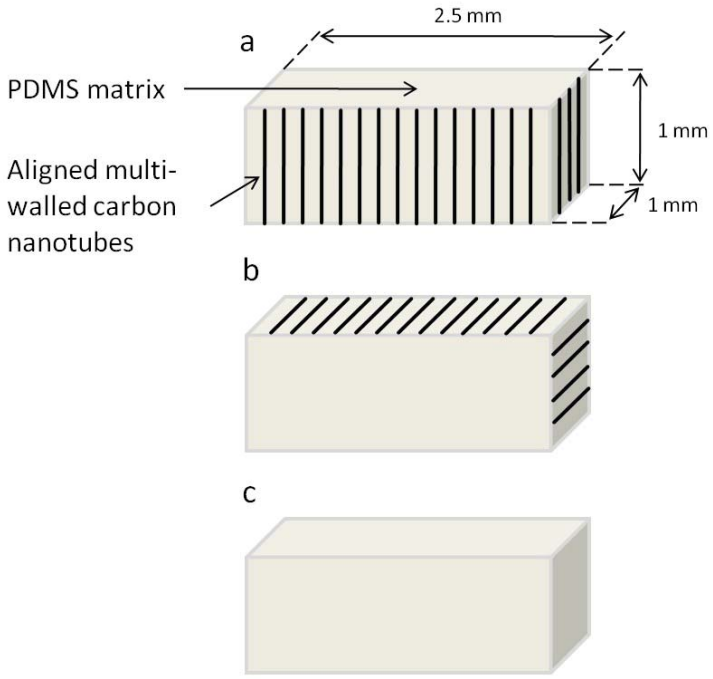

d **e**

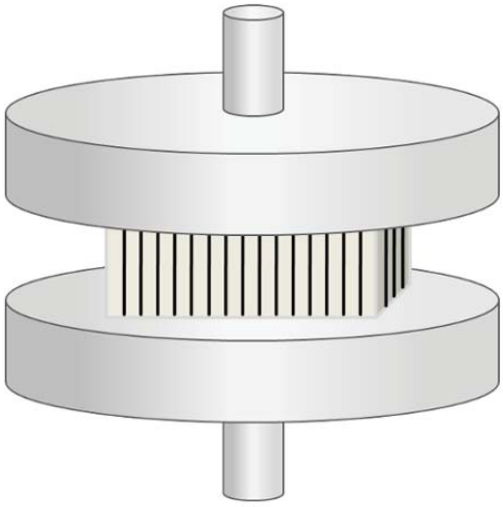

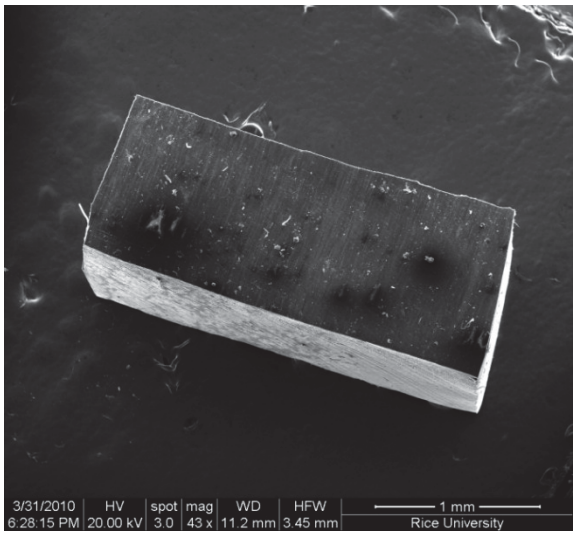

Figure 2.13 – Orientation-specific dynamic mechanical testing was conducted by cyclically compressing the composites along the (a) axial (longitudinal) and (b) radial (transverse) direction of CNT alignment, and then comparing to (c) a neat PDMS control. (d) Schematic of a sample between the compressive platens, and (e) a SEM image of a composite sample.

Fortunately, a recently-developed technique by Li and Hahm *et al.* allows for the impregnation of such delicate architectures through the creation of "sandwich structures" [204]. By spin coating a thin layer of the Sylgard 184 pre-cure on a glass slide, the exposed tips of a CNT forest can be introduced to this surface to initiate a local impregnation that does not penetrate the bulk of the forest. Using a hot plate, the polymer can be rapidly cured to anchor the tips of the CNTs and prevent their relative translation. After removing the sample from the substrate, the process can be repeated for the base of the forest to produce the structure illustrated in Figure 2.12.

2.4. Comparing MWNTs and FWNTs in PDMS Composites

Comparatively, these impregnated MWNT and FWNT forest composites are quite different. The thick-walled CNTs are quite robust, making them an excellent candidate for the mechanical reinforcement of polymeric materials. Alternatively, the high degree of alignment in the FWNTs can be exploited for the development of composite materials with highly-anisotropic properties. Coupled with the fact that very little (if any) interfacial bonding is expected between the PDMS and the carbon nanotubes [205], these materials provide an interesting and near-ideal system for studying the mechanical interaction of polymers and inclusive nanostructures.

In the following chapters, the dynamic mechanical response of these materials will be studied to provide insight into such mechanisms of deformation in nanostructured composites. Specifically, it will be shown that nanomaterials can be

used to induce unusual modes of deformation in composite materials that can be exploited to provide novel mechanical responses.

2.4.1. Sample Preparation

Unless otherwise noted, nanocomposite specimens were hand cut into rectangular blocks approximately 2.5 mm long x 1 mm wide x 1 mm thick—as illustrated in Figure 2.13—using a razor blade. Only samples whose thickness and cross-sectional area were within 10% of the ideal were used.

Chapter 3

Dynamic Mechanical Properties of Highly-Anisotropic Nanocomposites

Having manufactured two individual composites consisting of continuously-aligned carbon nanotubes embedded within a compliant elastomer matrix, in this chapter I will address Specific Aim I by probing their dynamic mechanical responses as a function of loading orientation. Due to the viscoelastic nature of PDMS and the high degree of alignment in the CNTs, it is possible to resolve the mechanics of deformation for such continuously-reinforced nanocomposite materials.

3.1. Unusual Behavior in Elastomer Composites and Nanotubes

Independently, elastomer composites and carbon nanotubes exhibit intriguing responses when mechanically loaded. From counterintuitive stress/strain relationships to unstable modes of deformation, these materials serve

as attractive candidates in the development of nanocomposite materials that boast unique and novel mechanical behavior when stressed.

3.1.1. Nonlinear Viscoelasticity in Filled Elastomers

The concept of viscoelasticity describes how materials will exhibit both viscous as well as elastic behavior when deformed. All materials are fundamentally viscoelastic by this definition, though this property is most commonly associated with polymers and other materials that experience internal flow or diffusion.

Most rheologically-simple viscoelastic materials have a distinct "linear viscoelastic region", where the stress applied scales linearly with the deformation strain. Such linear viscoelastic behavior represents that no plastic (*viz.* irreversible) changes are occurring in the material, and as a result, linear behavior is usually only common for small deformations [206]. It follows, then, that most viscoelastic materials respond nonlinearly when stressed. Unfortunately, nonlinear effects are not easily modeled, and their source in most materials—and particularly composite materials—is not always clear.

Elastomer vulcanizates of both natural and synthetic (e.g. silicone) rubbers are desired for their room temperature compliancy and pronounced viscoelastic characteristics. While the mechanics of deformation are fairly well understood for unfilled rubbers, those that are reinforced with particulate fillers inherit interesting and unique nonlinear behavior as a function of the ever-changing interaction between the two phases.

Most prominently, the stress/strain curve of these filled elastomer systems is known to depend on the maximum strain that the material has seen previously, an unusual property known as the Mullins effect (Figure 3.1a). In the early 1960s, Bueche was the first to implicate matrix/filler interaction as the origin of this behavior [207], [208]. By supposing that chemical bonding between the filler and matrix formed a "giant multifunctional network", his model proposed that the short interparticle segments of this network would rupture when sufficiently strained, leaving the network to respond elastically for subsequent loading events up to that strain level. While chemical interfacial bonding is known to occur in some filled elastomer systems, Dannenberg would later propose that the slippage and irrecoverable dewetting of short polymer chains physically adsorbed on the fillers provided a more likely explanation (Figure 3.1b) [209], [210].

Despite decades of research, the precise mechanism(s) of the Mullins effect is/are not completely resolved. While Bueche's "damage" model has received some support in the decades since [211], [212], chemical bonding is not anticipated to occur in all filled elastomer systems. Correspondingly, the "dewetting" model put forth by Dannenberg is considered the most likely candidate to explain the effect [97], [213].

Dannenberg's proposal of an ever-evolving matrix/filler interface has also been reasoned as the fundamental premise behind another strange property of elastomer composites, the Payne effect. First studied by Fletcher and Gent in 1953 [214] before being popularized by its namesake, Payne, in 1962 [215], the effect

describes the somewhat counterintuitive softening of dynamically-stressed elastomer composites for increasing strain amplitudes (Figure 3.2a).

a

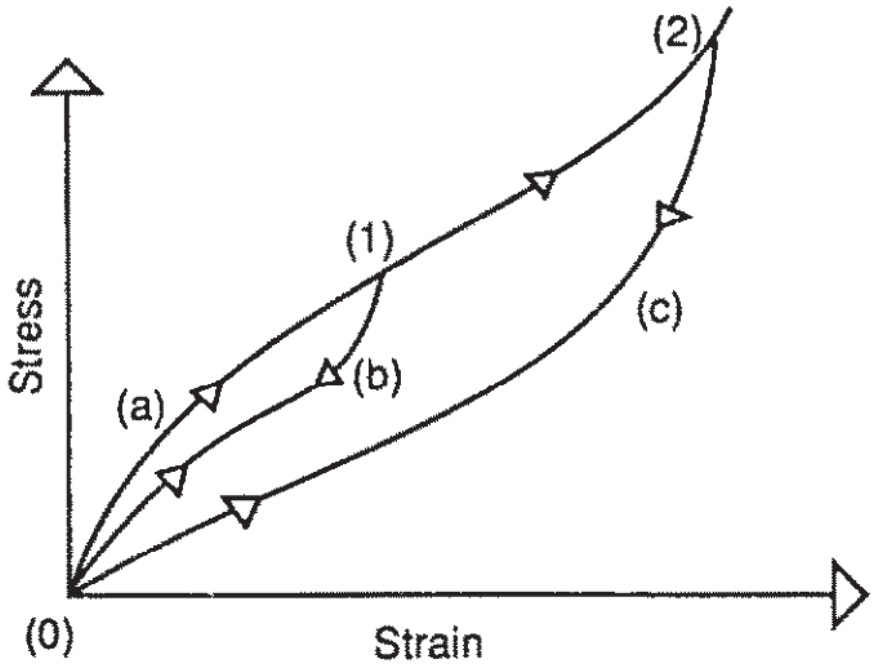

b

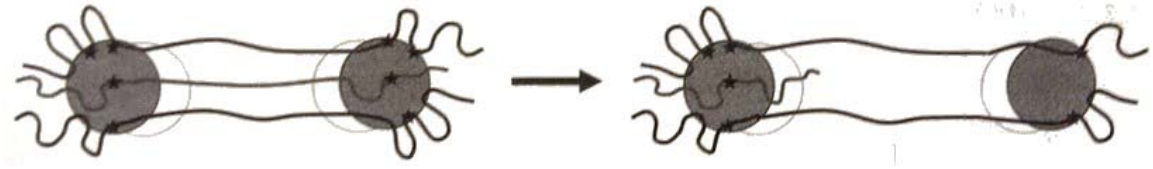

Figure 3.1 – (a) Plot representing the Mullins effect [211], and (b) schematic of the proposed interfacial dewetting mechanism (adapted from [97]).

a

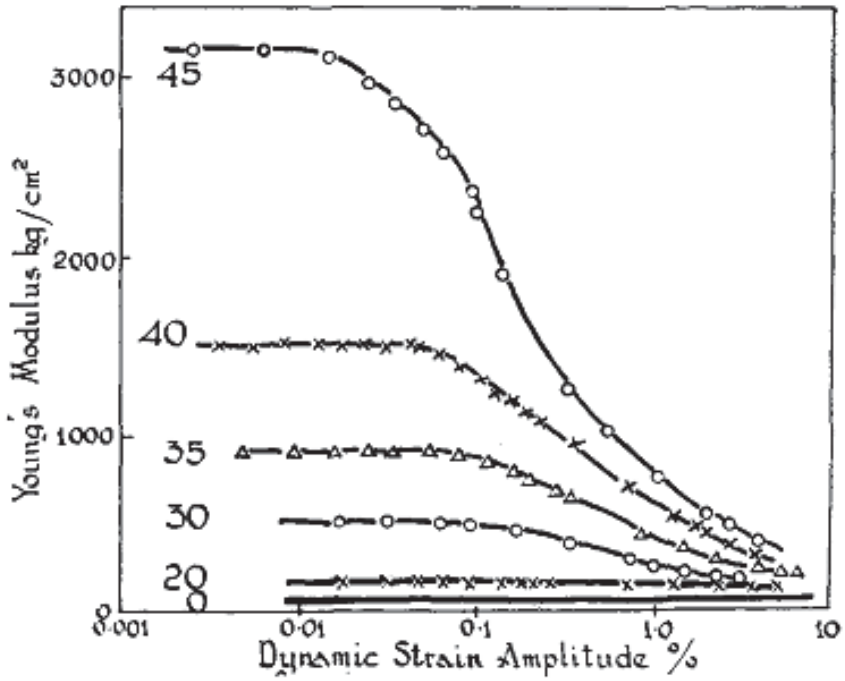

b

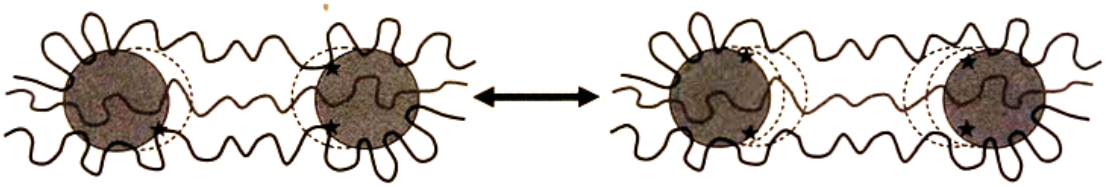

Figure 3.2 – (a) Plot representing the Payne effect [215], and (b) schematic of the proposed interfacial adsorption/desorption mechanism (adapted from [97]).

Specifically, the cyclic loading of a filled elastomer system beyond the previous maximum amplitude is expected to induce further slip of the interparticle chains, resulting in a decreasing modulus for increasing amplitudes (Figure 3.2b).

Recent work has qualified this mechanism, including experimental results that show a disappearance of the Payne effect when the fillers are modified to inhibit physical adsorption [216], as well as modeling that explains the "triboelastic" slip of polymer chains on a surface to produce "deep rearrangements of filler particles at high extensions" [217], [218].

3.1.2. Buckling, Kinking, and Negative Stiffness in Carbon Nanotubes

Carbon nanotubes are also regarded for their distinctive response to loading and deformation. Due to the strong in-plane strength of sp^2-hybridized bonding, CNTs have a remarkable ability to recover elastically from large strains [219]. Furthermore, due to their tubular shape and concentric structure, these macromolecules have also been shown to exhibit distinct mechanical instabilities when loaded axially. Such properties will vary as a function of a nanotube's aspect ratio [220] and number of concentric walls [21], resulting in three main deformation modes: (1) Euler (column) buckling, (2) kinking, and (3) shell buckling.

When uniaxially loaded, SWNTs and other few-walled CNTs will generally buckle as near-ideal Euler columns (Figure 3.3a). However, when sufficiently short, these elastic columns will kink, resulting in a "limit point instability" [220], [221]; further strain beyond this limit point provides increasingly less resistance, a phenomenon known as "negative stiffness" (Figure 3.3b) [21], [222]. This exotic physical behavior has been demonstrated in macroscopic rubber tubes [223], and has been utilized to provide excellent mechanical damping [224] for applications such as vibration neutralization [225]. Furthermore, negatively stiff inclusions

[226] have even been shown to increase the stiffness of composites beyond the conventional limit as defined by the rule of mixtures[227].

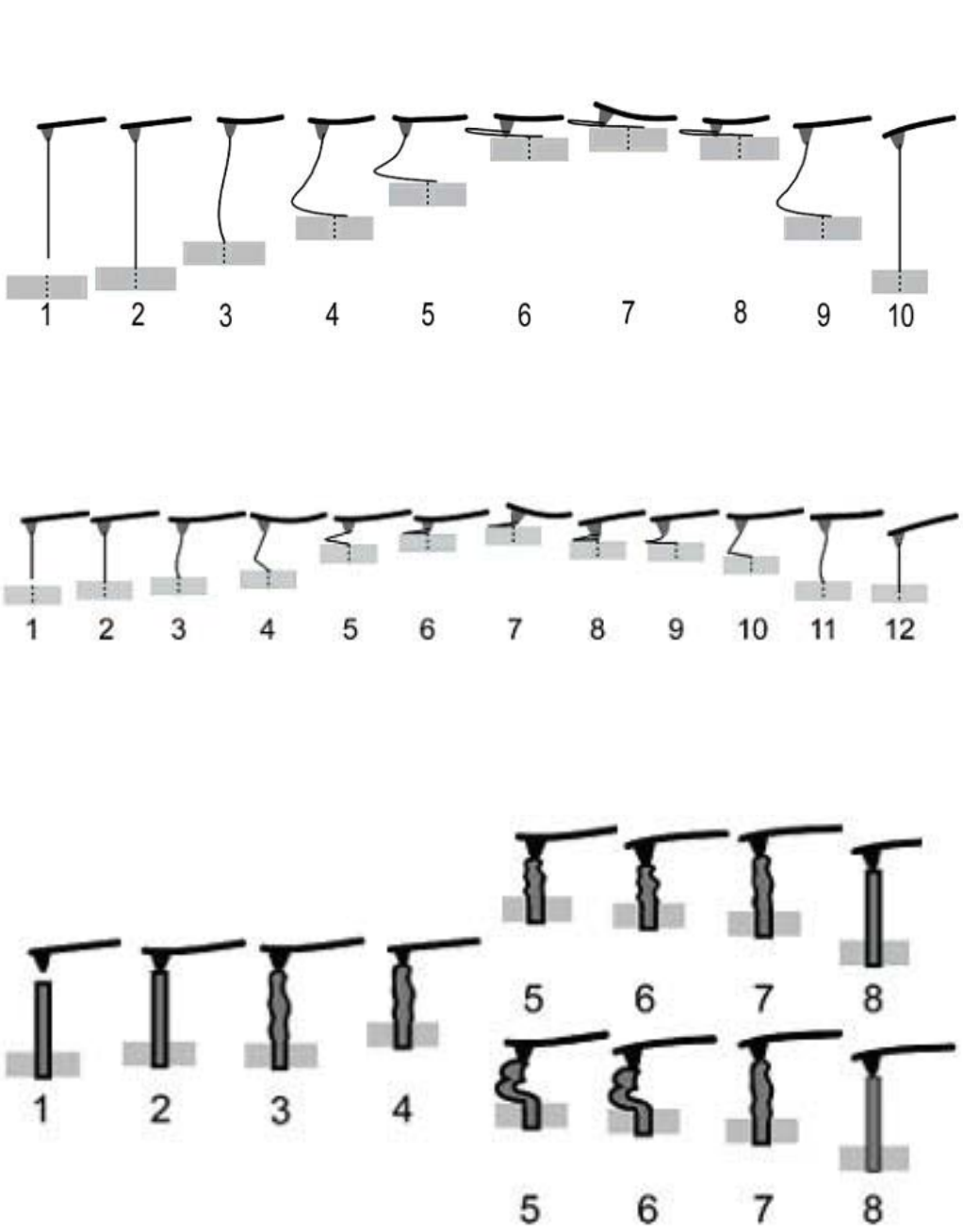

Figure 3.3 – The various modes of axial CNT deformation include (a) Euler (column) buckling, (b) kinking, and (c) symmetric (top) and asymmetric (bottom) shell buckling [21].

a

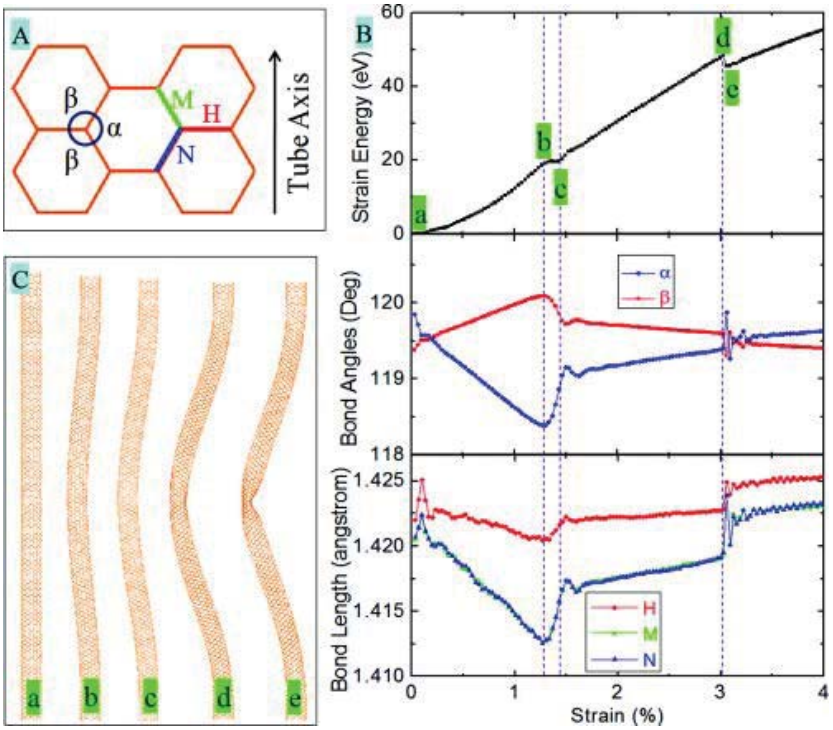

b

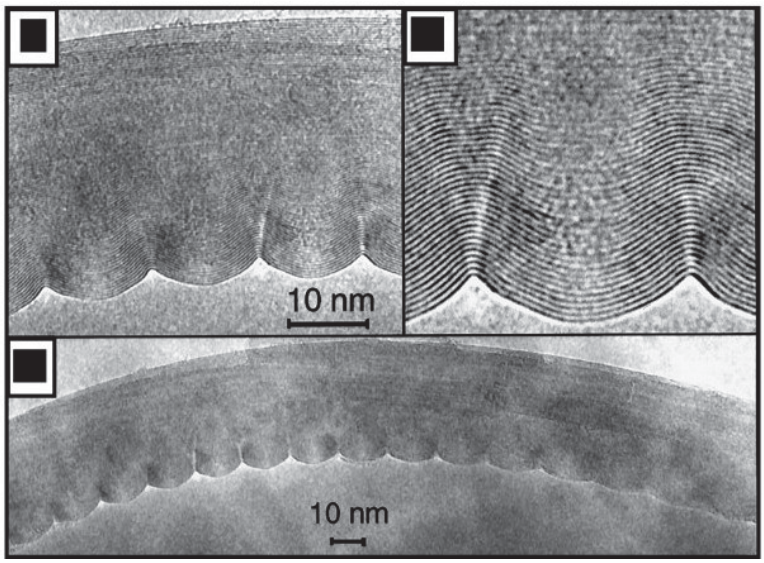

Figure 3.4 – (a) Modeling to support kinking in SWNTs [220], and (b) experimental observation of shell buckling in MWNTs[228].

While MWNTs are also capable of showing negative stiffness behavior [21], in contrast to few-walled CNTs they will generally deform in a much more complicated manner. Due to the complex mechanics of energy transfer between concentric walls [229] and other factors such as inter-layer slipping [230], these many-walled structures will exhibit what is known as shell buckling (Figure 3.3c) [228], [231]. This type of buckling can either be symmetric (collapsing about the central CNT axis) or asymmetric (Figure 3.4b), and has even been observed for CNTs encased within a polymer matrix [232].

Given these buckling modes, a forest of CNTs provides an interesting medium for the study of novel mechanical behavior in nanostructured materials. It has been both experimentally demonstrated [233], [234] and modeled [235] that, as with individual CNTs, self-assembled arrays such as those described in Chapter 2 can withstand numerous compressive cycles with little permanent deformation. Practically, however, these forests will irreversibly reconfigure beyond some threshold strain [236].

3.1.3. A Combination of These Unique Materials

By impregnating these CNT forests with a supportive, yet compliant elastomer matrix such as PDMS, this bed of springs can be reinforced to allow for high-cycle recoverability. Such a composite was previously demonstrated by Ci *et al.*, and it was reported that the material exhibited a clear anisotropy with an impressive six-fold improvement in the modulus along with a twenty-one-fold enhancement in damping over the neat polymer [187].

Beyond these benefits, such a material provides an attractive template for probing unusual nanomechanical behavior in polymer nanocomposites. Particularly, with respect to the discussion of nonlinear viscoelasticity in Section 3.1.1, there remain many questions as to how CNTs and other nanomaterials interface with a surrounding polymeric medium to either enhance contact [131], [237] or facilitate mechanical damping [154], [238]. Given that there is little-to-no chemical bonding between the CNTs and the matrix in this composite, it serves as a near-ideal system to probe such interactions during stressing. Also, due to the extremely high aspect ratio of the CNTs, an opportunity exists to isolate the internal mechanics of deformation to both improve the fundamental understanding of such interactions, as well as reveal interesting mechanical responses with practical utility.

3.1.4. Dynamic Mechanical Analysis

For the analysis of viscoelastic behavior in polymeric materials, dynamic mechanical analysis (DMA) can be a powerful technique. The cyclic deformation of a sample can be used to nondestructively reveal properties such as the storage (E') and loss (E") moduli and damping (tan δ). Also, by independently controlling the amplitude, frequency, and ambient temperature for this oscillatory loading, it is possible to resolve precise thermomechanical information, including second-order phase transitions such as the T_g and T_m.

One caveat of DMA is that the equations used to calculate the E' and E" assume that the material is being deformed within the linear viscoelastic region.

This is inconvenient for many polymer nanocomposites, as (per what was described in Section 3.1.1) these materials generally display nonlinear viscoelastic behavior. Accordingly, DMA was primarily used in this thesis work to impart cyclic loads on a sample to track its stiffness (a raw variable measured directly by the instrument) as a function of the input variables of strain amplitude, frequency, and temperature.

Also, while numerous variations of clamps are available, compression was the only viable testing mode due to the height limitations of the synthesized CNT forests. As such, unless otherwise noted, all samples (described in Section 2.4.1) were tested via uniaxial compression.

3.2. Cyclically Stressing Highly Anisotropic Nanocomposites

In agreement with what was observed previously in the static and low-cycle dynamic testing [187], the significant degree of nanotube alignment in this material results in highly anisotropic behavior when cyclically stressed. Both the "radial" (transverse to CNT alignment direction) as well as "axial" (longitudinal to CNT alignment direction) responses are distinct, and are observed in the FWNT and MWNT composites.

3.2.1. Unfilled PDMS

The mechanics of deformation for cross-linked elastomer networks are well understood, and the amplitude-dependent dynamic response can be used to neatly explain this behavior. Using a TA Instruments Q800 DMA, each sample was

subjected to a range of strain amplitudes up to its own ultimate compressive strain (evidenced by a sharp increase in the stiffness/stress at high strain). Experiments were conducted at room temperature, a frequency of 5 Hz, and were repeated 5 times to ensure consistency (Figure 3.5); a five-cycle average is presented in Figure 3.6 and Figure 3.7 for the FWNT and MWNT composites, respectively.

The idealized internal dynamics of an unmodified PDMS network described below serve as a basis of comparison for the nanocomposite sample. The Roman numeral designations correspond to the strain amplitudes denoted in Figure 3.6a and Figure 3.7a:

I. For low amplitude oscillations, only the shortest elements of the network are bearing load.

II. As the polymer network begins to stretch and extend, it will exhibit nonlinear behavior until the amplitude is sufficient that all elements of the network are being engaged.

III. In the linear region of deformation, all polymer chains connected to the network are now bearing load. The network continues to stretch and the individual chains will be preferentially aligned for large strains.

IV. At the amplitude where regions of the network reach full extension, the dynamic response will again become nonlinear. This nonlinearity will continue until the entire network reaches full extension, at which point the stiffness will rise dramatically and the sample will cease to displace.

3.2.2. Radial Deformation: Reminiscent of the Neat Polymer

At first glance, the amplitude-dependent response of the radially-stressed FWNT nanocomposite in Figure 3.6a bears little resemblance to the neat polymer. However, after close examination, a few very clear similarities emerge.

Most prominently, it is observed that the maximum amplitude of deformation (and, deductively, the ultimate compressive strain) is markedly lower for radial deformation. Secondly, aside from the obvious stiffness discrepancy between the two materials, the overall trend of the curve is quite similar to that of the polymer by itself.

Specifically, cyclic radial deformation results in a similar nonlinear response up to a 4% strain amplitude, followed by a linear region of deformation from 4% to 6% strain. From 6% to 10% strain, the trend is evocative of what is seen in the 10% to 14% amplitude range for pure PDMS. These observations are further supported by the stress/strain relationship, as seen in Figure 3.6b. Curiously, the trend of the radially-stressed composite closely matches that of the neat PDMS, with the exception of a much lower maximum compressive strain.

These similarities become even clearer when the materials are tested for a wide range of strain amplitudes and frequencies. Similar strain sweeps were conducted for numerous other frequencies (0.5 Hz, 1 Hz, 2 Hz, 7.5 Hz, and 10 Hz) and overlaid with the 5 Hz test in Figure 3.8b to reveal that, as with the neat polymer (Figure 3.8a), the radially stressed FWNT composite exhibits relatively consistent strain-dependent behavior over this range of frequencies.

a

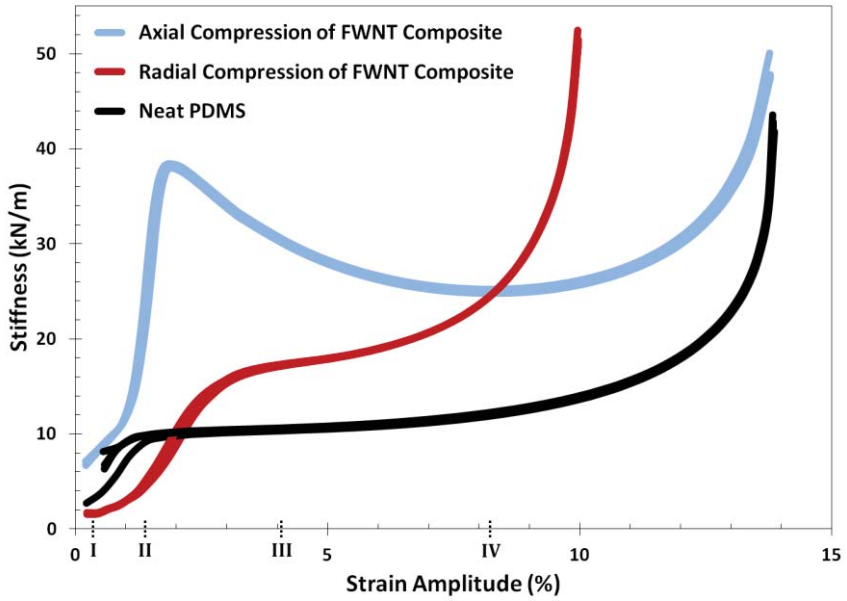

b

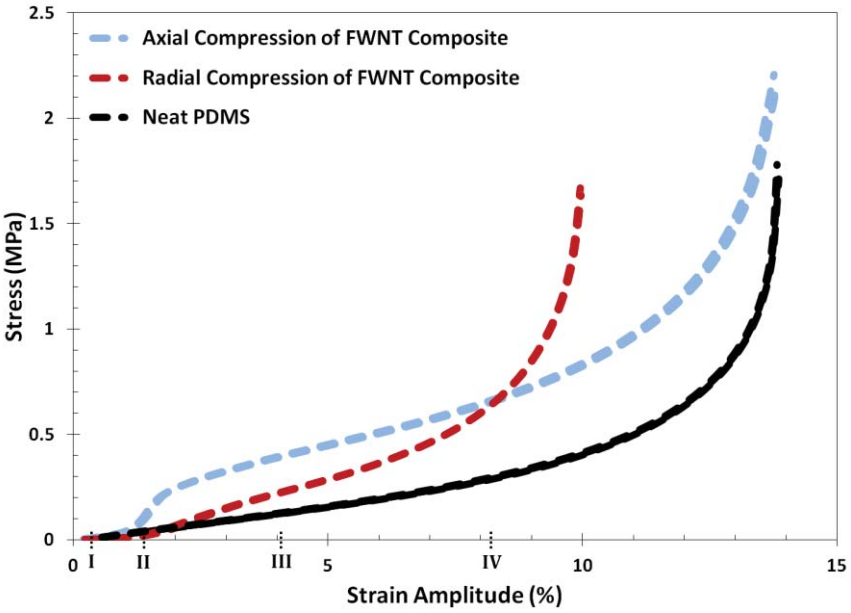

Figure 3.5 – The strain-dependent behavior of the aligned FWNT composite's (a) stiffness and (b) stress is repeatable over numerous cycles.

a

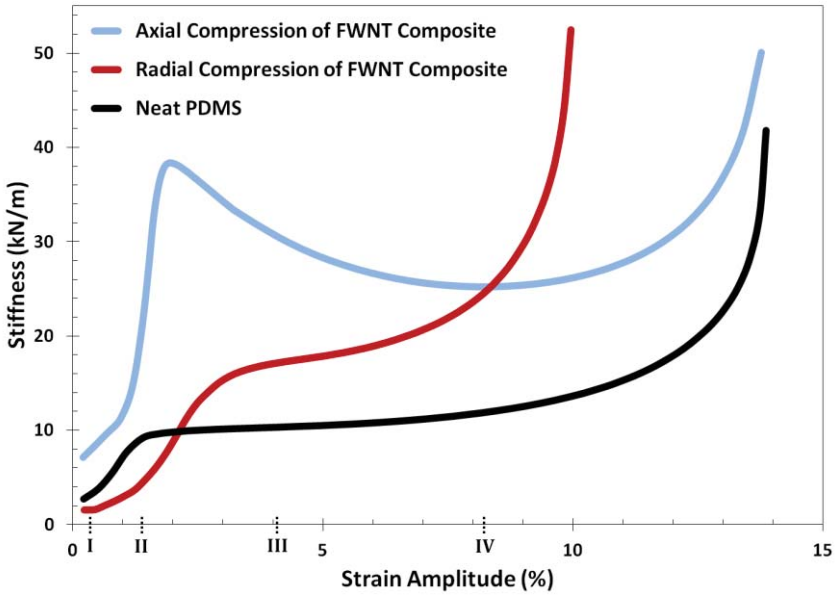

b

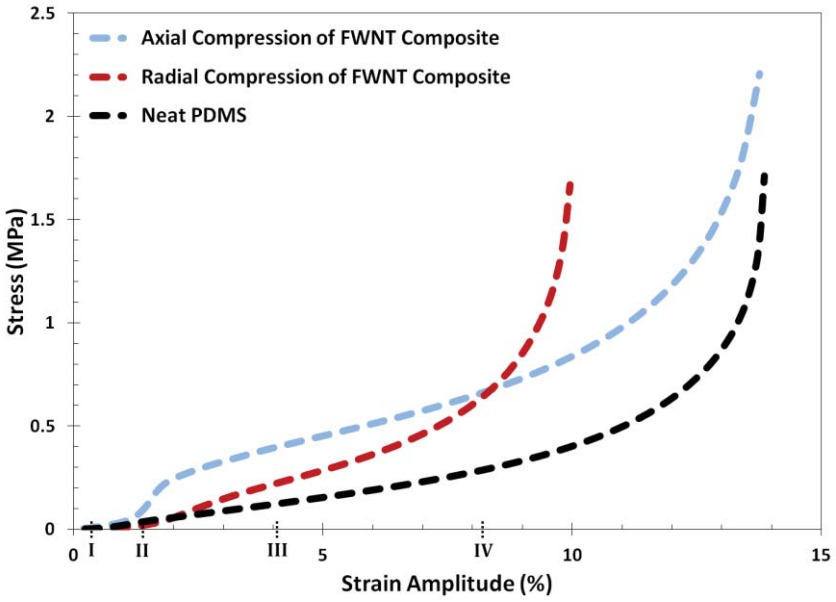

Figure 3.6 – Using a 5 cycle average for clarity, the strain-dependent response of the aligned FWNT composite is highly anisotropic, as evidenced by the (a) stiffness and (b) stress during cyclic loading.

a

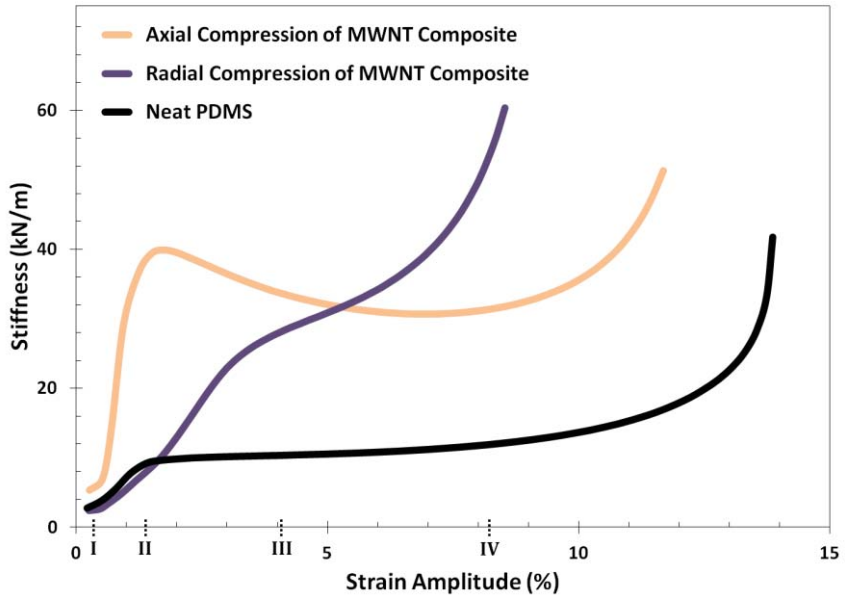

b

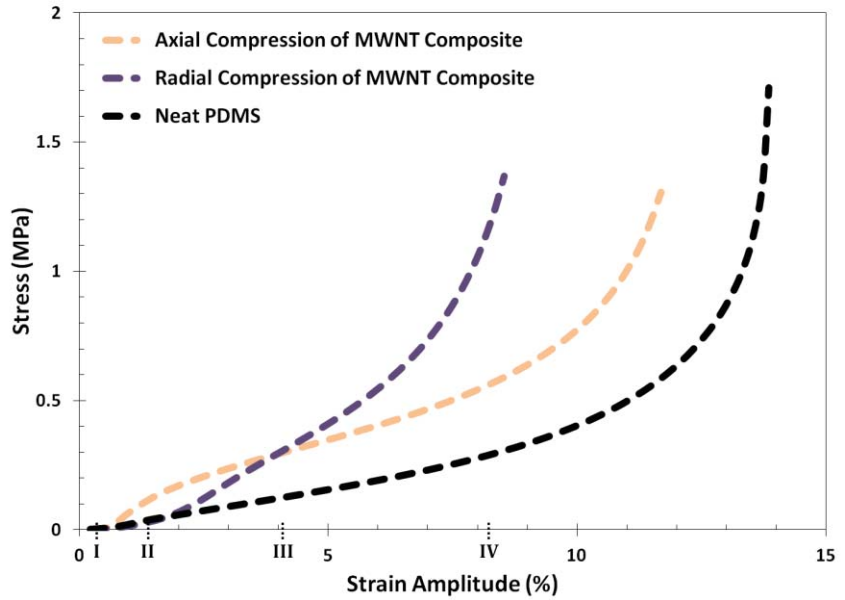

Figure 3.7 – As with the FWNT composite, the strain-dependent behavior of the aligned MWNT composite is highly anisotropic, as evidenced by the (a) stiffness and (b) stress during cyclic loading.

a

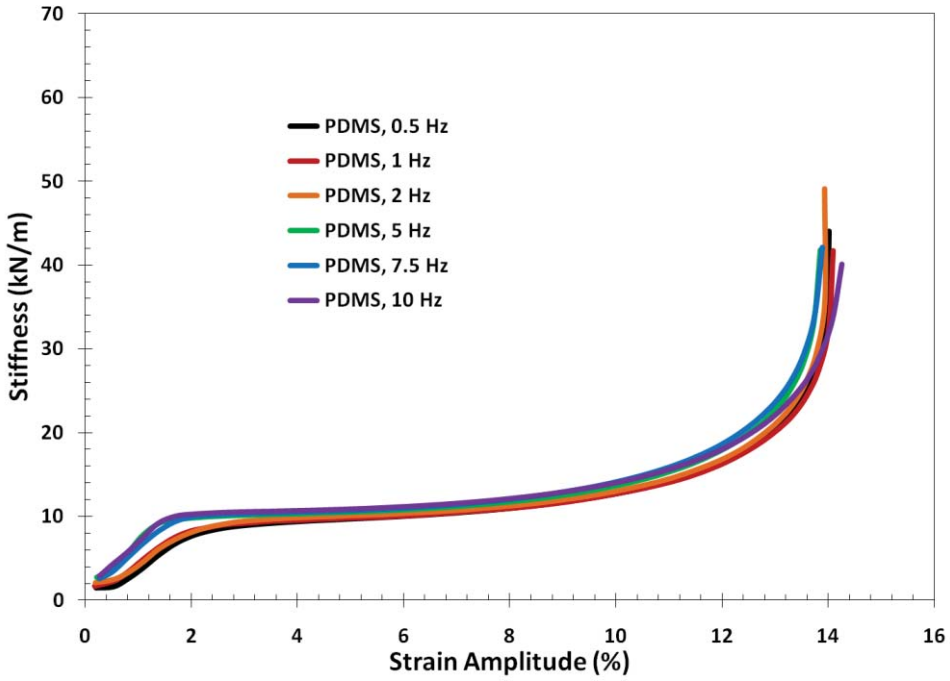
PDMS, 0.5 Hz
PDMS, 1 Hz
PDMS, 2 Hz
PDMS, 5 Hz
PDMS, 7.5 Hz
PDMS, 10 Hz
Stiffness (kN/m)
Strain Amplitude (%)
0
10
20
30
40
50
60
70
0
2
4
6
8
10
12
14
16

b

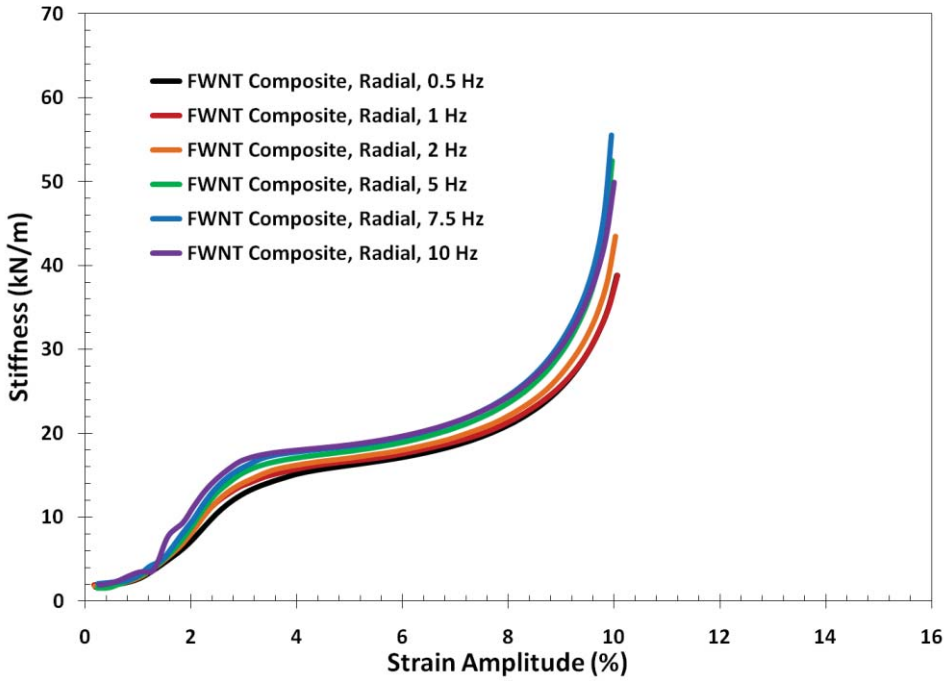
FWNT Composite, Radial, 0.5 Hz
FWNT Composite, Radial, 1 Hz
FWNT Composite, Radial, 2 Hz
FWNT Composite, Radial, 5 Hz
FWNT Composite, Radial, 7.5 Hz
FWNT Composite, Radial, 10 Hz
Stiffness (kN/m)
Strain Amplitude (%)
0
10
20
30
40
50
60
70
0
2
4
6
8
10
12
14
16

c

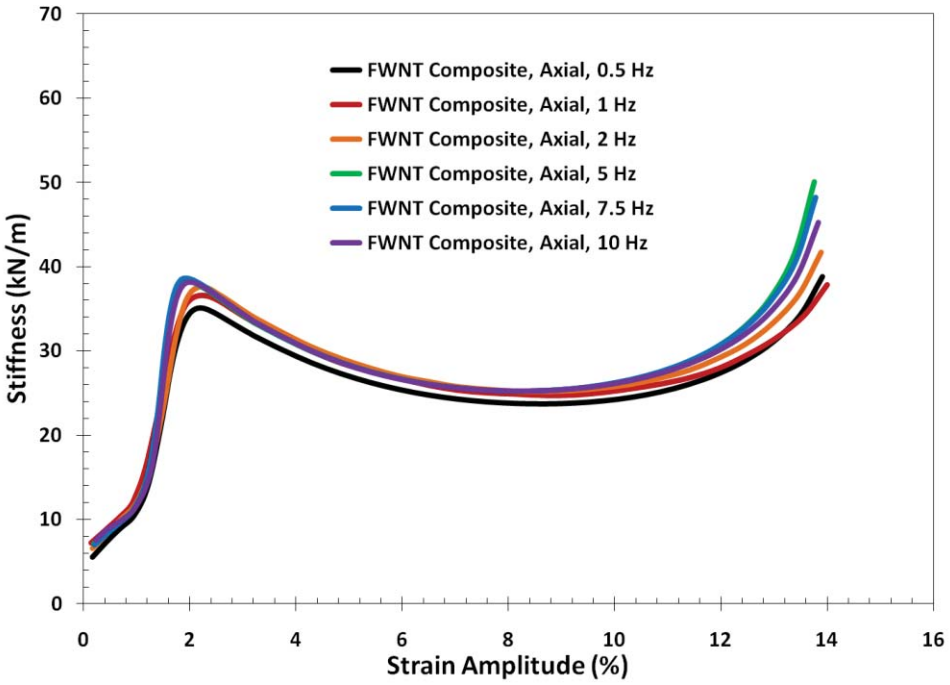

Figure 3.8 – Strain sweeps at low frequencies for (a) the neat PDMS and the composite stressed (b) radially and (c) axially. Divergent and/or convergent trends suggest a change in the mechanics of deformation.

The samples were then tested (using the same Q800 DMA) for frequency-dependent behavior from 0.5 Hz to 100 Hz for a range of strain amplitudes (0.5%, 1%, 2%, 3.5%, 5%, 7.5%), again with a 5 cycle average for consistency. These results were merged and are presented as a 3D surface plot in Figure 3.10 and Figure 3.11 for the FWNT and MWNT composites, respectively. While stiffness provides some perspective in this surface plot, the tan δ (damping) proved to be a much richer source of micromechanical information, revealing resonances within the material for particular strain/frequency combinations.

a

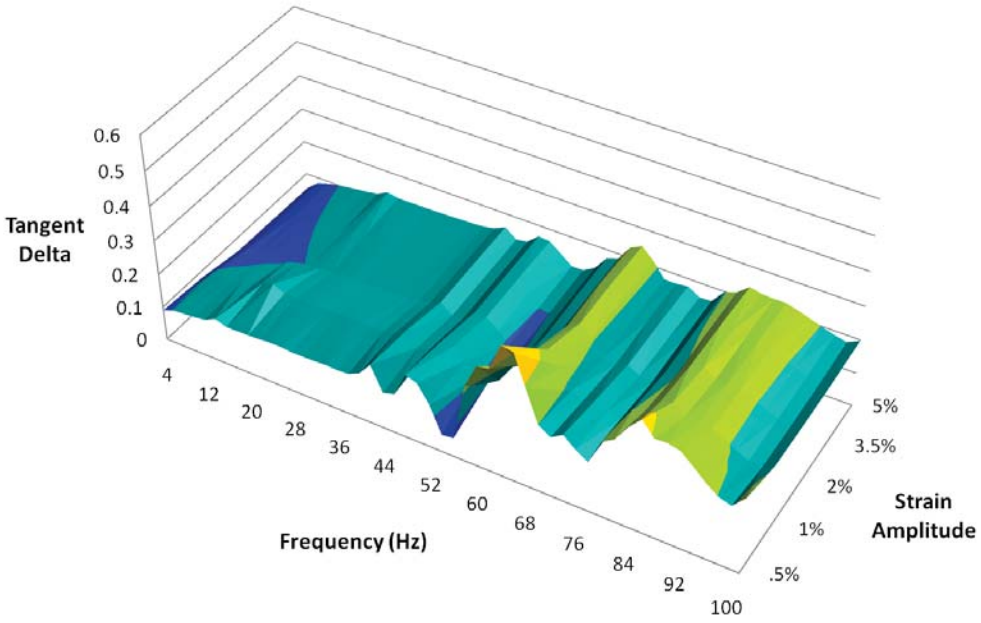

b

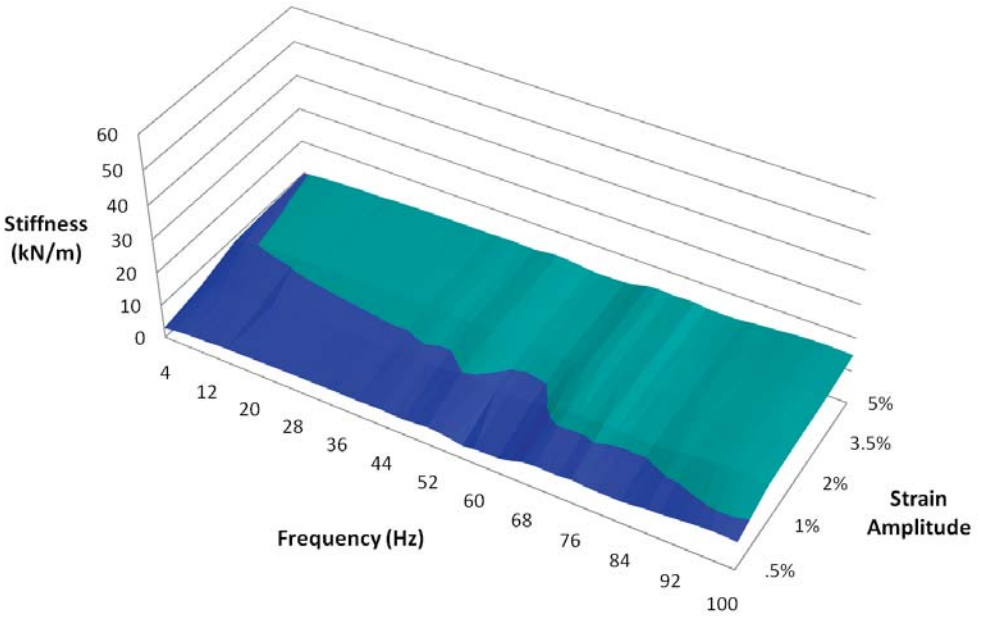

Figure 3.9 – (a) Tangent δ and (b) stiffness as a function of frequency and strain amplitude for neat PDMS.

a

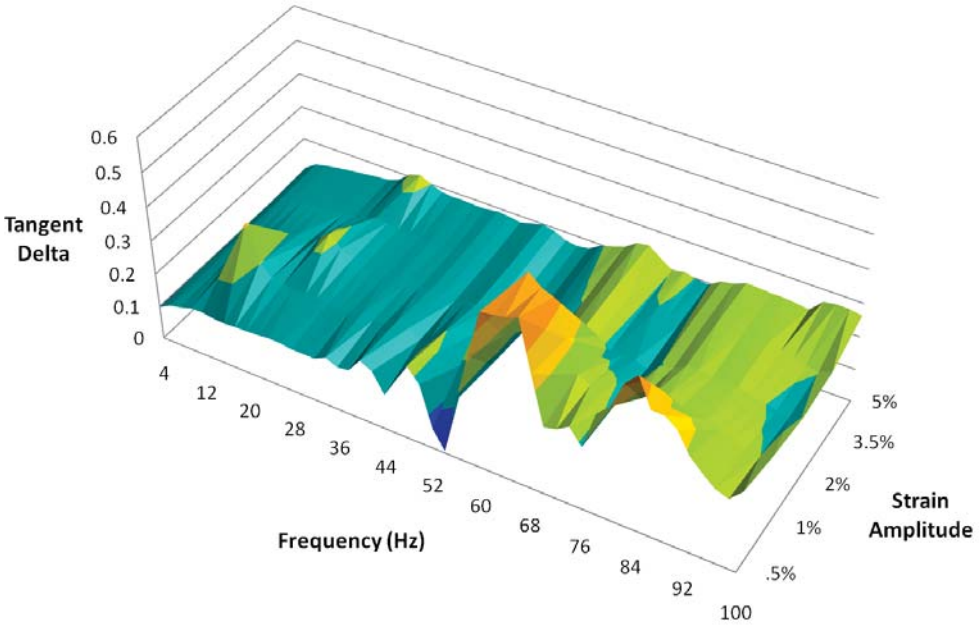

b

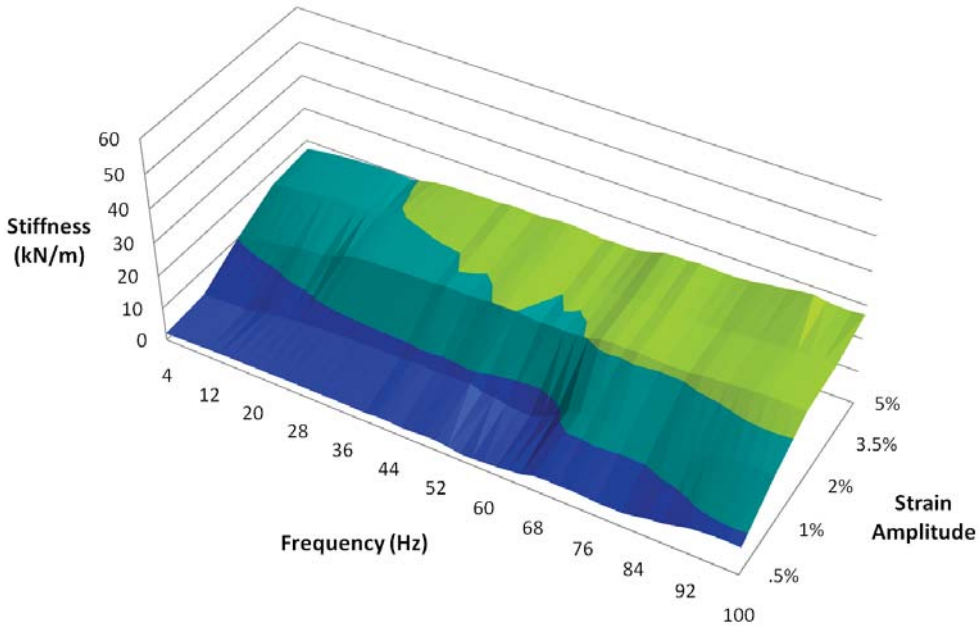

Figure 3.10 – (a) Tangent δ and (b) stiffness as a function of frequency and strain amplitude for a radially-stressed FWNT Composite.

a

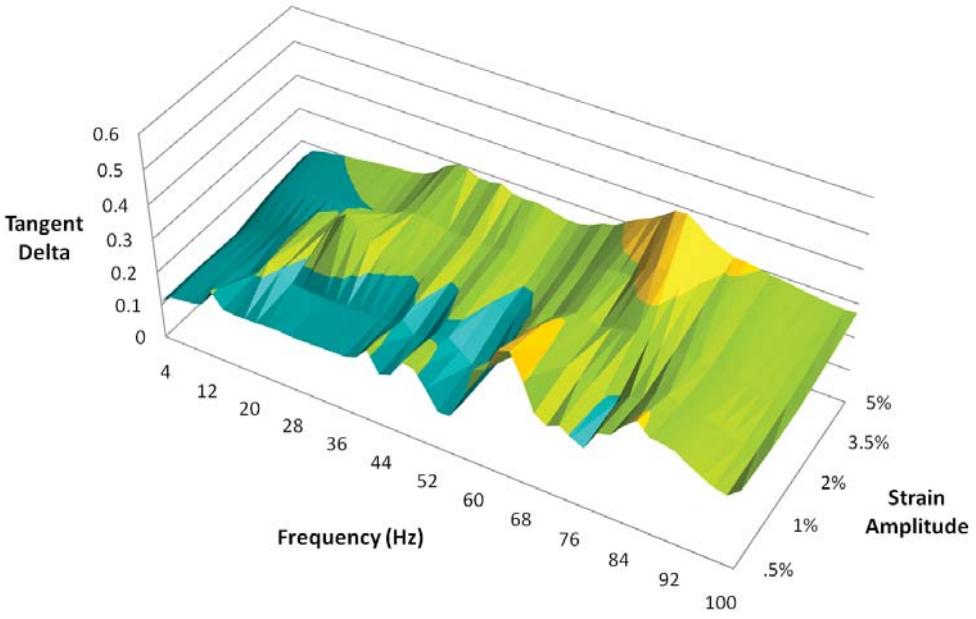

b

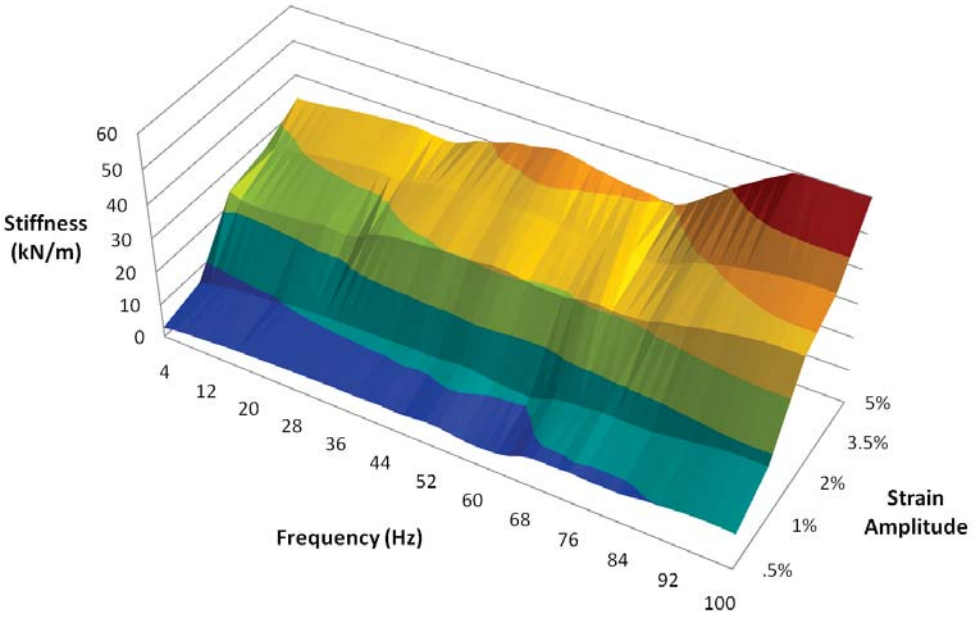

Figure 3.11 – (a) Tangent δ and (b) stiffness as a function of frequency and strain amplitude for a radially-stressed MWNT Composite.

a

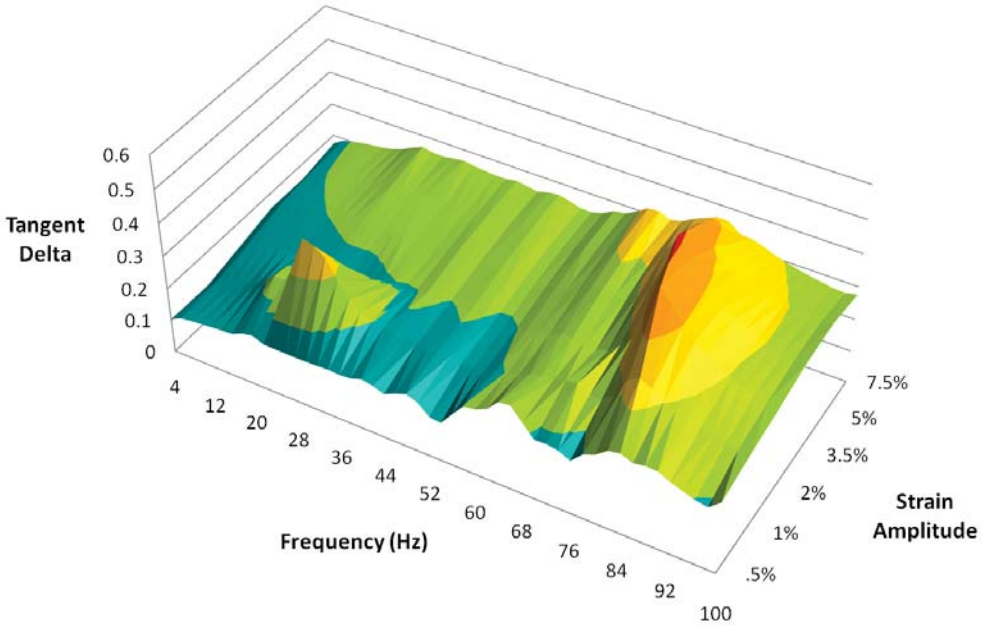

b

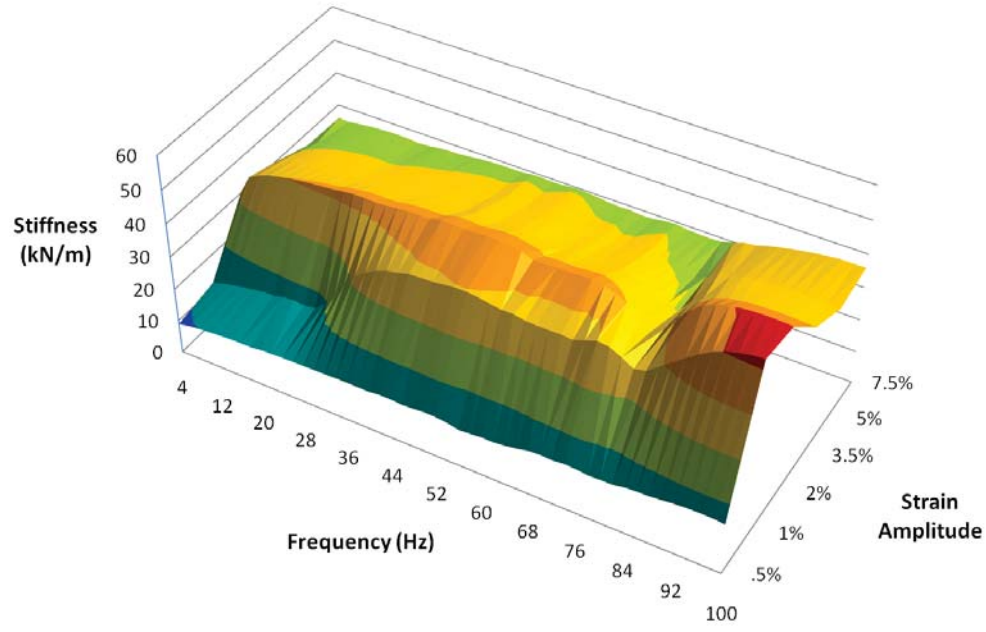

Figure 3.12 – (a) Tangent δ and (b) stiffness as a function of frequency and strain amplitude for an axially-stressed FWNT Composite.

a

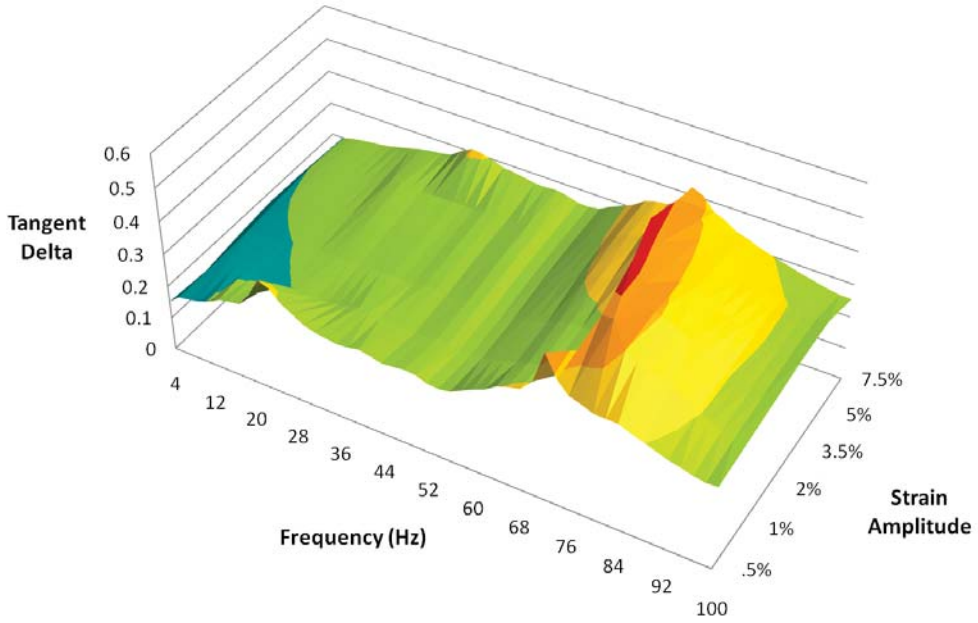

b

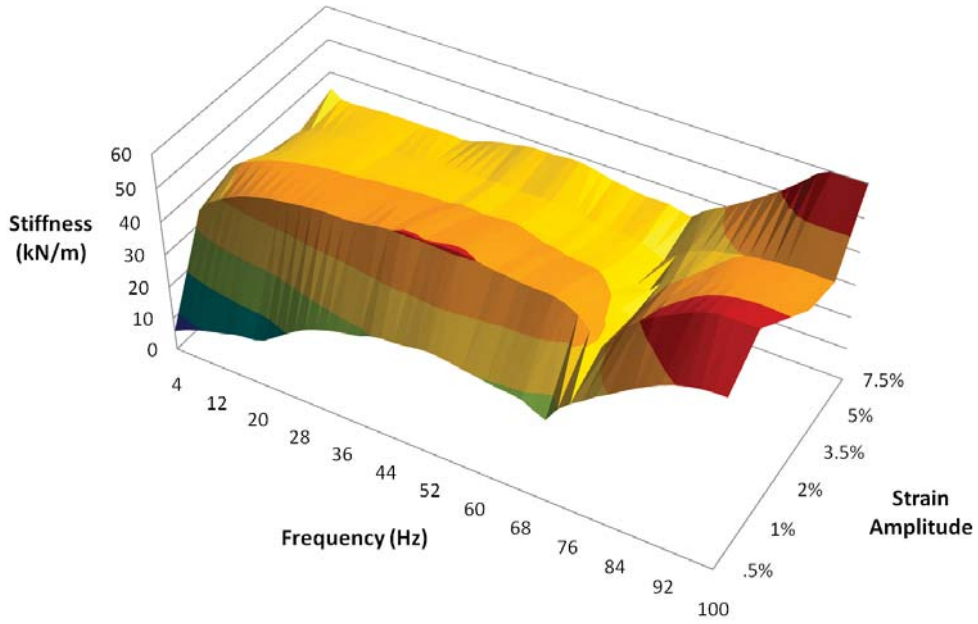

Figure 3.13 – (a) Tangent δ and (b) stiffness as a function of frequency and strain amplitude for an axially-stressed MWNT Composite.

a

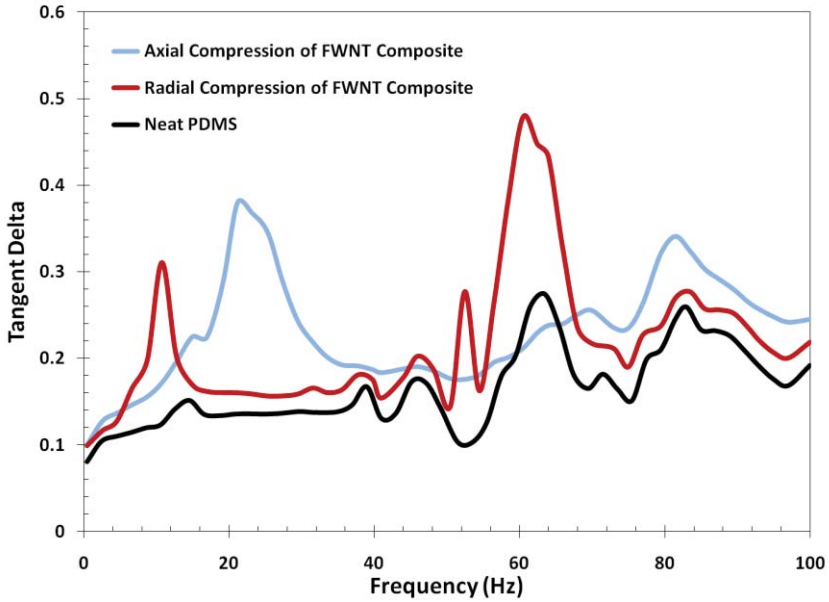

b

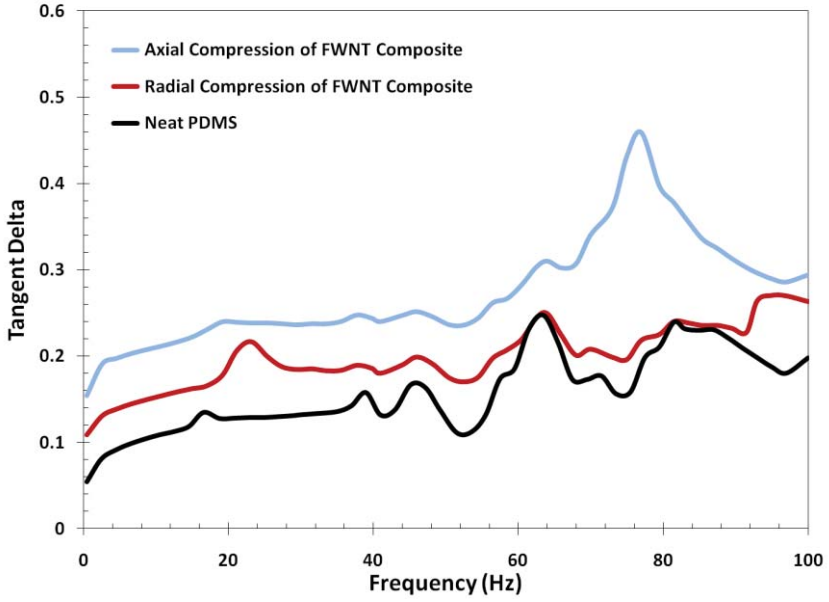

Figure 3.14 – By comparing the (a) pre- and (b) post-buckling regimes (1% and 5% strain amplitude, respectively) for frequency sweeps, resonances provide information regarding the mechanics of deformation in the material.

It is observed that the landscape of the tan δ for the radially-deformed composite bears a great resemblance to that of the neat PDMS (Figure 3.9), further strengthening the supposition that the mechanics of deformation are similar for these two materials. However, while the majority of the PDMS resonances are mirrored in the composite, below a 2% amplitude a few of those resonances are significantly amplified. By choosing individual frequency sweeps both below (1%) and above (5%) the 2% threshold, we see in Figure 3.14 that the 61 Hz PDMS resonance is greatly amplified for the radially-stressed composite for low amplitudes, while all resonances are muted at higher amplitudes.

It is difficult to index the amplified 61 Hz resonance, though the orientation of the CNTs may provide some insight. Shearing at the interface has been implicated in mechanical damping for nanocomposite materials, and given the near uniaxial orientation of the interface in this composite, it is conceivable that this event corresponds to the sample resonating longitudinal to the CNT alignment direction.

3.2.3. Axial Deformation: Dynamic Strain Softening

In contrast to radial deformation, these composites perform quite differently from the neat polymer when loaded along the axis of CNT alignment. This is immediately clear in Figure 3.6a and Figure 3.7a, where the dynamic stiffness of the composite is similar to PDMS up to approximately a 1% strain amplitude, after which it spikes rapidly at 2% strain to a four-fold improvement over the neat polymer. This then leads to a region of dynamic strain softening, where further increases in the oscillation amplitude will result in increasingly lower stiffness

values over the broad range of 2% to 9% strain. For higher amplitudes, the stiffness resumes a trend reminiscent of the PDMS before achieving a similarly high ultimate compressive strain (14%).

Despite this atypical response, the stress/strain behavior in Figure 3.6b reveals that the axially-loaded composite does resemble the neat PDMS for moderate-to-high strain amplitudes. In the absence of the anomaly below 2% strain, the plot for the axial deformation would almost exactly match up with the response of the pure polymer.

Unlike the radially-loaded sample, the axial strain sweeps for various frequencies are not entirely consistent. In Figure 3.8c, it can be seen that the stiffness of the composite begins to diverge for medium-to-high amplitudes; this suggests that, in this orientation, the dynamics of deformation are more viscous for large amplitudes.

These observations are further mirrored in the 3D surface plot, where the topography of the surfaces in Figure 3.12a and Figure 3.13a are unmistakably different than the unfilled PDMS for a wide range of frequencies and amplitudes. Interestingly, from the stiffness maps in Figure 3.12b and Figure 3.13b, it can be resolved by viewing in the depth direction that the dynamic strain softening behavior occurs up to 100 Hz, indicating the robustness of the effect.

Plotting the low strain frequency sweep in Figure 3.14a, a distinct resonance at 22 Hz is observed that does not seem to originate from any resonance in the polymer. That resonance completely disappears for the moderate strain frequency

sweep in Figure 3.14b, and gives rise to another resonance peak at 78 Hz that also does not appear to have any relation to the polymer. For the high-strain deformation, it is seen that the majority of the frequency range coincides with the muted response of the radial composite.

3.3. Determining the Mechanics of Deformation

As a first observation, it is curious that this continuously-reinforced elastomer nanocomposite material does not exhibit the Payne effect when cyclically deformed in either orientation. Axial deformation does display a similar strain softening effect, though for the reasons detailed below, this behavior is believed to be a function of the oriented CNT reinforcement and not the interface between the polymer and the CNTs.

Furthermore, while both composites exhibit the behavior detailed in Sections 3.2.2 and 3.2.3, it is observed that the FWNT composite is much more distinctly anisotropic as compared to the MWNT composite. This is expected, since—as discussed in Sections 2.2.1 and 2.3.1—the FWNTs are a much more "ideal" forest structure as compared to the MWNTs, which are much larger in diameter, not nearly as well-aligned, and have a greater degree of defects.

3.3.1. Radial Loading

In resolving the mechanics of deformation for the radially-stressed composite, it is first noted that there is no obvious signature of the CNTs in the

strain- and frequency-dependent behavior. This implicitly suggests that the internal mechanics of the composite in this orientation closely match that of an elastomer network, though the reduction in the ultimate compressive strain as compared to the neat polymer must be explained.

Engaging in a thought experiment to rationalize these observations, it is logical to contemplate how the mechanics of deformation for a cross-linked elastomer network—as detailed in Section 3.2.1—might be influenced by strong, continuous filaments coaxially organized orthogonal to the direction of deformation. During the polymer infiltration process, it is expected that the individual polymer chains take a random path as they pervade the forest structure and occupy the interstitial space. The cross-linking of these chains would result in a three-dimensional network around the preferentially-aligned CNTs.

As the sample is deformed and the material bulges outward (a phenomenon known as "barreling"), the polymer will progressively engage the nanotubes for increasing amplitudes. This growing radial tension on the CNTs is expected to promote the displacement and translation of the CNT filaments within the matrix and in relation to each other. Additionally, the CNTs would effectively serve as cylindrical pulleys, expediting the full extension of the polymer network. Such dynamics would explain the similarities to the mechanical response of the neat polymer, while explicating the lower ultimate compressive strain due to the role that the CNTs play in increasing the effective cross-link density of the matrix. A schematic representing this proposed mechanism is presented in Figure 3.15.

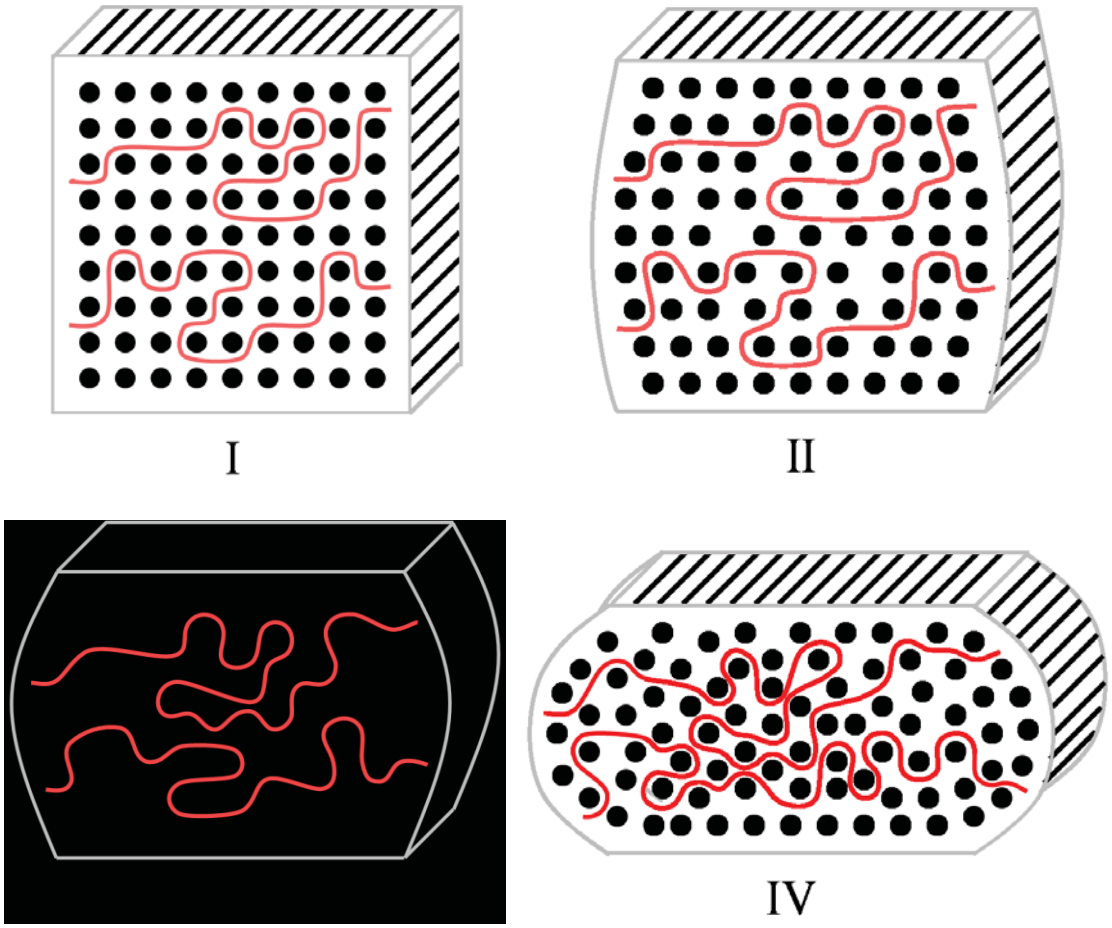

Figure 3.15 – Radial composite loading is expected to expedite the extension of the elastomer network. The Roman numeral designations correspond to approximate strain amplitudes, as indicated in Figure 3.6 and Figure 3.7.

3.3.2. Axial Loading

The mechanics of deformation are clearly much different for the axially-loaded composite. Dynamic strain softening—such as what occurs after 2% strain in Figure 3.6 and Figure 3.7—is reminiscent of the Payne effect, though the trends for low (<2%) and high (>9%) strain amplitudes do not coincide with the behavior seen in traditional filled elastomer systems (Figure 3.2a). As such, it is believed that

the unusual response of this nanocomposite material when cyclically loaded along the axis of the CNTs is owed to another mechanism.

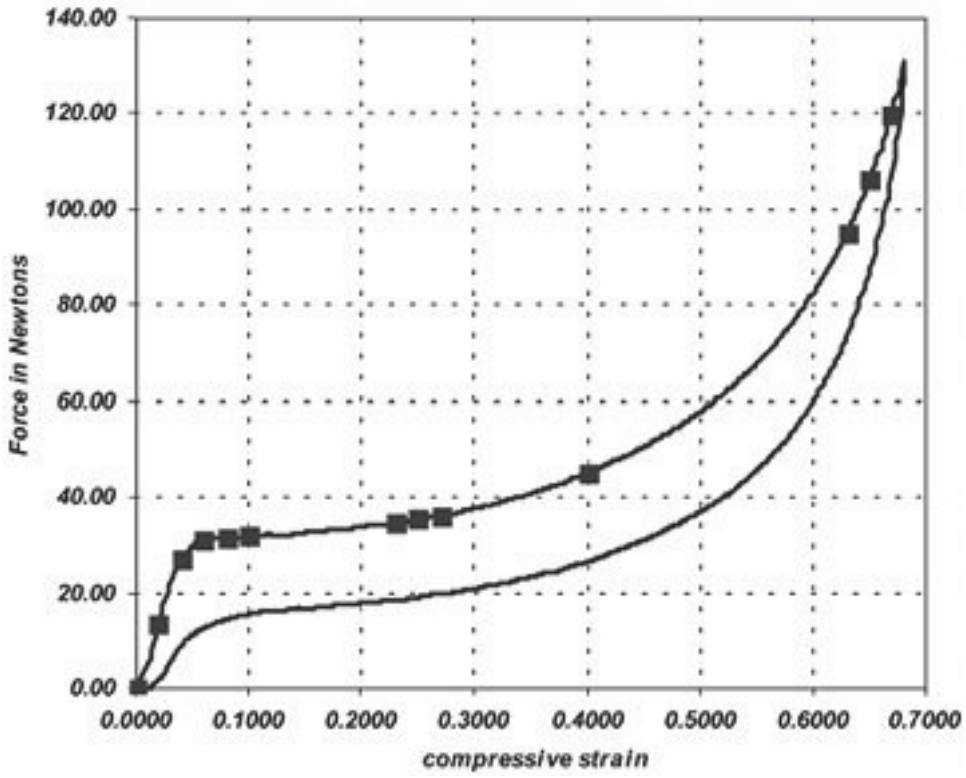

Figure 3.16 – The stress/strain behavior of open-cell foams bears a strong resemblance to the response of the axially-stressed nanocomposite in Figure 3.6b [239].

Firstly, the kinking or microstructural buckling of these long, slender CNTs to produce a negative stiffness response is improbable. While it has been reported that negatively stiff cylindrical inclusions could be stabilized by a positively stiff elastic coating or matrix [240], the results of Yap, Lakes, and Carpick provide strong evidence that CNTs of a sufficient aspect ratio (210 or above) will buckle but never kink when loaded along their central axis [21]. However, as mentioned in Section

3.1.2, forests of CNTs are known to collectively buckle when loaded axially, compressing in a manner that is largely recoverable, yet not completely elastic. Such arrays of nanotube struts have been shown to closely mimic the mechanics of open-cell foams by forming self-organized folded patterns that allow the forest to compress to less than 15% its free height [234].

Curiously, the stress/strain behavior of such foams very closely match that of the axially-stressed composite (Figure 3.16) [239], despite the fact that the interstitial space of these impregnated forests consists of a material that is much denser than air and not nearly as fluid. The modeling of nonlinear deformation in bulk open-cell foams has shown that long-wavelength buckling modes may occur under uniaxial compression due to the buckling of columnar constitutive elements (Figure 3.17) [241].

Given these similarities, it is proposed that the strain softening response for cyclic axial compression is owed to the collective Euler buckling of the CNTs, as illustrated in Figure 3.18. A transition from barreling to the cooperative buckling of the nanotube struts would account for the nonlinear response below 2% strain amplitude, and is conceptually rationalized by the strong confinement effect of the elastomer network in the radial direction; as seen in Figure 3.6a, the stiffness of the composite increases rapidly around 2% strain for radial deformation. It is expected that this axial buckling will continue until the elastomer network nears full extension, at which point the stiffness will rise rapidly in a manner that is analogous to the process of densification in foams.

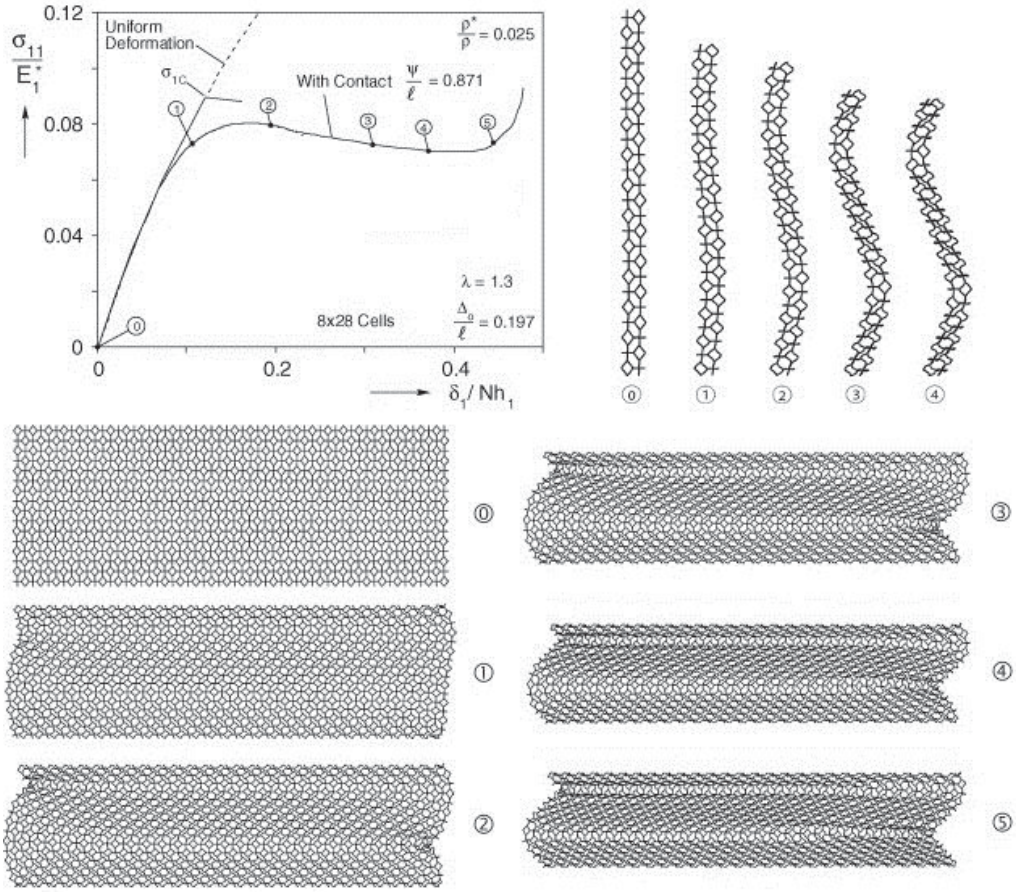

Figure 3.17 – The modeling of nonlinear crushing in open-cell foams portrays the collective buckling of an ensemble of columnar elements (adapted from [241]).

Such a mechanism neatly explains the experimental observations. Buckling of the CNTs is evidenced by the strong polymer-independent resonances in the pre- and post-buckled regimes (22 Hz in Figure 3.14a and 78 Hz in Figure 3.14b, respectively), and explains the divergence of the stiffness for large amplitudes of oscillation in Figure 3.8c. The additional force necessary to maintain the compression of an ensemble of buckled CNT struts also accounts for the enhancement in stress above 2% strain in Figure 3.6b (as compared to the neat

polymer). Moreover, such a coordinated deformation mechanism also explains how the composite is able to displace to the same strain as the neat polymer, despite the presence of high-aspect-ratio inclusions.

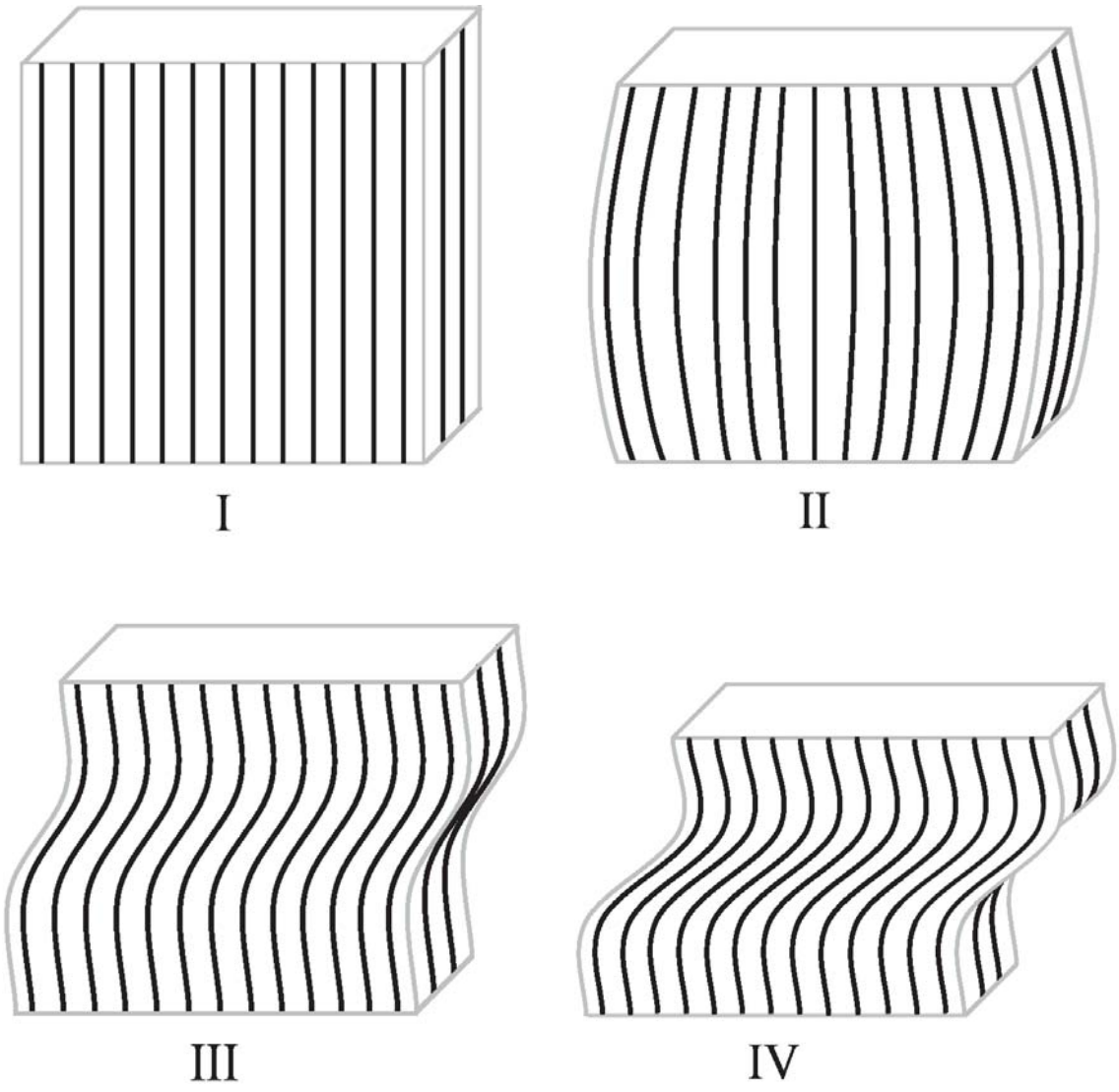

Figure 3.18 – Axial composite loading is proposed to enable the collective buckling of the CNTs. The Roman numeral designations correspond to approximate strain amplitudes, as indicated in Figure 3.6 and Figure 3.7.

The "spring-like" contribution of buckled CNTs is also perhaps responsible for the anomalous high-strain and high-frequency recovery of the axially-loaded composite as compared to the other samples and loading orientations. By themselves, the CNT forests have been shown to recover at a rate greater than 2 mm/sec [234]. In Figure 3.12 and Figure 3.13, it is seen that dynamic strain softening occurs for frequencies in excess of 100 Hz, and that only the axially-stressed composites were able to withstand the 100 Hz frequency range for a 7.5% strain amplitude.

As with the Euler buckling of freestanding columns, the buckling mode for this composite is expected to be some function of the boundary conditions. In this case, the sample is placed on a rigid platen and is compressed downward with a drive shaft that has the ability to deflect laterally. The simplification of Euler's buckling load formula for one "fixed" and one "guided" boundary is a sinusoid with a period of $\frac{L}{2}$, and while other buckling modes are conceivable, this mode was chosen for the schematic.

Chapter 4

Self-Stiffening in Nanocomposites: Isolating the Effect

Primed with insight into the complex mechanics of deformation in these aligned CNT/PDMS composites in Chapter 3, in this chapter I will address the challenges presented in Specific Aim II by outlining this material's unusual response to cyclic loading. To help define the limits and significance of the effect, the A-MWNT/PDMS composites were subjected to various forms of mechanical stressing and then probed for changes in their thermomechanical behavior.

4.1. Conventional Responses to Cyclic Stressing

When subjected to repeated mechanical stress, materials can experience microstructural damage that may ultimately lead to premature failure. This effect

(commonly known as “fatigue”) can weaken materials and ultimately lead to delamination, cracking, and other forms of fracture.

4.1.1. Preventing Fatigue

The most common method of preemptively addressing the risk of fatigue failure is to “strengthen” a material to ensure that its fatigue limit (the minimum stress that is necessary to enable fatigue) is well above the loads that it will be subjected to. Alternatively, efforts have been made to modify materials with fillers that can mitigate this risk by actively responding to such changes in microstructure. Examples include the addition of nanoscale ceramic particles to “pin” microcracks [242], interstitial carbon nanotubes that will bridge forming cracks and cavities [243], and even phase-separated PDMS healing agents to fill voids that may form during stressing [244].

4.1.2. Self-Strengthening and Work Hardening

However, not all materials need to be preemptively protected from the effects of fatigue. Bone, a composite material consisting of a porous hydroxylapatite framework filled with a collagen-rich matrix, will respond to repeated elastic loading by densifying and remodeling its structure to more-efficiently distribute subsequent loads. This metabolic process—popularly referred to as Wolff’s Law—helps to reduce the risk of fracture in areas of repeated loading. Similarly, networks of bundled actin/α-actinin have recently been shown to harden when cyclically sheared [245].

a

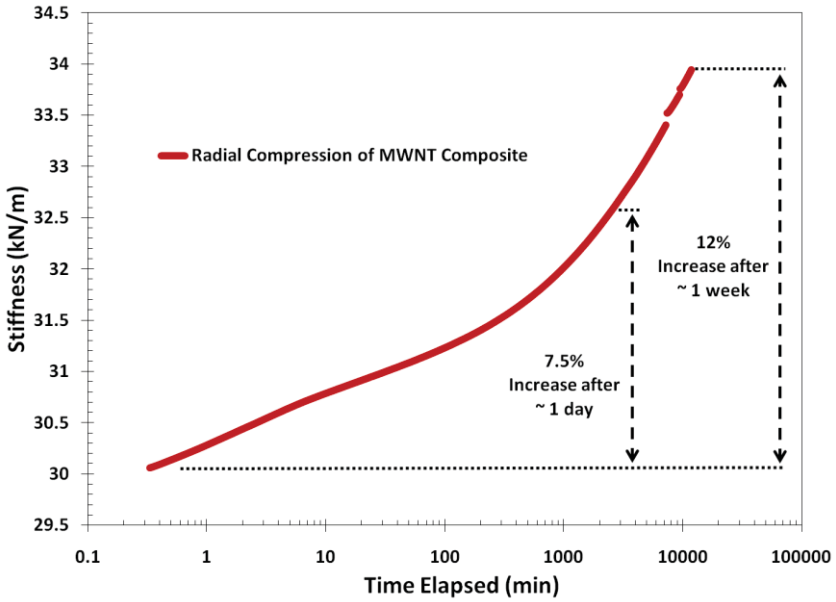

b

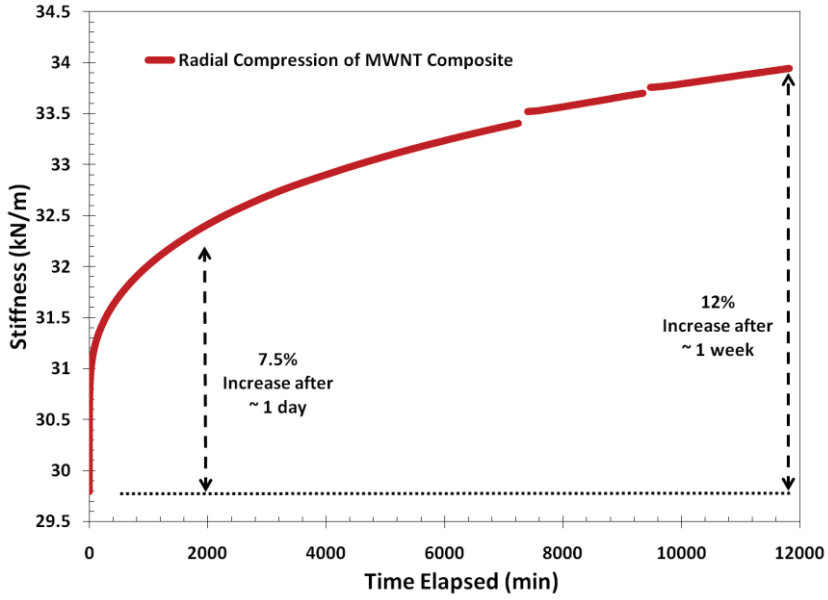

Figure 4.1 – PDMS/CNT composites exhibit self-stiffening during dynamic stress, an effect that has no observable ceiling. To illustrate the effect, the data is plotted on both (a) log and (b) linear time scales.

Conversely, and somewhat counterintuitively, plastic deformation can also lead to strengthening in materials. Work hardening is a preparatory technique that involves the strain-induced alteration of a material's crystalline microstructure to prevent further deformation. This process is common in metalworking, and occurs due to the creation and dispersion of defects (known as dislocations) in the crystal structure. The presence of these dislocations will inhibit further plastic deformation, thereby increasing the strength of the material.

A similar, but fundamentally unique response is seen in some polymeric materials under uniaxial tension. As first observed in a cross-linked hydrogel network consisting of poly(acrylic acid) and poly(ethylene glycol) [246], and subsequently in poly(ether ether ketone) [247] and ultrahigh molecular weight polyethylene reinforced with MWNTs [248], stretching beyond the yield point can result in "entanglement reinforcement" or the strain-induced alignment of the polymer network, respectively. These changes, known as strain hardening, improve the load-bearing ability of the material and can induce crystallization in the polymer. Similar strain-induced crystallization effects have been observed in elastomeric polymers [249], including PDMS [250].

4.2. Observation of Stiffening during Cyclic Elastic Stress

Samples identical to those described in Section 2.4.1 were used to test the effect of cyclic loading on this A-MWNT/PDMS nanocomposite material. Similar in premise to what occurs in bones, it was observed that repeated stressing causes the

stiffness of this nanocomposite to increase for as long as the loading is sustained. This behavior bears some resemblance to strain hardening, though it occurs for dynamic stressing within the matrix polymer's elastic region of deformation.

The dynamic compressive testing was conducted using a TA Instruments Q800 DMA with a 5% strain amplitude, a frequency of 5 Hz, and an ambient temperature of 45 °C (unless otherwise noted). The chosen amplitude and frequency allowed for compressive loading without the risk of resonant or inertial effects (as evidenced in the fundamental viscoelastic analysis presented previously in Figure 3.6 and Figure 3.7), while the temperature was selected as it is the lowest temperature that the DMA can reliably maintain without the aid of liquid nitrogen.

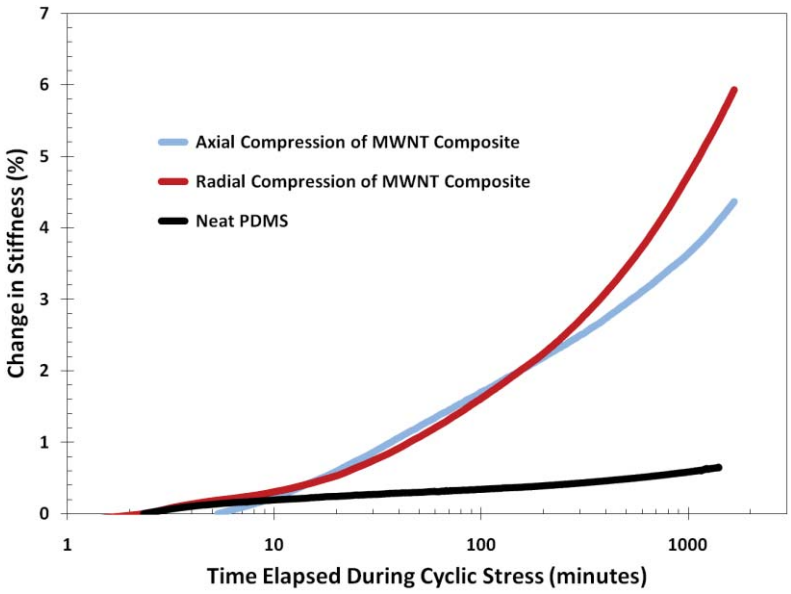

Figure 4.2 – The self-stiffening effect is not seen in the neat polymer, and is enhanced when the composite is loaded transverse to the CNT alignment direction.

As seen in Figure 4.1, the dynamic stiffness of the composite increases up to ~7.5% after one day of continuous stressing, and will persist to ~12% after one week (3.5 million loading cycles). Interestingly, the effect shows no indication of saturation, which suggests that there is potential for even greater improvement. As expected for elastic deformation, the neat polymer shows no noticeable change in stiffness when repeatedly stressed (Figure 4.2).

The high degree of CNT alignment provided further insight, and it was revealed that, for identical testing conditions, axial testing (compressing longitudinal to the CNT alignment) resulted in a 4.3% stiffness increase while radial testing (compressing transverse to CNT alignment) resulted in a 5.9% improvement. This observation is consistent with the orientation-specific mechanics of deformation in this material (as outlined in Chapter 3), and suggests that interfacial shear stress may play a role in the effect. Unless otherwise noted, all subsequent experiments are conducted using highly-aligned composite samples that were tested transverse to the CNT alignment direction (radially).

The effect does not appear to be specific to the particular experimental parameters that were chosen, nor does the high degree of alignment in the CNTs seem to be necessary for the self-stiffening to occur. As observed in Figure 4.3, self-stiffening during cyclic stressing was seen for various amplitudes and frequencies of compressive deformation. Also, a composite sample whose CNTs were randomly oriented showed a similar stiffness improvement after repeated stressing (Figure 4.4). Observation of the effect for this sample revealed a particularly interesting

property of the self-stiffening phenomenon; this randomly-dispersed composite had been prepared two years prior to testing [187], which suggests that the effect remains dormant before being activated by repeatedly stressing the material.

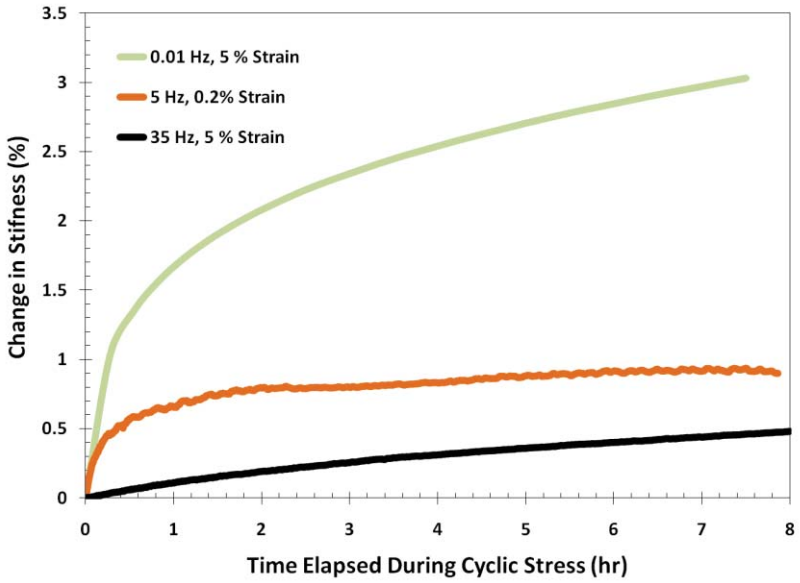

Figure 4.3 – The stiffening effect also occurs at low frequencies, as well as at low strain amplitudes and high frequencies to some extent.

In order to ascertain whether or not cyclic stress is necessary to induce an increase in stiffness, samples were tested using static loads. Composite samples were tested in stress relaxation mode in the Q800 DMA for a 10% strain at 45 °C. Such a displacement was chosen in order to achieve a strain that is comparable to the zero-point of oscillation for a dynamic test, and in Figure 4.5 it is observed that the relaxation modulus remains unchanged for all samples during static loading.

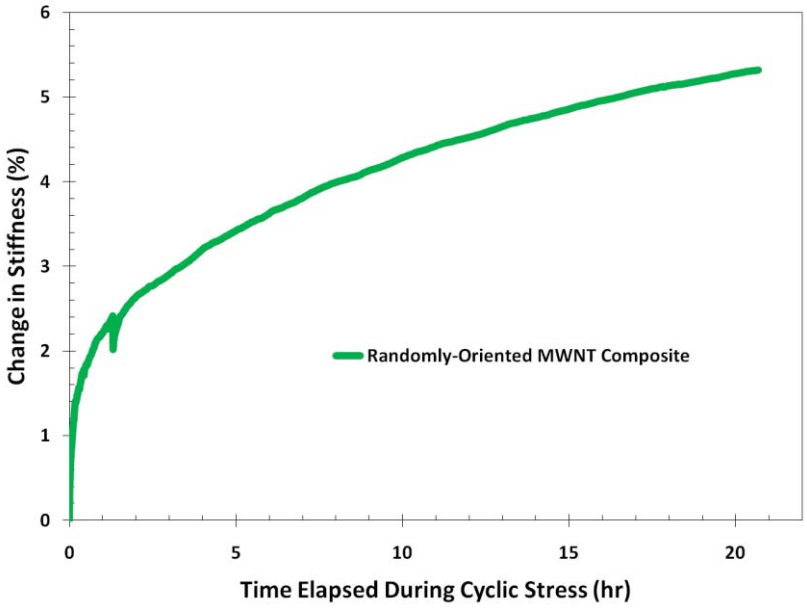

Figure 4.4 – Randomly-oriented CNT composites also display the self-stiffening behavior.

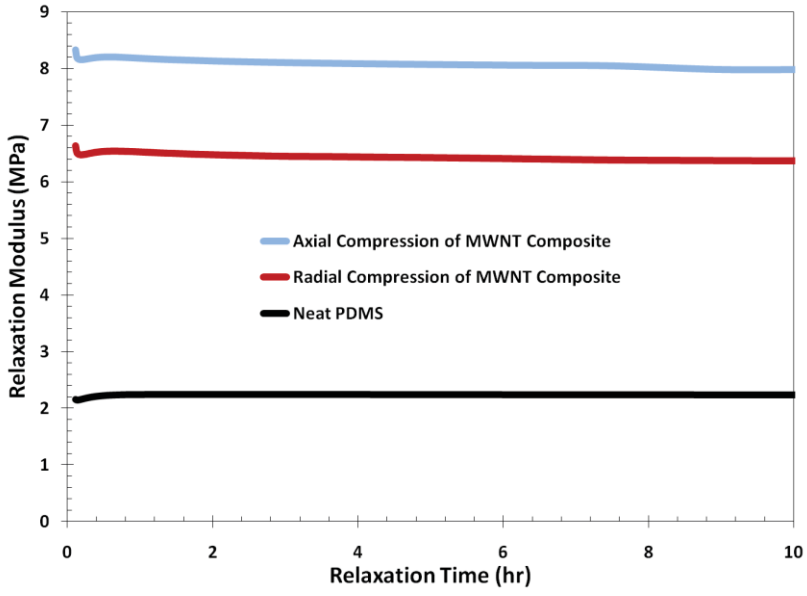

Figure 4.5 – Static loading showed no discernable change in the mechanical properties of the composite.

4.3. The Implications of Relaxation and Static Loading

To better understand the self-stiffening effect, experiments were designed to determine its limitations. One such test involved a brief 10 minute rest between individual bouts of dynamic stiffening, and as seen in Figure 4.6a, there is a partial relaxation after each session of dynamic stressing. It is clear that the stiffness for subsequent dynamic tests begins at a lower value, but will recover and resume the trend from the previous test. These partial relaxations become less substantial for each subsequent test, implying that there is a transition from temporary to permanent improvement as the effect proceeds. Similarly, another sample was annealed at 100 °C for one hour between individual cyclic stressing events, as seen in Figure 4.6b. Heat treatment appears to have very little effect on the stiffening mechanism, as it does not enhance nor reverse the stiffness improvement.

While the static loading tests support the conclusion that dynamic loading is necessary to induce self-stiffening, it is not immediately clear whether or not the dynamic stiffness (as measured during cyclic stressing) was affected by the stress relaxation experiment. To clearly delineate the contribution of each deformation mode, a test was devised to conduct alternating sessions of static and dynamic loads on an individual sample. Specifically, the sample was subjected to a static 1 MPa load for 24 hours, followed by the same static load with an added dynamic component consisting of a 5% strain amplitude. This process was repeated three times, and as seen in Figure 4.7a, (1) the sample relaxed identically at the offset of dynamic loading, and (2) the static tests did not contribute to any stiffness increase.

a

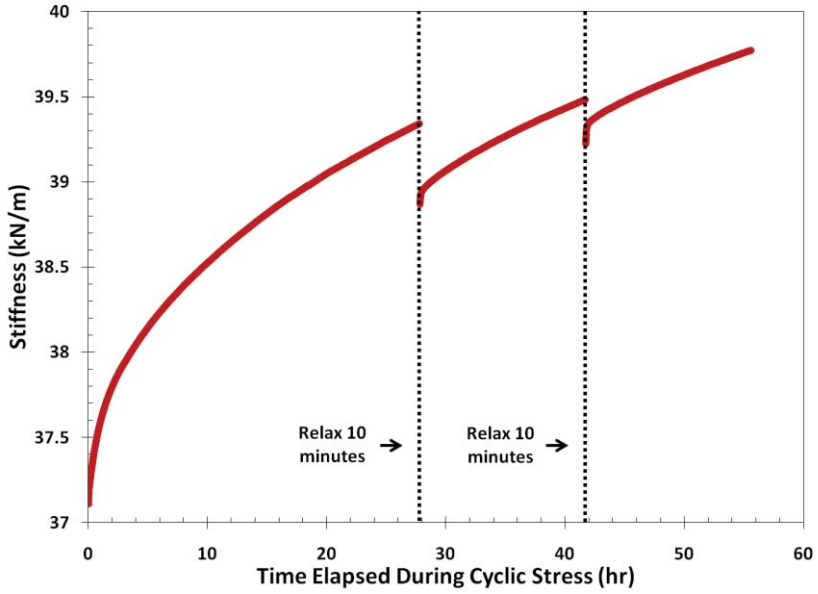

b

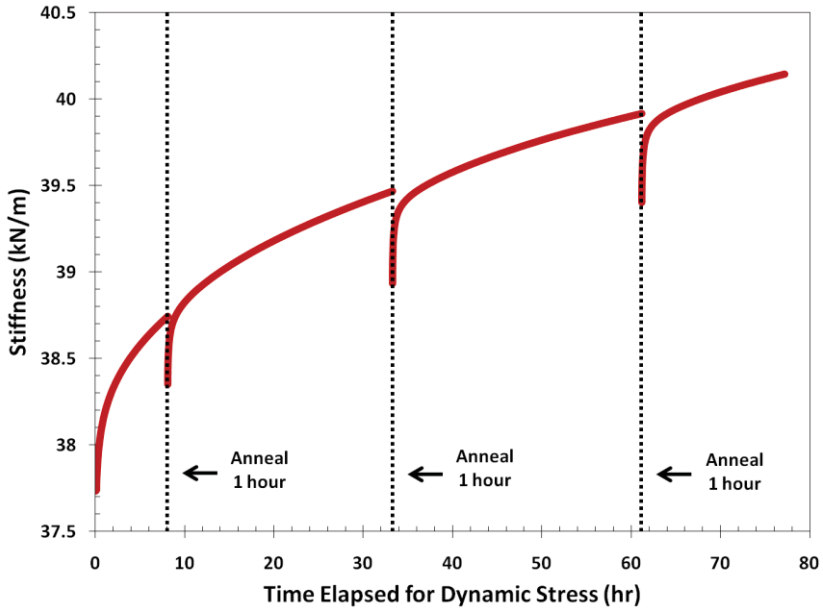

Figure 4.6 – (a) A partial, temporary relaxation of the stiffness improvement takes place at the offset of cyclic stressing. (b) This relaxation is not significantly impeded or assisted by heat treatment.

a

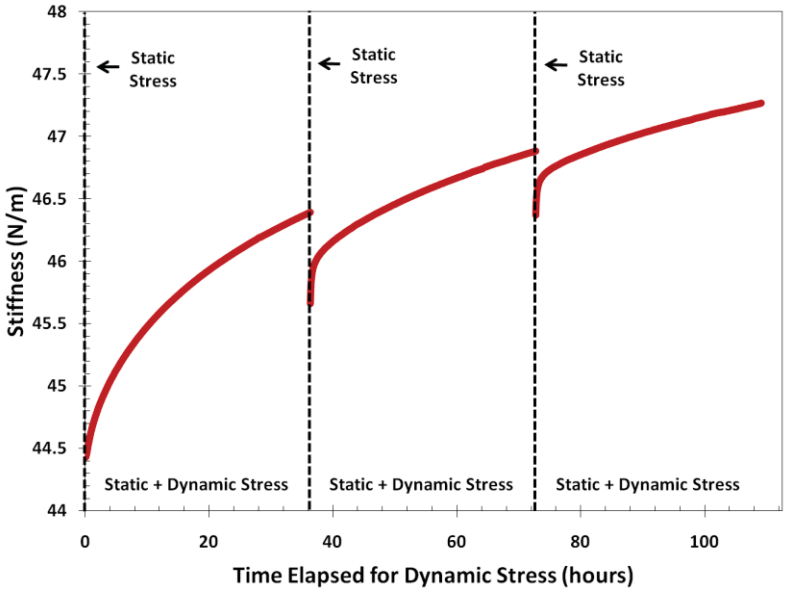

b

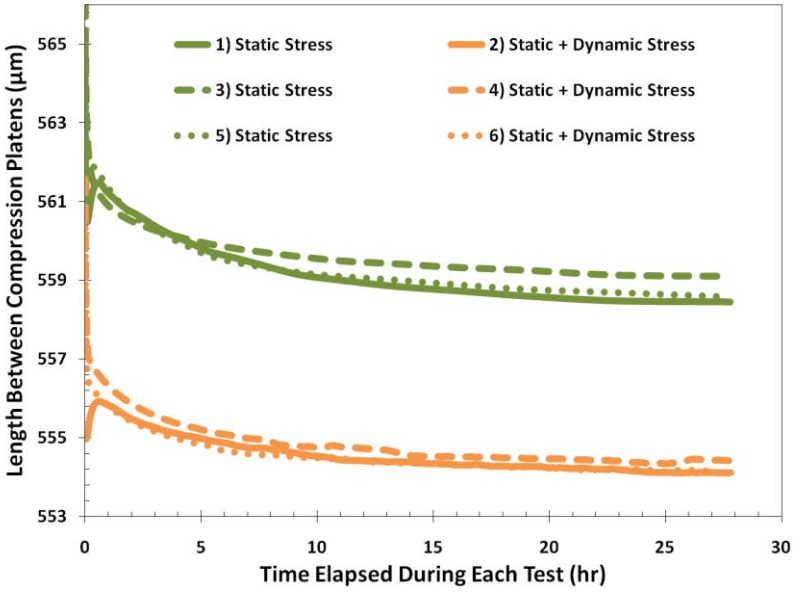

Figure 4.7 – (a) Static stress and relaxation have no combined impact on the stiffening effect, and (b) the sample creeps identically for each application of dynamic stress, confirming that the stiffness of the material is increasing.

This experiment also provides confirmation of a true change in the material during stiffening. As seen in Figure 4.7b, while the sample does displace during both static and dynamic tests, it fully recovers between each test, with each similar test creeping identically. These results eliminate any concern that sample creep or any other shift in the zero point of oscillation during dynamic stressing would artificially enhance the perceived increase in dynamic stiffness.

4.4. Delineating the Contribution of Polymer Cross-Linking

To further resolve the limitations for this effect, and to shed some light on the mechanisms contributing to the stiffness improvement, it is important to resolve the effect that chemical changes in the polymer matrix may have on the stiffening process.

The degree of cross-linking plays a large role in defining the mechanical properties of a vulcanizate, and Sylgard 184 is known for forming an imperfect network during curing; it has been reported that un-linked interstitial oligomers may leach out of the polymer network after curing [251]. This is particularly relevant for nanocomposite materials, as it has been recently determined that the CNT/polymer interface will interrupt cross-linking for both epoxy [146] as well as silicone elastomer [252] matrices. To understand the role that cross-linking may play in explaining the stiffening phenomenon, experiments were devised to compare the improvement for samples with varying degrees of curing.

a

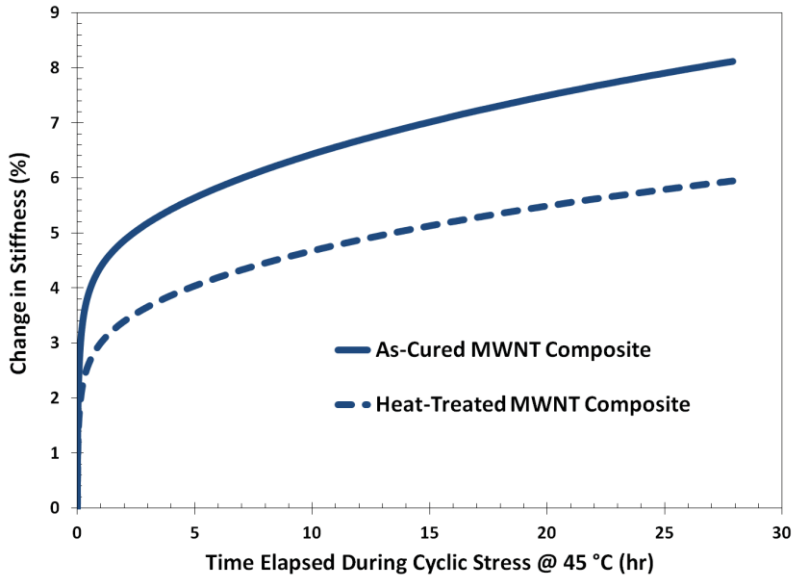

b

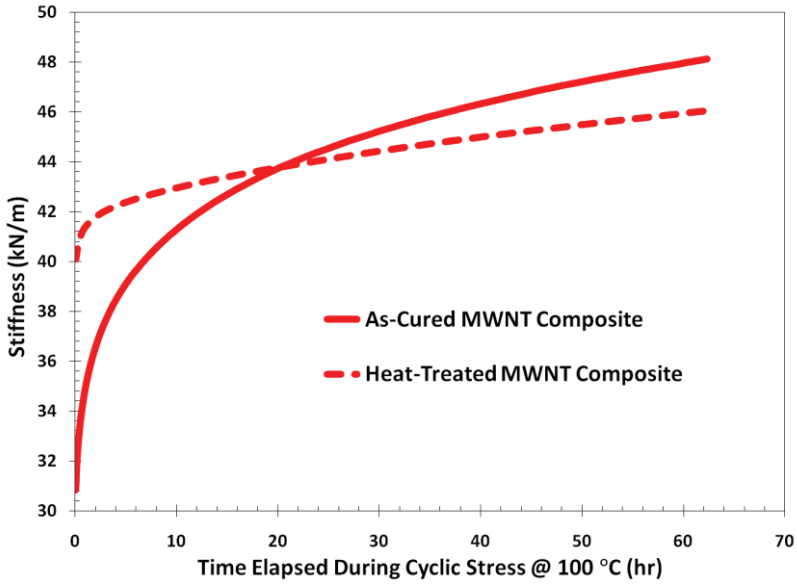

Figure 4.8 – (a) Additional curing (cross-linking) in the composite suppresses the stiffening effect, but does not eliminate it. (b) Similarly, when stiffened at 100 °C, the heat-treated composite starts at a higher stiffness, but does not have the same capacity to stiffen as the incompletely cured material.

By comparing the as-cured (1 hour at 100 °C) composite to an identical specimen that was given three days of additional heat treatment at 100 °C, it is possible to differentiate between the stiffening behavior and any changes in the stiffness that occur due to further cross-linking. Dynamic stress was first applied at 45 °C, and while it was observed that the heat treatment did indeed stifle the stiffening effect (Figure 4.8a), it is noted that the effect does still very much occur in both samples. This strongly suggests that the effect is not explained by further cross-linking in the elastomer matrix.

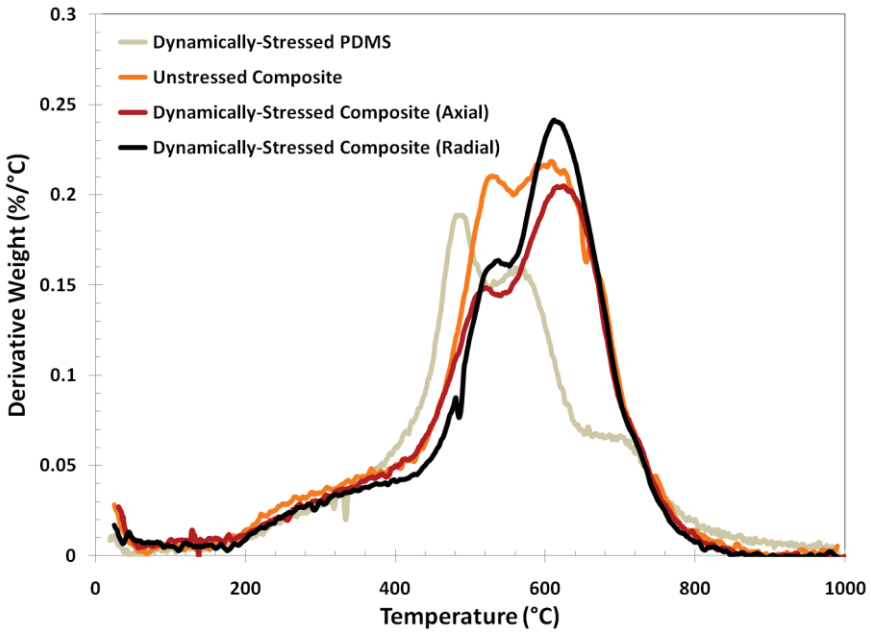

Figure 4.9 – Thermogravimetric analysis reveals that the degradability of the composite changes noticeably after the material has been stiffened.

Interestingly, by conducting the same test at 100 °C, it is first clear that both samples do not begin with the same stiffness (Figure 4.8b); this is expected, as a

higher cross-link density is proportional to increased stiffness. The interesting result from this test, however, is that the as-cured composite ultimately achieves a higher stiffness after dynamic stressing. This is significant, since the heat-treated material began the test with a greater stiffness and was, in total, subjected to the 100 °C environment for twice as long as the as-cured sample.

These tests strongly suggest that: (1) in agreement with the aforementioned work [146], [252], the composites are not fully cured after 1 hour of curing at 100 °C, and (2) while the cross-link density does indeed play a role in explaining (and even amplifying) the effect, some mechanism other than the further curing of the matrix must be responsible for the stiffness increase.

4.5. Subtle Clues from the Dynamics of Cold Crystallization

Outside of the curing kinetics, there are other factors that can profoundly influence the mechanical properties of polymers. It is known that interstitials (especially those with dimensions in the nanoscale) can greatly affect matrix morphology, though unfortunately these variations are subtle and can be rather difficult to resolve using microscopy or spectroscopy. The thermal behavior of polymeric materials, however, can be used to reveal information about such structural nuances through the kinetics of thermodynamic events. Using a TA Instruments SDT 2960 under 100 cm^3/min of dry nitrogen, thermogravimetric analysis (TGA) was conducted using a 10 °C/min ramp from room temperature to 1,000 °C. As evidenced by in Figure 4.9, the composite's degradation behavior

varies greatly from the neat polymer, including the onset of significant mass loss. Also noted are the prominent differences between the unstressed and dynamically-stressed composite samples.

4.5.1. Cold Crystallization in PDMS/CNT Composites

The resolution of second-order phase transitions can also reveal a great deal of information about polymeric materials. For crystallizable polymers, the strength of the glass transition translates to the quantity of amorphous polymer, while melting transitions reflect the percentage of the polymer that is bound within crystallites.

To measure such transitions, differential scanning calorimetry (DSC) was carried out using a TA Instruments Q100 modulated DSC with Tzero™ pans in a He atmosphere at 50 mL/min. The samples were immediately quenched to -150 °C to preserve the room temperature morphology, and a temperature ramp from -150 °C to 50 °C at 20 °C/min was subsequently conducted to provide a baseline signature of the material prior to cold crystallization. The samples were then cooled to -90 °C for three hours to induce the cold crystallization of the PDMS, followed by cooling back down to -150 °C to conduct the same thermal ramp on the post-crystallized composite. Lastly, the samples were quenched again to -150 °C and the thermal ramp was conducted a final time to confirm that the material returned to its pre-crystallized state. To eliminate any error due to the high thermal conductivity of the CNTs, the composite samples were arranged in the specimen pans such that the nanotubes were aligned horizontally.

a

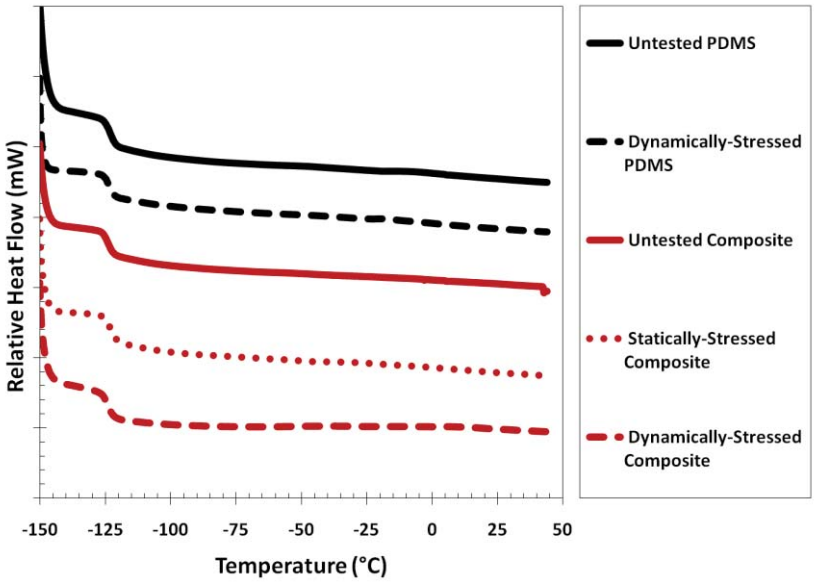

b

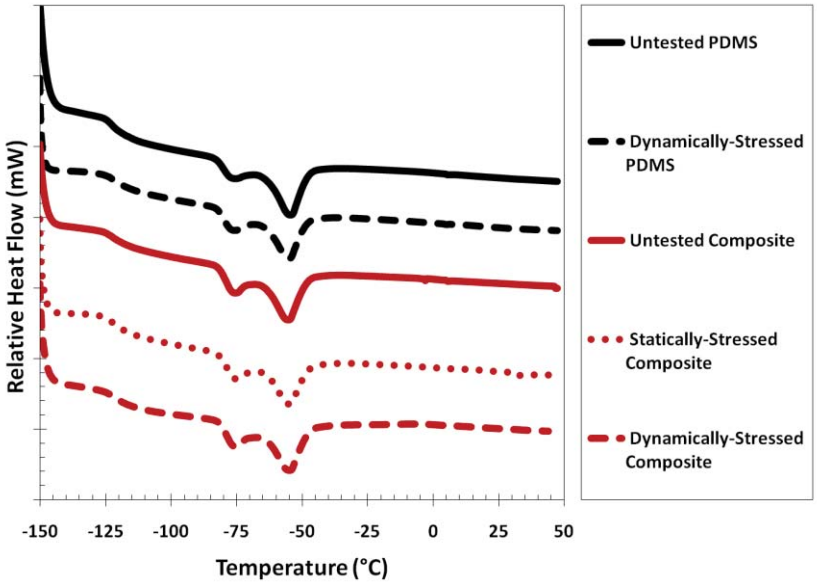

Figure 4.10 – Differential scanning calorimetry (DSC) reveals that the composites and neat polymer show identical second-order phase transitions (a) at room temperature and (b) after crystallization has occurred.

The thermal behavior for various iterations of stressing for the composite and neat polymer samples are presented in Figure 4.10. Firstly, it is noted that the pre- and post-crystallized scans are identical; as a result, only the post-crystallized scan is shown. More prominently, all samples display identical thermal transitions both before and after cold crystallization. This suggests that the degree of crystallization is not affected in any way by the presence of CNTs or the deformation history of the material.

These tests were replicated using the Q800 DMA, which allows for the thermomechanical determination of phase transitions and other thermal events. However, as the composite material can only be tested in compression, it was necessary to prepare thin, slender samples to remain within the stiffness resolution of the instrument as the sample transitions from rubbery to glassy (the stiffness of polymers will increase nearly four orders-of-magnitude during the glass transition, which can make compressive analysis testing quite challenging). Specimens measuring .5 mm wide x .5mm long x 2.5mm tall were compressed radially, and were tested using a frequency of 2 Hz and a 0.3% strain amplitude.

For thermomechanical analysis, thermal events are most readily observed through the temperature-dependent response of the tan δ, and as with the results from DSC, we see in Figure 4.11 that all of the samples display the same tan δ signature before and after crystallization. This method does, however, reveal a clue that strongly suggests that the PDMS in both materials is morphologically dissimilar, and that dynamic stressing induces some change in the structure of the matrix.

a

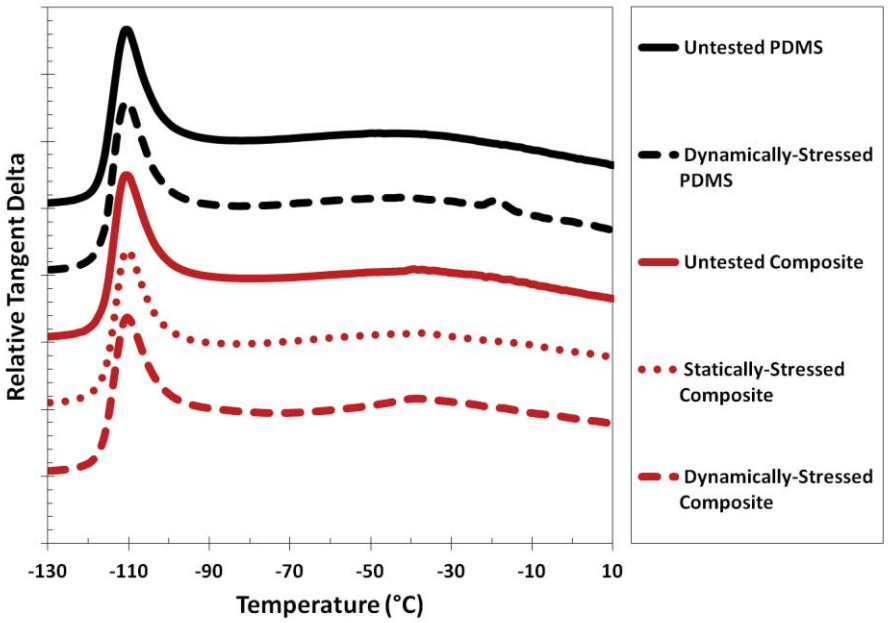
Relative Tangent Delta
-130
-110
-90
-70
-50
-30
-10
10
Temperature (°C)
Untested PDMS
Dynamically-Stressed PDMS
Untested Composite
Statically-Stressed Composite
Dynamically-Stressed Composite

b

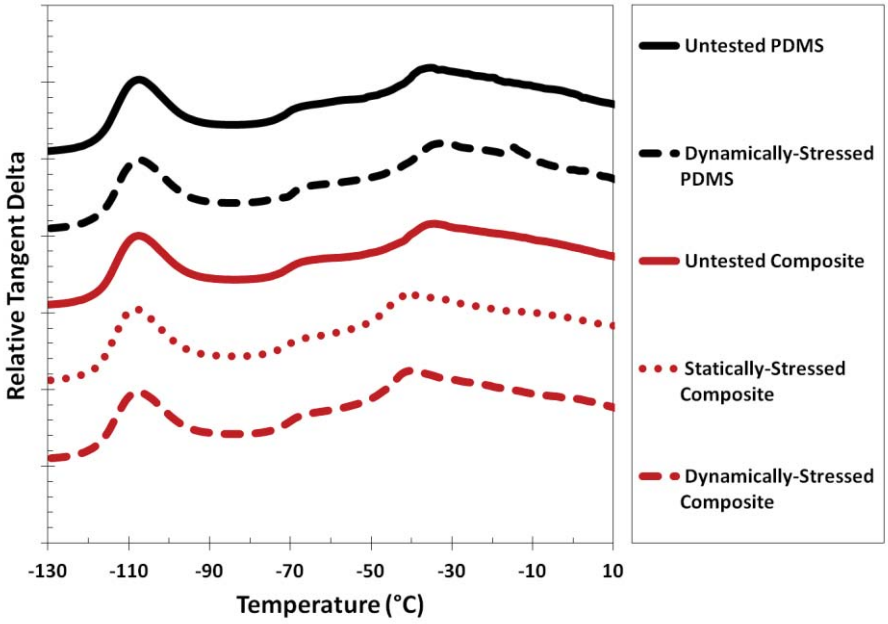
Relative Tangent Delta
-130
-110
-90
-70
-50
-30
-10
10
Temperature (°C)
Untested PDMS
Dynamically-Stressed PDMS
Untested Composite
Statically-Stressed Composite
Dynamically-Stressed Composite

c

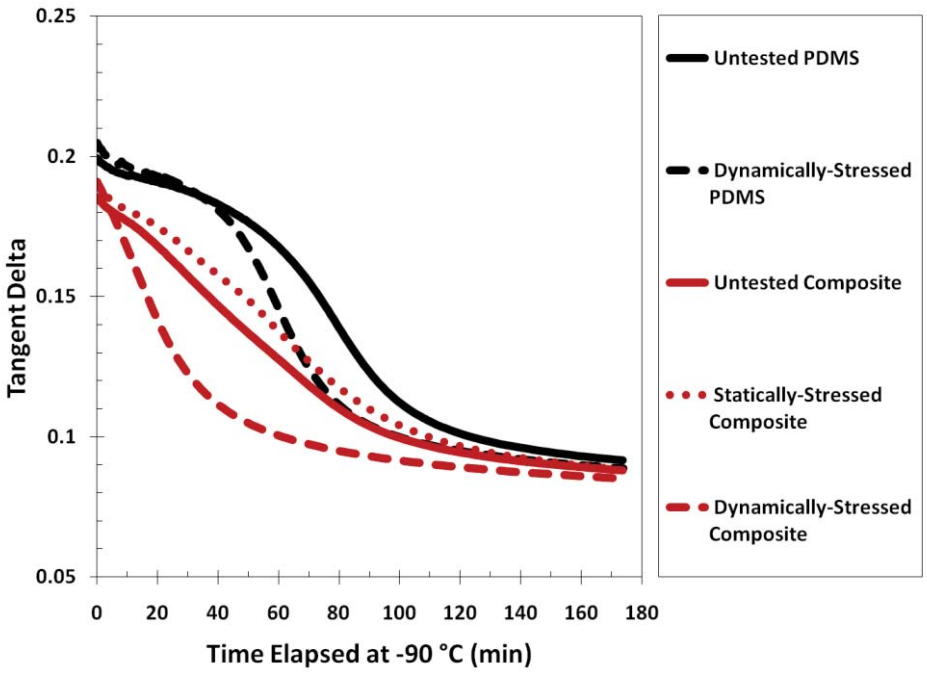

Figure 4.11 – Thermal analysis via DMA supports the conclusion of Figure 4.10, for the (a) pre- and (b) post-crystallized composite. (c) Interestingly, the crystallization rate is expedited for the stiffened material.

By tracking the tan δ during the cold crystallization process in Figure 4.11c, the rate that crystallites nucleate and grow during cold crystallization becomes apparent. Specifically, it is clear that approximately 40 minutes pass before the unstressed and dynamically-stressed neat PDMS samples began to crystallize, which is explained by the fact that there are no distinct nucleation sites for crystallites in the pure polymer. It is noted that the dynamically-stressed pure polymer sample does crystallize at a faster rate, suggesting that the PDMS chains can kinetically arrange into lamellae more rapidly after the material has been strained.

The composite samples, however, begin nucleating crystals much earlier than the neat polymer, and even appear to begin crystallizing immediately after the samples are cooled to the temperature range where crystallization will take place. Most interestingly, the stiffened composite nears full crystal saturation twice as quick in comparison to all of the other samples.

Recent molecular dynamics modeling has shown that the crystallization behavior of polymers is altered by the presence of nanoscale particles [253], and Dollase *et al.* experimentally demonstrated that the crystallization of PDMS will be expedited by the inclusion of ~250 nm agglomerates consisting of fumed silica nanoparticles [254]. The changes in the cold crystallization behavior for the dynamically-stressed composite suggest that a change in the interface/interphase might be responsible for the strain-induced mechanical improvement. In Chapter 5, I will scrutinize this region to implicate its role in explaining the self-stiffening effect.

Chapter 5

Self-Stiffening in Nanocomposites: Evolution of the Interphase

Having established an understanding of the self-stiffening effect and its limitations in Chapter 4, in this chapter I will focus more specifically on the challenges detailed in Specific Aim III, by resolving the particular morphological changes that take place in this PDMS/CNT nanocomposite material as a function of cyclic stressing. I will also propose a viable mechanism that builds off of a hypothesis for strengthening in elastomer-reinforced nanocomposite materials reported nearly 50 years ago.

5.1. Implicating the Interface/Interphase

Throughout the data presented in Chapter 4, there are clues that this behavior is anisotropic in nature. Specifically, in comparing the axial and radial

stiffening in Section 4.2, it is clear that radial deformation enhances the effect. From the insight provided by the idealized mechanics of deformation outlined in Chapter 3, one can infer that matrix/nanofiller interactions during deformation play a large role in facilitating the effect.

The cold crystallization experiments in Section 4.5 provide further insight. Nanoparticles have been shown to influence the kinetics of crystallization in polymer nanocomposites [255], and the observed discrepancies in the rate of crystallization between the unstressed and dynamically-stressed nanocomposites suggest that the interface/interphase evolves to readily nucleate crystallites in the stiffened material.

5.1.1. Bound Rubber

As detailed in Section 1.2.3, the region surrounding inclusive particles in polymer composites behaves differently than the bulk. For PDMS [145], [256] and other elastomeric polymers [134], [142], [144], this area is referred to as "bound rubber", and is defined by its retarded dynamics [257] and resilience to good solvents [144]. The depth of a bound rubber layer measures in the nanoscale, and it is known to form due to surface compatibility [258] as well as other properties of the matrix, such as the molecular weight of the polymer [145]. Bound rubber contributes substantively to the bulk mechanical properties of composite materials [123], [144], is explicitly temperature-dependent [134], and can even expedite the cross-linking process for vulcanized rubbers [259], [260].

While bound rubber is, in fact, "bound" to the surface of interstitial particles, such is not always the case for elastomer composites. Outside of extrinsic factors such as entanglement, polymer chains are known to be attracted to surfaces as a result of what is known as the "saturation condition", a phenomenon first described by de Gennes [136]. Put simply, this condition states that there is some equilibrium depth of the polymer layer on the surface of a filler that exists as a function of the free energy of the system. If any constituent polymer chain of that layer is removed, it will be replaced with another nearby chain.

As discussed in Section 3.1.1, this concept of structural evolution at the interface/interphase via slip and desorption/adsorption has been implicated as the molecular basis for nonlinear viscoelasticity in elastomers, including the well-known Mullins and Payne effects [97], [217]. However, a review of both historical and recent literature suggests that the morphology and structure of bound rubber is not well understood.

5.2. Direct Interrogation of the Interphase

Until recently, the techniques used to experimentally resolve bound rubber were nontrivial and could not be universally applied to all elastomer composite materials. However, in early 2011, Qu *et al.* utilized the height and phase signals of an atomic force microscopy (AFM) tapping mode line scan to denote the presence of bound rubber in hydrogenated nitrile butadiene rubber/carbon black composites [134]. By contrasting the topography of the surface with the phase lag while passing

over an embedded filler particle, a clear discrepancy in profile of these two signals was shown to denote the presence of a bound rubber state.

For this experiment, the interphasic morphology of a MWNT/PDMS composite was observed using an Asylum Research 3D Molecular Force Probe AFM, using silicon "OMCL AC240TS-W2" cantilevers from Olympus (the cantilevers have a nominal spring constant $k = \frac{2N}{m}$, with a nominal probe radius and conical semi-apex angle of 10 nm and 35 nm, respectively). Phase-lag images were acquired from the same area (measuring 1 mm x 1 mm) using AC (tapping) mode at room temperature (25 °C) and a scan rate of 1Hz.

For the pre-stiffened nanocomposite in Figure 5.1, it is clear that the phase signal does not cleanly overlap with the height, denoting the presence of bound rubber. Interestingly, such a distinction is no longer distinguishable when the same test is carried out for the stiffened composite material (Figure 5.2), indicating that the structure of the interphase transforms during cyclic stressing.

5.3. Clues from the Coefficient of Thermal Expansion

As presented in Chapter 3, the large aspect ratio of the CNT fillers and their high degree of alignment in this material enabled distinctly anisotropic behavior under mechanical loading. Given that the entirety of a nanotube's surface area is orthogonal to its alignment direction, such orientation gives rise to other anisotropic material properties (such as thermal expansion) that can be analyzed to deduce information about the interface/interphase.

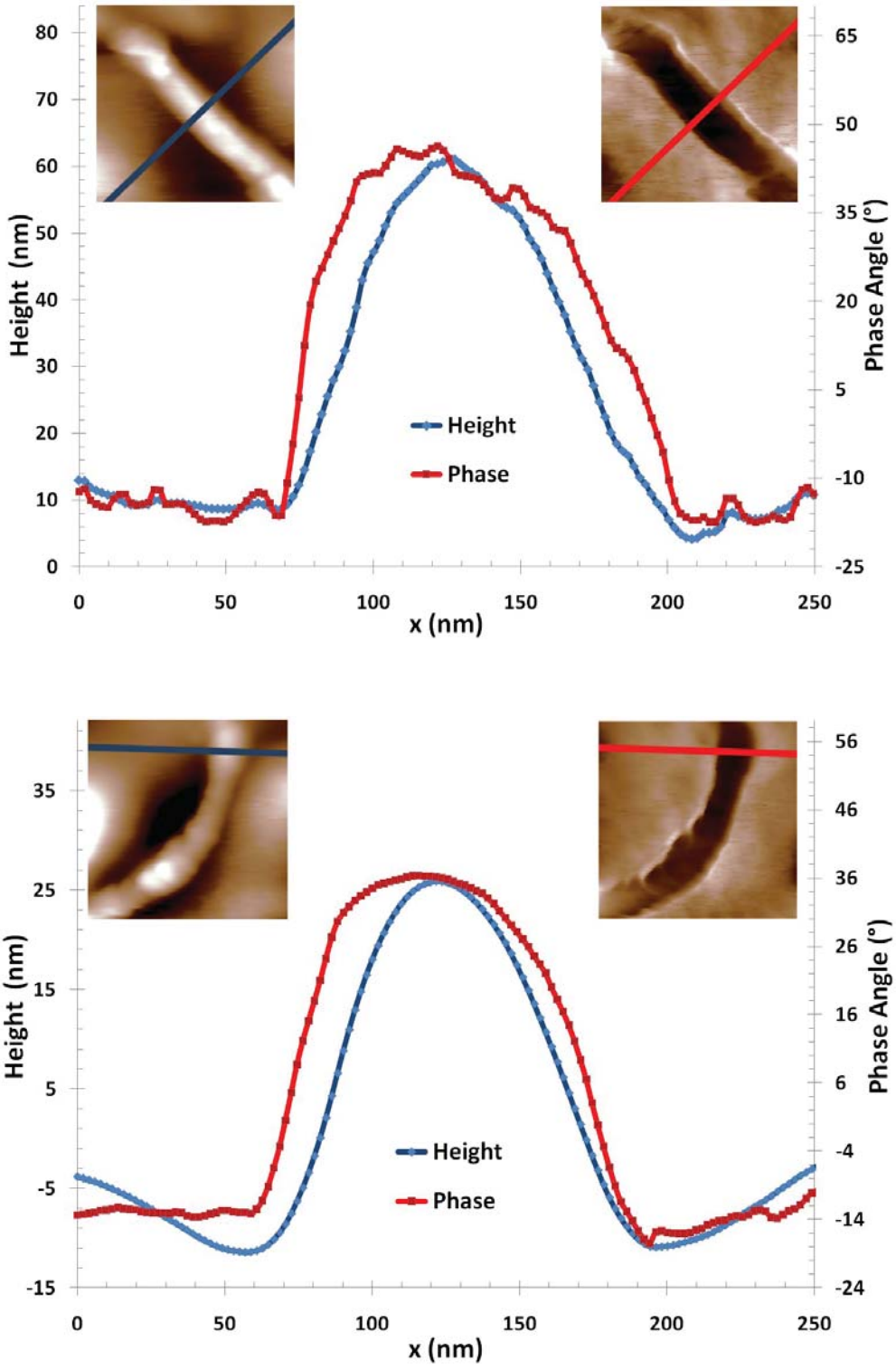

Figure 5.1 – Before stressing, atomic force microscopy (AFM) reveals a distinct bound rubber on the surface of the CNTs

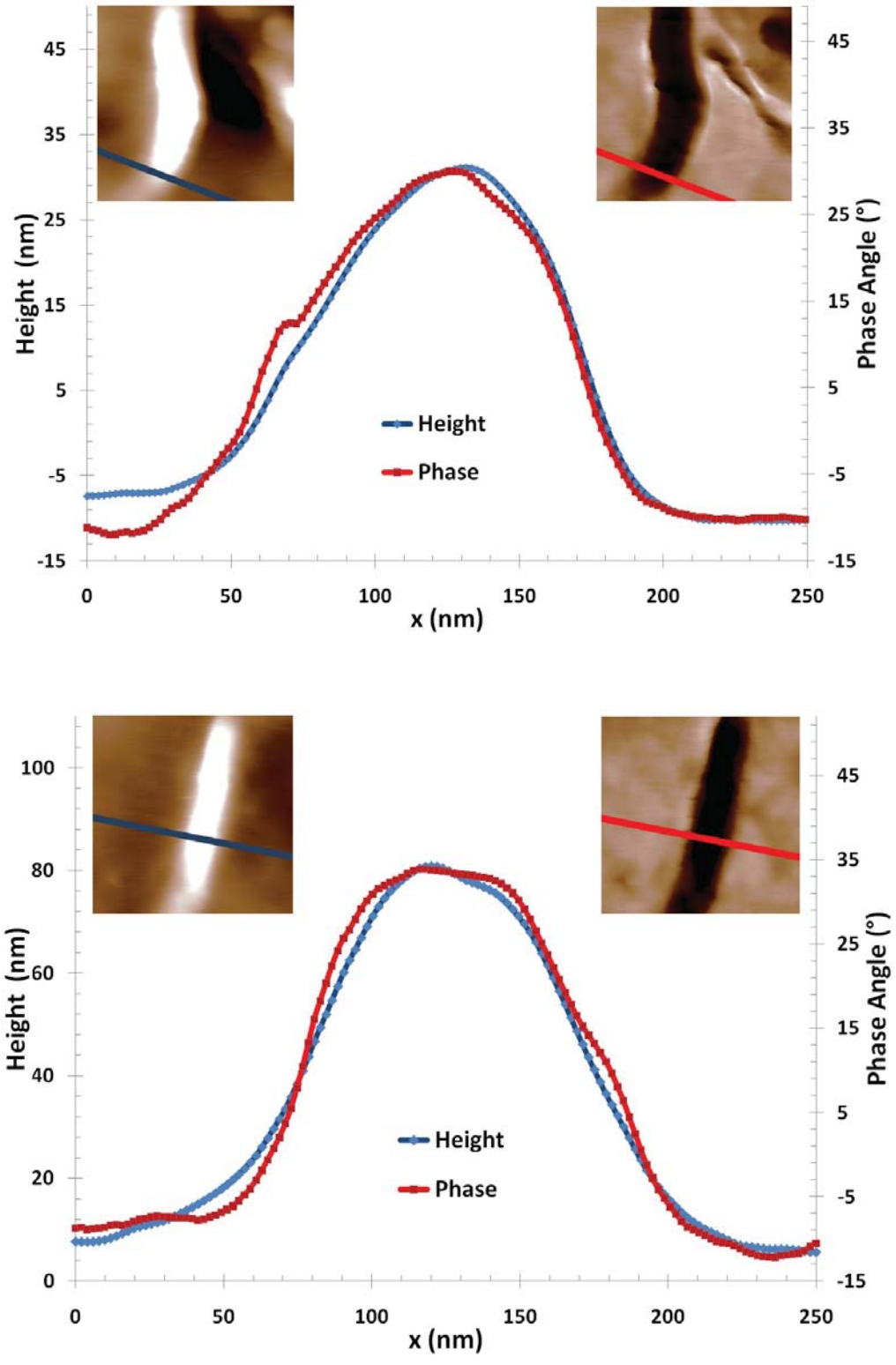

Figure 5.2 – After dynamic stiffening, AFM reveals that there is no longer a bound rubber on the surface of the CNTs.

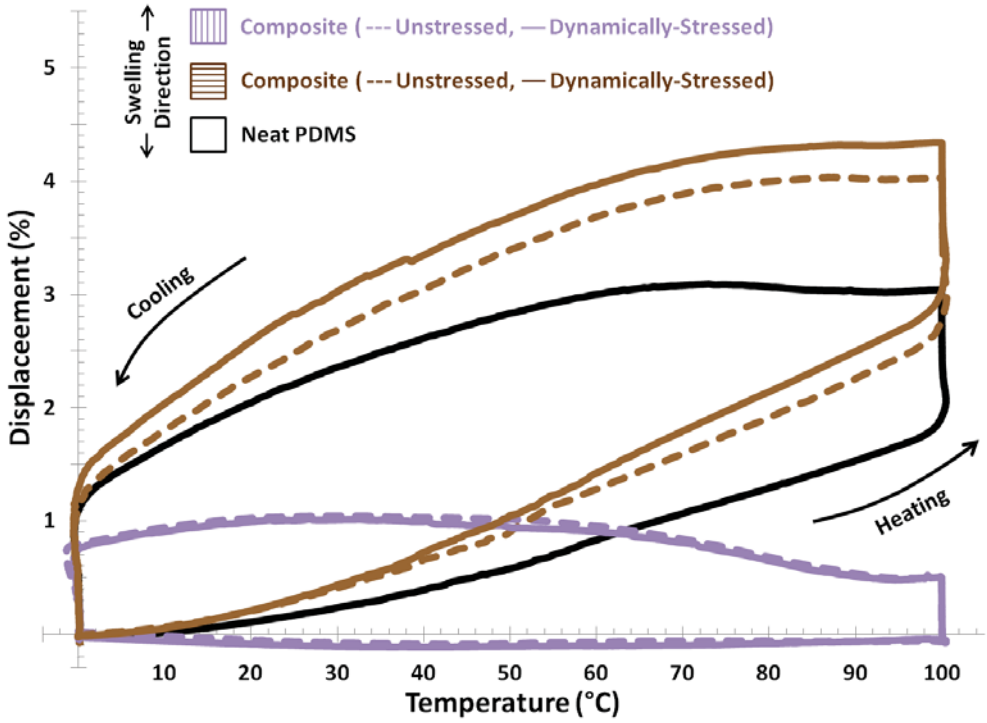

Figure 5.3 – Enhanced thermal expansion normal to the CNT alignment direction after stiffening supports the hypothesis that bound rubber is lost as a function of dynamically stressing the material.

Using the Q800 DMA, a 5 mN load was applied to the samples during a thermal cycling test that ramped from 0 °C to 100 °C at 5 °C/min. Each ramp was terminated with a 30 minute isothermal rest to account for both thermal lag and viscous flow in the material. A single sample was tested both axially and radially before being subjected to 24 hours of *in situ* stiffening (using the same procedure detailed in Section 4.2). The stiffened material was then tested again in both orientations, and the results were compared to the isotropic response of the neat polymer. The plots in Figure 5.3 represent these tests for a 5 cycle average.

For the pre-stiffened material, it is clear that the axial expansion differs substantially from the radial expansion, an observation that can be rationalized from the present understanding of this system. Firstly, the axial and radial coefficients of thermal expansion (CTEs) of CNTs are both more than two orders of magnitude less than PDMS [261], so this data is expected to predominantly represent the expansion of the polymer. Given the strong affinity that PDMS has for the surface of CNTs [188], it is reasonable to expect that axial expansion will be inhibited, and that the radial expansion will compensate to allow for volumetric expansion.

The interesting result from this experiment, however, comes from comparing these results to those from the sample after having been subjected to cyclic stress. The axial expansion shows no substantial change, while the radial expansion increases notably after stiffening. These results are more succinctly presented through the CTE, which was calculated using Equation 5.1, where L represents the length of the sample between the compressive platens after thermal equilibration, and T corresponds to temperature.

The calculated linear CTEs—presented in Table 5.1—represent that α_{axial} remains relatively unchanged, while α_{radial} is increased after stiffening. These results corroborate the observed loss of interphasic bound rubber after cyclic stressing, as polymer that is no longer bound to the filler particles would be expected to participate in the thermal swelling, thereby increasing the radial expansion.

$$\alpha = \frac{1}{L}\frac{\Delta L}{\Delta T}$$

Equation 5.1 – Calculation of the coefficient of linear thermal expansion.

	Neat PDMS	Unstressed Nanotube Composite	Stiffened Nanotube Composite
α_{axial} (10^{-6}/°C)	282	23.3	23.9
α_{radial} (10^{-6}/°C)	282	385	398

Table 5.1 – Axial (α_{axial}) and radial (α_{radial}) linear coefficients of thermal expansion.

5.4. Understanding the Interphase through X-Ray Scattering

With strong evidence that the structure of the polymer matrix is evolving in the interphase during stressing, x-ray scattering was attempted to detect the structural change in the PDMS after stiffening. A high flux of incident x-rays is necessary to resolve such a subtle morphological transformation in polymeric materials, so a synchrotron source was sought.

Simultaneous small- and wide-angle x-ray scattering (SAXS and WAXS, respectively) were conducted at the X9 end station at the National Synchrotron

Light Source at Brookhaven National Laboratory. X9 utilizes an undulator source that generates monochromatic x-rays at 12.0 keV (λ=0.103 nm), which are then focused to a beam size measuring ~100 μm tall and ~200 μm wide at the sample position using KB mirrors and a series of slits. Samples were measured under vacuum (~40 Pa) to suppress background scattering, and WAXS was collected using a 2D charged-coupled device (CCD) detector positioned 217 mm from the sample position, while SAXS was collected using a 2D CCD detector 5.28 m from the sample. Silver behenate powder was used for the conversion to *q*-space, and the scattering intensity was normalized using both an on-beam monitor (to account for variations in the beam flux), as well as the sample dimensions to correct for the scattering volume.

5.4.1. Wide-Angle X-Ray Scattering

Capable of resolving regularly-repeating structures in the sub-nanometer range, WAXS is typically used to identify crystalline structure and other forms of ordering in materials. In the figures denoted below, the WAXS scattering patterns are compared for both unstressed and dynamically-stressed samples of the following materials:

- Neat PDMS (Figure 5.4)
- Randomly-oriented MWNT/PDMS composite (Figure 5.5)
- Highly-aligned MWNT/PDMS composite (Figure 5.6)
- Highly-aligned FWNT/PDMS composite (Figure 5.7)

a

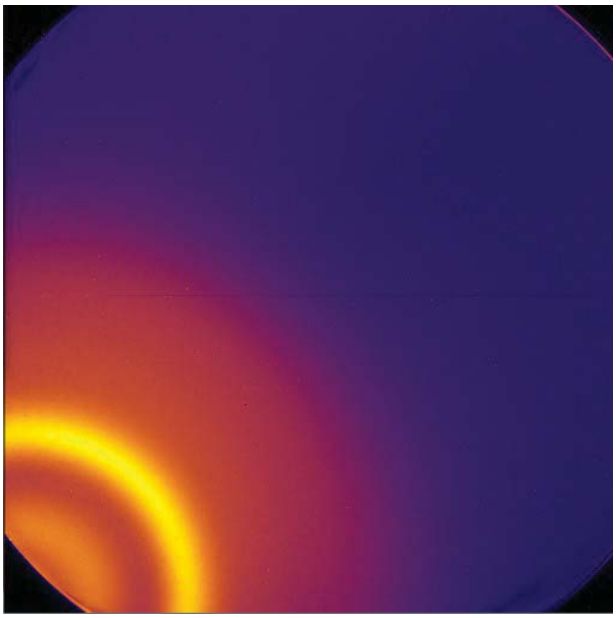

b

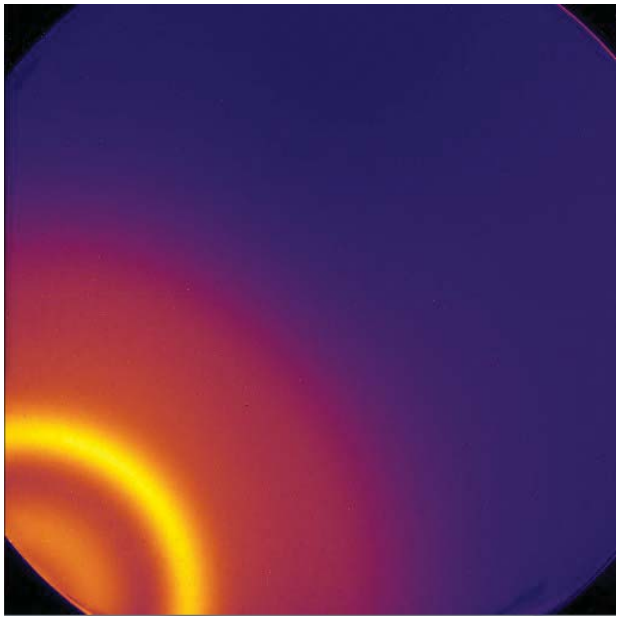

Figure 5.4 – WAXS scattering patterns for (a) unstressed and (b) dynamically-stressed neat PDMS samples.

a

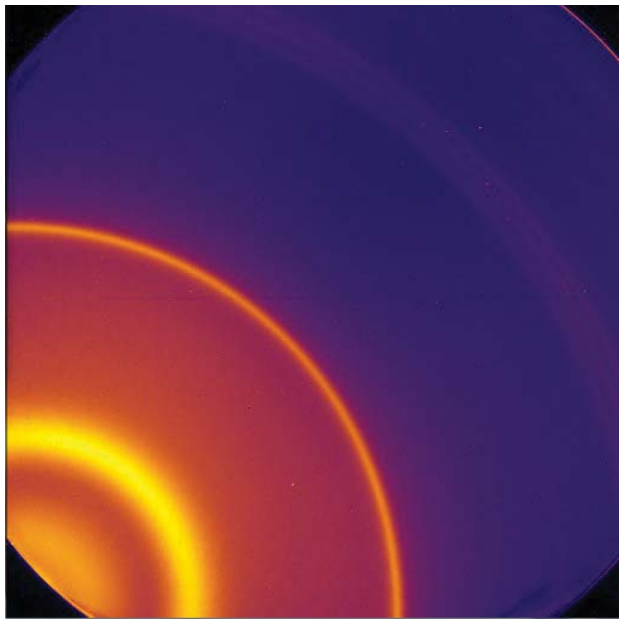

b

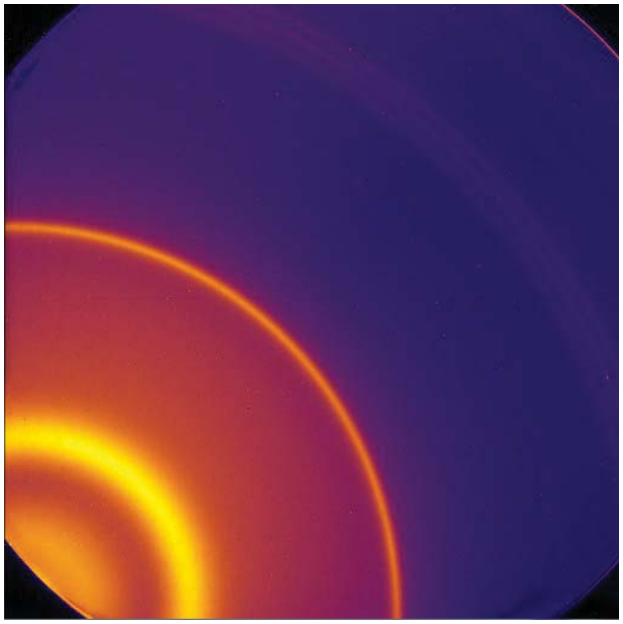

Figure 5.5 – WAXS scattering patterns for (a) unstressed and (b) dynamically-stressed randomly-oriented MWNT/PDMS composite samples.

a

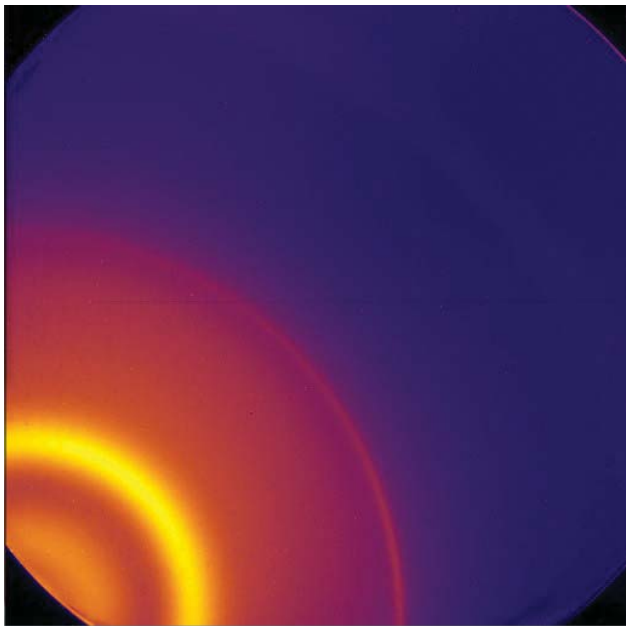

b

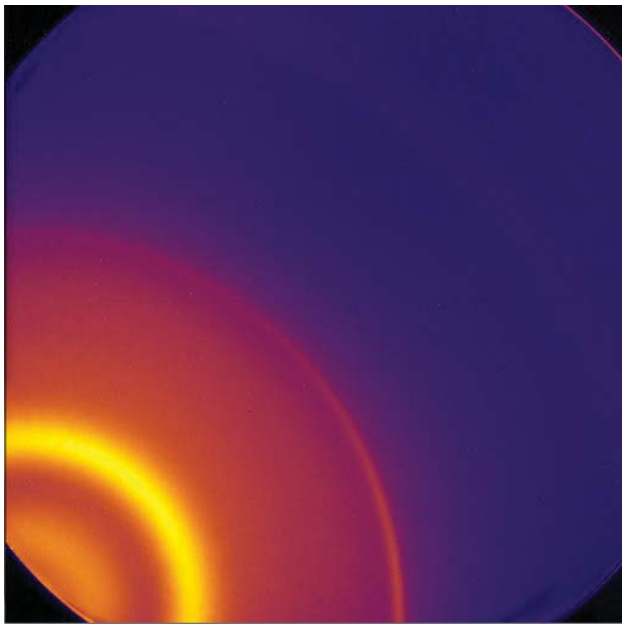

Figure 5.6 – WAXS scattering patterns for (a) unstressed and (b) dynamically-stressed highly-aligned MWNT/PDMS composite samples.

a

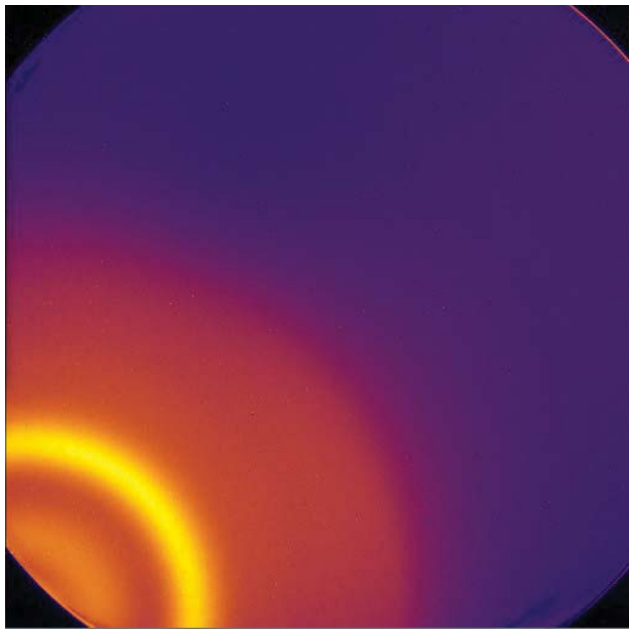

b

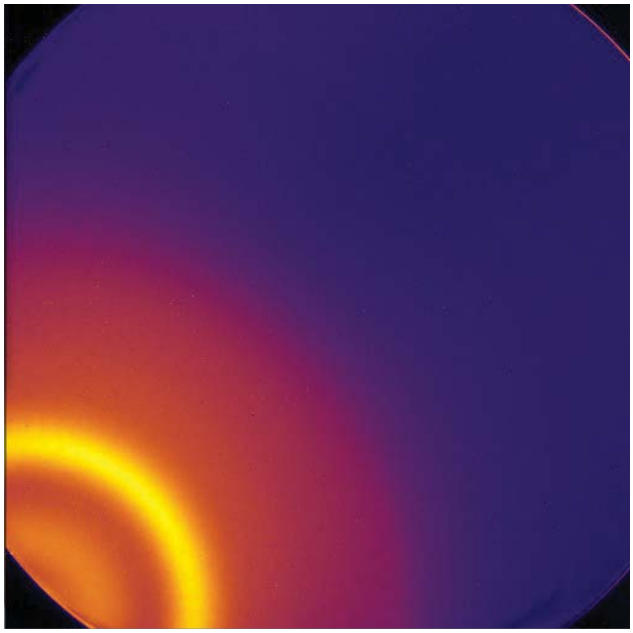

Figure 5.7 – WAXS scattering patterns for (a) unstressed and (b) dynamically-stressed highly-aligned FWNT/PDMS composite samples.

Treating the PDMS sample as a control, there is no observable difference in the polymer scattering when comparing these scattering patterns. There is, however, one distinguishing characteristic for the MWNT composite samples: a distinct ring at a scattering vector (q value) of 1.84 $Å^{-1}$, which corresponds to the .34 nm spacing between the coaxial nanotube walls. It is expected that this ring is not visible for the FWNTs due to the weak signal that such few concentric walls would produce.

The q-dependent scattering intensity of the MWNT composites and the PDMS control was integrated for various meridional angles χ (where χ=0° corresponds to the vertical and χ=90° to the horizontal) in Figure 5.8. At the outset, this scattering proves useful for qualitatively determining the MWNT orientation within the composite, as x-rays will scatter orthogonal to the central nanotube axis. Specifically, it is noted that the randomly-aligned MWNT composite is, in fact, isotropic, and that the aligned MWNT forest did indeed maintain its alignment during the infiltration process.

For the case of the highly-aligned MWNT composite, the preferred orientation of the CNTs allows for clear insight into the configuration of the fillers within the composite. By integrating the scattering intensity for the 1.84 $Å^{-1}$ peak as a function of χ for this sample before and after stiffening—as seen in Figure 5.9—the total integrated area of the scattering does not increase, yet there is greater anisotropy in the stiffened material. In and of itself, this provides evidence that

these high-aspect-ratio fillers translate and orient during repeated mechanical stressing.

To determine the effect that matrix crystallization has on the fillers, the samples were then subjected to isothermal cold crystallization at -80 °C overnight before being returned to room temperature and re-tested. Crystals in PDMS are unstable above a temperature of approximately -54 °C, so a comparison of the scattering after crystallization will help to resolve (1) how the growth of crystallites perturbed filler dispersion and/or orientation, and (2) how structural changes that take place during stiffening may alter this mechanism.

Interestingly, there is no discernible change in the unstressed composite after crystallization, while a total increase in the 1.84 $Å^{-1}$ scattering is seen for the stiffened material orthogonal to the alignment direction of the CNTs (Figure 5.9). Such an amplification in the measured scattering implies that some structural change in the material is either (1) allowing more of the scattered photons to reach the detector after stiffening, or (2) scattering more of the incident x-rays.

5.4.2. Small-Angle X-Ray Scattering

For the same samples, the SAXS data presents a similarly unusual result. As SAXS is principally used for the study of large-scale (~10 nm to ~300 nm) density fluctuations, it can be quite useful for resolving aggregation/bundling of fillers in composites. In Figure 5.10, it is clear that the stiffened material exhibits less low-q scattering for all χ. This behavior is representative of better filler dispersion.

a

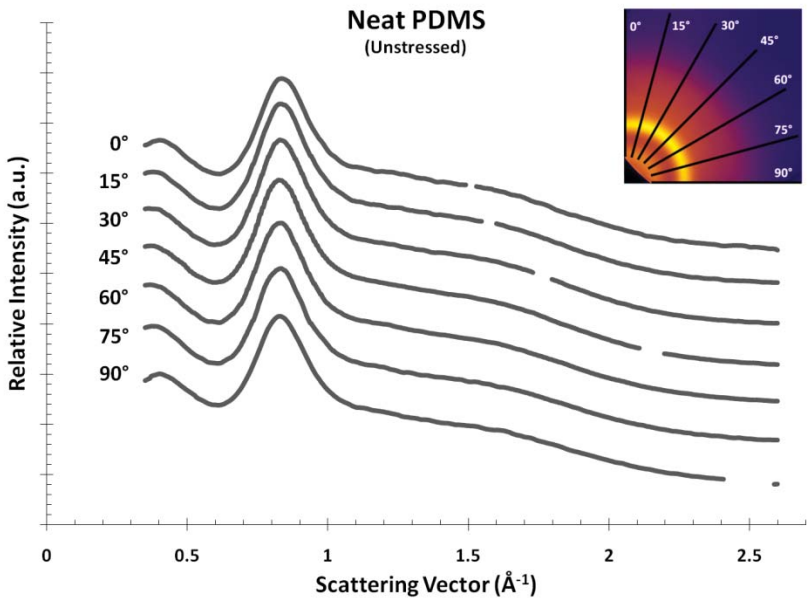
Neat PDMS
(Unstressed)
0°
15°
30°
45°
60°
75°
90°
Relative Intensity (a.u.)
0
0.5
1
1.5
2
2.5
Scattering Vector (Å-1)

b

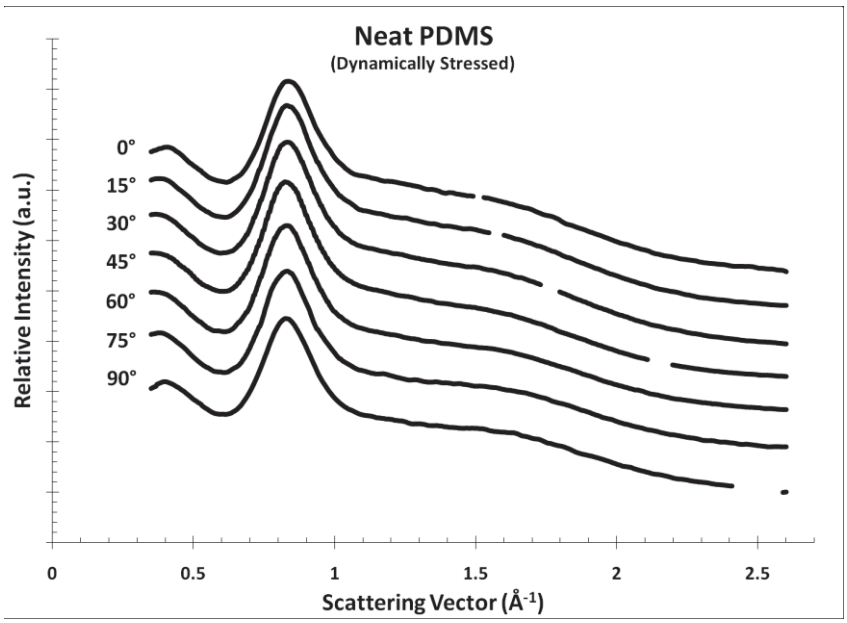
Neat PDMS
(Dynamically Stressed)
0°
15°
30°
45°
60°
75°
90°
Relative Intensity (a.u.)
0
0.5
1
1.5
2
2.5
Scattering Vector (Å-1)

c

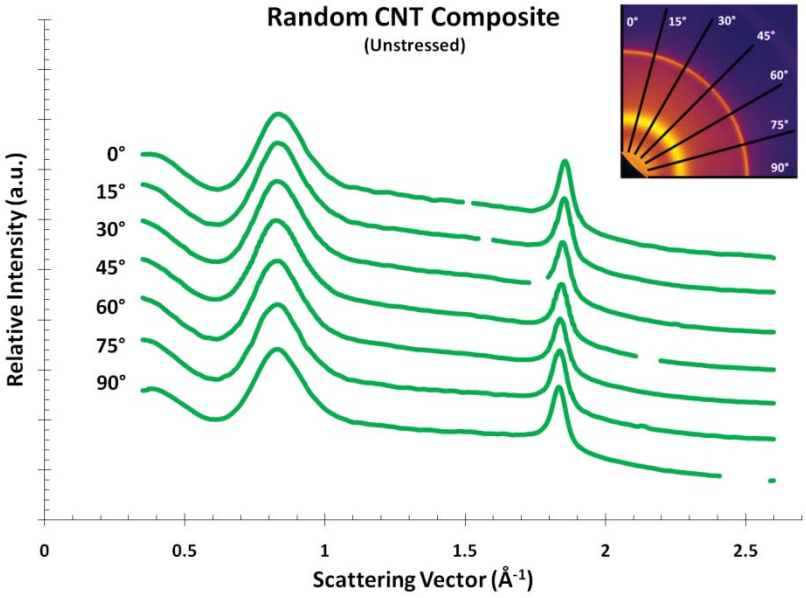
Random CNT Composite
(Unstressed)
0°
15°
30°
45°
60°
75°
90°
Relative Intensity (a.u.)
0
0.5
1
1.5
2
2.5
Scattering Vector (Å-1)

d

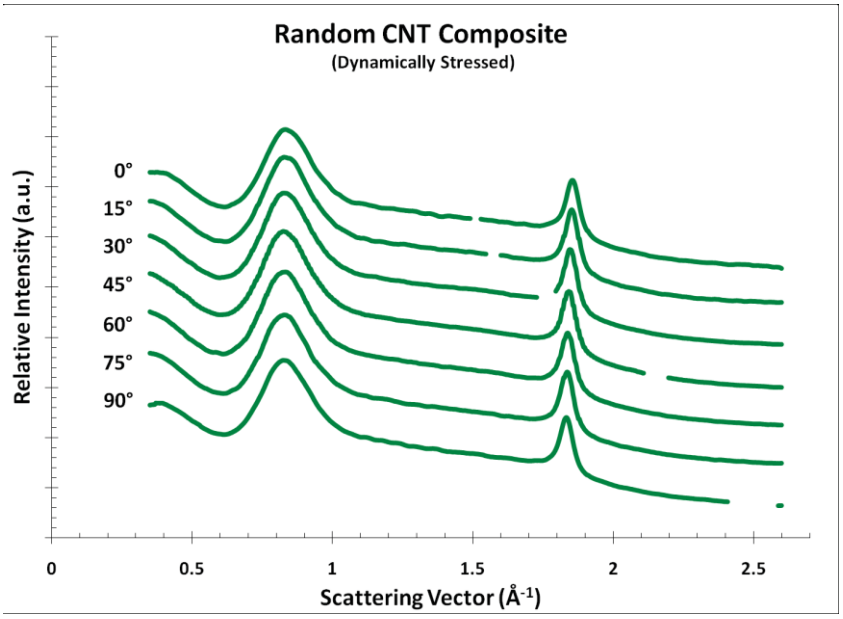
Random CNT Composite
(Dynamically Stressed)
0°
15°
30°
45°
60°
75°
90°
Relative Intensity (a.u.)
0
0.5
1
1.5
2
2.5
Scattering Vector (Å-1)

e

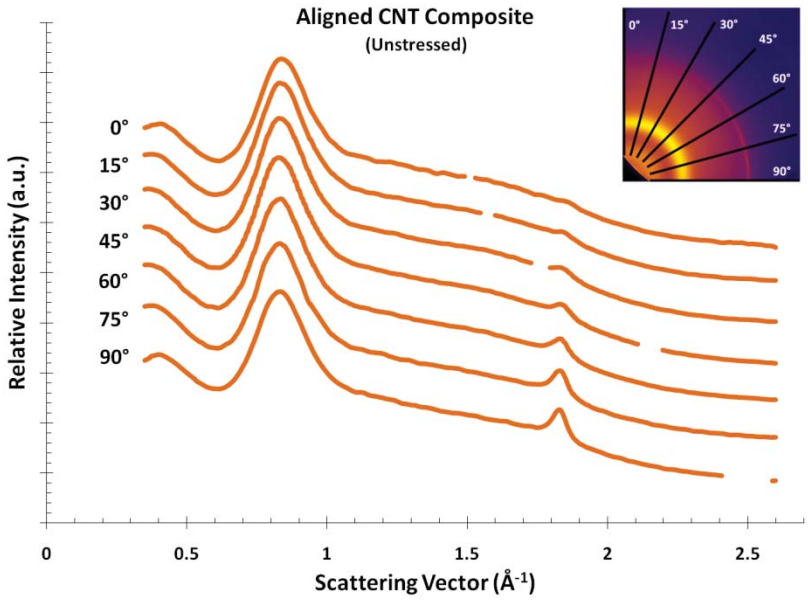

f

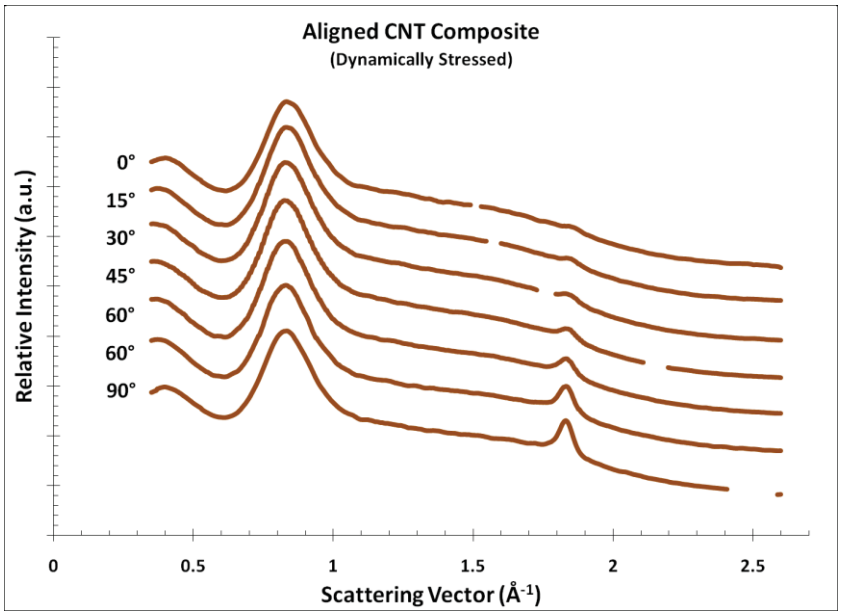

Figure 5.8 – Comparing the wide-angle x-ray scattering (WAXS) for the (a, b) neat PDMS, (c, d) a randomly-aligned MWNT composite, and (e, f) a A-MWNT composite, little difference is noted in the polymer scattering.

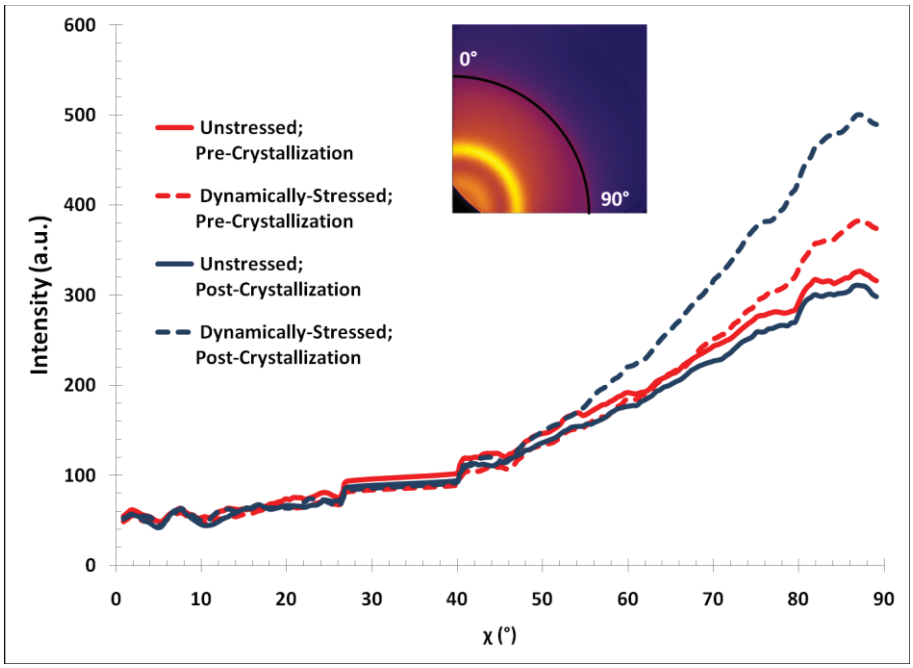

Figure 5.9 – Integrating the WAXS arc at 1.84 Å^{-1} (.34 nm), it is determined that the CNTs become more aligned after stressing. More notably, however, crystallization after stiffening leads to a significant enhancement of the WAXS normal to the alignment of the CNTs.

As with WAXS, cold crystallization provides a compelling result for small-angle scattering. Both the unstressed as well as stiffened composites exhibit an increase in total scattering across all χ, indicating that the cold crystallization process results in increased heterogeneity of the fillers. Unusually, the stiffened composite shows further enhancement normal to the alignment direction of the MWNTs.

5.4.3. Explaining the Post-Crystallization Scattering Behavior

To resolve the morphological subtleties that these post-crystallization scattering results represent, it is necessary to understand how CNTs affect the

crystallization process in polymers, and the resulting effect that growing crystallites have on filler dispersion.

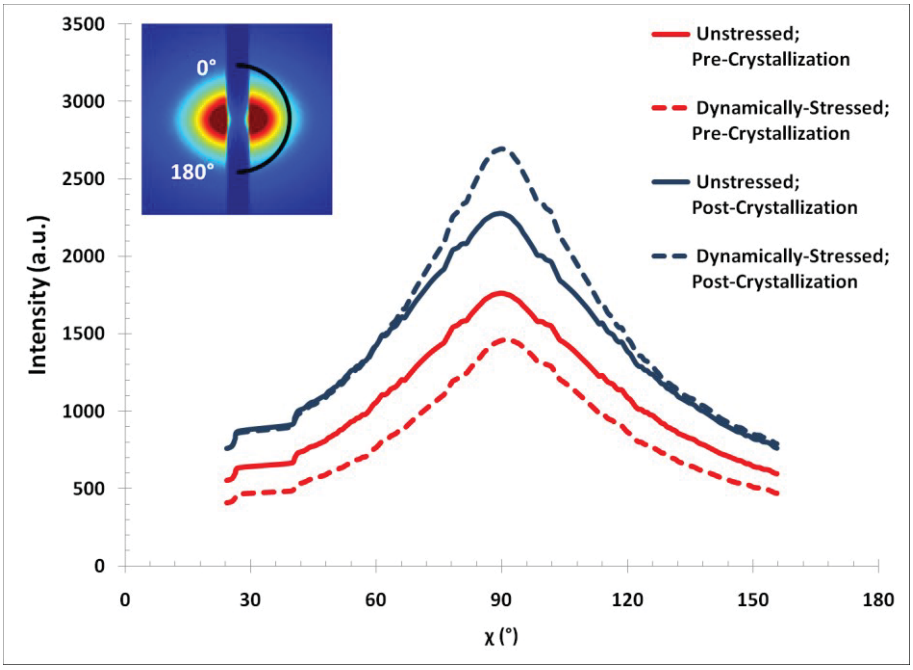

Figure 5.10 – Small-angle x-ray scattering (SAXS) reveals that the homogeneity of the A-CNT fillers changes after stiffening and/or cold crystallization.

With a few exceptions [262], the outer surface of CNTs are known to serve as an effective template for the growth of polymer crystals. Their presence can promote the formation of fibrillar crystals [263], transcrystals that grow along the fiber surface [264], [265], as well as other interesting architectures such as "shish-kebab" structures [262], [266–269]. The latter has been both experimentally [266] and theoretically [269] demonstrated, and it was explicitly noted by Haggenmueller, Fischer, and Winey that, in the case of polyethylene, CNTs will favor 2D shish

crystals over the typical 3D spherulites [267]. PDMS is similarly known to traditionally favor the growth of spherulitic crystallites from the melt [270].

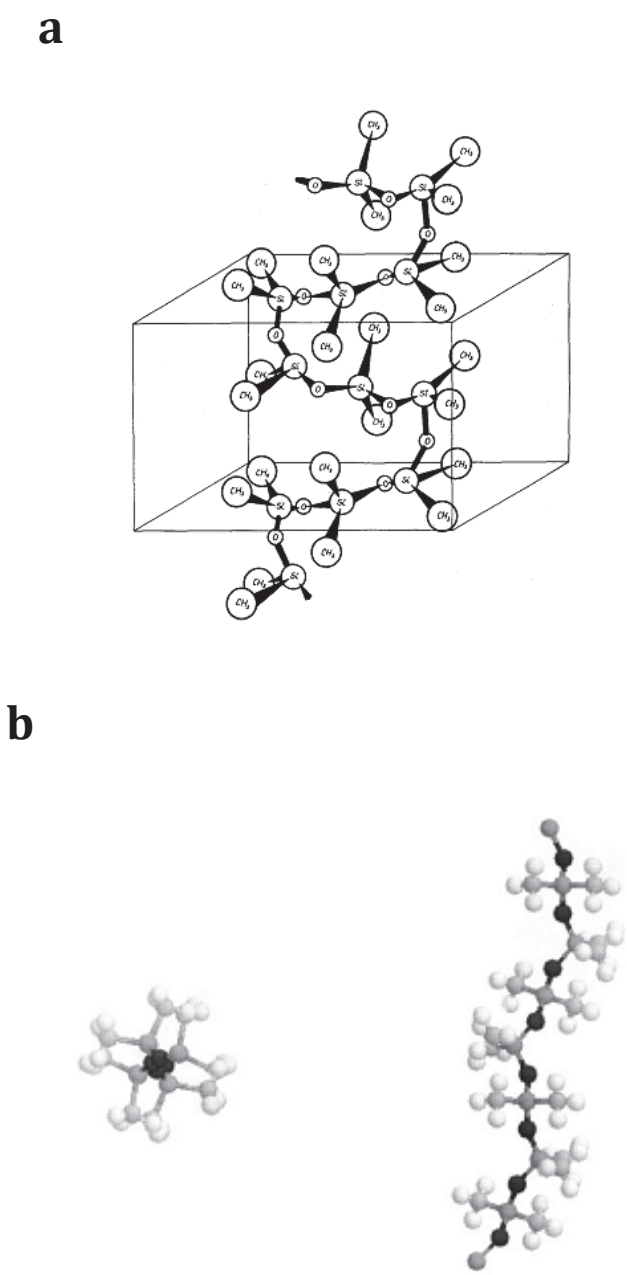

Figure 5.11 – (a) Crystallized PDMS was believed to form a two-fold helical conformation with monoclinic packing [271], but (b) was recently determined to favor a linear four-fold helical conformation with tetragonal packing [272].

a

b

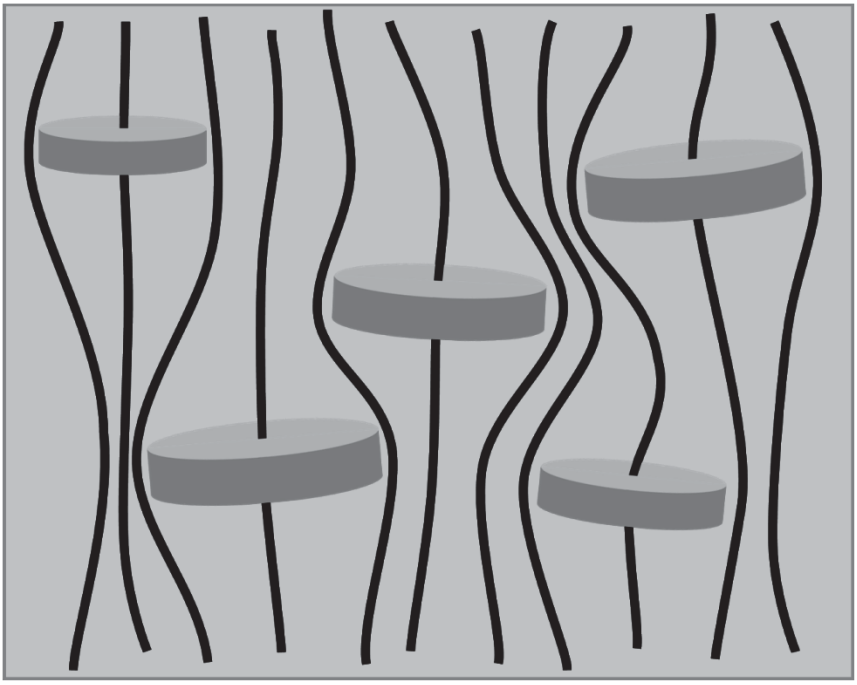

c

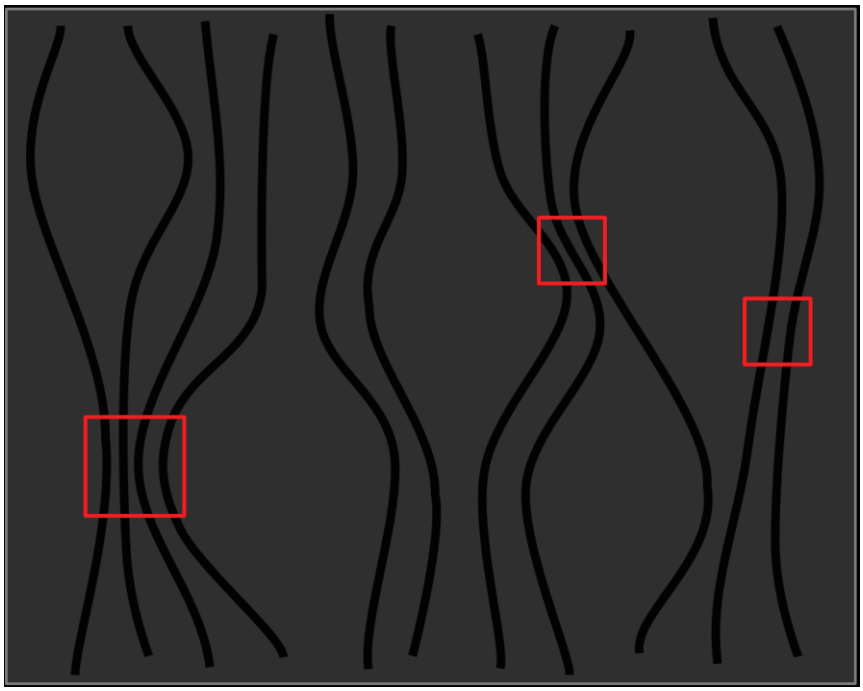

Figure 5.12 – In the event of (a) A-CNTs in the composite (b) serving as the nucleation point of crystallites, the CNTs will become less dispersed. (c) It is expected that this will result in areas of close CNT contact (bundling).

The nucleation of crystallites directly from the CNTs provides a reasonable explanation for the x-ray scattering results. It was recently reported by Khan *et al.* that nanoscale fillers can be actively displaced by the growth of polymer crystallites [273]. As illustrated in Figure 5.12, it is expected that the formation of shish–type crystals will redistribute the CNTs, decreasing the overall homogeneity of the system and producing regions of close contact between the nanotubes. Such a decrease in the filler dispersion would explain the enhancement in overall SAXS for both samples after crystallization.

Coupled with the loss of an entangled bound rubber layer, this mechanism accounts for the SAXS and WAXS enhancement orthogonal to the alignment direction of the CNTs after stiffening. In the case of the unstressed material, an interphasic bound rubber would increase the hydrodynamic radius of the nanotubes, effectively preventing close contact. If the stiffened material lacks this boundary layer, however, the CNTs would be able to form "tighter" bundles, thereby enhancing orthogonal SAXS. In the event of the elimination of most or all of the PDMS between two interstitial nanotubes, the concentric walls of the individual CNTs will correlate to enhance the orthogonal WAXS as well. A schematic interpretation of the SAXS and WAXS enhancement is illustrated in Figure 5.13.

To confirm the viability of a WAXS increase due to correlation between neighbor CNTs, a model was developed to understand the magnitude of potential amplification; the details of the model are presented in Appendix A. X-rays are sensitive to electron density, so the model represents a 2D cross-section of hollow, five-walled concentric structures embedded within a medium with the theoretical electron density of PDMS. For a three-CNT system in Figure 5.14, it is seen that close contact of the MWNTs can indeed enhance the scattering that corresponds to the concentric wall spacing (1.84 $Å^{-1}$). The model was then repeated for a six-CNT system (Figure 5.15), and it is observed that the enhancement is even more pronounced for larger bundles. It is expected that the actual bundles that form inside of the composites will comprise of many more CNTs, enhancing the effect beyond what is modeled.

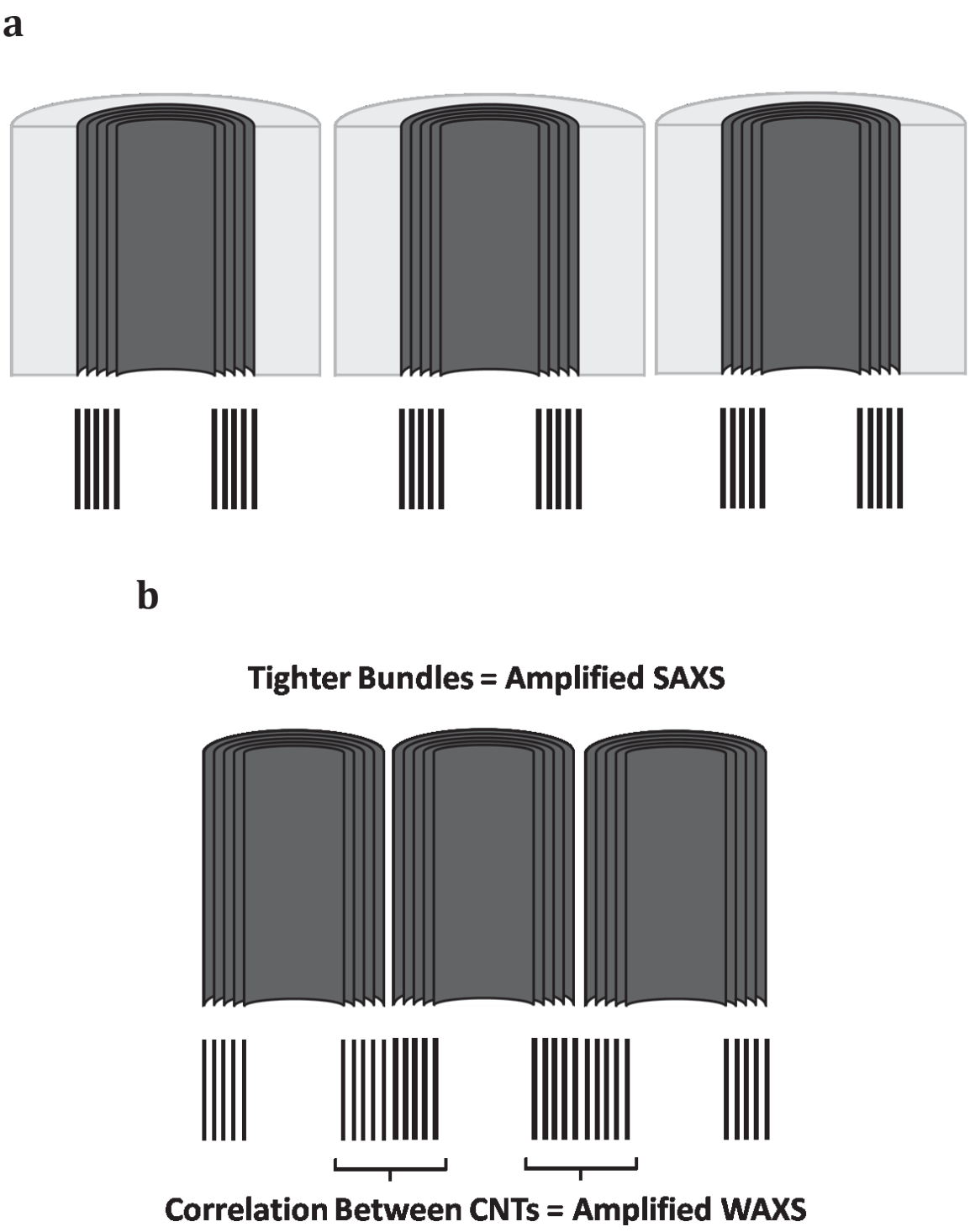

Figure 5.13 – The loss of (a) bound rubber on the surface of the MWNTs (b) after stressing provides an explaination for the SAXS and WAXS results.

a

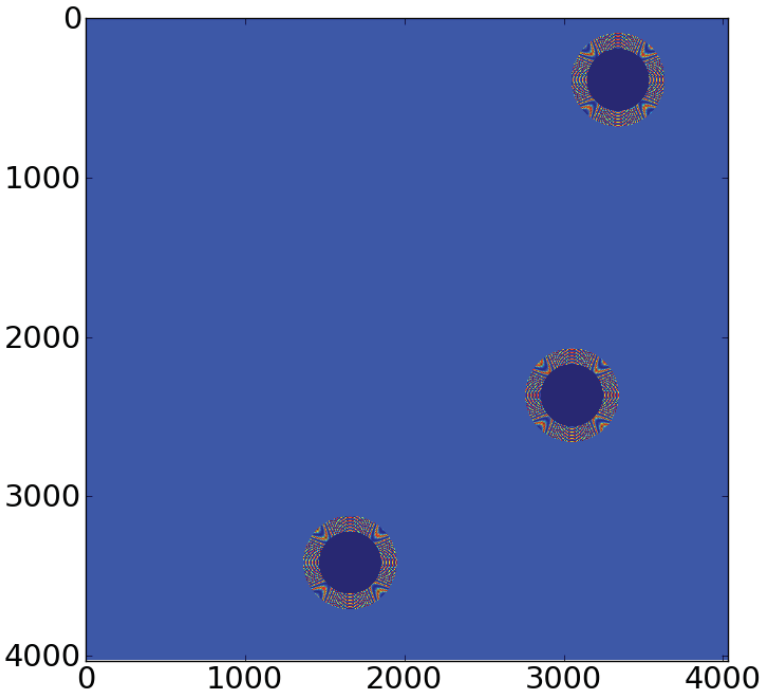
0
1000
2000
3000
4000
0
1000
2000
3000
4000

b

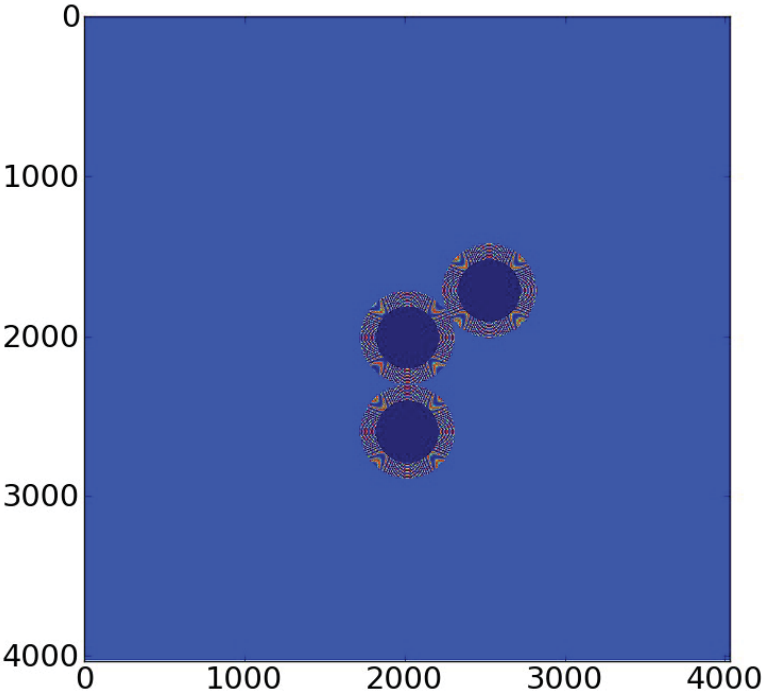
0
1000
2000
3000
4000
0
1000
2000
3000
4000

c

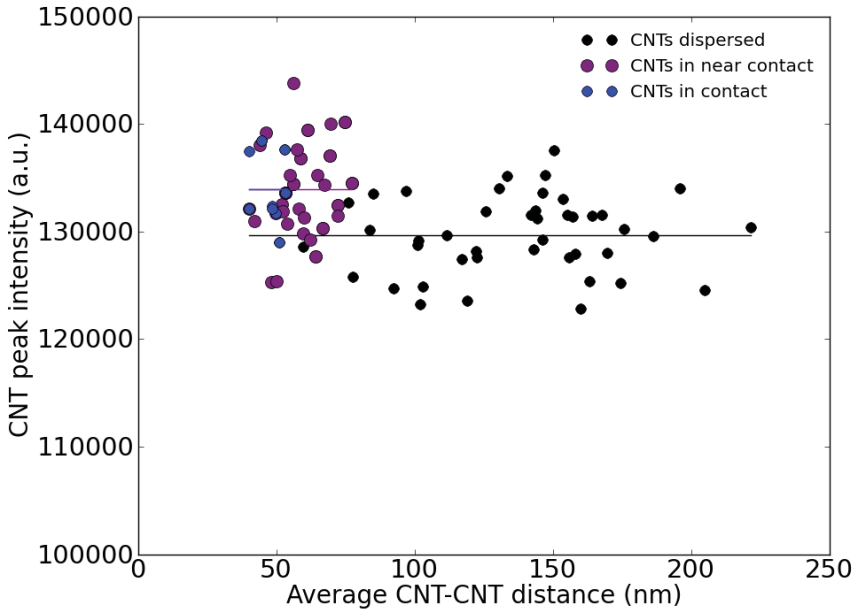

d

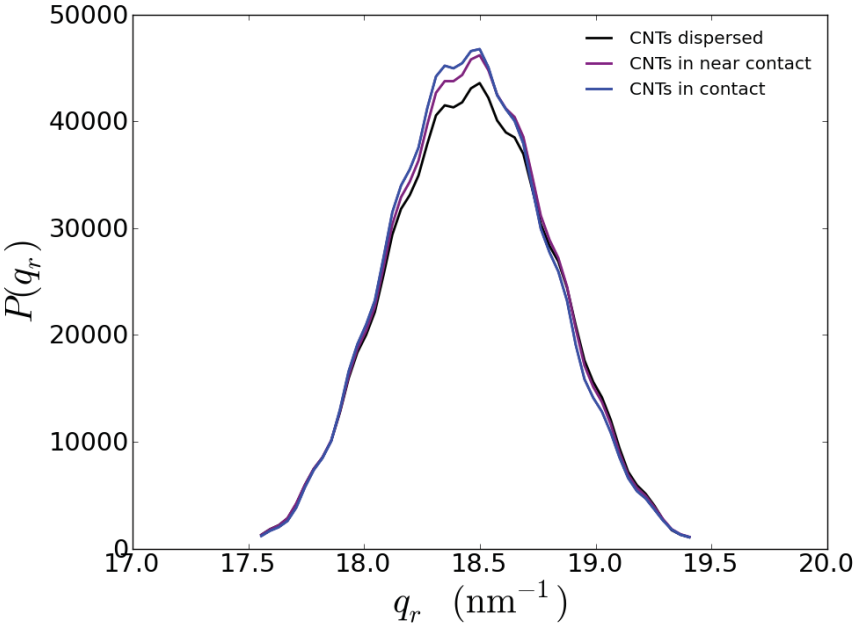

Figure 5.14 – Modeling of three individual MWNTs in various states of (a) dispersed and (b) bundled within a PDMS matrix shows that (c, d) the 1.84 Å^{-1} WAXS scattering can be enhanced if the CNTs come into close contact.

a

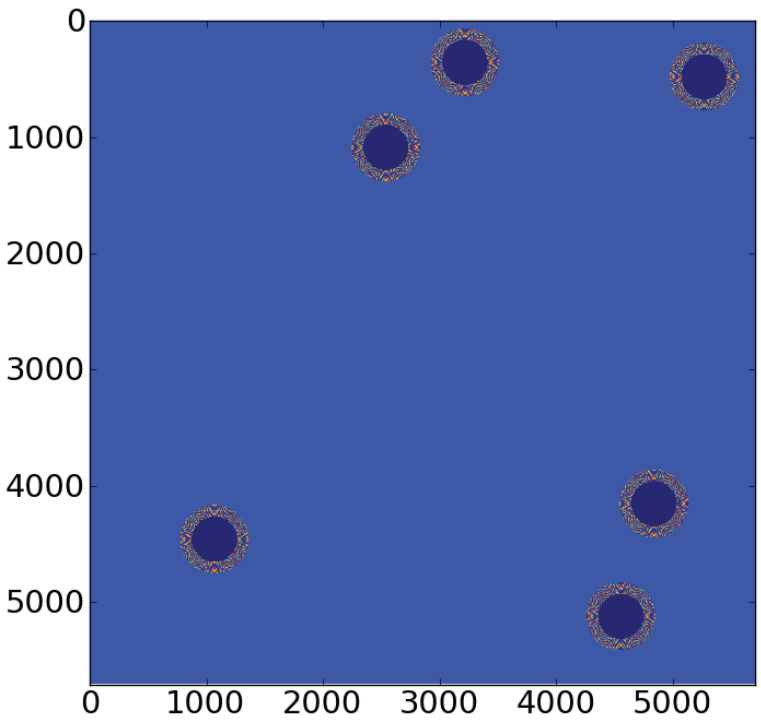
0
1000
2000
3000
4000
5000
0
1000
2000
3000
4000
5000

c

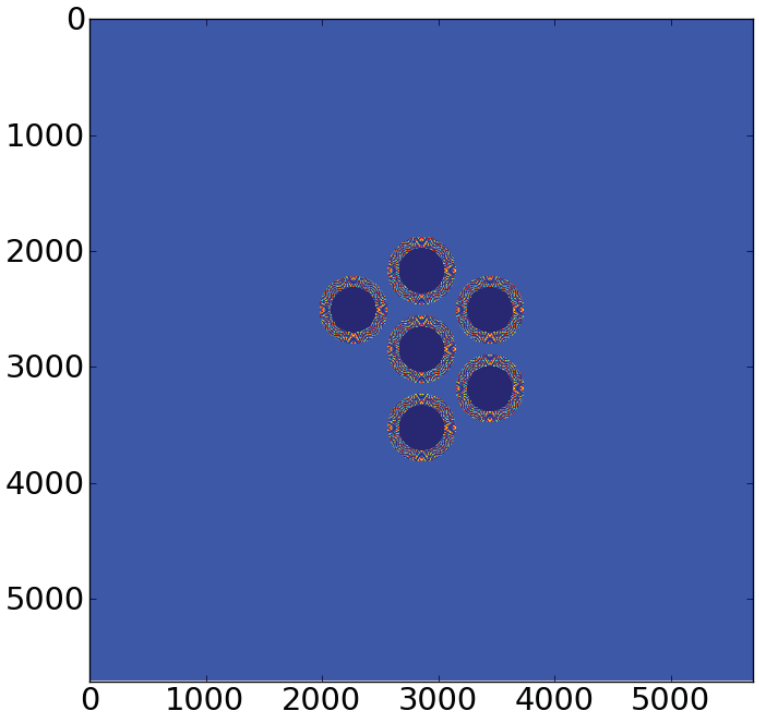
0
1000
2000
3000
4000
5000
0
1000
2000
3000
4000
5000

c

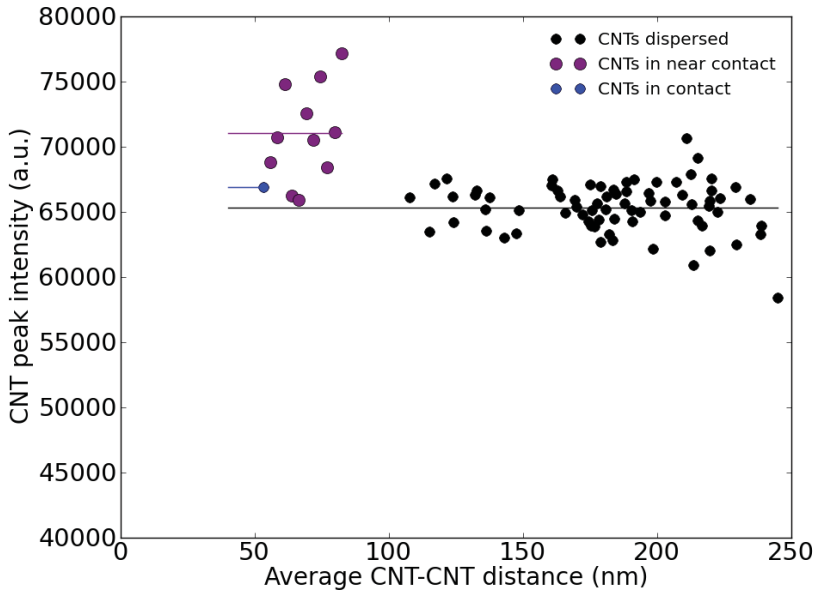

d

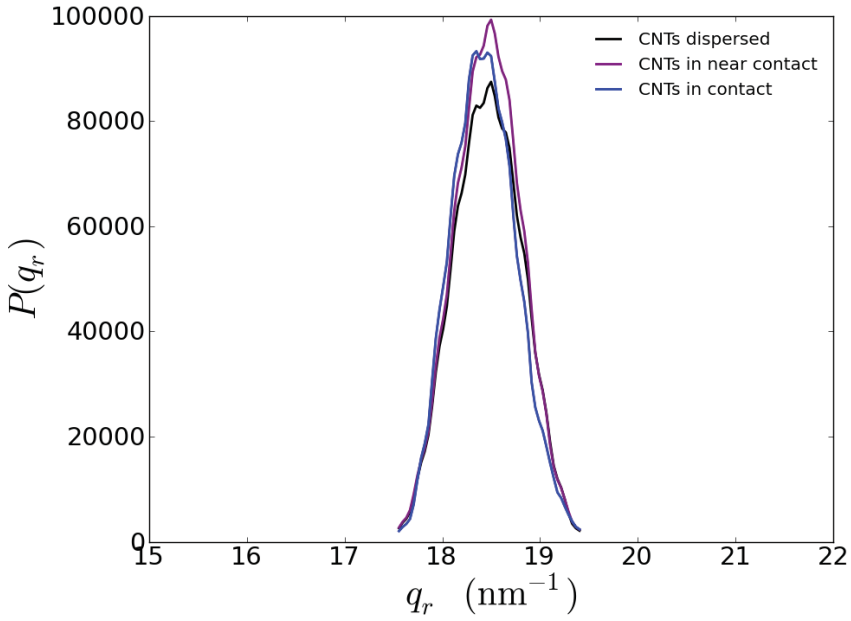

Figure 5.15 – Modeling of six individual MWNTs in various states of (a) dispersed and (b) bundled within a PDMS matrix shows that (c, d) the 1.84 Å^{-1} WAXS scattering enhancement is greater for larger bundles of CNTs.

5.5. Equating Interphasic Evolution to Mechanical Improvement

Directly from the data, we can ascertain that cyclic loading will both increase the homogeneity of the CNT fillers and cause them to become more preferentially aligned. It is conceivable that these mechanisms can be linked to a change in the stiffness of the material, and it has even been recently reported that the orientation evolution and effective persistence length of CNTs in an elastomer composite under tensile elongation can substantially affect the bulk properties of the composite [274]. However, it is unlikely that these mechanisms would continue contributing to a stiffness increase beyond 3.5 million cycles and one week of continuous stressing (Figure 4.1).

While the concept of interfacial slip and interphasic evolution introduced by Dannenberg in 1966 [209] has been widely accepted as the molecular basis for the Payne effect, the fundamental premise of his report was to propose a mechanism for the strengthening of elastomer composites through strain-induced changes in polymer morphology at the interface/interphase. A review of the available literature yielded no reports that validate the concept of interphase-moderated mechanical improvement in elastomer nanocomposites.

With support from the recent literature regarding the morphology and structure of the interphase in polymeric nanocomposites, a mechanism is proposed that would validate Dannenberg's mechanism to explain the stiffness improvement as a function of cyclic loading.

5.5.1. Detangling the Interphase

As referenced in Section 5.1, the structure of bound rubber has not yet been well defined, though there have been many reports that it may evolve during stressing. Becker *et al.* showed that the morphology of a polymer in the interphase significantly affects its stiffness [275], and it has also been shown that a rigid polymer shell on the surface of particles in filled elastomer systems will soften as a function of strain [147]. Theoretical [276] as well as experimental [277] studies have demonstrated how confinement will induce the unentangling of polymer chains, a claim supported by recent modeling efforts that have shown how polymer chains near the surface of CNTs will diffuse through the interphase, even in the case of matrix/filler bonding [278]. In accordance with the experimental results presented above, it is believed that the cyclic stressing of this composite material is stimulating the disentanglement of bound rubber on the nanotube surface.

This mechanism supports the recent results of Deng and Van Vliet, who utilized an analytical approach to resolve the effective mechanical properties of nanocomposite materials whose fillers were surrounded by a discrete interphase of finite thickness [135]. For elastomeric nanocomposites, their results indicated that the stiffness of the interphase is inversely proportional to the filler effectiveness.

Such a change in the polymer would also account for the increase in radial CTE described in Section 5.3. Confinement at the interface is known to significantly affect solvent swelling [279], as well as thermal expansion [280] in filled elastomer systems, and a decrease in the entanglement density near the CNT surface would

allow the interphasic polymer to participate in the thermal expansion. This explanation also fits nicely with modeling results suggesting that phonon modes and Brownian motion will augment the excluded volume of embedded CNT fillers, enhancing the thermal expansion of a polymer matrix [281]. Furthermore, a strongly-adsorbed interfacial layer will inhibit crystallization due to its slow dynamics [282]. A disentangling of the interphase also provides an explanation for the expedited crystallization kinetics presented in Section 4.5.1.

5.5.2. Interphasic Alignment and Interparticle Stress Distribution

While a disentangling of the bound rubber represents one mechanism in the stiffening process, as seen in Figure 5.16, there are two distinct regimes of stiffness improvement during cyclic stressing. Dannenberg's strengthening hypothesis was projected to induce "molecular orientation" [209], and an understanding of the crystallization kinetics in polymers provides evidence to support the conclusion that the PDMS chains become organized at the interface in the absence of bound rubber.

The conformation of PDMS within crystalline lamellae—as seen in Figure 5.11—was long believed to consist of a monoclinic structure supported by a two-fold helical conformation of the polymer chains [271]. Experimental results in 1991 conflicted with this model [283], and in 2000 Albouy would provide strong evidence for a linear four-fold helical conformation that favors tetragonal packing [272].

While the kinetics of polymer crystallization are not precisely understood, it is generally regarded that crystallites nucleate from ordered domains. Such a

process was first outlined by Strobl, who—as illustrated in Figure 5.17—conjectured that lamellar crystallites grow and form through intermediate states, beginning with ordered "mesomorphic layers" [284]. Such orientation has been shown to expedite crystallization in PDMS [285], and shish crystallites are known to nucleate from long, oriented segments in isotactic polypropylene [286].

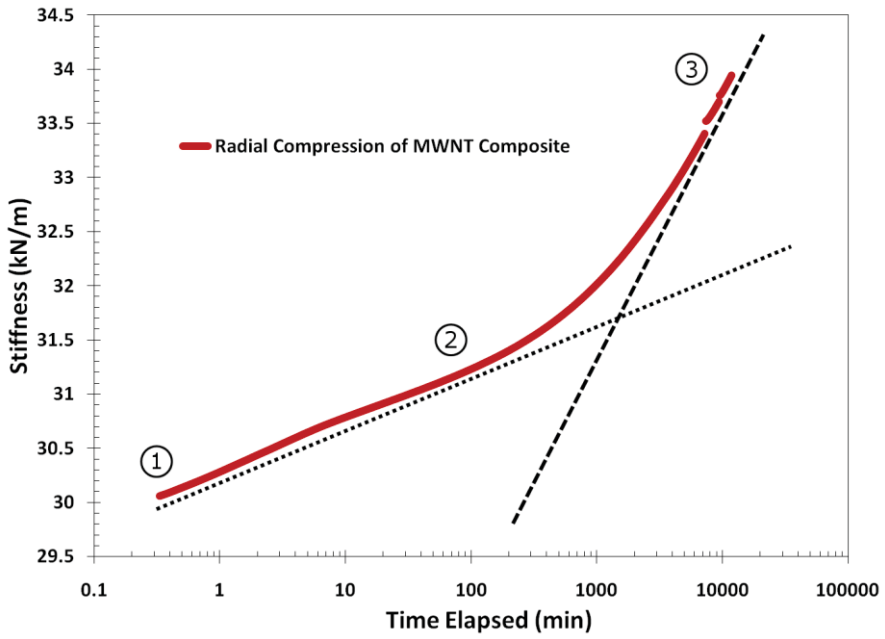

Figure 5.16 – Evaluation of the data in Figure 4.1 reveals the presence of two distinct logarithmic trends in the stiffening response, suggesting that two individual mechanisms are taking place.

Nanostructures have been known to promote these highly-ordered polymer morphologies along their surface. The degree of chain ordering on nanofillers has been shown to be a function of the molecular weight of the polymer chains [253], and has been observed for a number of common polymers, such as poly(vinyl alcohol) [287] and polyethylene [262]. A recent continuum-molecular model by

Svistkov proposes an impetus for the formation and growth of an oriented interphasic elastomer layer on nanofillers [288] that appears to build off of the aforementioned "saturation condition" proposed by de Gennes [136].

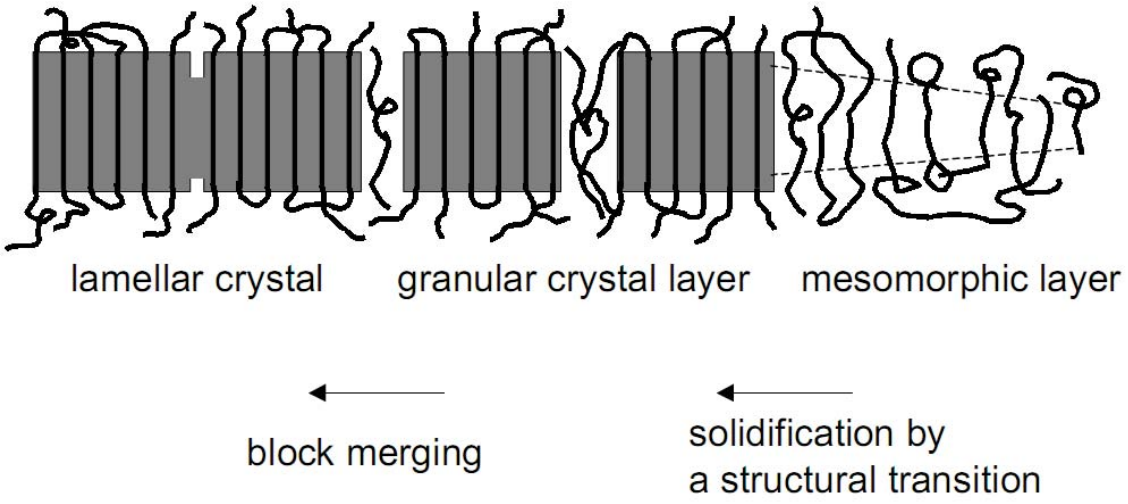

Figure 5.17 – It has been demonstrated that an ordered mesomorphic layer precedes the formation of polymer crystals [284].

Such ordered structures on the surface of fillers have also been convincingly linked to the mechanical properties of nanocomposites. Coleman *et al*. recently reported a direct correlation between an ordered polymer coating on the surface of CNTs, and their reinforcement capability [289]. Earlier, in 2004, Wei, Srivastava, and Cho employed a molecular dynamics model to predict the formation of discrete, well-oriented interfacial adsorption layers that enhanced load transfer to CNT fillers through improved van der Waals attraction [290].

It is conjectured that, in the absence of an entangled interfacial layer, cyclic stressing promotes an ordering of the polymer chains in the interphase, expediting

the crystallization kinetics and enhancing interfacial load transfer. 3D visualizations of this evolution hypothesis are presented in Figure 5.19.

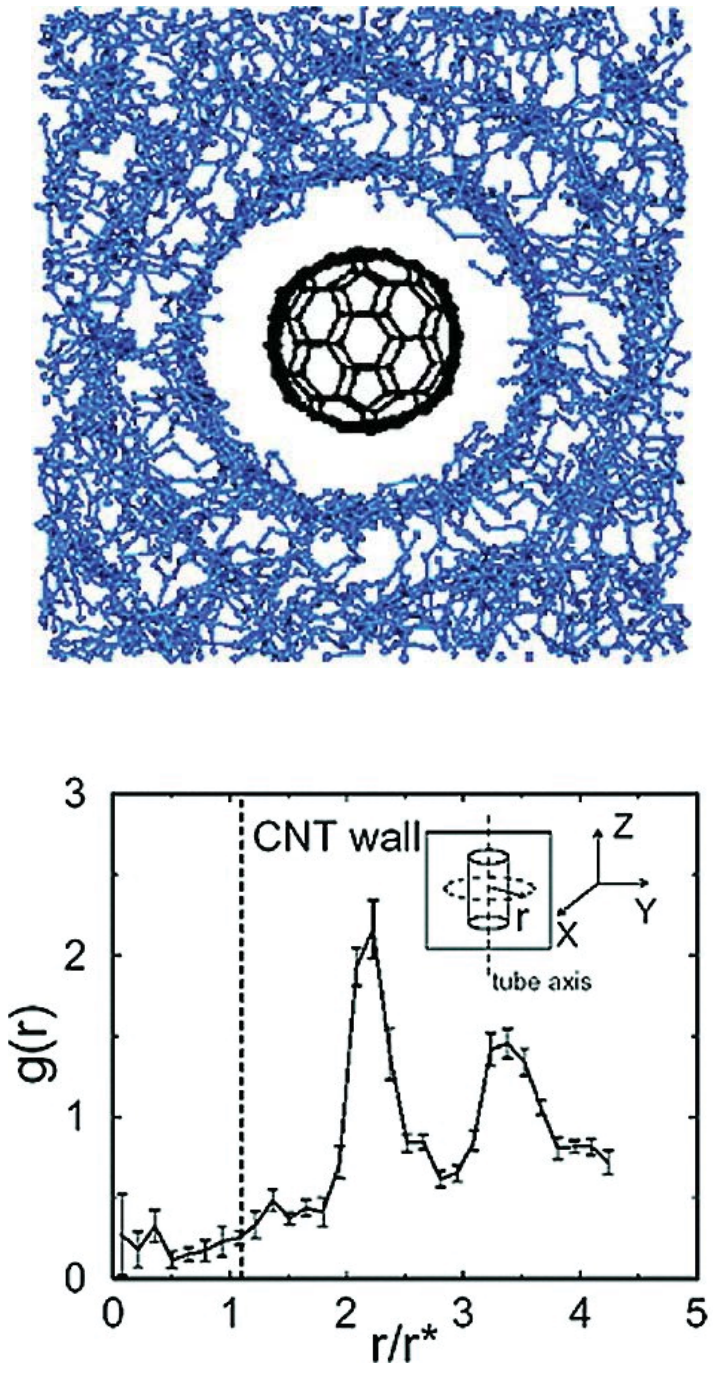

Figure 5.18 – Modeling reveals that polyethyene will form distinct adsorption layers on the surface of CNTs, improving the bulk modulus [290].

a

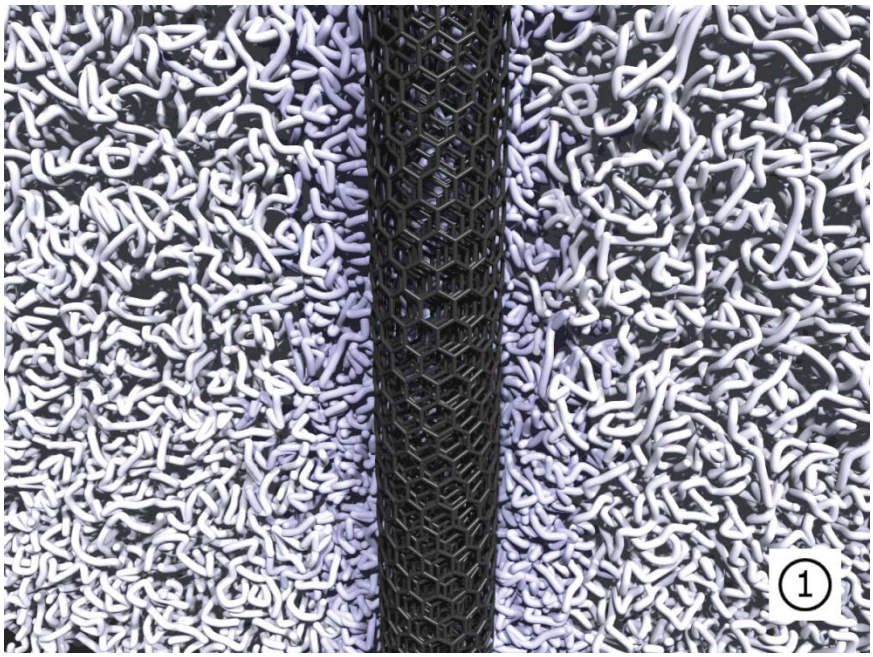

b

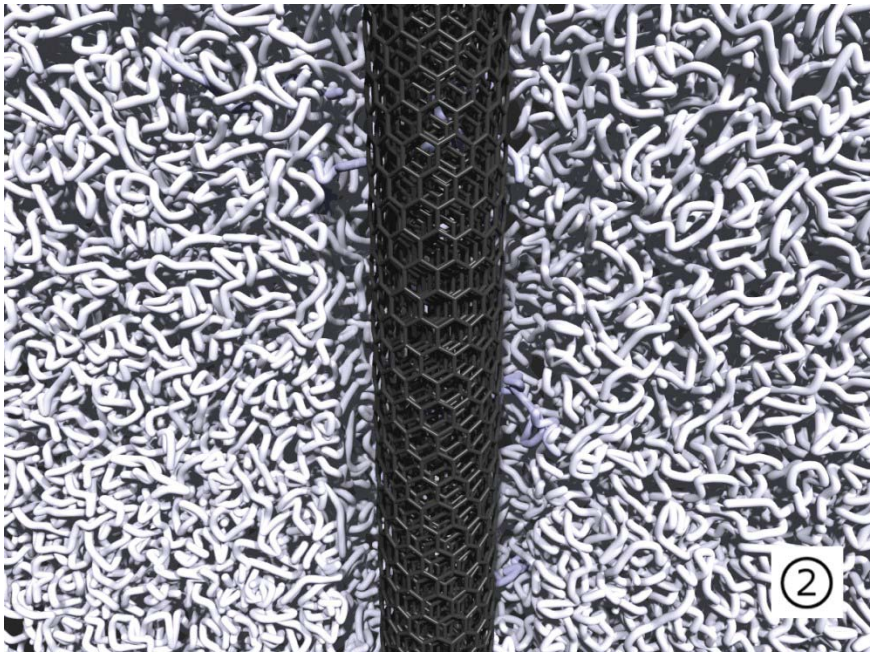

c

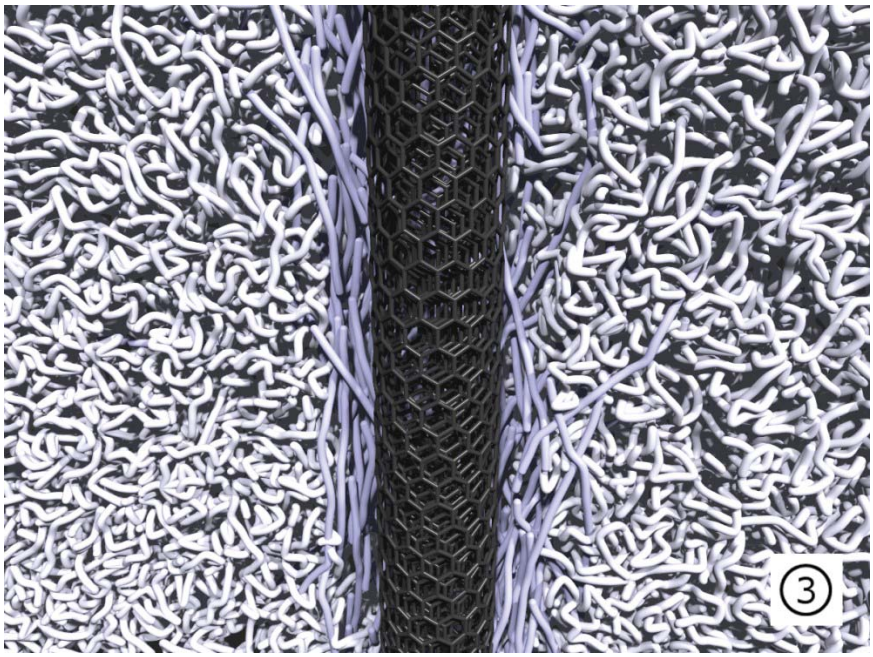

Figure 5.19 – 3D visualization further depicting the (a) interphasic bound rubber, (b) unentangled interphase, and (c) preferrentially-aligned PDMS in the stiffened nanocomposite material.

Additionally, Dannenberg's method of interphasic evolution was also suggested to "increase intermolecular attractions" through the homogenization of chain lengths between effective particles. This was rationalized by the expectation that interparticle tethers of a consistent length will evenly distribute stress during loading (Figure 5.20). Such a mechanism is implicit in the modern analysis by Leblanc, who explained that adsorption/desorption and other interphasic changes are localized, yet can contribute to long-range effects for properties such as flow mechanics due to the macromolecular structure of a cross-linked elastomer network [291]. Present day modeling has qualified this "triboelastic behavior", and provides

a realistic mechanism for the length homogenization between filler particles (Figure 5.21) [218], [292].

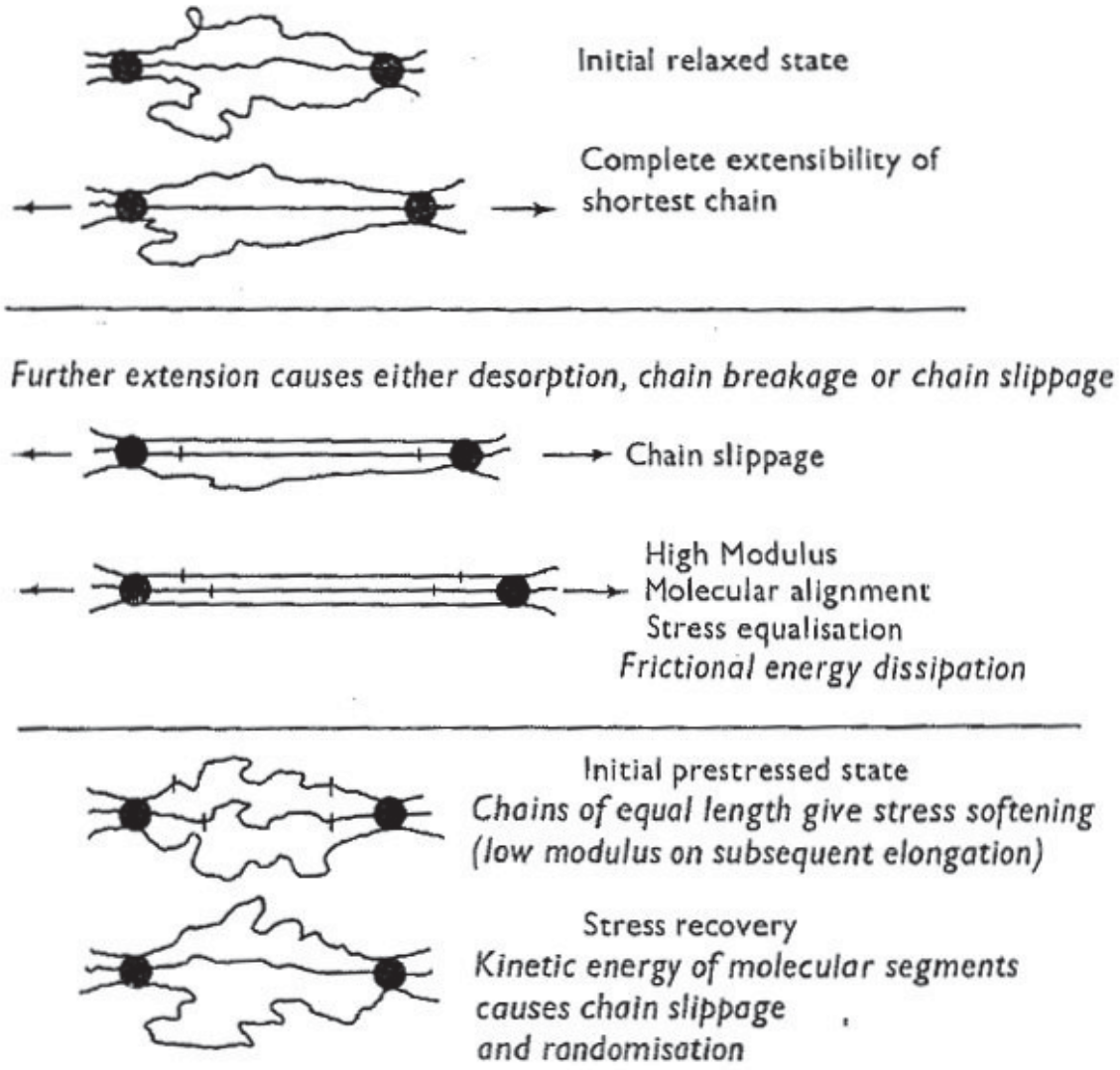

Figure 5.20 – Schematic representation of Dannenberg's "interfacial slippage" model of polymer chain homogenization [209].

The final step of Dannenberg's proposed mechanism (a relaxation of the system at the offset of stressing) is also embodied in the present data, as seen in

Figure 4.6. It was suggested that kinetic movements and the dynamic character of the physical adsorption process would give rise to a "randomization" of the interparticle chain lengths in the absence of loading. No more than a 50% recovery was expected, and in agreement with a recent study detailing the recovery behavior of prestressed elastomer nanocomposites [293], the data in the present work shows a partial relaxation that is quickly recovered when cyclic stressing is resumed (Figure 4.6).

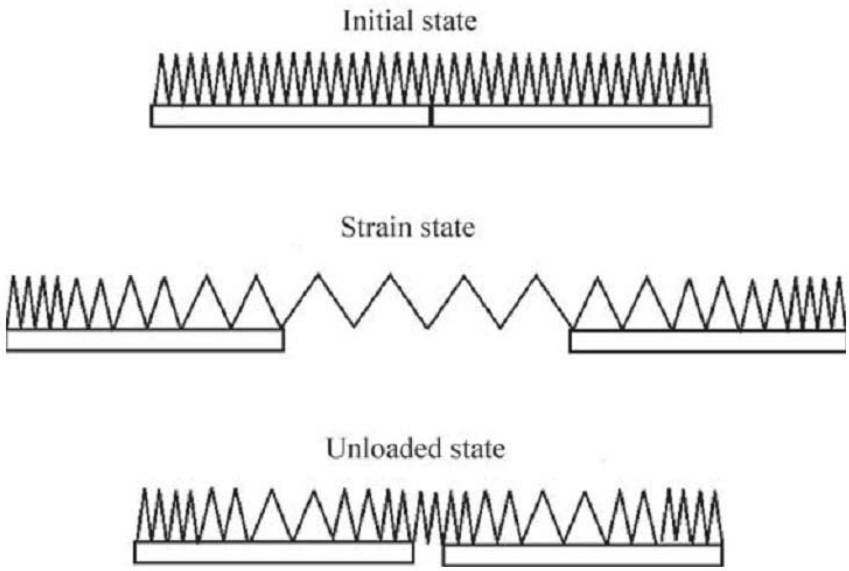

Figure 5.21 – Triboelastic behavior describes how interfacial slip can lead to the homogenization of interparticle polymer tethers [218].

5.5.3. The Combined Effect

A summation of the proposed interphasic alignment and interparticle chain homogenization mechanisms for a PDMS/CNT nanocomposite is detailed as a schematic in Figure 5.22. Such changes in the stiffened material account for the

effect's cumulative nature, and would explain why annealing does not reverse or otherwise affect the stiffening (as described in Section 4.3). Furthermore, this mechanism would be enhanced for a composite that is not completely networked, yet would still be feasible even for a vulcanizate that is fully cured—as seen in Section 4.4. The polymer used in this work (Sylgard 184) consists of an end-linked network of long, uninterrupted chains that can freely translate. Also, as a final note, the fact that this stiffening property was not seen previously in the fatigue testing of glassy nanocomposites indicates the importance of chain mobility in explaining the effect [243]; in the glassy state, polymer chains exhibit very little local mobility.

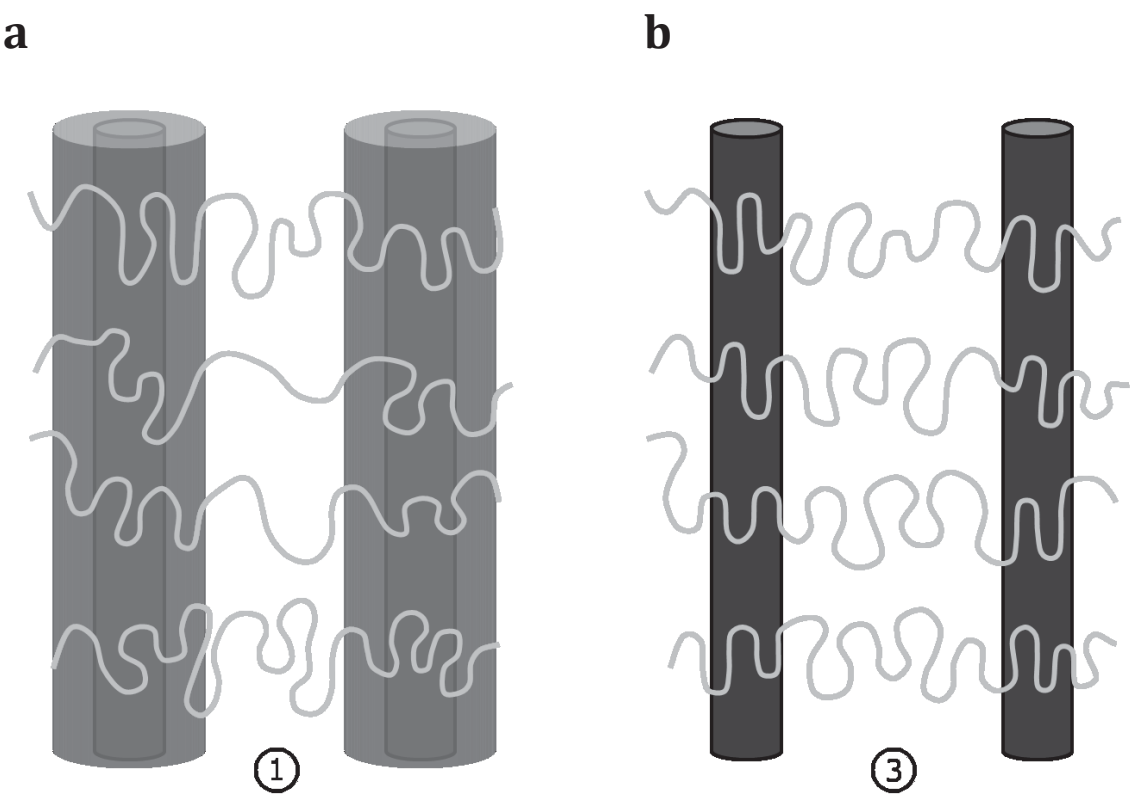

Figure 5.22 – Schematic representing the structural and morphological evolution of the interfacial and interparticle PDMS chains from the (a) unstressed to (b) stiffened nanocomposite material.

Chapter 6

Conclusions and Future Work

In this thesis, the novel mechanical properties of a compliant, continuously-reinforced elastomer nanocomposite are reported and explained. Such a material was created through the impregnation of self-assembled carbon nanotube forest structures, and correspondingly, the resulting composite exhibits a high degree of filler alignment.

The extreme anisotropy of this material is responsible for distinct orientation-specific deformation modes during dynamic compressive testing. When stressed orthogonal to the alignment direction of the CNTs, it will respond in a manner that is highly reminiscent of the neat polymer, though with a lower ultimate compressive strain. Conversely, compression along the axis of the CNT fillers will result in uncharacteristically high stiffness for low strain amplitudes, leading to a region of dynamic strain softening. This phenomenon is owed to the cooperative

buckling of the interstitial CNT struts, resulting in a mechanical response that bears a strong resemblance to the compressive behavior of open-cell foams.

It was then demonstrated that the same CNT/PDMS material will exhibit an active self-stiffening response when subjected to repeated compressive loads. This behavior was shown to be independent of the alignment of the nanotube fillers, and appears to result in a permanent improvement of the nanocomposite's mechanical response. Thermal analysis indicated that the kinetics of cold crystallization are expedited in the stiffened material, suggesting that the effect results in morphological changes to the elastomer matrix in the region surrounding the nanofillers.

Probing the effect further, strong similarities are drawn between this behavior and a mechanism for composite strengthening due to interfacial evolution in filled elastomers that was proposed in the mid 1960's. Through the direct interrogation of the polymer/matrix interface in these CNT/PDMS composites, it was determined that cyclic stress induces a change in the structure of the polymer bound to the nanofiller surface. Results from x-ray scattering and thermal expansion compliment this hypothesis, and with support from the current literature, a model for interphase-moderated stiffening in polymer nanocomposites is proposed.

Understanding the unusual behavior of this material provides insight into the complex interactions between nanoparticles and polymer matrices, and emphasizes the importance of interfacial/interphasic engineering in the development of strong

nanocomposite materials. These findings are also appealing for the design of compliant materials with unusual properties, including highly-damping surface coatings, as well as smart materials that can actively respond to applied mechanical loads.

Further study of these effects could include probing for similar responses in related materials, including other compliant polymer matrices and/or nanoparticle fillers. Additionally, experiments involving nanocomposites with either strong chemical bonding or poor interaction at the interface would provide additional insight into the specific mechanisms that contribute to these unique responses.

References

[1] S. Iijima, "Helical Microtubules of Graphitic Carbon," *Nature*, vol. 354, no. 6348, pp. 56–58, Nov. 1991.

[2] A. Jorio, M. S. Dresselhaus, and G. Dresselhaus, *Carbon Nanotubes: Advanced Topics in the Synthesis, Structure, Properties and Applications*, 1st ed. Springer, 2008.

[3] E. S. Snow, F. K. Perkins, E. J. Houser, S. C. Badescu, and T. L. Reinecke, "Chemical Detection with a Single-Walled Carbon Nanotube Capacitor," *Science*, vol. 307, no. 5717, pp. 1942–1945, Mar. 2005.

[4] C. Liu, Y. Y. Fan, M. Liu, H. T. Cong, H. M. Cheng, and M. S. Dresselhaus, "Hydrogen Storage in Single-Walled Carbon Nanotubes at Room Temperature," *Science*, vol. 286, no. 5442, pp. 1127–1129, Nov. 1999.

[5] W. A. de Heer, A. Chatelain, and D. Ugarte, "A Carbon Nanotube Field-Emission Electron Source," *Science*, vol. 270, no. 5239, pp. 1179–1180, Nov. 1995.

[6] A. E. Aliev, J. Oh, M. E. Kozlov, A. A. Kuznetsov, S. Fang, A. F. Fonseca, R. Ovalle, M. D. Lima, M. H. Haque, Y. N. Gartstein, M. Zhang, A. A. Zakhidov, and R. H. Baughman, "Giant-Stroke, Superelastic Carbon Nanotube Aerogel Muscles," *Science*, vol. 323, no. 5921, pp. 1575–1578, Mar. 2009.

[7] A. S. Brady-Estévez, S. Kang, and M. Elimelech, "A Single-Walled-Carbon-Nanotube Filter for Removal of Viral and Bacterial Pathogens," *Small*, vol. 4, no. 4, pp. 481–484, Mar. 2008.

[8] Y.-H. Li, J. Ding, Z. Luan, Z. Di, Y. Zhu, C. Xu, D. Wu, and B. Wei, "Competitive Adsorption of Pb2+, Cu2+ and Cd2+ Ions from Aqueous Solutions by Multiwalled Carbon Nanotubes," *Carbon*, vol. 41, no. 14, pp. 2787–2792, 2003.

[9] K. Kordás, G. Tóth, P. Moilanen, M. Kumpumäki, J. Vähäkangas, A. Uusimäki, R. Vajtai, and P. M. Ajayan, "Chip Cooling with Integrated Carbon Nanotube Microfin Architectures," *Appl. Phys. Lett.*, vol. 90, no. 12, p. 123105, 2007.

[10] C. Niu, E. K. Sichel, R. Hoch, D. Moy, and H. Tennent, "High Power Electrochemical Capacitors Based on Carbon Nanotube Electrodes," *Appl. Phys. Lett.*, vol. 70, no. 11, p. 1480, 1997.

[11] Y. Shirai, A. J. Osgood, Y. Zhao, K. F. Kelly, and J. M. Tour, "Directional Control in Thermally Driven Single-Molecule Nanocars," *Nano Lett.*, vol. 5, no. 11, pp. 2330–2334, Nov. 2005.

[12] C. T. White and T. N. Todorov, "Carbon Nanotubes as Long Ballistic Conductors," *Nature*, vol. 393, no. 6682, pp. 240–242, May 1998.

[13] M. M. J. Treacy, T. W. Ebbesen, and J. M. Gibson, "Exceptionally High Young's Modulus Observed for Individual Carbon Nanotubes," *Nature*, vol. 381, no. 6584, pp. 678–680, Jun. 1996.

[14] S. Berber, Y.-K. Kwon, and D. Tomanek, "Unusually High Thermal Conductivity of Carbon Nanotubes," *Phys. Rev. Lett.*, vol. 84, no. 20, p. 4613, May 2000.

[15] Z. Chen, K. Kobashi, U. Rauwald, R. Booker, H. Fan, W.-F. Hwang, and J. M. Tour, "Soluble Ultra-Short Single-Walled Carbon Nanotubes," *J. Am. Chem. Soc*, vol. 128, no. 32, pp. 10568–10571, 2006.

[16] X. Wang, Q. Li, J. Xie, Z. Jin, J. Wang, Y. Li, K. Jiang, and S. Fan, "Fabrication of Ultralong and Electrically Uniform Single-Walled Carbon Nanotubes on Clean Substrates," *Nano Letters*, vol. 9, no. 9, pp. 3137–3141, 2009.

[17] C. Zoican Loebick, R. Podila, J. Reppert, J. Chudow, F. Ren, G. L. Haller, A. M. Rao, and L. D. Pfefferle, "Selective Synthesis of Subnanometer Diameter Semiconducting Single-Walled Carbon Nanotubes," *Journal of the American Chemical Society*, vol. 132, no. 32, pp. 11125–11131, 2010.

[18] M.-F. Yu, O. Lourie, M. J. Dyer, K. Moloni, T. F. Kelly, and R. S. Ruoff, "Strength and Breaking Mechanism of Multiwalled Carbon Nanotubes Under Tensile Load," *Science*, vol. 287, no. 5453, pp. 637–640, Jan. 2000.

[19] B. Zhao, D. N. Futaba, S. Yasuda, M. Akoshima, T. Yamada, and K. Hata, "Exploring Advantages of Diverse Carbon Nanotube Forests with Tailored Structures Synthesized by Supergrowth from Engineered Catalysts," *ACS Nano*, vol. 3, no. 1, pp. 108–114, Jan. 2009.

[20] E. Bekyarova, M. E. Itkis, N. Cabrera, B. Zhao, A. Yu, J. Gao, and R. C. Haddon, "Electronic Properties of Single-Walled Carbon Nanotube Networks," *J. Am. Chem. Soc*, vol. 127, no. 16, pp. 5990–5995, Apr. 2005.

[21] H. W. Yap, R. S. Lakes, and R. W. Carpick, "Mechanical Instabilities of Individual Multiwalled Carbon Nanotubes under Cyclic Axial Compression," *Nano Lett.*, vol. 7, no. 5, pp. 1149–1154, May 2007.

[22] X. Yang and G. Wu, "The Study of Structural, Electronic and Optical Properties of Double-Walled Carbon Nanotube Bundles under Hydrostatic Pressure," *Europhysics Letters*, vol. 81, no. 4, p. 47003, Jan. 2008.

[23] C. Lamprecht, J. Danzberger, P. Lukanov, C.-M. Tîlmaciu, A.-M. Galibert, B. Soula, E. Flahaut, H. J. Gruber, P. Hinterdorfer, A. Ebner, and F. Kienberger, "AFM

Imaging of Functionalized Double-Walled Carbon Nanotubes," *Ultramicroscopy*, vol. 109, no. 8, pp. 899–906, Jul. 2009.

[24] M. C. Hersam, "Progress Towards Monodisperse Single-Walled Carbon Nanotubes," *Nat Nano*, vol. 3, no. 7, pp. 387–394, Jul. 2008.

[25] M. S. Arnold, A. A. Green, J. F. Hulvat, S. I. Stupp, and M. C. Hersam, "Sorting Carbon Nanotubes by Electronic Structure Using Density Differentiation," *Nat. Nanotechnol.*, vol. 1, no. 1, pp. 60–65, Oct. 2006.

[26] Y. Wang, M. J. Kim, H. Shan, C. Kittrell, H. Fan, L. M. Ericson, W.-F. Hwang, S. Arepalli, R. H. Hauge, and R. E. Smalley, "Continued Growth of Single-Walled Carbon Nanotubes," *Nano Lett.*, vol. 5, no. 6, pp. 997–1002, Jun. 2005.

[27] Y. Yao, C. Feng, J. Zhang, and Z. Liu, "'Cloning' of Single-Walled Carbon Nanotubes via Open-End Growth Mechanism," *Nano Lett.*, vol. 9, no. 4, pp. 1673–1677, Apr. 2009.

[28] G. U. Sumanasekera, A. R. Harutyunyan, G. Chen, T. M. Paronyan, E. M. Pigos, O. A. Kuznetsov, K. Hewaparakrama, S. M. Kim, D. Zakharov, and E. A. Stach, "Preferential Growth of Single-Walled Carbon Nanotubes with Metallic Conductivity," *Science*, vol. 326, no. 5949, pp. 116–120, Oct. 2009.

[29] O. Stephan, P. M. Ajayan, C. Colliex, P. Redlich, J. M. Lambert, P. Bernier, and P. Lefin, "Doping Graphitic and Carbon Nanotube Structures with Boron and Nitrogen," *Science*, vol. 266, no. 5191, pp. 1683 –1685, Dec. 1994.

[30] C. F. Chen, C. L. Tsai, and C. L. Lin, "The Characterization of Boron-Doped Carbon Nanotube Arrays," *Diam. Relat. Mater.*, vol. 12, no. 9, pp. 1500–1504, Sep. 2003.

[31] K. McGuire, N. Gothard, P. L. Gai, M. S. Dresselhaus, G. Sumanasekera, and A. M. Rao, "Synthesis and Raman Characterization of Boron-Doped Single-Walled Carbon Nanotubes," *Carbon*, vol. 43, no. 2, pp. 219–227, 2005.

[32] P. Ayala, J. Reppert, M. Grobosch, M. Knupfer, T. Pichler, and A. M. Rao, "Evidence for Substitutional Boron in Doped Single-Walled Carbon Nanotubes," *Appl. Phys. Lett.*, vol. 96, no. 18, p. 183110, 2010.

[33] K. Jiang, A. Eitan, L. S. Schadler, P. M. Ajayan, R. W. Siegel, N. Grobert, M. Mayne, M. Reyes-Reyes, H. Terrones, and M. Terrones, "Selective Attachment of Gold Nanoparticles to Nitrogen-Doped Carbon Nanotubes," *Nano Lett.*, vol. 3, no. 3, pp. 275–277, Mar. 2003.

[34] K. Gong, F. Du, Z. Xia, M. Durstock, and L. Dai, "Nitrogen-Doped Carbon Nanotube Arrays with High Electrocatalytic Activity for Oxygen Reduction," *Science*, vol. 323, no. 5915, pp. 760 –764, Feb. 2009.

[35] P. Ayala, R. Arenal, M. Rümmeli, A. Rubio, and T. Pichler, "The Doping of Carbon Nanotubes with Nitrogen and their Potential Applications," *Carbon*, vol. 48, no. 3, pp. 575–586, Mar. 2010.

[36] M. Foldvari and M. Bagonluri, "Carbon Nanotubes as Functional Excipients for Nanomedicines: I. Pharmaceutical Properties," *Nanomed. Nanotechnol. Biol. Med.*, vol. 4, no. 3, pp. 173–182, Sep. 2008.

[37] T. W. Ebbesen and P. M. Ajayan, "Large-Scale Synthesis of Carbon Nanotubes," *Nature*, vol. 358, no. 6383, pp. 220–222, Jul. 1992.

[38] T. Guo, P. Nikolaev, A. Thess, D. T. Colbert, and R. E. Smalley, "Catalytic Growth of Single-Walled Nanotubes by Laser Vaporization," *Chem. Phys. Lett.*, vol. 243, no. 1–2, pp. 49–54, Sep. 1995.

[39] M. José-Yacamán, M. Miki-Yoshida, L. Rendón, and J. G. Santiesteban, "Catalytic Growth of Carbon Microtubules with Fullerene Structure," *Appl. Phys. Lett.*, vol. 62, no. 2, p. 202, 1993.

[40] M. Endo, K. Takeuchi, S. Igarashi, K. Kobori, M. Shiraishi, and H. W. Kroto, "The Production and Structure of Pyrolytic Carbon Nanotubes (PCNTs)," *J. Phys. Chem. Solids*, vol. 54, no. 12, pp. 1841–1848, Dec. 1993.

[41] S. Chakrabarti, K. Gong, and L. Dai, "Structural Evaluation along the Nanotube Length for Super-long Vertically Aligned Double-Walled Carbon Nanotube Arrays," *J. Phys. Chem. C*, vol. 112, no. 22, pp. 8136–8139, Jun. 2008.

[42] S. B. Sinnott, R. Andrews, D. Qian, A. M. Rao, Z. Mao, E. C. Dickey, and F. Derbyshire, "Model of Carbon Nanotube Growth Through Chemical Vapor Deposition," *Chem. Phys. Lett.*, vol. 315, no. 1–2, pp. 25–30, Dec. 1999.

[43] P. Nikolaev, M. J. Bronikowski, R. K. Bradley, F. Rohmund, D. T. Colbert, K. A. Smith, and R. E. Smalley, "Gas-Phase Catalytic Growth of Single-Walled Carbon Nanotubes from Carbon Monoxide," *Chem. Phys. Lett.*, vol. 313, no. 1–2, pp. 91–97, Nov. 1999.

[44] B. Kitiyanan, W. E. Alvarez, J. H. Harwell, and D. E. Resasco, "Controlled Production of Single-Wall carbon Nanotubes by Catalytic Decomposition of CO on Bimetallic Co-Mo Catalysts," *Chem. Phys. Lett.*, vol. 317, no. 3–5, pp. 497–503, Feb. 2000.

[45] S. Hofmann, R. Sharma, C. Ducati, G. Du, C. Mattevi, C. Cepek, M. Cantoro, S. Pisana, A. Parvez, F. Cervantes-Sodi, A. C. Ferrari, R. Dunin-Borkowski, S. Lizzit, L. Petaccia, A. Goldoni, and J. Robertson, "In situ Observations of Catalyst Dynamics during Surface-Bound Carbon Nanotube Nucleation," *Nano Lett.*, vol. 7, no. 3, pp. 602–608, Mar. 2007.

[46] S. Helveg, C. Lopez-Cartes, J. Sehested, P. L. Hansen, B. S. Clausen, J. R. Rostrup-Nielsen, F. Abild-Pedersen, and J. K. Norskov, "Atomic-Scale Imaging of Carbon Nanofibre Growth," *Nature*, vol. 427, no. 6973, pp. 426–429, Jan. 2004.

[47] H. Amara, C. Bichara, and F. Ducastelle, "Understanding the Nucleation Mechanisms of Carbon Nanotubes in Catalytic Chemical Vapor Deposition," *Phys. Rev. Lett.*, vol. 100, no. 5, p. 056105, Feb. 2008.

[48] F. Ding, A. R. Harutyunyan, and B. I. Yakobson, "Dislocation Theory of Chirality-Controlled Nanotube Growth," *Proc. Nat. Acad. Sci.*, vol. 106, no. 8, pp. 2506 – 2509, Feb. 2009.

[49] W. Z. Li, S. S. Xie, L. X. Qian, B. H. Chang, B. S. Zou, W. Y. Zhou, R. A. Zhao, and G. Wang, "Large-Scale Synthesis of Aligned Carbon Nanotubes," *Science*, vol. 274, no. 5293, pp. 1701–1703, Dec. 1996.

[50] Y. Chen, Z. Lin Wang, J. Song Yin, D. J. Johnson, and R. H. Prince, "Well-Aligned Graphitic Nanofibers Synthesized by Plasma-Assisted Chemical Vapor Deposition," *Chem. Phys. Lett.*, vol. 272, no. 3–4, pp. 178–182, Jun. 1997.

[51] T. Yamada, T. Namai, K. Hata, D. N. Futaba, K. Mizuno, J. Fan, M. Yudasaka, M. Yumura, and S. Iijima, "Size-Selective Growth of Double-Walled Carbon Nanotube Forests from Engineered Iron Catalysts," *Nat. Nanotechnol.*, vol. 1, no. 2, pp. 131–136, Nov. 2006.

[52] L. Ci, R. Vajtai, and P. M. Ajayan, "Vertically Aligned Large-Diameter Double-Walled Carbon Nanotube Arrays Having Ultralow Density," *J. Phys. Chem. C*, vol. 111, no. 26, pp. 9077–9080, Jul. 2007.

[53] S. Fan, M. G. Chapline, N. R. Franklin, T. W. Tombler, A. M. Cassell, and H. Dai, "Self-Oriented Regular Arrays of Carbon Nanotubes and Their Field Emission Properties," *Science*, vol. 283, no. 5401, pp. 512–514, Jan. 1999.

[54] K. Hata, D. N. Futaba, K. Mizuno, T. Namai, M. Yumura, and S. Iijima, "Water-Assisted Highly Efficient Synthesis of Impurity-Free Single-Walled Carbon Nanotubes," *Science*, vol. 306, no. 5700, pp. 1362–1364, Nov. 2004.

[55] P. B. Amama, C. L. Pint, L. McJilton, S. M. Kim, E. A. Stach, P. T. Murray, R. H. Hauge, and B. Maruyama, "Role of Water in Super Growth of Single-Walled Carbon Nanotube Carpets," *Nano Lett.*, vol. 9, no. 1, pp. 44–49, Jan. 2009.

[56] L. Ci, S. M. Manikoth, X. Li, R. Vajtai, and P. M. Ajayan, "Ultrathick Freestanding Aligned Carbon Nanotube Films," *Adv. Mater.*, vol. 19, no. 20, pp. 3300–3303, 2007.

[57] E. Flahaut, R. Bacsa, A. Peig, and C. Laurent, "Gram-Scale CCVD Synthesis of Double-Walled Carbon Nanotubes," *Chem. Commun.*, no. 12, pp. 1442–1443, 2003.

[58] M. Moniruzzaman and K. I. Winey, "Polymer Nanocomposites Containing Carbon Nanotubes," *Macromolecules*, vol. 39, no. 16, pp. 5194–5205, 2006.

[59] R. Andrews, D. Jacques, A. M. Rao, F. Derbyshire, D. Qian, X. Fan, E. C. Dickey, and J. Chen, "Continuous Production of Aligned Carbon Nanotubes: A Step Closer to Commercial Realization," *Chem. Phys. Lett.*, vol. 303, no. 5–6, pp. 467–474, Apr. 1999.

[60] R. Kamalakaran, M. Terrones, T. Seeger, P. Kohler-Redlich, M. Rühle, Y. A. Kim, T. Hayashi, and M. Endo, "Synthesis of Thick and Crystalline Nanotube Arrays by Spray Pyrolysis," *Appl. Phys. Lett.*, vol. 77, no. 21, p. 3385, 2000.

[61] M. Mayne, N. Grobert, M. Terrones, R. Kamalakaran, M. Rühle, H. W. Kroto, and D. R. M. Walton, "Pyrolytic Production of Aligned Carbon Nanotubes from Homogeneously Dispersed Benzene-Based Aerosols," *Chem. Phys. Lett.*, vol. 338, no. 2–3, pp. 101–107, Apr. 2001.

[62] E. T. Thostenson, W. Z. Li, D. Z. Wang, Z. F. Ren, and T. W. Chou, "Carbon Nanotube/Carbon Fiber Hybrid Multiscale Composites," *J. Appl. Phys.*, vol. 91, no. 9, p. 6034, 2002.

[63] B. Q. Wei, R. Vajtai, Y. Jung, J. Ward, R. Zhang, G. Ramanath, and P. M. Ajayan, "Microfabrication Technology: Organized Assembly of Carbon Nanotubes," *Nature*, vol. 416, no. 6880, pp. 495–496, Apr. 2002.

[64] R. Guzmán de Villoria, A. J. Hart, and B. L. Wardle, "Continuous High-Yield Production of Vertically Aligned Carbon Nanotubes on 2D and 3D Substrates," *ACS Nano*, vol. 5, no. 6, pp. 4850–4857, 2011.

[65] P. M. Ajayan, L. S. Schadler, and P. V. Braun, *Nanocomposite Science and Technology*. Wiley-VCH, 2003.

[66] Z. Tang, N. A. Kotov, S. Magonov, and B. Ozturk, "Nanostructured Artificial Nacre," *Nat. Mater.*, vol. 2, pp. 413–418, May 2003.

[67] H. D. Espinosa, A. L. Juster, F. J. Latourte, O. Y. Loh, D. Gregoire, and P. D. Zavattieri, "Tablet-Level Origin of Toughening in Abalone Shells and

Translation to Synthetic Composite Materials," *Nat. Commun.*, vol. 2, p. 173, Feb. 2011.

[68] Y.-Y. Hu, A. Rawal, and K. Schmidt-Rohr, "Strongly Bound Citrate Stabilizes the Apatite Nanocrystals in Bone," *Proc. Nat. Acad. Sci.*, vol. 107, no. 52, pp. 22425 – 22429, Dec. 2010.

[69] C. Sanchez, H. Arribart, and M. M. Giraud Guille, "Biomimetism and Bioinspiration as Tools for the Design of Innovative Materials and Systems," *Nat. Mater.*, vol. 4, no. 4, pp. 277–288, Apr. 2005.

[70] J. R. Capadona, K. Shanmuganathan, D. J. Tyler, S. J. Rowan, and C. Weder, "Stimuli-Responsive Polymer Nanocomposites Inspired by the Sea Cucumber Dermis," *Science*, vol. 319, no. 5868, pp. 1370–1374, Mar. 2008.

[71] G.-D. Zhan, J. D. Kuntz, J. Wan, and A. K. Mukherjee, "Single-Wall Carbon Nanotubes as Attractive Toughening Agents in Alumina-Based Nanocomposites," *Nat. Mater.*, vol. 2, pp. 38–42, Dec. 2002.

[72] M. Sennett, C. Sekyung, R. H. Doremus, R. W. Siegel, P. M. Ajayan, and L. S. Schadler, "Improved Performance of Alumina Ceramics with Carbon Nanotube Reinforcement," *Ceram. Trans.*, vol. 134, pp. 551–556, 2002.

[73] I. Szlufarska, A. Nakano, and P. Vashishta, "A Crossover in the Mechanical Response of Nanocrystalline Ceramics," *Science*, vol. 309, no. 5736, pp. 911 – 914, 2005.

[74] S. Zhang, D. Sun, Y. Fu, and H. Du, "Recent Advances of Superhard Nanocomposite Coatings: A Review," *Surf. Coat. Tech.*, vol. 167, no. 2–3, pp. 113–119, Apr. 2003.

[75] W. X. Chen, J. P. Tu, L. Y. Wang, H. Y. Gan, Z. D. Xu, and X. B. Zhang, "Tribological Application of Carbon Nanotubes in a Metal-Based Composite Coating and Composites," *Carbon*, vol. 41, no. 2, pp. 215–222, Feb. 2003.

[76] L. Y. Wang, J. P. Tu, W. X. Chen, Y. C. Wang, X. K. Liu, C. Olk, D. H. Cheng, and X. B. Zhang, "Friction and Wear Behavior of Electroless Ni-Based CNT Composite Coatings," *Wear*, vol. 254, no. 12, pp. 1289–1293, Nov. 2003.

[77] M. Kireitseu, D. Hui, and G. Tomlinson, "Advanced Shock-Resistant and Vibration Damping of Nanoparticle-Reinforced Composite Material," *Compos. Part B-Eng.*, vol. 39, no. 1, pp. 128–138, Jan. 2008.

[78] S. R. Bakshi, V. Singh, K. Balani, D. G. McCartney, S. Seal, and A. Agarwal, "Carbon Nanotube Reinforced Aluminum Composite Coating via Cold Spraying," *Surf. Coat. Tech.*, vol. 202, no. 21, pp. 5162–5169, Jul. 2008.

[79] H. J. Choi, S. M. Lee, and D. H. Bae, "Wear Characteristic of Aluminum-Based Composites Containing Multi-Walled Carbon Nanotubes," *Wear*, vol. 270, no. 1, pp. 12–18, 2010.

[80] A. M. K. Esawi, K. Morsi, A. Sayed, M. Taher, and S. Lanka, "Effect of Carbon Nanotube (CNT) Content on the Mechanical Properties of CNT-Reinforced Aluminium Composites," *Compos. Sci. Technol.*, vol. In Press, Accepted Manuscript, May 2010.

[81] C. Deng, X. Zhang, D. Wang, Q. Lin, and A. Li, "Preparation and Characterization of Carbon Nanotubes/Aluminum Matrix Composites," *Mater. Lett.*, vol. 61, no. 8–9, pp. 1725–1728, Apr. 2007.

[82] E. Carreño-Morelli, J. Yang, E. Couteau, K. Hernadi, J. W. Seo, C. Bonjour, L. Forró, and R. Schaller, "Carbon Nanotube/Magnesium Composites," *Phys. Status Solidi A*, vol. 201, no. 8, p. R53–R55, 2004.

[83] T. Tokunaga, K. Kaneko, and Z. Horita, "Production of Aluminum-Matrix Carbon Nanotube Composite Using High Pressure Torsion," *Mater. Sci. Eng.: A*, vol. 490, no. 1–2, pp. 300–304, Aug. 2008.

[84] C. F. Deng, D. Z. Wang, X. X. Zhang, and A. B. Li, "Processing and Properties of Carbon Nanotubes Reinforced Aluminum Composites," *Mater. Sci. Eng.: A*, vol. 444, no. 1–2, pp. 138–145, Jan. 2007.

[85] T. Laha and A. Agarwal, "Effect of Sintering on Thermally Sprayed Carbon Nanotube Reinforced Aluminum Nanocomposite," *Mat. Sci. Eng. A*, vol. 480, no. 1–2, pp. 323–332, May 2008.

[86] A. K. Srivastava, C. L. Xu, B. Q. Wei, R. Kishore, and K. N. Sood, "Microstructural and Mechanical Properties of Carbon Nanotubes Reinforced Aluminum-Based Metal Matrix Composites," *Indian J. Eng. Mater. S.*, vol. 15, pp. 247–255, 2008.

[87] S. Shaikh, K. Lafdi, and E. Silverman, "The Effect of a CNT Interface on the Thermal Resistance of Contacting Surfaces," *Carbon*, vol. 45, no. 4, pp. 695–703, Apr. 2007.

[88] R. Cross, B. A. Cola, T. Fisher, X. Xu, K. Gall, and S. Graham, "A Metallization and Bonding Approach for High Performance Carbon Nanotube Thermal Interface Materials," *Nanotechnology*, vol. 21, no. 44, p. 445705, Nov. 2010.

[89] O. Hjortstam, P. Isberg, S. Söderholm, and H. Dai, "Can We Achieve Ultra-Low Resistivity in Carbon Nanotube-Based Metal Composites?," *Appl. Phys. A-Mater.*, vol. 78, no. 8, pp. 1175–1179, May 2004.

[90] J. Jang, "Conducting Polymer Nanomaterials and Their Applications," in *Emissive Materials Nanomaterials*, vol. 199, Berlin/Heidelberg: Springer-Verlag, 2006, pp. 189–260.

[91] C. F. Deng, Y. X. Ma, P. Zhang, X. X. Zhang, and D. Z. Wang, "Thermal Expansion Behaviors of Aluminum Composite Reinforced with Carbon Nanotubes," *Mater. Lett.*, vol. 62, no. 15, pp. 2301–2303, May 2008.

[92] B. Lim, C. Kim, B. Kim, U. Shim, S. Oh, B. Sung, J. Choi, and S. Baik, "The Effects of Interfacial Bonding on Mechanical Properties of Single-Walled Carbon Nanotube Reinforced Copper Matrix Nanocomposites," *Nanotechnology*, vol. 17, no. 23, pp. 5759–5764, Dec. 2006.

[93] K. T. Kim, S. I. Cha, T. Gemming, J. Eckert, and S. H. Hong, "The Role of Interfacial Oxygen Atoms in the Enhanced Mechanical Properties of Carbon-Nanotube-Reinforced Metal Matrix Nanocomposites," *Small*, vol. 4, no. 11, pp. 1936–1940, 2008.

[94] L. Ci, Z. Ryu, N. Y. Jin-Phillipp, and M. Rühle, "Investigation of the Interfacial Reaction Between Multi-Walled Carbon Nanotubes and Aluminum," *Acta Mater.*, vol. 54, no. 20, pp. 5367–5375, Dec. 2006.

[95] R. George, K. T. Kashyap, R. Rahul, and S. Yamdagni, "Strengthening in Carbon Nanotube/Aluminium (CNT/Al) Composites," *Scripta Mater.*, vol. 53, no. 10, pp. 1159–1163, Nov. 2005.

[96] A. K. Keshri, K. Balani, S. R. Bakshi, V. Singh, T. Laha, S. Seal, and A. Agarwal, "Structural Transformations in Carbon Nanotubes During Thermal Spray Processing," *Surf. Coat. Tech.*, vol. 203, no. 16, pp. 2193–2201, May 2009.

[97] J. E. Mark, B. Erman, and F. R. Eirich, *Science and Technology of Rubber*, 3rd ed. Academic Press, 2005.

[98] Y. Lu, Y. Yang, A. Sellinger, M. Lu, J. Huang, H. Fan, R. Haddad, G. Lopez, A. R. Burns, D. Y. Sasaki, J. Shelnutt, and C. J. Brinker, "Self-Assembly of Mesoscopically Ordered Chromatic Polydiacetylene/Silica Nanocomposites," *Nature*, vol. 410, no. 6831, pp. 913–917, Apr. 2001.

[99] E. J. McCumiskey, N. Chandrasekhar, and C. R. Taylor, "Nanomechanics of CdSe Quantum Dot–Polymer Nanocomposite Films," *Nanotechnology*, vol. 21, no. 22, p. 225703, Jun. 2010.

[100] J. Zhu, P. Start, K. A. Mauritz, and C. A. Wilkie, "Thermal Stability and Flame Retardancy of Poly(methyl methacrylate)-Clay Nanocomposites," *Polym. Degrad. Stab.*, vol. 77, no. 2, pp. 253–258, 2002.

[101] K. Shanmuganathan, S. Deodhar, N. A. Dembsey, Q. Fan, and P. K. Patra, "Condensed-Phase Flame Retardation in Nylon 6-Layered Silicate Nanocomposites: Films, Fibers, and Fabrics," *Polym. Sci. Eng.*, vol. 48, no. 4, pp. 662–675, 2008.

[102] P. Podsiadlo, A. K. Kaushik, E. M. Arruda, A. M. Waas, B. S. Shim, J. Xu, H. Nandivada, B. G. Pumplin, J. Lahann, A. Ramamoorthy, and N. A. Kotov, "Ultrastrong and Stiff Layered Polymer Nanocomposites," *Science*, vol. 318, no. 5847, pp. 80–83, Oct. 2007.

[103] T. Ramanathan, A. A. Abdala, S. Stankovich, D. A. Dikin, M. Herrera-Alonso, R. D. Piner, D. H. Adamson, H. C. Schniepp, X. Chen, R. S. Ruoff, S. T. Nguyen, I. A. Aksay, R. K. Prud'Homme, and L. C. Brinson, "Functionalized Graphene Sheets for Polymer Nanocomposites," *Nat. Nanotechnol.*, vol. 3, no. 6, pp. 327–331, Jun. 2008.

[104] I. Srivastava, R. J. Mehta, Z.-Z. Yu, L. Schadler, and N. Koratkar, "Raman Study of Interfacial Load Transfer in Graphene Nanocomposites," *Appl. Phys. Lett.*, vol. 98, no. 6, p. 063102, 2011.

[105] B. O. Dabbousi, M. G. Bawendi, O. Onitsuka, and M. F. Rubner, "Electroluminescence from CdSe Quantum-Dot/Polymer Composites," *Appl. Phys. Lett.*, vol. 66, no. 11, p. 1316, 1995.

[106] S. Wang, Y. Hu, L. Song, Z. Wang, Z. Chen, and W. Fan, "Preparation and Thermal Properties of ABS/Montmorillonite Nanocomposite," *Polym. Degrad. Stab.*, vol. 77, no. 3, pp. 423–426, 2002.

[107] T. V. Sreekumar, T. Liu, S. Kumar, L. M. Ericson, R. H. Hauge, and R. E. Smalley, "Single-Wall Carbon Nanotube Films," *Chem. Mater.*, vol. 15, no. 1, pp. 175–178, Jan. 2003.

[108] A. Rehab and N. Salahuddin, "Nanocomposite Materials based on Polyurethane Intercalated into Montmorillonite Clay," *Mater. Sci. Eng.: A*, vol. 399, no. 1–2, pp. 368–376, Jun. 2005.

[109] Y. Kang and T. A. Taton, "Micelle-Encapsulated Carbon Nanotubes: A Route to Nanotube Composites," *J. Am. Chem. Soc*, vol. 125, no. 19, pp. 5650–5651, 2003.

[110] H. Z. Geng, R. Rosen, B. Zheng, H. Shimoda, L. Fleming, J. Liu, and O. Zhou, "Fabrication and Properties of Composites of Poly(ethylene oxide) and Functionalized Carbon Nanotubes," *Adv. Mater.*, vol. 14, no. 19, pp. 1387–1390, 2002.

[111] D. F. Schmidt, F. Clément, and E. P. Giannelis, "On the Origins of Silicate Dispersion in Polysiloxane/Layered-Silicate Nanocomposites," *Adv. Funct. Mater.*, vol. 16, no. 3, pp. 417–425, 2006.

[112] Y. Zhu, Z. Du, H. Li, and C. Zhang, "Preparation and Crystallization Behavior of Multiwalled Carbon Nanotubes/Poly(vinyl alcohol) Nanocomposites," *Polym. Eng. Sci.*, 2011.

[113] G.-M. Kim, D.-H. Lee, B. Hoffmann, J. Kressler, and G. Stöppelmann, "Influence of Nanofillers on the Deformation Process in Layered Silicate/Polyamide-12 Nanocomposites," *Polymer*, vol. 42, no. 3, pp. 1095–1100, Feb. 2001.

[114] K. Wang, S. Liang, R. Du, Q. Zhang, and Q. Fu, "The Interplay of Thermodynamics and Shear on the Dispersion of Polymer Nanocomposite," *Polymer*, vol. 45, no. 23, pp. 7953–7960, Oct. 2004.

[115] A. Yasmin, J. L. Abot, and I. M. Daniel, "Processing of Clay/Epoxy Nanocomposites by Shear Mixing," *Scripta Mater.*, vol. 49, no. 1, pp. 81–86, Jul. 2003.

[116] Y. Li and H. Shimizu, "High-Shear Processing Induced Homogenous Dispersion of Pristine Multiwalled Carbon Nanotubes in a Thermoplastic Elastomer," *Polymer*, vol. 48, no. 8, pp. 2203–2207, Apr. 2007.

[117] J. W. Cho and D. R. Paul, "Nylon 6 Nanocomposites by Melt Compounding," *Polymer*, vol. 42, no. 3, pp. 1083–1094, Feb. 2001.

[118] T. McNally, W. Raymond Murphy, C. Y. Lew, R. J. Turner, and G. P. Brennan, "Polyamide-12 Layered Silicate Nanocomposites by Melt Blending," *Polymer*, vol. 44, no. 9, pp. 2761–2772, Apr. 2003.

[119] H. Koerner, D. Misra, A. Tan, L. Drummy, P. Mirau, and R. Vaia, "Montmorillonite-Thermoset Nanocomposites via Cryo-Compounding," *Polymer*, vol. 47, no. 10, pp. 3426–3435, May 2006.

[120] K. Wakabayashi, C. Pierre, D. A. Dikin, R. S. Ruoff, T. Ramanathan, L. C. Brinson, and J. M. Torkelson, "Polymer–Graphite Nanocomposites: Effective Dispersion and Major Property Enhancement via Solid-State Shear Pulverization," *Macromolecules*, vol. 41, no. 6, pp. 1905–1908, Sep. 2011.

[121] A. Vermogen, K. Masenelli-Varlot, R. Séguéla, J. Duchet-Rumeau, S. Boucard, and P. Prele, "Evaluation of the Structure and Dispersion in Polymer-Layered Silicate Nanocomposites," *Macromolecules*, vol. 38, no. 23, pp. 9661–9669, Sep. 2011.

[122] L. Chen, X.-J. Pang, and Z.-L. Yu, "Study on Polycarbonate/Multi-Walled Carbon Nanotubes Composite Produced by Melt Processing," *Mat. Sci. Eng. A*, vol. 457, no. 1–2, pp. 287–291, May 2007.

[123] U. Khan, P. May, A. O'Neill, J. J. Vilatela, A. H. Windle, and J. N. Coleman, "Tuning the Mechanical Properties of Composites from Elastomeric to Rigid Thermoplastic by Controlled Addition of Carbon Nanotubes," *Small*, vol. 7, no. 11, pp. 1579–1586, Jun. 2011.

[124] J. Chen, M. A. Hamon, H. Hu, Y. Chen, A. M. Rao, P. C. Eklund, and R. C. Haddon, "Solution Properties of Single-Walled Carbon Nanotubes," *Science*, vol. 282, no. 5386, pp. 95 –98, Oct. 1998.

[125] J. Liu, A. G. Rinzler, H. Dai, J. H. Hafner, R. K. Bradley, P. J. Boul, A. Lu, T. Iverson, K. Shelimov, C. B. Huffman, F. Rodriguez-Macias, Y.-S. Shon, T. R. Lee, D. T. Colbert, and R. E. Smalley, "Fullerene Pipes," *Science*, vol. 280, no. 5367, pp. 1253 –1256, May 1998.

[126] C. A. Mitchell, J. L. Bahr, S. Arepalli, J. M. Tour, and R. Krishnamoorti, "Dispersion of Functionalized Carbon Nanotubes in Polystyrene," *Macromolecules*, vol. 35, no. 23, pp. 8825–8830, Nov. 2002.

[127] M. Moniruzzaman, J. Chattopadhyay, W. E. Billups, and K. I. Winey, "Tuning the Mechanical Properties of SWNT/Nylon 6,10 Composites with Flexible Spacers at the Interface," *Nano Lett.*, vol. 7, no. 5, pp. 1178–1185, May 2007.

[128] Y. Hou, J. Tang, H. Zhang, C. Qian, Y. Feng, and J. Liu, "Functionalized Few-Walled Carbon Nanotubes for Mechanical Reinforcement of Polymeric Composites," *ACS Nano*, vol. 3, no. 5, pp. 1057–1062, May 2009.

[129] A. H. Barber, S. R. Cohen, and H. D. Wagner, "Measurement of Carbon Nanotube--Polymer Interfacial Strength," *Appl. Phys. Lett.*, vol. 82, no. 23, pp. 4140–4142, Jun. 2003.

[130] A. Eitan, K. Jiang, D. Dukes, R. Andrews, and L. S. Schadler, "Surface Modification of Multiwalled Carbon Nanotubes: Toward the Tailoring of the Interface in Polymer Composites," *Chem. Mater.*, vol. 15, no. 16, pp. 3198–3201, 2003.

[131] P. M. Ajayan and J. M. Tour, "Materials Science: Nanotube Composites," *Nature*, vol. 447, no. 7148, pp. 1066–1068, Jun. 2007.

[132] M. J. O'Connell, P. Boul, L. M. Ericson, C. Huffman, Y. Wang, E. Haroz, C. Kuper, J. Tour, K. D. Ausman, and R. E. Smalley, "Reversible Water-Solubilization of Single-Walled Carbon Nanotubes by Polymer Wrapping," *Chem. Phys. Lett.*, vol. 342, no. 3–4, pp. 265–271, Jul. 2001.

[133] D. Brown, P. Mele, S. Marceau, and N. D. Alberola, "A Molecular Dynamics Study of a Model Nanoparticle Embedded in a Polymer Matrix," *Macromolecules*, vol. 36, no. 4, pp. 1395–1406, 2003.

[134] M. Qu, F. Deng, S. M. Kalkhoran, A. Gouldstone, A. Robisson, and K. J. Van Vliet, "Nanoscale Visualization and Multiscale Mechanical Implications of Bound Rubber Interphases in Rubber–Carbon Black Nanocomposites," *Soft Mater.*, vol. 7, pp. 1066–1077, 2011.

[135] F. Deng and K. J. Van Vliet, "Prediction of Elastic Properties for Polymer–Particle Nanocomposites Exhibiting an Interphase," *Nanotechnology*, vol. 22, no. 16, p. 165703, Apr. 2011.

[136] P. G. de Gennes, "Polymers At an Interface; A Simplified View," *Adv. Colloid Interface Sci.*, vol. 27, no. 3–4, pp. 189–209, Jul. 1987.

[137] R. Krishnamoorti, R. A. Vaia, and E. P. Giannelis, "Structure and Dynamics of Polymer-Layered Silicate Nanocomposites," *Chem. Mater.*, vol. 8, no. 8, pp. 1728–1734, 1996.

[138] F. W. Starr, T. B. Schroder, and S. C. Glotzer, "Molecular Dynamics Simulation of a Polymer Melt with a Nanoscopic Particle," *Macromolecules*, vol. 35, no. 11, pp. 4481–4492, May 2002.

[139] A. Bansal, H. Yang, C. Li, K. Cho, B. C. Benicewicz, S. K. Kumar, and L. S. Schadler, "Quantitative Equivalence between Polymer Nanocomposites and Thin Polymer Films," *Nat. Mater.*, vol. 4, no. 9, pp. 693–698, 2005.

[140] P. Rittigstein, R. D. Priestley, L. J. Broadbelt, and J. M. Torkelson, "Model Polymer Nanocomposites Provide an Understanding of Confinement Effects in Real Nanocomposites," *Nat. Mater.*, vol. 6, no. 4, pp. 278–282, Apr. 2007.

[141] K. Parker, R. T. Schneider, R. W. Siegel, R. Ozisik, J. C. Cabanelas, B. Serrano, C. Antonelli, and J. Baselga, "Molecular Probe Technique for Determining Local Thermal Transitions: The Glass Transition at Silica/PMMA Nanocomposite Interfaces," *Polymer*, vol. 51, no. 21, pp. 4891–4898, Oct. 2010.

[142] S.-S. Choi, "Influence of Storage Time and Temperature and Silane Coupling Agent on Bound Rubber Formation in Filled Styrene-Butadiene Rubber Compounds," *Polym. Test.*, vol. 21, no. 2, pp. 201–208, 2002.

[143] T. Ramanathan, H. Liu, and L. C. Brinson, "Functionalized SWNT/Polymer Nanocomposites for Dramatic Property Improvement," *J. Polym. Sci., Polym. Phys.*, vol. 43, no. 17, pp. 2269–2279, Sep. 2005.

[144] V. M. Litvinov, R. A. Orza, M. Kluppel, M. van Duin, and P. C. M. M. Magusin, "Rubber–Filler Interactions and Network Structure in Relation to Stress–Strain Behavior of Vulcanized, Carbon Black Filled EPDM," *Macromolecules*, vol. 44, no. 12, pp. 4887–4900, Jun. 2011.

[145] M. I. Aranguren, E. Mora, and C. W. Macosko, "Compounding Fumed Silicas into Polydimethylsiloxane: Bound Rubber and Final Aggregate Size," *J. Colloid Interface Sci.*, vol. 195, no. 2, pp. 329–337, Nov. 1997.

[146] K. W. Putz, M. J. Palmeri, R. B. Cohn, R. Andrews, and L. C. Brinson, "Effect of Cross-Link Density on Interphase Creation in Polymer Nanocomposites," *Macromolecules*, vol. 41, no. 18, pp. 6752–6756, 2008.

[147] H. Montes, F. Lequeux, and J. Berriot, "Influence of the Glass Transition Temperature Gradient on the Nonlinear Viscoelastic Behavior in Reinforced Elastomers," *Macromolecules*, vol. 36, no. 21, pp. 8107–8118, Oct. 2003.

[148] E. Herve and A. Zaoui, "n-Layered Inclusion-Based Micromechanical Modelling," *Int. J. Eng. Sci.*, vol. 31, no. 1, pp. 1–10, Jan. 1993.

[149] M. P. Lutz and R. W. Zimmerman, "Effect of the Interphase Zone on the Bulk Modulus of a Particulate Composite," *J. Appl. Mech.*, vol. 63, no. 4, pp. 855–861, Dec. 1996.

[150] K. Ding and G. J. Weng, "The Influence of Moduli Slope of a Linearly Graded Matrix on the Bulk Moduli of Some Particle- and Fiber-Reinforced Composites," *J. Elast.*, vol. 53, no. 1, pp. 1–22, 1998.

[151] S. Nie and C. Basaran, "A Micromechanical Model for Effective Elastic Properties of Particulate Composites with Imperfect Interfacial Bonds," *Int. J. Solids Struct.*, vol. 42, no. 14, pp. 4179–4191, Jul. 2005.

[152] M. R. Ayatollahi, S. Shadlou, and M. M. Shokrieh, "Multiscale Modeling for Mechanical Properties of Carbon Nanotube Reinforced Nanocomposites Subjected to Different Types of Loading," *Compos. Struct.*, vol. 93, no. 9, pp. 2250–2259, Aug. 2011.

[153] X. Frielinghaus, M. Brodeck, O. Holderer, and H. Frielinghaus, "Confined Polymer Dynamics on Clay Platelets," *Langmuir*, vol. 26, no. 22, pp. 17444–17448, Nov. 2010.

[154] J. N. Coleman, U. Khan, W. J. Blau, and Y. K. Gun'ko, "Small but Strong: A Review of the Mechanical Properties of Carbon Nanotube-Polymer Composites," *Carbon*, vol. 44, no. 9, pp. 1624–1652, Aug. 2006.

[155] D. Okawa, S. J. Pastine, A. Zettl, and J. M. J. Fréchet, "Surface Tension Mediated Conversion of Light to Work," *J. Am. Chem. Soc*, vol. 131, no. 15, pp. 5396–5398, Apr. 2009.

[156] P. M. Ajayan, O. Stephan, C. Colliex, and D. Trauth, "Aligned Carbon Nanotube Arrays Formed by Cutting a Polymer Resin--Nanotube Composite," *Science*, vol. 265, no. 5176, pp. 1212–1214, Aug. 1994.

[157] H. D. Wagner, O. Lourie, Y. Feldman, and R. Tenne, "Stress-Induced Fragmentation of Multiwall Carbon Nanotubes in a Polymer Matrix," *Appl. Phys. Lett.*, vol. 72, no. 2, pp. 188–190, Jan. 1998.

[158] Z. Jia, Z. Wang, C. Xu, J. Liang, B. Wei, D. Wu, and S. Zhu, "Study on Poly(methyl methacrylate)/Carbon Nanotube Composites," *Mat. Sci. Eng. A*, vol. 271, no. 1–2, pp. 395–400, Nov. 1999.

[159] M. Weisenberger, R. Andrews, and T. Rantell, "Carbon Nanotube Polymer Composites: Recent Developments in Mechanical Properties," in *Physical Properties of Polymers Handbook*, 2007, pp. 585–598.

[160] L. Bokobza, "Multiwall Carbon Nanotube Elastomeric Composites: A Review," *Polymer*, vol. 48, no. 17, pp. 4907–4920, Aug. 2007.

[161] M. Xu, D. N. Futaba, M. Yumura, and K. Hata, "Tailoring Temperature Invariant Viscoelasticity of Carbon Nanotube Material," *Nano Lett.*, vol. 0, no. 0, 2011.

[162] M. J. Green, N. Behabtu, M. Pasquali, and W. W. Adams, "Nanotubes as Polymers," *Polymer*, vol. 50, no. 21, pp. 4979–4997, Oct. 2009.

[163] Y. J. Jung, S. Kar, S. Talapatra, C. Soldano, G. Viswanathan, X. Li, Z. Yao, F. S. Ou, A. Avadhanula, R. Vajtai, S. Curran, O. Nalamasu, and P. M. Ajayan, "Aligned Carbon Nanotube–Polymer Hybrid Architectures for Diverse Flexible Electronic Applications," *Nano Lett.*, vol. 6, no. 3, pp. 413–418, Mar. 2006.

[164] L. Z. Chen, C. H. Liu, C. H. Hu, and S. S. Fan, "Electrothermal Actuation Based on Carbon Nanotube Network in Silicone Elastomer," *Appl. Phys. Lett.*, vol. 92, no. 26, p. 263104–3, Jun. 2008.

[165] C. Li, Y. Liu, C. Lo, and H. Jiang, "Reversible White-Light Actuation of Carbon Nanotube Incorporated Liquid Crystalline Elastomer Nanocomposites," *Soft Matter*, 2011.

[166] S. Hudziak, A. Darfeuille, R. Zhang, T. Peijs, G. Mountjoy, G. Bertoni, and M. Baxendale, "Magnetoresistive Phenomena in an Fe-Filled Carbon

Nanotube/Elastomer Composite," *Nanotechnology*, vol. 21, no. 12, p. 125505, Mar. 2010.

[167] S.-H. Park, P. Theilmann, P. Asbeck, and P. Bandaru, "Enhanced Electromagnetic Interference Shielding Through the Use of Functionalized Carbon-Nanotube-Reactive Polymer Composites," *IEEE T. Nano.*, vol. 9, no. 4, Jul. 2010.

[168] C. X. Liu and J. W. Choi, "Strain-Dependent Resistance of PDMS and Carbon Nanotubes Composite Microstructures," *IEEE T. Nano.*, vol. 9, no. 5, pp. 590–595, 2010.

[169] X. Gui, H. Li, L. Zhang, Y. Jia, L. Liu, Z. Li, J. Wei, K. Wang, H. Zhu, Z. Tang, D. Wu, and A. Cao, "A Facile Route to Isotropic Conductive Nanocomposites by Direct Polymer Infiltration of Carbon Nanotube Sponges," *ACS Nano*, vol. 5, no. 6, pp. 4276–4283, 2011.

[170] N. Yamamoto, A. John Hart, E. J. Garcia, S. S. Wicks, H. M. Duong, A. H. Slocum, and B. L. Wardle, "High-Yield Growth and Morphology Control of Aligned Carbon Nanotubes on Ceramic Fibers for Multifunctional Enhancement of Structural Composites," *Carbon*, vol. 47, no. 3, pp. 551–560, Mar. 2009.

[171] X. Sui and H. D. Wagner, "Tough Nanocomposites: The Role of Carbon Nanotube Type," *Nano Lett.*, vol. 9, no. 4, pp. 1423–1426, Apr. 2009.

[172] G. N. Toepperwein and J. J. de Pablo, "Cavitation and Crazing in Rod-Containing Nanocomposites," *Macromolecules*, vol. 44, no. 13, pp. 5498–5509, 2011.

[173] X. Gong, J. Liu, S. Baskaran, R. D. Voise, and J. S. Young, "Surfactant-Assisted Processing of Carbon Nanotube/Polymer Composites," *Chem. Mater.*, vol. 12, no. 4, pp. 1049–1052, Apr. 2000.

[174] Y.-P. Sun, K. Fu, Y. Lin, and W. Huang, "Functionalized Carbon Nanotubes: Properties and Applications," *Acc. Chem. Res.*, vol. 35, no. 12, pp. 1096–1104, Dec. 2002.

[175] G. Viswanathan, N. Chakrapani, H. Yang, B. Wei, H. Chung, K. Cho, C. Y. Ryu, and P. M. Ajayan, "Single-Step in Situ Synthesis of Polymer-Grafted Single-Wall Nanotube Composites," *J. Am. Chem. Soc*, vol. 125, no. 31, pp. 9258–9259, 2003.

[176] C. A. Dyke and J. M. Tour, "Overcoming the Insolubility of Carbon Nanotubes Through High Degrees of Sidewall Functionalization," *Chem. Eur.-J.*, vol. 10, no. 4, pp. 812–817, 2004.

[177] R. Krishnamoorti and R. A. Vaia, "Polymer Nanocomposites," *J. Polym. Sci., Polym. Phys.*, vol. 45, no. 24, pp. 3252–3256, Dec. 2007.

[178] L. Jin, C. Bower, and O. Zhou, "Alignment of Carbon Nanotubes in a Polymer Matrix by Mechanical Stretching," *Appl. Phys. Lett.*, vol. 73, no. 9, p. 1197, 1998.

[179] R. Haggenmueller, H. H. Gommans, A. G. Rinzler, J. E. Fischer, and K. I. Winey, "Aligned Single-Wall Carbon Nanotubes in Composites by Melt Processing Methods," *Chem. Phys. Lett.*, vol. 330, no. 3–4, pp. 219–225, Nov. 2000.

[180] B. J. Carey, "Tailoring Vertically-Aligned Carbon Nanotube Growth for Poly(dimethylsiloxane)-Infiltrated Nanocomposites," M.S., Rice University, Houston, TX, 2010.

[181] X. Li, X. Zhang, L. Ci, R. Shah, C. Wolfe, S. Kar, S. Talapatra, and P. M. Ajayan, "Air-Assisted Growth of Ultra-Long Carbon Nanotube Bundles," *Nanotechnology*, vol. 19, no. 45, p. 455609, Nov. 2008.

[182] H. Liu, J. Zhai, and L. Jiang, "Wetting and Anti-Wetting on Aligned Carbon Nanotube Films," *Soft Matter*, vol. 2, no. 10, pp. 811–821, 2006.

[183] N. R. Raravikar, L. S. Schadler, A. Vijayaraghavan, Y. Zhao, B. Wei, and P. M. Ajayan, "Synthesis and Characterization of Thickness-Aligned Carbon Nanotube–Polymer Composite Films," *Chem. Mater.*, vol. 17, no. 5, pp. 974–983, Mar. 2005.

[184] S. Boncel, K. K. K. Koziol, K. Z. Walczak, A. H. Windle, and M. S. P. Shaffer, "Infiltration of Highly Aligned Carbon Nanotube Arrays with Molten Polystyrene," *Mater. Lett.*, vol. 65, no. 14, pp. 2299–2303, Jul. 2011.

[185] E. J. Garcia, A. J. Hart, B. L. Wardle, and A. H. Slocum, "Fabrication of Composite Microstructures by Capillarity-Driven Wetting of Aligned Carbon Nanotubes with Polymers," *Nanotechnology*, vol. 18, no. 16, p. 165602, 2007.

[186] W. Chen, L. Qu, D. Chang, L. Dai, S. Ganguli, and A. Roy, "Vertically-Aligned Carbon Nanotubes Infiltrated with Temperature-Responsive Polymers: Smart Nanocomposite Films for Self-Cleaning and Controlled Release," *Chem. Commun.*, no. 2, p. 163, 2008.

[187] L. Ci, J. Suhr, V. Pushparaj, X. Zhang, and P. M. Ajayan, "Continuous Carbon Nanotube Reinforced Composites," *Nano Lett.*, vol. 8, no. 9, pp. 2762–2766, 2008.

[188] A. H. Barber, S. R. Cohen, and H. D. Wagner, "Static and Dynamic Wetting Measurements of Single Carbon Nanotubes," *Phys. Rev. Lett.*, vol. 92, no. 18, p. 186103, May 2004.

[189] K. L. Mittal and A. Pizzi, *Handbook of Sealant Technology*. CRC Press, 2009.

[190] S. W. Sides, J. Curro, G. S. Grest, M. J. Stevens, T. Soddemann, A. Habenschuss, and J. D. Londono, "Structure of Poly(dimethylsiloxane) Melts: Theory, Simulation, and Experiment," *Macromolecules*, vol. 35, no. 16, pp. 6455–6465, Jul. 2002.

[191] J. E. Mark, *Polymer Data Handbook*, 2nd ed. New York: Oxford University Press, 2009.

[192] J. C. McDonald and G. M. Whitesides, "Poly(dimethylsiloxane) as a Material for Fabricating Microfluidic Devices," *Acc. Chem. Res.*, vol. 35, no. 7, pp. 491–499, Jul. 2002.

[193] M. J. Owen, "Why Silicones Behave Funny." Dow Corning, 2005.

[194] S. R. Quake and A. Scherer, "From Micro- to Nanofabrication with Soft Materials," *Science*, vol. 290, no. 5496, pp. 1536–1540, Nov. 2000.

[195] S. J. Clarson, K. Dodgson, and J. A. Semlyen, "Studies of Cyclic and Linear Poly(dimethylsiloxanes): 19. Glass Transition Temperatures and Crystallization Behaviour," *Polymer*, vol. 26, no. 6, pp. 930–934, Jun. 1985.

[196] M. I. Aranguren, "Crystallization of Polydimethylsiloxane: Effect of Silica Filler and Curing," *Polymer*, vol. 39, no. 20, pp. 4897–4903, Sep. 1998.

[197] J. D. Helmer and K. E. Polmanteer, "Supercooling of Polydimethylsiloxane," *J. Appl. Polym. Sci.*, vol. 13, no. 10, pp. 2113–2118, Oct. 1969.

[198] E. L. Warrick, "Crystallinity and Orientation in Silicone Rubber II: Physical Measurements," *J. Polym. Sci.*, vol. 27, no. 115, pp. 19–38, Jan. 1958.

[199] "Polydimethylsiloxane - Wikipedia, the free encyclopedia." [Online]. Available: http://en.wikipedia.org/wiki/Polydimethylsiloxane. [Accessed: 25-Mar-2010].

[200] R. M. Sok, H. J. C. Berendsen, and W. F. van Gunsteren, "Molecular Dynamics Simulation of the Transport of Small Molecules Across a Polymer Membrane," *J. Chem. Phys.*, vol. 96, no. 6, p. 4699, 1992.

[201] D. Hofmann, L. Fritz, J. Ulbrich, and D. Paul, "Molecular Modelling of Amorphous Membrane Polymers," *Polymer*, vol. 38, no. 25, pp. 6145–6155, 1997.

[202] J. N. Lee, C. Park, and G. M. Whitesides, "Solvent Compatibility of Poly(dimethylsiloxane)-Based Microfluidic Devices," *Anal. Chem.*, vol. 75, no. 23, pp. 6544–6554, Dec. 2003.

[203] X. Li, "Tailoring Vertically Aligned Carbon Nanotube Growth and Fabrication of Carbon Nanotube Membrane Filters," Ph.D., Rensselaer Polytechnic Institute, Troy, NY, 2007.

[204] B. Li, M. G. Hahm, Y. L. Kim, H. Y. Jung, S. Kar, and Y. J. Jung, "Highly Organized Two- and Three-Dimensional Single-Walled Carbon Nanotube–Polymer Hybrid Architectures," *ACS Nano*, vol. 5, no. 6, pp. 4826–4834, 2011.

[205] B. J. Carey, P. K. Patra, L. Ci, G. G. Silva, and P. M. Ajayan, "Observation of Dynamic Strain Hardening in Polymer Nanocomposites," *ACS Nano*, vol. 5, no. 4, pp. 2715–2722, Apr. 2011.

[206] M. Motamedi, M. Eskandari, and M. Yeganeh, "Effect of Straight and Wavy Carbon Nanotube on the Reinforcement Modulus in Nonlinear Elastic Matrix Nanocomposites," *Mater. Design*, vol. In Press, Corrected Proof, 2011.

[207] F. Bueche, "Molecular Basis for the Mullins Effect," *J. Appl. Polym. Sci.*, vol. 4, no. 10, pp. 107–114, Jul. 1960.

[208] F. Bueche, "Mullins Effect and Rubber-Filler Interaction," *J. Appl. Polym. Sci.*, vol. 5, no. 15, pp. 271–281, May 1961.

[209] E. M. Dannenberg, "Molecular Slippage Mechanism of Reinforcement," *Trans. Inst. Rub. Ind.*, vol. 42, pp. 26–42, 1966.

[210] E. M. Dannenberg, "The Effects of Surface Chemical Interactions on the Properties of Filler-Reinforced Rubbers," *Rubber Chemistry and Technology*, vol. 48, p. 410, 1975.

[211] S. Govindjee and J. Simo, "A Micro-Mechanically Based Continuum Damage Model for Carbon Black-Filled Rubbers Incorporating Mullins' Effect," *J. Mechan. Phys. Sol.*, vol. 39, no. 1, pp. 87–112, 1991.

[212] R. W. Ogden and D. G. Roxburgh, "A Pseudo–Elastic Model for the Mullins Effect in Filled Rubber," *Proc. Roy. Soc. A*, vol. 455, no. 1988, pp. 2861 –2877, 1999.

[213] N. Aksel and C. Hubner, "The Influence of Dewetting in Filled Elastomers on the Changes of Their Mechanical Properties," *Arch. Appl. Mech.*, vol. 66, no. 4, pp. 231–241, 1996.

[214] W. P. Fletcher and A. N. Gent, "Nonlinearity in the Dynamic Properties of Vulcanized Rubber Compounds," *Rubber Chem. Technol.*, vol. 27, p. 209, 1954.

[215] A. R. Payne, "The Dynamic Properties of Carbon Black-Loaded Natural Rubber Vulcanizates. Part I," *J. Appl. Polym. Sci.*, vol. 6, no. 19, pp. 57–63, Jan. 1962.

[216] J. Ramier, C. Gauthier, L. Chazeau, L. Stelandre, and L. Guy, "Payne Effect in Silica-Filled Styrene–Butadiene Rubber: Influence of Surface Treatment," *J. Polym. Sci., Polym. Phys.*, vol. 45, no. 3, pp. 286–298, Feb. 2007.

[217] V. V. Moshev and S. E. Evlampieva, "Potentiality of the Triboelastic Approach for Clarifying the Filler Reinforcement Mechanism in Elastomers," *Int. J. Solids Struct.*, vol. 42, no. 18–19, pp. 5129–5139, Sep. 2005.

[218] V. V. Moshev and S. E. Evlampieva, "Role of Triboelasticity in Cyclic Behavior of Elastomeric Nanocomposites," *Compos: Mech. Comp. Appl.*, vol. 1, no. 1, pp. 37–44, 2010.

[219] M. R. Falvo, G. J. Clary, R. M. Taylor, V. Chi, F. P. Brooks, S. Washburn, and R. Superfine, "Bending and Buckling of Carbon Nanotubes Under Large Strain," *Nature*, vol. 389, no. 6651, pp. 582–584, Oct. 1997.

[220] J. Feliciano, C. Tang, Y. Zhang, and C. Chen, "Aspect Ratio Dependent Buckling Mode Transition in Single-Walled Carbon Nanotubes Under Compression," *J. Appl. Phys.*, vol. 109, no. 8, p. 084323, 2011.

[221] B. I. Yakobson, C. J. Brabec, and J. Bernholc, "Nanomechanics of Carbon Tubes: Instabilities Beyond Linear Response," *Phys. Rev. Lett.*, vol. 76, no. 14, p. 2511, Apr. 1996.

[222] H. W. Yap, R. S. Lakes, and R. W. Carpick, "Negative Stiffness and Enhanced Damping of Individual Multiwalled Carbon Nanotubes," *Phys. Rev. B*, vol. 77, no. 4, p. 045423, Jan. 2008.

[223] R. Lakes, "Extreme Damping in Compliant Composites with a Negative-Stiffness Phase," *Phil. Mag. Lett.*, vol. 81, no. 2, pp. 95–100, Feb. 2001.

[224] R. A. Ibrahim, "Recent Advances in Nonlinear Passive Vibration Isolators," *J. Sound Vib.*, vol. 314, no. 3–5, pp. 371–452, Jul. 2008.

[225] D. L. Platus, "Negative-Stiffness-Mechanism Vibration Isolation Systems," in *Proceedings of SPIE*, Denver, CO, USA, 1999, pp. 98–105.

[226] T. Jaglinski, D. Kochmann, D. Stone, and R. S. Lakes, "Composite Materials with Viscoelastic Stiffness Greater Than Diamond," *Science*, vol. 315, no. 5812, pp. 620 –622, Feb. 2007.

[227] Z. Hashin and S. Shtrikman, "A Variational Approach to the Theory of the Elastic Behaviour of Multiphase Materials," *J. Mechan. Phys. Sol.*, vol. 11, no. 2, pp. 127–140, Mar. 1963.

[228] P. Poncharal, Z. L. Wang, D. Ugarte, and W. A. de Heer, "Electrostatic Deflections and Electromechanical Resonances of Carbon Nanotubes," *Science*, vol. 283, no. 5407, pp. 1513 –1516, Mar. 1999.

[229] L. Zalamea, H. Kim, and R. B. Pipes, "Stress Transfer in Multi-Walled Carbon Nanotubes," *Compos. Sci. Technol.*, vol. 67, no. 15–16, pp. 3425–3433, Dec. 2007.

[230] C. Q. Ru, "Degraded Axial Buckling Strain of Multiwalled Carbon Nanotubes due to Interlayer Slips," *J. Appl. Phys.*, vol. 89, no. 6, p. 3426, 2001.

[231] A. Pantano, D. M. Parks, and M. C. Boyce, "Mechanics of Deformation of Single- and Multi-Wall Carbon Nanotubes," *J. Mechan. Phys. Sol.*, vol. 52, no. 4, pp. 789–821, Apr. 2004.

[232] C. Bower, R. Rosen, L. Jin, J. Han, and O. Zhou, "Deformation of Carbon Nanotubes in Nanotube-Polymer Composites," *Appl. Phys. Lett.*, vol. 74, no. 22, pp. 3317–3319, May 1999.

[233] J. Suhr, V. Pushparaj, L. Ci, S. Sreekala, X. Zhang, O. Nalamasu, and P. M. Ajayan, "Fatigue Resistance of Aligned Carbon Nanotube Arrays Under Cyclic Compression," *Nat. Nanotechnol.*, vol. 2, no. 7, pp. 417–421, Jul. 2007.

[234] A. Cao, P. L. Dickrell, W. G. Sawyer, M. N. Ghasemi-Nejhad, and P. M. Ajayan, "Super-Compressible Foamlike Carbon Nanotube Films," *Science*, vol. 310, no. 5752, pp. 1307–1310, Nov. 2005.

[235] S. B. Hutchens, A. Needleman, and J. R. Greer, "Analysis of Uniaxial Compression of Vertically Aligned Carbon Nanotubes," *J. Mechan. Phys. Sol.*, vol. 59, no. 10, pp. 2227–2237, 2011.

[236] A. A. Zbib, S. D. Mesarovic, E. T. Lilleodden, D. McClain, J. Jiao, and D. F. Bahr, "The Coordinated Buckling of Carbon Nanotube Turfs Under Uniform Compression," *Nanotechnology*, vol. 19, no. 17, p. 175704, Apr. 2008.

[237] H. D. Wagner and R. A. Vaia, "Nanocomposites: Issues at the Interface," *Mater. Today*, vol. 7, no. 11, pp. 38–42, Nov. 2004.

[238] J. Suhr and N. Koratkar, "Energy Dissipation in Carbon Nanotube Composites: A Review," *J. Mater. Sci.*, vol. 43, no. 13, pp. 4370–4382, Jul. 2008.

[239] J. A. Elliot, A. H. Windle, J. R. Hobdell, G. Eeckhaut, R. J. Oldman, W. Ludwig, E. Boller, P. Cloetens, and J. Baruchel, "In-situ Deformation of an Open-Cell Flexible Polyurethane Foam Characterised by 3D Computed Microtomography," *J. Mater. Sci.*, vol. 37, pp. 1547–1555, 2002.

[240] D. M. Kochmann and W. J. Drugan, "Dynamic Stability Analysis of an Elastic Composite Material Having a Negative-Stiffness Phase," *J. Mechan. Phys. Sol.*, vol. 57, no. 7, pp. 1122–1138, Jul. 2009.

[241] L. Gong and S. Kyriakides, "Compressive Response of Open Cell Foams Part II: Initiation and Evolution of Crushing," *Int. J. Solids Struct.*, vol. 42, no. 5–6, pp. 1381–1399, Mar. 2005.

[242] B. Wetzel, P. Rosso, F. Haupert, and K. Friedrich, "Epoxy Nanocomposites - Fracture and Toughening Mechanisms," *Eng. Fract. Mech.*, vol. 73, no. 16, pp. 2375–2398, Nov. 2006.

[243] W. Zhang, R. C. Picu, and N. Koratkar, "Suppression of Fatigue Crack Growth in Carbon Nanotube Composites," *Appl. Phys. Lett.*, vol. 91, no. 19, p. 193109, 2007.

[244] S. H. Cho, H. M. Andersson, S. R. White, N. R. Sottos, and P. V. Braun, "Polydimethylsiloxane-Based Self-Healing Materials," *Adv. Mater.*, vol. 18, no. 8, pp. 997–1000, 2006.

[245] K. M. Schmoller, P. Fernandez, R. C. Arevalo, D. L. Blair, and A. R. Bausch, "Cyclic Hardening in Bundled Actin Networks," *Nat. Commun.*, vol. 1, no. 9, p. 134, Dec. 2010.

[246] D. Myung, W. Koh, J. Ko, Y. Hu, M. Carrasco, J. Noolandi, C. N. Ta, and C. W. Frank, "Biomimetic Strain Hardening in Interpenetrating Polymer Network Hydrogels," *Polymer*, vol. 48, no. 18, pp. 5376–5387, Aug. 2007.

[247] F. Daver, A. Blake, and M. Cakmak, "Stages of Structural Ordering Leading to Stress Induced Crystallization of PEEK Films: A Mechano-Optical Study on Deformation, Relaxation and Retraction," *Macromolecules*, vol. 42, no. 7, pp. 2626–2633, Apr. 2009.

[248] H. Mahfuz, M. R. Khan, T. Leventouri, and E. Liarokapis, "Investigation of MWCNT Reinforcement on the Strain Hardening Behavior of Ultrahigh Molecular Weight Polyethylene," *J. Nanotech.*, vol. 2011, pp. 1–9, 2011.

[249] S. Toki, I. Sics, B. S. Hsiao, S. Murakami, M. Tosaka, S. Poompradub, S. Kohjiya, and Y. Ikeda, "Structural Developments in Synthetic Rubbers During Uniaxial Deformation by in situ Synchrotron X-Ray Diffraction," *J. Polym. Sci., Polym. Phys.*, vol. 42, no. 6, pp. 956–964, Mar. 2004.

[250] E. Klimov, G. G. Hoffmann, A. Gumenny, and H. W. Siesler, "Low-Temperature FT-NIR Spectroscopy of Strain-Induced Orientation and Crystallization in a Poly(dimethylsiloxane) Network," *Macromol. Rapid Comm.*, vol. 26, no. 13, pp. 1093–1098, 2005.

[251] K. J. Regehr, M. Domenech, J. T. Koepsel, K. C. Carver, S. J. Ellison-Zelski, W. L. Murphy, L. A. Schuler, E. T. Alarid, and D. J. Beebe, "Biological Implications of Polydimethylsiloxane-Based Microfluidic Cell Culture," *Lab Chip*, vol. 9, p. 2132, 2009.

[252] J. Xu, K. M. Razeeb, and S. Roy, "Thermal Properties of Single Walled Carbon Nanotube-Silicone Nanocomposites," *J. Polym. Sci., Polym. Phys.*, vol. 46, no. 17, pp. 1845–1852, 2008.

[253] D. Zhang and H. Meyer, "Molecular Dynamics Study of Polymer Crystallization in the Presence of a Particle," *J. Polym. Sci., Polym. Phys.*, vol. 45, no. 16, pp. 2161–2166, 2007.

[254] T. Dollase, M. Wilhelm, H. W. Spiess, Y. Yagen, R. Yerushalmi-Rozen, and M. Gottlieb, "Effect of Interfaces on the Crystallization Behavior of PDMS," *Interface Sci.*, vol. 11, no. 2, pp. 199–209, Apr. 2003.

[255] H. Li and S. Yan, "Surface-Induced Polymer Crystallization and the Resultant Structures and Morphologies," *Macromolecules*, vol. 44, no. 3, pp. 417–428, Feb. 2011.

[256] P. Levresse, D. L. Feke, and I. Manas-Zloczower, "Analysis of the Formation of Bound Poly(dimethylsiloxane) on Silica," *Polymer*, vol. 39, no. 17, pp. 3919–3924, Aug. 1998.

[257] D. Fragiadakis, L. Bokobza, and P. Pissis, "Dynamics Near the Filler Surface in Natural Rubber-Silica Nanocomposites," *Polymer*, vol. 52, no. 14, pp. 3175–3182, Jun. 2011.

[258] B. Meissner, "Theory of Bound Rubber," *J. Appl. Polym. Sci.*, vol. 18, no. 8, pp. 2483–2491, Aug. 1974.

[259] S. Choi, K. Hwang, and B. Kim, "Influence of Bound Polymer on Cure Characteristics of Natural Rubber Compounds Reinforced with Different Types of Carbon Blacks," *J. Appl. Polym. Sci.*, vol. 98, no. 5, pp. 2282–2289, Dec. 2005.

[260] J. Berriot, F. Martin, H. Montes, L. Monnerie, and P. Sotta, "Reinforcement of Model Filled Elastomers: Characterization of the Cross-Linking Density at the Filler-Elastomer Interface by 1H NMR Measurements," *Polymer*, vol. 44, no. 5, pp. 1437–1447, Mar. 2003.

[261] J. W. Jiang, J. S. Wang, and B. Li, "Thermal Expansion in Single-Walled Carbon Nanotubes and Graphene: Nonequilibrium Green's Function Approach," *Phys. Rev. B*, vol. 80, no. 20, p. 205429, Nov. 2009.

[262] X. Zheng and Q. Xu, "Comparison Study of Morphology and Crystallization Behavior of Polyethylene and Poly(ethylene oxide) on Single-Walled Carbon Nanotubes," *J. Phys. Chem. B*, vol. 114, no. 29, pp. 9435–9444, Jul. 2010.

[263] E. Assouline, A. Lustiger, A. H. Barber, C. A. Cooper, E. Klein, E. Wachtel, and H. D. Wagner, "Nucleation Ability of Multiwall Carbon Nanotubes in Polypropylene Composites," *J. Polym. Sci., Polym. Phys.*, vol. 41, no. 5, pp. 520–527, 2003.

[264] S. Zhang, M. L. Minus, L. Zhu, C.-P. Wong, and S. Kumar, "Polymer Transcrystallinity Induced by Carbon Nanotubes," *Polymer*, vol. 49, no. 5, pp. 1356–1364, Mar. 2008.

[265] K. Lu, N. Grossiord, C. E. Koning, H. E. Miltner, B. van Mele, and J. Loos, "Carbon Nanotube/Isotactic Polypropylene Composites Prepared by Latex Technology: Morphology Analysis of CNT-Induced Nucleation," *Macromolecules*, vol. 41, no. 21, pp. 8081–8085, Nov. 2008.

[266] C. Y. Li, L. Li, W. Cai, S. L. Kodjie, and K. K. Tenneti, "Nanohybrid Shish-Kebabs: Periodically Functionalized Carbon Nanotubes," *Adv. Mater.*, vol. 17, no. 9, pp. 1198–1202, May 2005.

[267] R. Haggenmueller, J. E. Fischer, and K. I. Winey, "Single Wall Carbon Nanotube/Polyethylene Nanocomposites: Nucleating and Templating Polyethylene Crystallites," *Macromolecules*, vol. 39, no. 8, pp. 2964–2971, Apr. 2006.

[268] L. Li, B. Li, M. A. Hood, and C. Y. Li, "Carbon Nanotube Induced Polymer Crystallization: The Formation of Nanohybrid Shish–Kebabs," *Polymer*, vol. 50, no. 4, pp. 953–965, Feb. 2009.

[269] W. Hu, D. Frenkel, and V. B. F. Mathot, "Simulation of Shish-Kebab Crystallite Induced by a Single Prealigned Macromolecule," *Macromolecules*, vol. 35, no. 19, pp. 7172–7174, 2002.

[270] P. R. Sundararajan, "Crystalline Morphology of Poly(dimethylsiloxane)," *Polymer*, vol. 43, no. 5, pp. 1691–1693, Mar. 2002.

[271] G. Damaschun, "Rontgenographische Untersuchung der Struktur von Silikongummi," *Colloid Polym. Sci.*, vol. 180, no. 1, pp. 65–67, Jan. 1962.

[272] P. A. Albouy, "The Conformation of Poly(dimethylsiloxane) in the Crystalline State," *Polymer*, vol. 41, no. 8, pp. 3083–3086, Apr. 2000.

[273] J. Khan, S. E. Harton, P. Akcora, B. C. Benicewicz, and S. K. Kumar, "Polymer Crystallization in Nanocomposites: Spatial Reorganization of Nanoparticles," *Macromolecules*, vol. 42, no. 15, pp. 5741–5744, 2009.

[274] F. Deng, M. Ito, T. Noguchi, L. Wang, H. Ueki, K. Niihara, Y. A. Kim, M. Endo, and Q.-S. Zheng, "Elucidation of the Reinforcing Mechanism in Carbon Nanotube/Rubber Nanocomposites," *ACS Nano*, vol. 5, no. 5, pp. 3858–3866, May 2011.

[275] J. S. Becker, R. D. Brown, D. R. Killelea, H. Yuan, and S. J. Sibener, "Comparative Surface Dynamics of Amorphous and Semicrystalline Polymer Films," *Proceedings of the National Academy of Sciences*, vol. 108, no. 3, pp. 977 –982, Jan. 2011.

[276] Y. Li, D. Wei, C. C. Han, and Q. Liao, "Dynamics of Polymer Melts Confined by Smooth Walls: Crossover from Nonentangled Region to Entangled Region," *J. Chem. Phys.*, vol. 126, no. 20, p. 204907, 2007.

[277] J. Martín, M. Krutyeva, M. Monkenbusch, A. Arbe, J. Allgaier, A. Radulescu, P. Falus, J. Maiz, C. Mijangos, J. Colmenero, and D. Richter, "Direct Observation of Confined Single Chain Dynamics by Neutron Scattering," *Phys. Rev. Lett.*, vol. 104, no. 19, p. 197801, May 2010.

[278] A. Karatrantos and N. Clarke, "A Theoretical Model for the Prediction of Diffusion in Polymer/SWCNT Nanocomposites," *Soft Matter*, 2011.

[279] J. L. Valentín, I. Mora-Barrantes, J. Carretero-González, M. A. López-Manchado, P. Sotta, D. R. Long, and K. Saalwächter, "Novel Experimental Approach To Evaluate Filler–Elastomer Interactions," *Macromolecules*, vol. 43, no. 1, pp. 334–346, Jan. 2010.

[280] J. Berriot, F. Lequeux, H. Montes, and H. Pernot, "Reinforcement of Model Filled Elastomers: Experimental and Theoretical Approach of Swelling Properties," *Polymer*, vol. 43, no. 23, pp. 6131–6138, 2002.

[281] C. Wei, D. Srivastava, and K. Cho, "Thermal Expansion and Diffusion Coefficients of Carbon Nanotube-Polymer Composites," *Nano Lett.*, vol. 2, no. 6, pp. 647–650, Jun. 2002.

[282] D. Bordeaux and J. P. Cohen-Addad, "Silica-Filled Polydimethylsiloxane: Crystallization Process of the Adsorbed Layer," *Polymer*, vol. 31, no. 4, pp. 743–748, Apr. 1990.

[283] F. C. Schilling, M. A. Gomez, and A. E. Tonelli, "Solid-State NMR Observations of the Crystalline Conformation of Poly(dimethylsiloxane)," *Macromolecules*, vol. 24, no. 24, pp. 6552–6553, Nov. 1991.

[284] G. Strobl, "From the Melt via Mesomorphic and Granular Crystalline Layers to Lamellar Crystallites: A Major Route Followed in Polymer Crystallization?," *Eur. Phys. J. E*, vol. 3, no. 2, pp. 165–183, Oct. 2000.

[285] A. Maus and K. Saalwächter, "Crystallization Kinetics of Poly(dimethylsiloxane) Molecular-Weight Blends - Correlation with Local Chain Order in the Melt?," *Macromol. Chem. Physic.*, vol. 208, no. 19–20, pp. 2066–2075, 2007.

[286] S. Kimata, T. Sakurai, Y. Nozue, T. Kasahara, N. Yamaguchi, T. Karino, M. Shibayama, and J. A. Kornfield, "Molecular Basis of the Shish-Kebab Morphology in Polymer Crystallization," *Science*, vol. 316, no. 5827, pp. 1014 –1017, May 2007.

[287] M. L. Minus, H. G. Chae, and S. Kumar, "Single Wall Carbon Nanotube Templated Oriented Crystallization of Poly(vinyl alcohol)," *Polymer*, vol. 47, no. 11, pp. 3705–3710, May 2006.

[288] A. L. Svistkov, "A Continuum-Molecular Model of Oriented Polymer Region Formation in Elastomer Nanocomposite," *Mech. Solids*, vol. 45, no. 4, pp. 562–574, Oct. 2010.

[289] J. N. Coleman, M. Cadek, K. P. Ryan, A. Fonseca, J. B. Nagy, W. J. Blau, and M. S. Ferreira, "Reinforcement of Polymers with Carbon Nanotubes. The Role of an Ordered Polymer Interfacial Region. Experiment and Modeling," *Polymer*, vol. 47, no. 26, pp. 8556–8561, Dec. 2006.

[290] C. Wei, D. Srivastava, and K. Cho, "Structural Ordering in Nanotube Polymer Composites," *Nano Lett.*, vol. 4, no. 10, pp. 1949–1952, Oct. 2004.

[291] J. L. Leblanc, "Rubber-Filler Interactions and Rheological Properties in Filled Compounds," *Prog. Polym. Sci.*, vol. 27, no. 4, pp. 627–687, May 2002.

[292] L. A. Golotina, L. L. Kozhevnikova, and T. B. Koshkina, "Investigation of the Mechanical Behavior of Two-Component Granular Composites in Terms of Structural Models," *Mech. Compos. Mater.*, vol. 43, no. 2, pp. 127–132, Mar. 2007.

[293] P. Cassagnau and F. Mélis, "Non-Linear Viscoelastic Behaviour and Modulus Recovery in Silica Filled Polymers," *Polymer*, vol. 44, no. 21, pp. 6607–6615, Oct. 2003.

Appendix A – WAXS Modeling

This model was developed by Dr. Kevin Yager, Assistant Materials Scientist at the Center for Functional Nanomaterials, Brookhaven National Laboratory

The MWNT wall spacing of $d = 0.34$ nm leads to a scattering peak at $q = 2\pi/d = 1.84$ Å^{-1} in reciprocal space. Although the intensity of this WAXS scattering peak arises predominantly from the intra-tube layer correlations, we demonstrate that inter-tube interactions or correlations can also affect the scattering intensity. A straightforward model is used wherein a candidate realspace electron density distribution is simulated within a finite and discretized simulation box. We use a theoretical scattering-length-density (SLD) for PDMS of $SLD_{\mathrm{PDMS}} \approx 8.86\times10^{-6}$ Å^{-2} for the matrix. The MWNT walls are simulated using concentric rings, which have a Gaussian radial profile, and whose average electron density is matched to that for bulk graphite: $SLD_{\mathrm{MWNT}} \approx 18.32\times10^{-6}$ Å^{-2}. The center of the MWNT is assumed to be empty (0×10^{-6} Å^{-2}). For simplicity we model perfectly aligned infinite tubes, in which case a representative 2D cross-section is used to compute the in-plane scattering (q_r direction). The reciprocal space scattering is computed from the realspace electron density distribution using Equation 6.1.

Where $F(q_x,q_y)$ is the two-dimensional form factor for the simulation volume, which is computed by integrating the realspace electron density distribution, $\rho(x,y)$. The outer integral averages over all possible in-plane orientations, P, which adds an assumption of in-plane isotropy and converts the scattering to a one-dimensional

profile. The equation was solved numerically for a wide range of MWNT configurations. Specifically, six MWNTs were added to the simulation volume. For some simulations, the MWNTs were intentionally placed in direct contact. In other simulations, a small gap was placed between the MWNTs. Finally, random configurations of the nanotubes were simulated to account for a 'well-dispersed' phase.

$$
\begin{aligned}
P(q_r) &= \int_0^{2\pi} |F(q_x, q_y)|^2 \, \mathrm{d}\phi \\
&= \int_0^{2\pi} \left| \int \rho(\mathbf{r}) e^{i\mathbf{q}\cdot\mathbf{r}} \mathrm{d}V \right|^2 \mathrm{d}\phi \\
&= \int_0^{2\pi} \left| \int_{-\infty}^{+\infty} \int_{-\infty}^{+\infty} \rho(x,y) e^{iq_x x} e^{iq_y y} \mathrm{d}x\mathrm{d}y \right|^2 \mathrm{d}\phi \\
&= \int_0^{2\pi} \left| \int_{-\infty}^{+\infty} \int_{-\infty}^{+\infty} \rho(x,y) e^{iq_r \sin(\phi) x} e^{iq_r \cos(\phi) y} \mathrm{d}x\mathrm{d}y \right|^2 \mathrm{d}\phi
\end{aligned}
$$

Equation 6.1 – Calculation of reciprocal space scattering.

The scattering intensity near the peak of interest was summed in order to provide a measure of expected WAXS signal. It was seen that MWNTs in direct (or near) contact had, on average, higher scattering at the peak of interest as compared to the average for 'dispersed' nanotubes. This is to be expected, since MWNTs in

direct contact will have constructive correlations between their individual wall/wall scattering, which will enhance the overall signal. In essence, the structure factor for well-associated nanotubes has a maximum near small tube/tube distances. We note that the present simulation likely underestimates the difference between the states, because in all cases the tubes were assumed to be perfectly aligned. In a physical system, tubes in near contact will have a tendency to align with respect to each other, whereas tubes further apart (i.e. dispersed) will have lower correlation between their orientations. Uncorrelated orientations would be expected to further reduce the intra-nanotube component of the scattering peak.